



HAL
open science

Quantum and dynamical back-action effects using a gram-scale mechanical resonator in a high-finesse optical cavity

Alexandros Tavernarakis

► **To cite this version:**

Alexandros Tavernarakis. Quantum and dynamical back-action effects using a gram-scale mechanical resonator in a high-finesse optical cavity. Atomic Physics [physics.atom-ph]. Université Pierre et Marie Curie - Paris VI, 2012. English. NNT: . tel-00813308

HAL Id: tel-00813308

<https://theses.hal.science/tel-00813308>

Submitted on 15 Apr 2013

HAL is a multi-disciplinary open access archive for the deposit and dissemination of scientific research documents, whether they are published or not. The documents may come from teaching and research institutions in France or abroad, or from public or private research centers.

L'archive ouverte pluridisciplinaire **HAL**, est destinée au dépôt et à la diffusion de documents scientifiques de niveau recherche, publiés ou non, émanant des établissements d'enseignement et de recherche français ou étrangers, des laboratoires publics ou privés.

LABORATOIRE KASTLER BROSSSEL



Ph.D thesis of the Université Paris VI

Speciality : Quantum Physics

defended by

Alexandros Tavernarakis

to obtain the title of Ph.D. of science of the Université Paris VI

Thesis title:

Quantum and dynamical back-action effects using a gram-scale mechanical resonator in a high-finesse optical cavity

Defended in front of the commission composed by:

M.	Philippe BOUYER	Examinator
M.	Tristan BRIANT	Invited member
M.	Fabien CAVALIER	Examinator
M.	Jack HARRIS	Reviewer
M.	Antoine HEIDMANN	Thesis supervisor
M.	Jean-Philippe POIZAT	Reviewer
Mme	Catherine SCHWOB	Examinator

Contents

Remerciements	v
Introduction	1
1 Optomechanical coupling	5
1.1 Small-displacement measurements	5
1.2 Sensitivity improvement with a cavity	6
1.3 Optomechanical coupling in a movable mirror cavity	8
1.3.1 Quantum nature of light	8
1.3.2 Movable mirror cavity	11
1.3.3 Solving the evolution equations	13
1.3.4 Fluctuations in a movable mirror cavity	15
1.4 Limits in interferometric measurements	16
1.4.1 Measurement noise	17
1.4.2 Radiation-pressure back-action	18
1.4.3 The standard quantum limit	19
1.5 Observing quantum fluctuations	21
1.5.1 Thermal noise	21
1.5.2 Introducing Optomechanical Correlations	23
1.5.3 Squeezing with a movable mirror cavity	24
1.6 Experiment: basic elements	25
1.6.1 Movable mirror cavity	25
1.6.2 Laser source	28
1.6.3 Tunable double injection	29
1.6.4 Frequency stabilization: the Pound-Drever-Hall technique	33
1.6.5 Homodyne Detection	37
1.6.6 Complete measurement sensitivity	39
1.7 Position calibration	39
1.7.1 Pound-Drever-Hall calibration	40
1.7.2 Calibration peaks	41
1.8 Group past experimental results	42
1.8.1 Thermal noise observation and measurement sensitivity	42
1.8.2 Full mechanical characterization	43
1.8.3 Cold damping	45
1.8.4 Back-action cancellation	47
1.9 Optomechanics worldwide	48
2 Radiation pressure effects	51
2.1 Optomechanical classical correlations	51
2.1.1 Implementing the modulator	52
2.1.2 Optical isolation	53
2.1.3 Construction of a classical intensity noise	54

2.1.3.1	Hardware	55
2.1.3.2	Software	56
2.1.4	Experimental results	59
2.1.4.1	Experimental protocol	60
2.1.4.2	Out of mechanical resonance	61
2.1.4.3	At mechanical resonance	62
2.1.5	Optomechanical correlations in the thermal regime: averaging	63
2.1.5.1	Experimental demonstration	64
2.1.6	Averaging restrictions	65
2.1.6.1	Averaging time	66
2.2	Backaction amplification	72
2.2.1	Sensitivity improvement in a detuned cavity	72
2.2.2	Experimental protocol and results	75
3	Development of the experimental setup	79
3.1	Balanced detection	79
3.1.1	Designing the photodetectors	80
3.1.2	Constructing the detector	81
3.1.3	Balancing of the detector	84
3.2	Mode cleaner cavity	86
3.2.1	Optical calibration	86
3.2.2	High-finesse filtering cavity	90
3.2.3	Cavity lock-in	95
3.2.4	Implementation of the filtering cavity	97
3.2.5	Difficulties met while implementing the high-finesse filtering cavity	99
3.2.6	Feed-forward stabilization	101
3.2.6.1	Homodyne detection changes	102
3.2.7	Use of an Acousto-Optic Modulator	105
3.2.8	Piezoelectric-implemented measurement cavity	111
4	Contamination feedback loop	115
4.1	Contamination effect in a detuned cavity	115
4.2	Contamination effect on optomechanical correlations	117
4.3	Characterization of the contamination effect	119
4.4	A lock-in scheme	120
4.5	Contamination-based lock-in	123
4.5.1	Experimental realization	124
4.5.1.1	Low-frequency measurement of a signal	128
4.5.2	Experimental limits	130
4.5.2.1	Slope fluctuations	130
4.5.2.2	Detection noise	132
4.5.3	Comparison with the Pound-Drever scheme	132

5	Towards quantum correlations at ambient temperature	135
5.1	Multi-modal response of the movable mirror	135
5.1.1	Thermal background effect on the response	137
5.2	Measurement of the mirror response to a radiation-pressure force	138
5.2.1	Experimental setup	138
5.2.2	Experimental results and signal-to-noise ratio	140
5.3	Towards quantum radiation-pressure effects at room temperature	143
5.4	Stability criterion	144
5.5	Laser drift effects in optomechanical correlations	144
5.5.1	Experimental setup	147
5.5.2	Experimental results	151
	Conclusion	157
	Bibliography	161

Remerciements

Ce manuscrit décrit les travaux que j'ai effectués pendant presque 4 ans de thèse au Laboratoire Kastler Brossel.

Tout d'abord, j'aimerais remercier Paul Indelicato qui m'a accueilli dans le laboratoire qu'il dirigeait. Merci à Catherine Schwob pour avoir accepté d'être la présidente du jury. Je tiens à remercier mes deux rapporteurs, Jean-Philippe Poizat et Jack Harris, qui malgré leurs emplois du temps chargés ont trouvé le temps de lire ce manuscrit avec beaucoup d'attention et m'ont fait de nombreuses remarques constructives. Merci enfin à Fabien Cavalier et Philippe Bouyer de s'être déplacés pour faire aussi partie du jury.

Je dois une gratitude infinie à mon directeur de thèse, Antoine Heidmann. Il m'a donné l'opportunité de faire une thèse dans des conditions presque idéales : l'accès à une expérience conçue à la perfection, un soutien logistique sans défaut et un encadrement intense et complet, malgré ses nombreuses obligations administratives. Merci pour ton soutien, ta patience et ta volonté de me suivre même dans la salle de manip pour tourner les boutons avec moi quand j'en avais besoin ! Merci de m'avoir appris plein de choses; au sein de ton équipe, j'ai pu devenir un peu plus grand.

J'aimerais aussi remercier mon co-directeur de thèse Tristan Briant, de loin le meilleur optomécanicien que je connais. Merci de m'avoir supporté chaque fois que je venais t'interrompre dans ton bureau pour te parler de mes soucis expérimentaux. Après cette petite aventure, je sens que non seulement j'ai eu un encadrant avec plein de qualités pédagogiques mais, en plus, j'ai aussi gagné un ami.

Un grand merci aussi à mon troisième chef, Pierre-François. J'ai beaucoup apprécié ta rapidité intellectuelle, les discussions toujours très denses et bien sûr ton humour cynique qui me faisait toujours marrer. Un merci particulier pour le support critique que tu m'as offert à la toute fin de cette thèse. (Je n'oublie pas ta côte de boeuf magique sur ta terrasse...)

Je dois un énorme merci à Pierre Verlot sans qui je n'aurais jamais pu finir cette thèse. Il m'a fait découvrir la manip "historique" de l'équipe et son dopage psychologique dans des moments difficiles de la thèse a été crucial. Merci pour les bouteilles de Martini qu'on buvait comme de l'eau, les nombreuses entrecôtes, les goûts musicaux (un peu kitsch des fois...) qu'on a partagés et les sessions de "metallo-jam" qu'on faisait.

Merci aussi aux anciens doctorants de l'équipe qui, même si je n'ai jamais eu la chance de les rencontrer, ont contribué au développement de cette manip : Yassine Hadjar et Thomas Caniard.

J'ai eu la chance aussi de partager la même salle de manip avec Aurélien, un vrai champion pas seulement en physique expérimentale mais également -et c'est bien plus important- en cuisine : les soirées dans votre (merci aussi Sophie !) cuisine font partie de mes souvenirs parisiens les plus chaleureux ! J'ai eu un grand overlap avec un jeune cadre du PS : Thomas Antoni qui est maintenant MdC à l'Ecole Centrale. Merci pour toutes les soirées à "L'inévitable", et pour m'avoir aidé à comprendre "comment ça marche". Je souhaite que tu obtiennes tout ce dont tu rêvais dans ton nouveau métier. Je remercie Chiara Molinelli pour sa gentillesse et son sourire. Je n'oublie pas Kevin à qui je souhaite une fin de thèse bien réussie. Pendant cette thèse, j'ai eu aussi l'opportunité d'interagir avec de nombreux stagiaires : Manu Van Brackel, Sophie, Mathieu, Val, Elie, Juliette et Cédric. Merci à tous.

Je remercie les nouveaux arrivants de l'équipe et je leurs souhaite plein de succès : Sam, Dani, Thibault et Salim. Un grand merci à Leo (ou alors Justin...) avec qui non seulement j'ai partagé un peu la même salle de manip mais aussi le même appartement, et avec qui j'ai appris à courir sur les quais de Seine.

J'ai aussi envie de remercier beaucoup d'autres personnes qui, d'une façon ou d'une autre, ont contribué à mon bien-être pendant toutes ces années : Lucile, pour avoir accepté mon tempérament un peu direct. Merci d'avoir écouté mes histoires et d'être devenue ma partenaire de tennis numéro 1 ! Pu, pour les nombreuses bières qu'on a bues ensemble quand tout le monde était parti du labo, pour le voyage en Chine que j'ai presque fait... Claire, pour ton très grand sourire. Giulia, pour les emails avec des chansons gréco-turques que tu m'envoyais, pour ta chaleur et ton optimisme. Alberto et Andre, pour m'avoir donné la motivation de reprendre le tennis après tellement longtemps. Val, pour tes renders 3D (voir la figure 3.7) et pour les moments géniaux dans la salle de manip qu'on a partagés. Depuis, l'alignement d'une cavité est devenu une expérience inoubliable... Clément, pour les 20 euros que tu m'as avancés pour que je puisse rentrer chez moi. Panayotis, pour toutes les fois où tu es passé me voir dans mon bureau pour m'encourager. Jonathan, for just being a good ol'american guy. Oxana, ma Russe préférée, pour ta curiosité infinie. Merci à tous les autres thésards/post-docs pour les petits moments qu'on a partagés (je n'ai plus de place) : Benoît, Michaël, Jérôme, Jean-François, Romain, Roman... Georges et Fred, pour les sessions de double guitare de metallica que l'on faisait. François, pour les moments de tension qu'on a partagés sur un court de tennis. Grâce à toi, je suis devenu un meilleur joueur de tennis. Sergi, pour toutes les pseudointellectuelles discussions qu'on faisait en se promenant à Paris. Fred, Ben, pour les petits moments d'amitié qu'on a partagés ; merci également à Quentin et Seb.

Joanna, parce que tu étais à mes côtés dans les bons moments, mais surtout parce que tu ne m'as pas lâché dans les mauvais.

Margarita, Betty, Popi, pour les plats délicieux que vous me prépariez à Anafi quand je rédigeais les 70 premières pages de ce manuscrit. Les frères Gorgorapti, pour tous les étés qu'on a passés ensemble et les souvenirs inoubliables que j'ai avec vous.

Les personnes du secrétariat ont joué un rôle plus qu'important pour le bon déroulement de ce travail : Monique, Laëtitia et Geneviève ont été terriblement efficaces et présentes chaque fois que j'ai eu un problème administratif. Vous m'avez beaucoup facilité la vie et pour cela je vous remercie. La même chose est valable pour l'atelier électronique dans lequel j'ai passé quand même beaucoup de temps. J'ai pu y profiter des conseils précieux de Brigitte et de Jean-Pierre. Merci aussi à Serge Begon pour son support informatique, mais aussi pour la petite clope de temps en temps à l'entrée de la pyramide. Merci également à Corinne Poisson. L'atelier de mécanique a contribué à ce travail à de nombreuses occasions. Merci à vous, Jean-Michel, Pascal et tous les autres de l'atelier. Merci à Annick pour son aide précieuse à la préparation du pot de thèse.

Finalement, je tiens à remercier les chercheurs permanents que j'ai eu la chance de croiser dans les couloirs du laboratoire pendant ces quatre années : Nicolas, Pierre, Brahim, Julien, Elisabeth, Claude, Alberto, Dominique et Lucile.

Introduction

In the beginning of the twentieth century a new theory came and completely changed the way physicists interpret the world. This theory was given the name 'Quantum Mechanics' inspired from various experimental evidence indicating that physical quantities, such as the energy of a particle for instance, only exist with discrete values called quanta. Quantum Mechanics arose great controversy amongst contemporary scientists; it suffices for us to remember the legendary debates between Albert Einstein and Niels Bohr on the interpretation of this, then, new theory. It's easy to understand why Quantum Mechanics has gathered so much controversy as its foundations come in direct contradiction to the world as it is directly observed by our senses or as it is described by Newtonian classical mechanics; the trajectory of a classical particle, the deterministic motion of a mass to name a few. Indeed, there lies the revolutionary aspect of Quantum Mechanics since it gave scientists the tools to further understand the microscopic world and helped put into the same theoretical framework almost all of the four fundamental interactions.

One of the grave fundamental ambiguities of the Quantum Mechanics is the quantum measurement problem. It is known that in contrast to a classical system, where the evolution of an object may be repeatedly measured, the measurement of a quantum system leads to its permanent perturbation, leading to the state reduction of the measured object, what is described in standard Quantum Mechanics textbooks as von Neumann's reduction postulate. It is a relatively difficult notion to comprehend conceptually and many thought experiments such as Heisenberg's microscope have helped towards this direction. It consists in attaching a stick to a body whose position one wants to measure. A photon flux is then sent towards the stick and the experimenter awaits that one photon is scattered by the stick towards a photographic plate leaving a trace of its position. However, the photon presents a momentum, a part of which is imported to the stick, thus perturbing its position. This perturbation leads to an imprecision of the object's measured position and it is known as the quantum back-action effect describing the interaction between the quantum system and the probe apparatus. Experimentally, this effect sets a lower quantum limit to the sensitivity of a measurement. The work of this thesis is directly related to the experimental study of this effect.

Indeed, our field of study concerns the optomechanical coupling between the light and a movable mirror; a system presenting direct analogies to Heisenberg's microscope. A probe field is coupled to the mirror in order to measure its position with a great accuracy. A momentum exchange between the field photons and the mirror occurs, leading to a fundamental disturbance of the mirror and finally setting a limit to the measurement sensitivity. The observation of this limit, and thus the quantum-back action effect of the displacement measurement caused by the probe field radiation pressure, presents a great experimental challenge and is the main goal of this work.

Interferometry has been a great tool in this direction as it helped to drastically improve the sensitivity of optical measurements. For instance, the homodyne detection, the principal tool used to detect mirror displacements in our experimental setup, is nothing more than a sophisticated Michelson interferometer, sensible enough in order to observe radiation-pressure effects. In fact, related techniques are expected, in the near-future, to allow for the detection variations on the spacetime metric when a gravitational wave induces a small apparent length

variation of the interferometer's arm. Gravitational waves are predicted by Einstein's general relativity and until now their existence is only prove indirectly [1, 2] To this purpose giant gravitational antennas have been constructed in various parts of the world. The experimental observation of the quantum-back action effect on a table-top system, can also be seen under this point of view: an effort in order to increase the sensitivity of optical measurements. Indeed, the sensitivity of these gravitational antennas is expected to be quantum-limited and the use of squeezed sources of light will be required to further increase the sensitivity by surpassing the standard quantum limits of the measurement. In fact, the field of research of optomechanics as a sensitivity study of optical measurement, has emerged in the beginning of the 80's for such motivations.

Although the measurement apparatus can provide the necessary sensitivity to observe quantum phenomena, a great experimental limitation has prevented until now to do so. This limitation is imposed by the residual thermal noise of the mirror, whose effect is significantly greater than that of quantum effects and has forced research groups to use cryogenic techniques drastically increasing the experimental complexity.

The first chapter is an introduction providing all the theoretical framework of the optomechanical coupling most notably the introduction of the small-displacement measurement of a movable mirror, the use of a Fabry-Perot cavity in order to increase the measurement sensitivity [3–8] and the semi-classical approach permitting to write down the associated quantum fluctuations leading to the so-called Standard Quantum Limit which, in turn, defines the optimal sensitivity for a given incident optical power. In the following, the strategy in order to experimentally demonstrate the associated quantum limit will be described. The optomechanical correlations will then be introduced as a direct method to experimentally demonstrate the measurement back-action effects; the idea being to couple to the cavity two different laser beams -a pump and a probe- one used to induce a mirror displacement and the other one to measure it. We will end this chapter by describing the past experimental results obtained by the group.

In the second chapter we will describe two experiments demonstrating radiation-pressure effects. The first is a demonstration of pump-probe optomechanical correlations using a classical intensity noise to simulate intensity quantum fluctuations. The most spectacular result of this experiment is in fact the demonstration of optomechanical correlations, even with a very low signal-to-noise ratio, via a time-averaging technique in order to suppress the associated thermal noise. In particular, we have shown that at low temperature (4 K) the experiment has the necessary sensitivity to demonstrate the measurement quantum back-action. In addition, all the limitations will be described: the contamination effect masking any optomechanical correlations imposing a strict laser frequency stability criterion and the needed averaging time. The second experiment we will describe is about radiation-pressure effects in a detuned cavity and is directly related to gravitational-wave research. It is known that at a detuned cavity, an optical spring is created leading to an effective mechanical susceptibility of the mirror that results in a frequency shift of the mirror's movement. The optical spring can the be used to amplify an apparent length variation of the cavity (a laser frequency modulation or a passing gravitational wave for instance) and can lead to a sensitivity better than the associated standard quantum limit.

The third chapter describes all the developments made to the existing experimental setup during this work. Most notably, the update of the detectors (homodyne and balanced detectors) and the implementation of a high-finesse mode-cleaner cavity capable of providing a quantum-

noise limited laser beam up to 10 mW at 1 MHz. This last point is considered to be a critical one as it can increase the signal-to-noise ratio S_x^{rad}/S_x^T by one order of magnitude. We will then describe all the complexities induced to the experimental setup by this cavity and the consequent set-up changes concerning the various feedback loops.

In the fourth chapter, we will describe a novel technique which may be used to lock the laser frequency on a cavity via a feedback loop. Indeed, a great limitation towards the observation of quantum optomechanical correlations is the fact that locking imperfections result in a contamination effect of the measured intensity quadrature severely damaging the optomechanical correlations. We will describe how a direct measurement of the cavity detuning can be made using this contamination effect. This technique is based on the derivation of an error signal based on a coherent drive of the movable mirror, resulting in a contamination signal in the reflected intensity of the field coupled to the cavity. We will finally attempt a comparison between this novel technique and the traditional Pound-Drever-Hall technique widely used in this kind of table-top experiments.

In the final fifth chapter, we will describe how we have implemented all the work described in the two previous chapters in order to design an experiment capable of observing quantum optomechanical correlations at room temperature.

Optomechanical coupling

Since the invention of the laser in the late sixties the research domain dealing with the experimental demonstration of intriguing concepts of quantum mechanics has exploded. Light-matter interaction has given rise to some beautiful experiments. They have helped researchers to test theoretical concepts developed in the beginning of the twentieth century and to examine the limits between the classical and the quantum world, a subject widely discussed by physicists and philosophers until today. In parallel, a great scientific effort has started in the late seventies: the experimental observation of gravitational waves [9–14] and, thus, a direct proof of Albert Einstein general relativity theory. Giant Michelson interferometers were constructed for this reason and some physicists [15, 16] developed theories on the fundamental quantum properties of light and their impact to the sensitivity limits of the gravitational antennas. These theories finally resulted in a slightly different form of a light-matter interaction compared to the usual ones, based on atoms or non-linear media: the interaction between light and a moving mirror, or in other words the optomechanical coupling. When a photon flux is reflected on a mirror the photons will slightly push the mirror, thus resulting in its motion. This movement will, in return, induce a phase shift of the reflecting beam. This simple concept can be a tool to explore some very interesting aspects of the quantum world such as the fundamental quantum limits in interferometric measurements, the understanding of back-action effects in quantum measurements and even the manipulation of both the light and the mirror by the optomechanical coupling, allowing for example to perform quantum optics experiments with optomechanical systems.

In this first chapter we will briefly describe the physics behind the optomechanical coupling and we will discuss fundamental phenomena that can be demonstrated using this coupling. Some major experimental results obtained by both the international community working on the optomechanical coupling and the group at the Laboratoire Kastler Brossel will be briefly described as well. We will present the main issues concerning radiation-pressure effects and quantum limits in optical measurements, and we will describe the basic elements of our experimental setup. We will finally explain how our experiment can measure very small displacements of mirrors, at an unprecedented sensitivity of about 10^{-20} m, and we will briefly present previous results obtained with this setup.

1.1 Small-displacement measurements

Interference effects have been demonstrated, or used, in the past by well known physicists. Isaac Newton first demonstrated this effect with his famous interference rings, Young gave another demonstration of this effect with his brilliant two-slits experiment which continues until today to give very useful insight into the physical meaning of the Heisenberg uncertainties.

Another well known experiment is of course the Michelson and Morley experiment where they used an interferometer in order to observe the mysterious “ether”. In fact, -thanks to its great sensitivity reaching resolutions of a small fraction of a wavelength- interferometry techniques are nowadays widely used in numerous scientific applications : optical cavities, spectrometers, wavemeters, holography, astronomy, and many more.

The core of our table-top experiment is the small-displacement measurement of a vibrating mirror. An elaborated interferometer technique is used in order to perform this measurement which will be described in detail in the following. We will start by describing the interferometry-based displacement measurement using a laser beam and a single moving mirror and we will continue by describing how a robust small-displacement measurement can be performed by using a Fabry-Perot cavity instead of a single mirror.

The simplest system consists in a suspended mirror and a light beam reflected upon it. The mirror undergoes the radiation-pressure force of the beam resulting in a displacement δx , as depicted in Figure 1.1. Consequently, the optical path of the laser beam will be altered. It is well known that the phase shift of the reflected beam will contain the information on the mirror displacement, which can easily be accessed by an interferometric technique. In particular, the reflected beam phase will be shifted by a quantity equal to:

$$\delta\phi_{out} = 4\pi \frac{\delta x}{\lambda}, \quad (1.1)$$

where λ is the laser wavelength. This expression shows that the displacement of the mirror can be measured by comparing it to the light wavelength. There lies the core of the detection of the mirror displacements since the phase shift of the reflected beam is sensitive to the position of the mirror, δx . Experimentally, a Michelson interferometer is used to measure this phase shift, achieving a resolution of a small fraction of the wavelength.

1.2 Sensitivity improvement with a cavity

The sensitivity of the displacement measurement can be considerably increased by using a single input Fabry-Perot cavity instead of a single moving mirror. Let us consider a system similar to the one depicted in Figure 1.2(a), with a second mirror (so-called the coupling mirror), exhibiting a non-zero transmission placed in front of the moving mirror which is assumed to be perfectly reflecting. This system drastically increases the sensitivity of the displacement measurement. Indeed, a Fabry-Perot cavity exhibits constructive interferences when the cavity length L is a multiple of the half wavelength $\lambda/2$. As the cavity approaches such an optical resonance, the intracavity intensity follows a Lorentzian dependence known as an Airy peak.

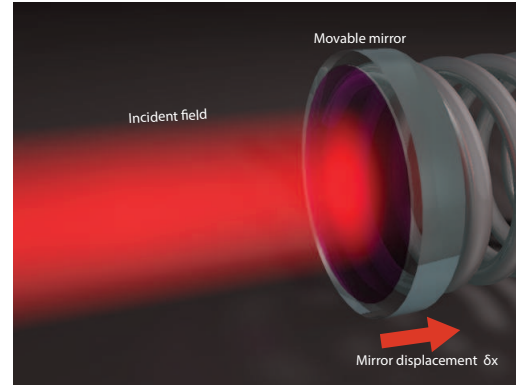


Figure 1.1: Simple model of optomechanical coupling: a laser beam gets reflected by a mirror. Due to momentum exchange between the two, the mirror is displaced and, in turn, the reflected beam is phase shifted.

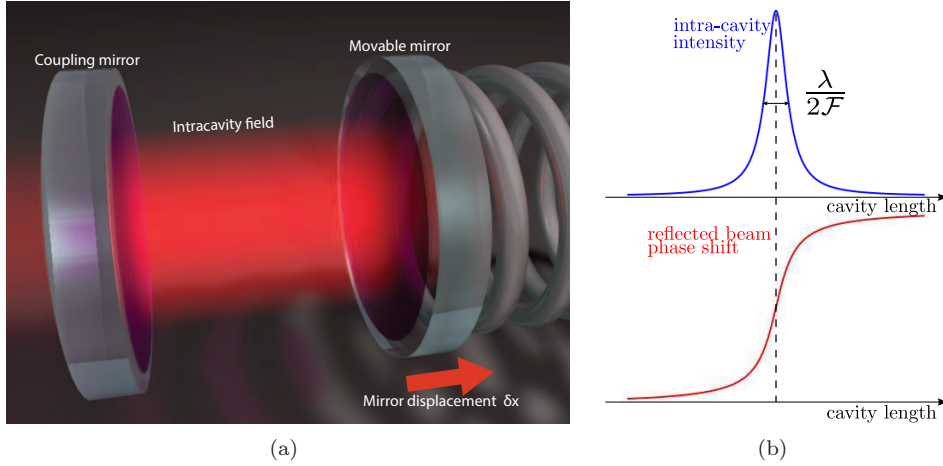


Figure 1.2: Sensitivity increase with a cavity. (a) A Fabry-Perot single-input cavity with a movable mirror. (b) The upper graph depicts the intracavity intensity dependence with the cavity detuning, while the lower one shows the phase shift occurring at the cavity resonance.

The maximum value of the intracavity intensity I is reached at resonance and is equal to [17]:

$$I = \frac{2}{\pi} \mathcal{F} I^{in}, \quad (1.2)$$

where I^{in} is the incident intensity. The cavity finesse \mathcal{F} is defined as the ratio between the distance of two successive resonances (Free Spectral Range) and the Full Width at Half Maximum (FWHM) of the Airy peak as depicted in Figure 1.2(b). It is directly related to the cavity dissipation processes associated to the coupling mirror transmission and to the mirror losses. It can also be interpreted as the mean number of round-trips made by the photons in the cavity. Figure 1.2(b) also shows the phase of the reflected field as a function of the cavity detuning: at resonance the slope of this phase shift becomes maximal. It can be shown [17] that the phase shift of the reflected field is equal to:

$$\delta\phi_{out} = 8\mathcal{F} \frac{\delta x}{\lambda}. \quad (1.3)$$

The advantage of using a high-finesse optical cavity in order to measure the mirror displacement clearly appears by comparing equations (1.1) and (1.3): the cavity finesse increases the resulting phase shift by a factor of $2\mathcal{F}/\pi$.

The effect of a displacement δx should be compared to sources of noise present into the measured phase shift. These noises can be larger than the signal thus limiting the measurement sensitivity. We can distinguish them into two main categories: classical noise, such as thermal or seismic noises, and quantum noise. It turns out that the measured phase shift is contaminated by noises of both origin. We will show in the following how quantum noises induce fundamental limits to the sensitivity of the displacement measurement.

1.3 Optomechanical coupling in a movable mirror cavity

The goal of this section is to derive the equations describing the optomechanical coupling between a laser beam and a single-input Fabry-Perot cavity, taking into account quantum noises. For this purpose, we use into a semi-classical input-output formalism [18–20].

1.3.1 Quantum nature of light

According to quantum optics, the electromagnetic field can be decomposed into a series of modes, each mode corresponding to a harmonic oscillator. Here, we will be interested in a mono-modal analysis since the presence of a single-input cavity will select one electromagnetic mode. As the energy of the quantum harmonic oscillator is quantized and the energy levels are equidistant from each other, we can describe the oscillator and the electromagnetic field by using the photon creation and annihilation operators \hat{a}^\dagger and \hat{a} , respectively. These operators obey the following commutation rule:

$$[\hat{a}, \hat{a}^\dagger] = 1. \quad (1.4)$$

We also define the operators \hat{a}_1 and \hat{a}_2 , which are called the quadrature operators of the electromagnetic field:

$$\hat{a}_1 = \hat{a} + \hat{a}^\dagger, \quad \hat{a}_2 = i(\hat{a}^\dagger - \hat{a}), \quad (1.5)$$

which correspond to the position and the momentum in the case of a harmonic oscillator. Since the annihilation and creation operators do not commute with each other, the two associated quadrature operators will not commute either. The fluctuations of these observables will then verify a Heisenberg uncertainty relation:

$$\Delta\hat{a}_1\Delta\hat{a}_2 \geq 1. \quad (1.6)$$

Quantum fluctuations of both observables thus arise in a natural manner. In fact, it can be shown that a laser field can be described by a minimum uncertainty state called a coherent state. In that case the above Heisenberg uncertainty relation (1.6) becomes:

$$\Delta\hat{a}_1\Delta\hat{a}_2 = 1. \quad (1.7)$$

In the following pages, a semi-classical approach will be used to describe these fluctuations.

Quantum fluctuations, a semi-classical approach

In order to describe the evolution of the quantum fluctuations after their interaction with a system -a cavity for example- a semi-classical approach has been proposed [18]. The semi-classical representation consists in associating to the operators \hat{a} and \hat{a}^\dagger two pseudo-random variables, α and α^* , whose statistics are described by a Wigner quasi-probability distribution \mathcal{W} in such a way that the mean value of the product $f(\hat{a}, \hat{a}^\dagger)$ coincides with the quantum value:

$$\langle f(\hat{a}, \hat{a}^\dagger) \rangle = \int d\alpha d\alpha^* \mathcal{W}(\alpha, \alpha^*) f(\alpha, \alpha^*). \quad (1.8)$$

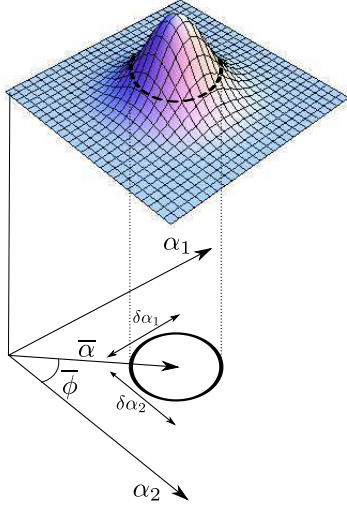


Figure 1.3: A three-dimensional representation of quasi-probability Wigner distribution and its projection in the phase space (α_1, α_2) .

The random variable α characterizes the quantum field and we can decompose it into the sum of a mean value $\bar{\alpha}$ characterizing the classical static part of the field, and its quantum fluctuations $\delta\alpha$ governed by the probability law \mathcal{W} . The field will then become:

$$\alpha = \bar{\alpha} + \delta\alpha. \quad (1.9)$$

Figure 1.3 depicts the Wigner distribution for a coherent state. The horizontal plane defines the phase space whose axes are given by the semi-classical quadratures α_1 and α_2 which correspond to the real and imaginary parts of the field, respectively. The mean intensity $|\alpha|^2$ and phase $\bar{\phi}$ of the laser field are also shown in the figure. For a coherent state the Wigner distribution is a Gaussian distribution taking only positive values, centered around the mean value $\bar{\alpha}$. The fluctuations of the two quadratures are given by the projection of the distribution on each axis and they are equal to 1 for a coherent state. In Figure 1.3 we also see the

phasor diagram derived from the Wigner distribution of a coherent state. It is a contour drawn at the half maximum value of the Wigner distribution. We then define any quadrature of the field in the following way:

$$\alpha_\theta = e^{-i\theta}\alpha + e^{i\theta}\alpha^*, \quad (1.10)$$

which is simply a rotation by an angle θ of the quadrature α_1 . In a coherent state, the dispersion is always equal to 1 for any angle θ :

$$\Delta\alpha_\theta = 1. \quad (1.11)$$

Two quadratures will have a particular importance for our purposes: the phase and the intensity of the field. For a given realisation of the field, represented by a point in the phase space, the distance from the axes' origin and the angle with respect to the axe α_1 give the amplitude and the phase of the field:

$$\alpha = \sqrt{N}e^{i\phi}, \quad (1.12)$$

where $N = |\alpha|^2$ is the number of photons in the field and ϕ the phase of the field. Let us now linearise the expression (1.12) around the field mean value $\bar{\alpha} = \sqrt{N}e^{i\bar{\phi}}$. The amplitude and phase fluctuations will then become:

$$\delta N = |\bar{\alpha}|\delta a_{\bar{\phi}}, \quad (1.13)$$

$$\delta\phi = \frac{1}{2|\bar{\alpha}|}\delta a_{\bar{\phi}+\pi/2}. \quad (1.14)$$

Intensity and phase fluctuations respectively depend on the fluctuations of the quadrature $a_{\bar{\phi}}$, parallel to the field mean value, and $a_{\bar{\phi}+\pi/2}$, perpendicular to the field mean value.

From the two equations (1.13) and (1.11) it can be derived that the intensity fluctuations

for a coherent state are equal to:

$$\Delta N^2 = \bar{N}, \quad (1.15)$$

The dispersion ΔN of the field amplitude scales as the photon number square root. This is a well expected property since the photons statistics of a coherent source follow a Poissonian distribution. We note as well that the relative fluctuations will decrease as the intensity increases.

$$\frac{\Delta N}{\bar{N}} = \frac{1}{\sqrt{\bar{N}}}. \quad (1.16)$$

The dispersion of the phase fluctuations can be derived from equations (1.11) and (1.14). It is equal to:

$$\Delta\phi^2 = \frac{1}{4\bar{N}}, \quad (1.17)$$

and is inversely proportional to the photon mean number. This result can be comprehended as follows: the phase dispersion $\Delta\phi$ corresponds to the angle under which the field distribution is seen from the origin. Since the width of the distribution is always equal to 1 for a coherent state, $\Delta\phi$ decreases as the intensity increases.

Equations (1.13) and (1.14) show that the dispersions of the observables N and ϕ depend on two orthogonal, and then non-commuting, quadratures. Using equation (1.6) and performing a simple rotation the following, Heisenberg inequality is derived:

$$\Delta N \Delta\phi \geq \frac{1}{2}, \quad (1.18)$$

showing the intensity-phase non-commutativity. According to equations (1.15) and (1.17), a coherent state corresponds to a minimum state for the above inequality.

The previous description relies on a static field description and a field quantification model in a finite, three-dimensional box. The semi-classical framework is an input-output theory adapted to fields propagating in a physical system. It is obtained by considering time dependent variables instead of static ones. The field is thus no longer characterised by the photon number N but by the photon flux $I(t)$ which is the propagating photon number by second. The results presented in this section can then be used in order to completely characterise the field fluctuations at all time t , or equivalently at all frequencies. In this framework, any given quantity $A(t)$ can be decomposed into the sum of its mean value \bar{A} and its fluctuations $\delta A(t)$:

$$A(t) = \bar{A} + \delta A(t). \quad (1.19)$$

In the Fourier space, A is then characterised by its fluctuations $\delta A[\Omega]$ at the angular frequency Ω , defined by the Fourier transform:

$$\delta A[\Omega] = \int dt e^{-i\Omega t} \delta A(t) \quad (1.20)$$

and by its noise spectrum $S_A[\Omega]$ defined by:

$$\langle \delta A[\Omega] \delta A[\Omega'] \rangle = 2\pi \delta(\Omega + \Omega') S_A[\Omega], \quad (1.21)$$

where $\langle \dots \rangle$ represents the statistical mean value of the Wigner distribution.

In particular, if we consider a coherent state, the phase fluctuations $\delta\phi$ do not depend on

the frequency and are inversely proportional to the square root of the mean photon flux \bar{I} . The spectrum of the phase fluctuations then become:

$$S_\phi[\Omega] = \frac{1}{4\bar{I}}, \quad (1.22)$$

while the spectrum of the intensity fluctuations is:

$$S_I[\Omega] = \bar{I}. \quad (1.23)$$

We note that both spectra do not depend on the frequency. A coherent state is characterized by intensity and phase white noises. It is also interesting to note how the two quadratures scale with the mean intensity of the field. The intensity spectrum increases linearly with the mean intensity whereas the phase spectrum decreases. This fundamental difference will yield to the so-called Standard Quantum Limit [15, 21] to the displacement measurement sensitivity, which will be described in detail in section 1.4.3. We will first describe the input-output relation for a laser beam in a Fabry-Perot cavity.

1.3.2 Movable mirror cavity

In this section we will use the semi-classical method in order to derive the evolution of a coherent field interacting with a cavity. We will consider a realistic cavity including its losses, composed of one coupling mirror and one movable end-mirror. The coupling mirror has an amplitude transmission \sqrt{T} and a reflection coefficient $\sqrt{1-T}$, with $T \ll 1$. In an ideal lossless cavity the movable end-mirror would be characterized by a total reflectivity. In a real cavity, however, optical losses may have a drastic impact on the optical characteristics of the cavity. We will describe losses as an additional transmission coefficient \sqrt{P} of the end mirror, leading to a reflection coefficient $\sqrt{1-P}$, with $P \ll 1$. The coefficient P actually includes the residual transmission T_2 of the end mirror and other cavity losses, such as the diffraction D and the absorption A on both mirrors. We then have for the cavity global losses:

$$P = T_2 + A + D. \quad (1.24)$$

Figure 1.4 depicts the amplitudes of the incident α_{in} , reflected α_{out} , intracavity α and α' and vacuum α_v fields. The conservation of energy at the coupling mirror allows one to write down the linear and unitary transformation between the field amplitudes:

$$\alpha(t) = \sqrt{T}\alpha_{\text{in}}(t) + \sqrt{1-T}\alpha'(t) \quad (1.25)$$

$$\alpha_{\text{out}}(t) = \sqrt{T}\alpha'(t) - \sqrt{1-T}\alpha_{\text{in}}(t), \quad (1.26)$$

where the minus sign ensures the energy conservation. The intracavity field $\alpha(t)$ at time t , is the sum of the transmitted part of the input field $\alpha_{\text{in}}(t)$ and the reflected part of the intracavity field $\alpha'(t)$ having already done a cavity round trip. Similarly, the reflected field $\alpha_{\text{out}}(t)$ is the superposition of the transmitted intracavity field and the reflected input field on the coupling mirror. In order to find the similar transformation on the end mirror, we have to take into account the fields propagation in the cavity. The movable mirror induces a time delay and a phase shift which depends on the total cavity length $L(t) = L_0 + x(t)$ where $x(t)$ is the mirror

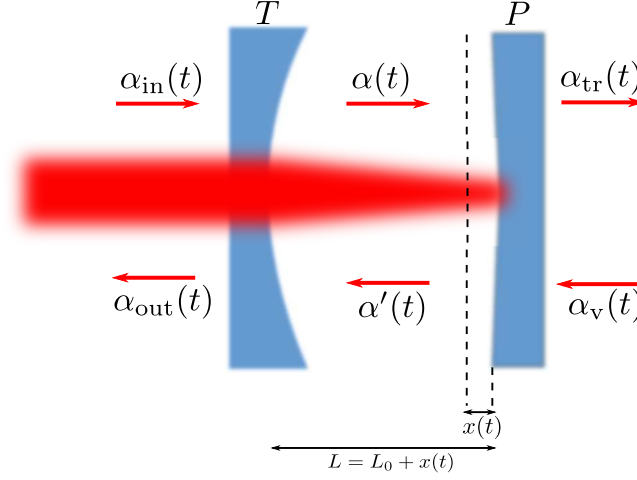


Figure 1.4: The description of the incident $\alpha_{\text{in}}(t)$, intracavity $\alpha(t)$, reflected $\alpha_{\text{out}}(t)$ and transmitted $\alpha_{\text{tr}}(t)$ fields associated to the coupling between a laser beam and a Fabry-Perot cavity with a movable mirror.

displacement. We thus define the round trip time τ and the phase shift Ψ as:

$$\Psi = 2kL(t)[2\pi] \quad (1.27)$$

$$\tau = \frac{2L_x}{c} \simeq \frac{2L_0}{c}. \quad (1.28)$$

We have assumed that the mirror displacement is small enough so that the round trip τ time can be considered as independent of $x(t)$. The fields transformation on the movable mirror is then given by:

$$\alpha'(t + \tau/2)e^{-i\Psi/2} = \sqrt{P}\alpha_v(t) + \sqrt{1-P}\alpha(t - \tau/2)e^{i\Psi/2}, \quad (1.29)$$

$$\alpha_{\text{tr}}(t) = \sqrt{P}\alpha(t - \tau/2)e^{i\Psi/2} - \sqrt{1-P}\alpha_v(t). \quad (1.30)$$

We have already considered the case of a high-finesse cavity with $P, T \ll 1$. By also considering a cavity close to resonance ($\Psi \ll 1$) the field envelope varies slowly during a round trip. By first combining and linearising equations (1.25) and (1.29) and keeping only first order terms (Ψ , $\tau \frac{d}{dt}$, \sqrt{T} and \sqrt{P}) we obtain the input-output field equations:

$$\tau \frac{d\alpha}{dt} = \sqrt{T}\alpha_{\text{in}} + \sqrt{P}\alpha_v + (i\Psi - \gamma)\alpha(t) \quad (1.31)$$

$$\alpha_{\text{out}}(t) = \sqrt{T}\alpha(t) - \alpha_{\text{in}}(t) \quad (1.32)$$

$$\alpha_{\text{tr}}(t) = \sqrt{P}\alpha(t) - \alpha_v(t), \quad (1.33)$$

where we noted γ the total losses of the cavity: $2\gamma = T + P$. The phase shift is time dependent:

$$\Psi(t) = \Psi_0 + 2kx(t), \quad (1.34)$$

where $\Psi_0 = 2kL_0 [2\pi]$ represents the phase shift of the cavity when the mirror is at rest. It can also be understood as the cavity detuning. In the following, we will solve the above set of equations within the semi-classical framework.

1.3.3 Solving the evolution equations

From equation (1.9) we decompose the field into the sum of its mean value and its time-dependent fluctuations in order to linearize the equations. The different fields and the phase shift can then be written:

$$\begin{aligned}\alpha(t) &= \bar{\alpha} + \delta\alpha(t), \\ \Psi(t) &= \bar{\Psi} + \delta\Psi(t),\end{aligned}\tag{1.35}$$

where $\delta\Psi(t) = 2k\delta x(t)$ and $\bar{\Psi} = \Psi_0 + 2k\bar{x}$ represent the fluctuations and mean detunings of the cavity, taking into account the mean recoil of the mirror.

Steady States

First, we are interested in the steady states solutions of our system. By replacing the time-dependent variables of the equations (4.1), (4.2) and (1.33) with their mean values we obtain:

$$\bar{\alpha} = \frac{\sqrt{T}}{\gamma - i\bar{\Psi}} \bar{\alpha}_{\text{in}},\tag{1.36}$$

$$\bar{\alpha}_{\text{out}} = \frac{\gamma - P + i\bar{\Psi}}{\gamma - i\bar{\Psi}} \bar{\alpha}_{\text{in}},\tag{1.37}$$

$$\bar{\alpha}_{\text{tr}} = \frac{\sqrt{TP}}{\gamma - i\bar{\Psi}} \bar{\alpha}_{\text{in}}.\tag{1.38}$$

We note that the vacuum field has a null mean value: since its Wigner distribution is centered around zero it contains only fluctuations. At an optical resonance of the cavity ($\bar{\Psi} = 0$), the fields mean values become:

$$\bar{\alpha} = \frac{\sqrt{T}}{\gamma} \bar{\alpha}_{\text{in}}, \quad \bar{\alpha}_{\text{out}} = \frac{\gamma - P}{\gamma} \bar{\alpha}_{\text{in}}, \quad \bar{\alpha}_{\text{tr}} = \frac{\sqrt{TP}}{\gamma} \bar{\alpha}_{\text{in}},\tag{1.39}$$

showing that all fields are in phase. The intracavity intensity exhibits a Lorentzian profile as a function of the cavity detuning (see Fig. 1.2(b)) with a full-width at half-maximum (FWHM) equal to the total cavity losses 2γ , while the reflected intensity profile is described by a negative Lorentzian peak as the cavity is swept around its resonance (see equation (1.37)). We thus define a reflection coefficient \mathcal{R}_0 that relates the reflected intensity with the cavity losses. It is equal to the ratio between the reflected intensity at resonance ($\bar{\Psi} = 0$) and the reflected intensity far from resonance ($\bar{\Psi} = \pm\infty$):

$$\mathcal{R}_0 = \frac{\bar{I}_{\text{out}}^{\bar{\Psi}=0}}{\bar{I}_{\text{out}}^{\bar{\Psi}=\pm\infty}} = \frac{|\alpha_{\text{out}}^{\bar{\Psi}=0}|^2}{|\alpha_{\text{out}}^{\bar{\Psi}=\pm\infty}|^2} = \left(\frac{T - P}{T + P} \right)^2.\tag{1.40}$$

The cavity finesse introduced earlier can also be written as the ratio between the distance between two consecutive resonances (Free Spectral Range) equal to $\bar{\Psi} = 2\pi$, and the full-width of the cavity resonance 2γ :

$$\mathcal{F} = \frac{2\pi}{2\gamma} = \frac{2\pi}{T + P}. \quad (1.41)$$

It is also interesting to write down the transmission of the cavity using equation (1.38):

$$\bar{I}_{tr} = \frac{4TT_2}{(T + P)^2} \bar{I}_{in} \quad (1.42)$$

The three latter equations give the expression of three measurable quantities: the finesse, the transmission and the reflection of a cavity. Upon experimental measurement of these quantities, we can access the transmission of both mirrors as well as the sum $A + D = P - T_2$ of the absorption and diffusion losses. However, these equations do not completely represent reality. It has actually been assumed that the incident field is perfectly coupled to the fundamental resonant mode of the cavity. If this is not the case, a portion of light resonates with other cavity modes; this portion does not enter the cavity and changes both the mean reflected and transmitted fields. The above equations need to be adjusted by a mode matching coefficient which will have an impact not only to the reflection and transmission of the cavity, but also the sensitivity of the small displacement measurements, as we will see in section 1.4.

Mode matching

In order to take into account the mode matching we decompose the incident field $\mathcal{E}_{in}(\mathbf{r}, t)$ into the sum of the cavity fundamental mode, whose spatial profile is $v_0(\mathbf{r}) \sim e^{-r^2/w_0^2}$, with w_0 being the waist, and the transverse ones $v_{n \neq 0}$:

$$\mathcal{E}_{in}(\mathbf{r}, t) = \alpha_0(t)v_0(\mathbf{r}, t)e^{-i\omega_0 t} + \mathcal{E}'_{in}(t)(\mathbf{r}, t), \quad (1.43)$$

where \mathcal{E}'_{in} is the contribution of all the transverse modes. We then define the parameter η_{cav} characterizing the mode matching quality as the ratio between the intensity $|\bar{\alpha}_0|^2$ actually coupled to the cavity and the total incident intensity \bar{I}_{in} :

$$\eta_{cav} = \frac{|\bar{\alpha}_0|^2}{\bar{I}_{in}}. \quad (1.44)$$

In the case of an imperfect mode matching ($\eta_{cav} < 1$), the transverse modes will be directly reflected by the cavity and only a portion $\eta_{cav}\bar{I}_{in}$ of the incident intensity \bar{I}_{in} will be coupled to the cavity. Furthermore, imperfections on the mode matching will also affect the reflected field while, at resonance, only the intensity coupled to the cavity will undergo the cavity losses. Hence, the reflected intensity becomes:

$$\bar{I}_{out}^{\Psi=0} = \left(\frac{T - P}{T + P} \right)^2 |\bar{\alpha}_0|^2 + \mathcal{E}'_{in}. \quad (1.45)$$

The reflected intensity is thus equal to the reflected fraction of light coupled to the cavity plus all transverse modes simply reflected by the cavity. Let us then correct the reflection coefficient

knowing that $\bar{I}_{out}^{\Psi=\infty} = \bar{I}_{in} = |\bar{\alpha}_0|^2 + \mathcal{E}'_{in}$:

$$\mathcal{R}_0 = \eta_{cav} \left[\left(\frac{T-P}{T+P} \right)^2 - 1 \right] + 1. \quad (1.46)$$

If $\eta_{cav} = 1$, we get a perfect mode matching and the reflection coefficient (1.46) is similar to the one given by equation (1.40). In order to have a good mode matching, the position and the width of the incident beam waist must be adapted to the geometrical properties of the cavity. We usually work with Fabry-Perot cavities consisting of two mirrors, one plane and one concave. The wavefronts of the beam must exactly match the curvature of the mirrors, meaning that the waist of the beam -where the wavefront is plane- must be set on the plane mirror, and its width should be set in such a way that its wavefront on the concave mirror matches its curvature. It can be found [22] that for a plano-concave Fabry-Perot cavity, the width of the waist must be equal to:

$$w_0^2 = \frac{\lambda}{\pi} \sqrt{L(R-L)}, \quad (1.47)$$

where L is the cavity length, R the radius of curvature of the concave mirror and λ the wavelength of the laser.

1.3.4 Fluctuations in a movable mirror cavity

Let us now study the dynamical evolution of the field fluctuations. We will first write the equations by considering a perfect mode matching ($\eta_{cav} = 1$). We will take into account the imperfect mode matching in the final expressions. For this purpose, we will consider that the cavity is at resonance ($\bar{\Psi} = 0$). Furthermore, it will be easier to work in the Fourier domain, using the fluctuations $\delta\alpha[\Omega]$ at frequency Ω related to the time-dependent fluctuations $\delta\alpha(t)$ by equation (1.20). In the framework of the semi-classical approach, we linearize equations (4.1), (4.2) and (1.33) around the fields mean value and we apply the Fourier transform to the time-dependent fluctuations quadratures. We obtain:

$$(\gamma - i\Omega\tau)\delta\alpha[\Omega] = \sqrt{T}\delta\alpha_{in}[\Omega] + \sqrt{P}\delta\alpha_v[\Omega] + 2i\bar{\alpha}k\delta x[\Omega], \quad (1.48)$$

$$\delta\alpha_{out}[\Omega] = \sqrt{T}\delta\alpha[\Omega] - \delta\alpha_{in}[\Omega], \quad (1.49)$$

$$\delta\alpha_{tr}[\Omega] = \sqrt{P}\delta\alpha[\Omega] - \delta\alpha_v[\Omega], \quad (1.50)$$

where we have used the relation $\delta\Psi[\Omega] = 2k\delta x[\Omega]$. Next, we will be interested in writing down the evolution equations for the intensity p and phase q . Using the definition of any quadrature of angle θ (equation 1.10) and the phase/intensity fluctuations definitions (equations 1.13 and 1.14), the intensity and phase quadratures respectively correspond to $\theta = 0$ and $\theta = \pi/2$ respectively as the mean fields can be all chosen real. We then get:

$$\delta p[\Omega] = \delta\alpha[\Omega] + \delta\alpha^*[\Omega], \quad \delta q[\Omega] = i(-\delta\alpha[\Omega] + \delta\alpha^*[\Omega]). \quad (1.51)$$

Or, equivalently:

$$\delta\alpha[\Omega] = \frac{\delta p[\Omega] + i\delta q[\Omega]}{2}, \quad \delta\alpha^*[\Omega] = \frac{\delta p[\Omega] - i\delta q[\Omega]}{2}. \quad (1.52)$$

Finally, by combining the above set of equations, the intracavity and reflected intensity and phase fluctuations can be written as a function of the incident ones:

$$\delta p[\Omega] = \frac{\sqrt{T}}{\gamma - i\Omega\tau} \delta p_{\text{in}}[\Omega] + \frac{\sqrt{P}}{\gamma - i\Omega\tau} \delta p_{\text{v}}[\Omega], \quad (1.53)$$

$$\delta q[\Omega] = \frac{\sqrt{T}}{\gamma - i\Omega\tau} \delta q_{\text{in}}[\Omega] + \frac{\sqrt{P}}{\gamma - i\Omega\tau} \delta q_{\text{v}}[\Omega] + \frac{4k\bar{\alpha}}{\gamma - i\Omega\tau} \delta x[\Omega], \quad (1.54)$$

$$\delta p_{\text{out}}[\Omega] = \frac{\gamma - P + i\Omega\tau}{\gamma - i\Omega\tau} \delta p_{\text{in}}[\Omega] + \frac{\sqrt{TP}}{\gamma - i\Omega\tau} \delta p_{\text{v}}[\Omega], \quad (1.55)$$

$$\delta q_{\text{out}}[\Omega] = \frac{\gamma - P + i\Omega\tau}{\gamma - i\Omega\tau} \delta q_{\text{in}}[\Omega] + \frac{\sqrt{TP}}{\gamma - i\Omega\tau} \delta q_{\text{v}}[\Omega] + \frac{4\sqrt{T}k\bar{\alpha}}{\gamma - i\Omega\tau} \delta x[\Omega]. \quad (1.56)$$

From equations (1.53) and (1.55), we deduce that the intracavity and reflected amplitude fluctuations δp and δp_{out} are completely decoupled from the phase and position fluctuations δq_{in} , δq_{v} and δx . We can understand this by noting that the cavity working point is at the maximum of the Airy peak where the intensity does not depend on the phase shift and, thus, the optical path fluctuations. On the other hand, this is no longer true out of resonance. We also note that in the case of a lossless cavity ($P = 0$), the incident intensity fluctuations exit the cavity unaltered since: $|\delta p_{\text{out}}| = |\delta I_{\text{in}}|$ (see equation (1.55)). According to equations (1.53) to (1.56) all terms are divided by an additional term $1/(\gamma - i\Omega\tau)$ corresponding to a low-pass filtering by the cavity. This leads us to define the cavity bandwidth as follows:

$$\Omega_{\text{cav}} = \frac{\gamma}{\tau}. \quad (1.57)$$

As a consequence, intensity and phase fluctuations at frequencies larger than the cavity bandwidth ($\Omega \gg \Omega_{\text{cav}}$) will not interact with the cavity, they will essentially be reflected by the cavity without affecting intracavity fluctuations. Similarly, the position fluctuations of the movable mirror for frequencies $\Omega \gg \Omega_{\text{cav}}$ will have no effect onto the reflected phase shift. By assuming $P = 0$, equation (1.56) becomes:

$$\delta q_{\text{out}}[\Omega] = \frac{\gamma + i\Omega\tau}{\gamma - i\Omega\tau} \delta q_{\text{in}}[\Omega] + \frac{4\sqrt{T}k\bar{\alpha}}{\gamma - i\Omega\tau} \delta x[\Omega] \quad (1.58)$$

In other words, the cavity is averaging the position fluctuations during a characteristic time given by the cavity photon storage time $2\pi/\Omega_{\text{cav}} = 2\mathcal{F}\tau$.

1.4 Limits in interferometric measurements

In this section we will study the displacement measurement sensitivity and the consequences set to it by the quantum nature of light. We will describe the two different noises associated with the displacement measurement: the measurement noise and the radiation-pressure noise and we will show how their compromise lead to the existence of the so-called Standard Quantum Limit which correspond to the smallest measurable displacement of the movable mirror.

1.4.1 Measurement noise

First we will determine the sensitivity of the measurement in a realistic case where the cavity losses and the mode matching are taken into consideration. The fact that the reflected phase fluctuations include not only the fluctuations of the mirror position but also the incident phase fluctuations will set a limit to the sensitivity of the measurement. We will first calculate the spectrum of the reflected phase fluctuations (equation (1.56)) using the spectrum definition (1.21). Since phase, vacuum and displacement fluctuations are independent from each other, the squared sum of these three quantities are equal to the sum of the squared quantities. Hence we find:

$$S_q^{\text{out}}[\Omega] = 1 + \left(\frac{16\mathcal{F}}{\lambda}\right)^2 \left(\frac{T}{T+P}\right)^2 \frac{\eta_{\text{cav}}\bar{I}_{\text{in}}}{1 + (\Omega/\Omega_{\text{cav}})^2} S_x[\Omega], \quad (1.59)$$

where we have considered the incident field to be in a coherent state and thus both the vacuum and the incident phase spectra S_q^{v} and S_q^{in} are equal to 1. Equation (1.59) gives the spectrum of the reflected phase containing the information on the mirror displacement. It is equal to the sum of the incident phase noise ($S_q^{\text{in}} = 1$) and the signal which is proportional to the displacement spectrum S_x . The sensitivity limit is achieved when the signal is at least equal to the noise, corresponding to a signal-to-noise ratio equal to 1. Hence, the smallest measurable mirror is equal to:

$$\delta x_{\text{shot}} = \frac{\lambda}{16\mathcal{F}} \frac{T+P}{T} \sqrt{\frac{1 + (\Omega/\Omega_{\text{cav}})^2}{\eta_{\text{cav}}\bar{I}_{\text{in}}}}. \quad (1.60)$$

The frequency dependence shows that the sensitivity is reduced at high frequency ($\Omega \geq \Omega_{\text{cav}}$) as the cavity acts like a low-pass filter. As the resonance frequency of the movable mirror is typically about 1 MHz, a cavity bandwidth larger than 1 MHz should be used in order to achieve the optimal sensitivity. The cavity bandwidth being inversely proportional to the cavity length, short cavities must be used. In our experiment cavities length of a few hundreds of μm are used. We note as well the possible degradation of the sensitivity if an proper mode matching is not achieved. The sensibility may also be reduced by a factor $T/(T+P)$ which is directly related to the cavity losses. It is therefore crucial to minimize the losses P , as compared to the transmission T , so that the factor $T/(T+P)$ is the largest possible. We use for this purpose a movable mirror with losses less than 1 ppm. Losses also play an important role to the sensitivity via the cavity finesse appears at the denominator of δx_{shot} . A proper choice of the coupler transmission T thus corresponds to a compromise between a transmission giving a high optical finesse and at the same time keeping a high loss ratio $T/(T+P)$. In our case a transmission T of 20 ppm has been chosen, allowing to achieve a finesse \mathcal{F} of up to 300 000. The measurement noise associated to the shot-noise given by equation (1.60) then gives a spectral density $\delta x_{\text{shot}} \simeq 2.6 \cdot 10^{-21} \text{m}/\sqrt{\text{Hz}}$.

Finally, the sensitivity is improved as the incident intensity increases. One could suggest that an arbitrary sensitivity could be achieved by increasing the incident intensity. As we will see in the next section, this is not the case as an additional fundamental noise will disturb the position of the mirror and, therefore, will deteriorate the sensibility of the measurement. This noise is related to radiation-pressure effects on the mirror and the back-action of the measurement: it is actually a consequence of the basic concepts of quantum measurement as any measurement induces a perturbation on the measured system.

1.4.2 Radiation-pressure back-action

As shown by equation (1.18), the incident intensity exhibits fluctuations of quantum nature. The movable mirror will thus undergo radiation-pressure fluctuations, resulting in a displacement noise. We will first describe the mirror response to a force and we will pursue by applying this formalism to the case of a radiation-pressure force.

Mirror movement

For small displacements, the linear response theory [23] can be used to express the mirror displacement as a function of the forces applied to it. In the Fourier domain, the mirror displacement is then given by:

$$x[\Omega] = \chi[\Omega]F[\Omega], \quad (1.61)$$

where $\chi[\Omega]$ is the mechanical susceptibility describing the mirror response and F represents the forces exerted on the mirror to the radiation-pressure. We assume that this motion can be modelled by a simple harmonic oscillator so that it has the following Lorentzian dependency:

$$\chi[\Omega] = \frac{1}{M[\Omega_M^2 - \Omega^2 - i\Omega\Omega_M/Q]}, \quad (1.62)$$

where M is the oscillator mass, Ω_M is the resonance frequency of the oscillator and Q is its quality factor. This expression proves to be a very realistic approximation in our case: the substrate of the mirror presents internal vibration modes that are excited by the radiation pressure of the light beam; it has been shown [24] that the displacement of the surface of the mirror is completely equivalent to a global translation of the mirror. In the case of a movable mirror of a plano-convex geometry made of silica, used throughout this work, a frequency $\Omega_M/2\pi \simeq 1$ MHz, a mass $M \simeq 0.1$ mg and a quality factor $Q \simeq 1\,000\,000$ are achieved.

Displacement noise

When a photon gets reflected onto a movable mirror, it gives a momentum kick $2\hbar k$ to the mirror resulting in a radiation-pressure force:

$$F_{\text{rad}} = 2\hbar k I(t) \quad (1.63)$$

where k is the photon wave vector and $I(t)$ is the photon flux expressed in photons per seconds. We will first evaluate the mean displacement \bar{x}_{rad} of the mirror by writing down equations (1.61) and (1.62) at zero frequency:

$$\bar{x}_{\text{rad}} = x[0] = \chi[0]\bar{F}_{\text{rad}}, \quad \chi[0] = \frac{1}{M\Omega_M^2}, \quad \bar{F}_{\text{rad}} = 2\hbar k\bar{I}. \quad (1.64)$$

It follows that:

$$\bar{x}_{\text{rad}} = \frac{2\hbar k\bar{I}}{M\Omega_M^2}. \quad (1.65)$$

For a cavity finesse $\mathcal{F} = 300\,000$ and an incident power $P_{\text{in}} = 1.5$ mW the mean radiation-pressure force upon the mirror is $\bar{F}_{\text{rad}} \simeq 2 \cdot 10^{-6}$ N. Such a force will lead to a mean displacement $\bar{x}_{\text{rad}} \simeq 5 \cdot 10^{-13}$, where we used the mirror mechanical parameters given at the beginning of the

section.

Equation (1.61) allows one to express the mirror displacement fluctuations δx_{rad} induced by radiation-pressure. Since the intensity noise is given by $\delta I = \bar{\alpha}\delta p$, the position fluctuations produced by the fluctuations δF_{rad} of the radiation pressure (equation (1.63)) are equal to:

$$\delta x_{rad}[\Omega] = \chi[\Omega]\delta F_{rad}[\Omega] = \chi[\Omega]2\hbar k\delta I[\Omega] \quad (1.66)$$

$$= \chi[\Omega]2\hbar k\bar{\alpha}\delta p[\Omega]. \quad (1.67)$$

Using equation (1.39) and (1.53) we find:

$$\delta x_{rad}[\Omega] = \frac{4\hbar k\sqrt{\eta_{cav}\bar{I}_{in}}}{\gamma - i\Omega\tau} \chi[\Omega] \frac{T\delta p_{in}[\Omega] + \sqrt{T\bar{P}}\delta p_v[\Omega]}{T + P}. \quad (1.68)$$

As the two incident fluctuations δp_{in} and δp_v are not correlated, the spectrum of the position fluctuations can be derived from the previous expression :

$$S_x^{rad} = \left(\frac{8\mathcal{F}}{\lambda}\right)^2 \frac{T}{T + P} \hbar^2 |\chi[\Omega]|^2 \frac{\eta_{cav}\bar{I}_{in}}{1 + (\Omega/\Omega_{cav})^2}. \quad (1.69)$$

This equation shows that the position fluctuations induced by the radiation-pressure increase as the intensity increases. It is therefore hopeless to improve arbitrarily the measurement sensitivity by increasing the incident intensity as this noise will become dominant and will limit the achievable sensitivity. We note that at the resonance frequency Ω_M the displacement induced by the radiation-pressure is of the order of 10^{-17} m/ $\sqrt{\text{Hz}}$, that is 4 orders of magnitude above the shot-noise limit. It is thus unavoidable to take into consideration this effect to the total measurement sensitivity.

1.4.3 The standard quantum limit

We aim to measure with an optimal sensitivity a signal δx_{sig} that corresponds either to a real displacement of the mirror or to an apparent length variation of the cavity. The total cavity length variation is then $\delta x = \delta x_{rad} + \delta x_{sig}$ when taking into account the displacement δx_{rad} . We have already calculated the corresponding sensitivity (see equation (1.60)) without taking into consideration the radiation-pressure-induced displacement δx_{rad} which is also included in the reflected phase quadrature (equation 1.56)). The complete expression of the reflected phase quadrature then becomes:

$$\delta q_{out}[\Omega] = \frac{\gamma - P + i\Omega\tau}{\gamma - i\Omega\tau} \delta q_{in}[\Omega] + \frac{\sqrt{T\bar{P}}}{\gamma - i\Omega\tau} \delta p_v[\Omega] + \frac{4\sqrt{T}k\bar{\alpha}}{\gamma - i\Omega\tau} (\delta x_{rad}[\Omega] + \delta x_{sig}[\Omega]). \quad (1.70)$$

where δx_{sig} is the displacement signal we want to measure. It is obvious that in order to find the smallest measurable displacement, the signal must be compared to both the incident phase fluctuations and the radiation-pressure-induced position fluctuations. As all fluctuations in equation (1.70) are uncorrelated, the total noise is actually the quadratic sum of the shot-noise δx_{shot} (equation (1.60)) and the radiation-pressure noise δx_{rad} (equation (1.69)). When the incident power is increased the phase fluctuations decrease as they scale as $1/\sqrt{\bar{I}_{in}}$. On the other hand, radiation-pressure effects increase as the squared root of the intensity $\sqrt{\bar{I}_{in}}$. A compromise between the two effects will, therefore, give the maximum sensitivity corresponding

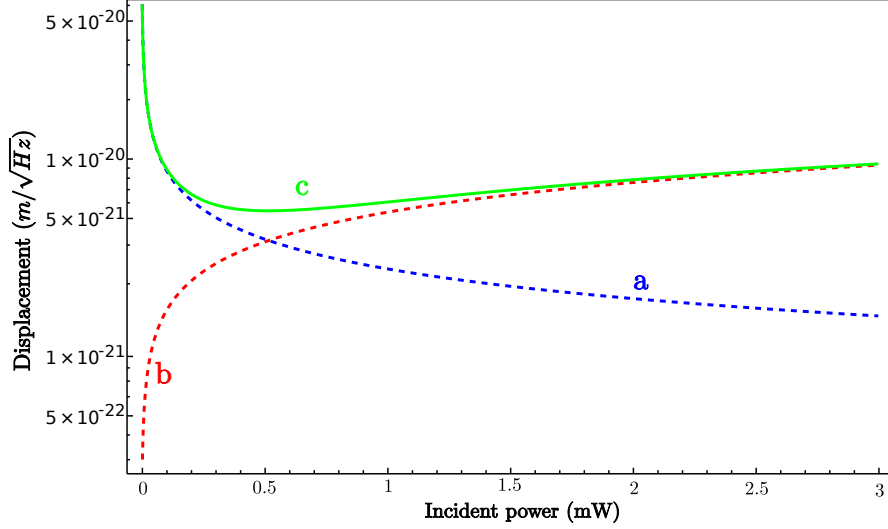


Figure 1.5: Displacement measurement sensitivity as a function of the incident power, at low frequency ($\Omega \ll \Omega_M$). The sensitivity limit (c) is set by radiation-pressure (b) and incident phase noises (a). These limits have been calculated for a resonator of mass $M=0.1$ mg, a resonance frequency $\Omega_M/2\pi = 1$ MHz, a finesse $\mathcal{F}=300\,000$, a wavelength $\lambda = 810$ nm, a perfect mode-matching $\eta_{\text{cav}} = 1$ and no losses $P = 0$.

to the so-called Standard Quantum Limit (SQL). At a given frequency Ω , it is reached when the shot-noise is equal to the radiation-pressure noise ($S_x^{\text{shot}}=S_x^{\text{rad}}$), that is for an incident intensity given by:

$$\bar{I}_{\text{in}}^{\text{sql}} = \left(\frac{\lambda}{8\mathcal{F}}\right)^2 \left(\frac{T+P}{T}\right)^{3/2} \frac{1}{2\hbar|\chi[\Omega]|} \frac{(1 + (\Omega/\Omega_{\text{cav}})^2)\lambda^2}{\eta_{\text{cav}}}. \quad (1.71)$$

The smallest measurable signal, δx_{sql} is obtained using equation (1.70) with an incident intensity $\bar{I}_{\text{in}}^{\text{sql}}$: it corresponds to a signal-to-noise ratio equal to 1.

$$\delta x_{\text{sql}} = \sqrt{\hbar|\chi[\Omega]|} \left(\frac{T+P}{T}\right)^{1/4}, \quad (1.72)$$

This fundamental quantum limit appears in any optical measurement where a light beam is used to get information on the position of a mirror, that is in every interferometric measurement. As the laser beam extracts the information about the position -via its phase- it unavoidably perturbs the position -via its intensity noise. The Standard Quantum Limit is thus a fundamental limit derived from the Heisenberg uncertainty between two conjugate observables of our measurement apparatus: the phase and the intensity of the laser beam. Hence, there is an optimal coupling strength (equation (1.71)) where the compromise between the phase and intensity noises gives the optimal sensitivity. Figure 1.5 depicts this Standard Quantum Limit. It corresponds to the minimum of the green curve (c), reached for an intensity $\bar{I}_{\text{in}}^{\text{sql}} = 0.25$ mW for the given parameters. It corresponds to a smallest measurable displacement $\delta x_{\text{sql}}[0] \sim 5 \cdot 10^{-21}$ m/ $\sqrt{\text{Hz}}$ at low frequency with no losses ($P = 0$). According to equation (1.72), when neglecting the mirror losses, this limit only depends on the mirror characteristics. The sensitivity is inversely proportional to the mirror mechanical susceptibility. For the purpose of this thesis,

it is thus preferable to choose a resonator with a large mechanical response in order to observe these radiation-pressure effects.

We should finally note that the Standard Quantum Limit is not an ultimate limit and, therefore, can be overcome using quantum noise reduction schemes. Many ideas have been proposed: the use of squeezed light [25], [26], [27], back-action cancellation [28], back-action amplification [29]. There nevertheless exists an Ultimate Quantum Limit (UQL) which is found [30] to only depend on the mirror dissipation mechanism for a lossless cavity:

$$\delta x_{UQL} = \sqrt{\hbar |\text{Im}[\Omega]|}. \quad (1.73)$$

1.5 Observing quantum fluctuations

The optomechanical coupling offers a simple macroscopic playground where fundamental aspects of the quantum measurement can be examined. The radiation-pressure noise of a coherent light, when coupled to a movable mirror, is directly related to a back-action effect limiting the measurement sensitivity. The observation of quantum fluctuations will offer important experimental insight to fundamental quantum measurement concepts by creating ultra-sensitive sensors and pushing even further the sensitivity limits of a macroscopic measurement. The experimental observation of the Standard Quantum Limit is one of the holy grails of the quantum optics research for the past two decades. It is connected to attempts made to detect extremely weak signals caused by gravitational waves passing through the Earth. These waves are actually predicted by the Albert Einstein general relativity theory; they are emitted by tremendous stellar events such as a supernova explosion or at two-star coalescence. They will induce a relative displacement of the order of $\delta L/L \simeq 10^{-22}$. Giant Michelson interferometers have been constructed (such as the french-italian VIRGO and american LIGO interferometers) whose sensitivity is limited by thermal noise and shot noise. However, the second generation of these detectors is expected to be mostly limited by quantum noises. The work of this thesis is thus closely related to these efforts. The first stage being the observation of the Standard Quantum Limit, the second would be the application of quantum optic schemes in order to overcome these limits. The use of squeezed light would diminish the back-action effect and would lead to a sensitivity better than the SQL limit. In the following we will describe the necessary experimental conditions in order to observe the Standard Quantum Limit. In particular, we will introduce the thermal noise which is the main experimental limitation.

1.5.1 Thermal noise

The mirror, being coupled to a thermal bath at a temperature T , is subjected to both thermal fluctuations and dissipation processes. These dissipation processes introduce a damping effect described by the imaginary part of the mirror mechanical susceptibility. Thermal fluctuations can be described by a zero-mean-value Langevin force F_T whose spectrum can be found by using the fluctuation-dissipation theorem [23] which relates this spectrum to the imaginary part of the mechanical susceptibility:

$$S_T[\Omega] = -\frac{2k_B T}{\Omega} \text{Im} \left[\frac{1}{\chi[\Omega]} \right], \quad (1.74)$$

where k_B is the Boltzmann constant and the Langevin force spectrum is defined as the Fourier transform of its autocorrelation function:

$$S_T[\Omega] = \int_{-\infty}^{\infty} d\tau \langle F_T(t) F_T(t + \tau) \rangle e^{-i\Omega\tau}. \quad (1.75)$$

Which is equivalent to equation (1.21) for a stationary process. Using equations (1.61), (1.62) and (1.74), the thermal noise spectrum is deduced:

$$S_x^T = 2k_B T M \frac{\Omega_M}{Q} |\chi[\Omega]|^2. \quad (1.76)$$

As seen by comparing with equation (1.69), both thermal and radiation-pressure noises have the same frequency dependence, when neglecting cavity filtering effects: they both scale as the square of the mechanical susceptibility absolute value. The thermal noise spectral amplitude will thus also present a Lorentzian profile as a function of the frequency, at least for a single mechanical oscillator. Hence, the signal-to-noise ratio between radiation-pressure and thermal effects does not depend on the frequency. Using equations (1.69) and (1.76) it is found to be:

$$\frac{S_x^{\text{rad}}}{S_x^T} \simeq 32 \frac{\hbar^2 \mathcal{F}^2 \bar{I}^{\text{in}}}{\lambda^2} \frac{Q}{k_B T M \Omega_M}. \quad (1.77)$$

However, the resonator mass M varies depending on the analysis frequency. At zero frequency the static mass M_0 (at $\Omega = 0$) is several orders of magnitude smaller than the typical mass M on the resonance frequency ($\Omega = \Omega_M$). At zero frequency we can consider a mass $M_0 = 0.3$ mg, while a typical mass M of a single vibrational mode is 100 mg [31]. Consequently, the signal-to-noise ratio is optimal on the static regime. Indeed, at a temperature of $T = 4$ K -using a helium cryostat for example- thermal noise is less important than radiation-pressure induced displacement. On the other hand, at resonance, by considering a mass $M = 100$ mg, equation (1.77) gives a signal-to-noise ratio 1000 times smaller, meaning that a cryogenic temperature of $T = 4$ mK would be necessary to observe radiation-pressure effects; a temperature that requires non-disposable cryogenic techniques.

The presence of thermal noise sets a number of experimental difficulties that must be overcome for our system to observe radiation-pressure effects. There are two important parameters that determine a favourable signal-to-noise ratio. First, the amplitude of the radiation-pressure fluctuations applied on the movable mirror must be maximised (the term $\mathcal{F}\bar{I}^{\text{in}}$). It is then necessary to obtain cavities with a very high finesse. For this purpose, the Laboratoire des Matériaux Avancés has been able to fabricate mirror coating tolerating an intracavity intensity of the order of $\mathcal{F}\bar{I}^{\text{in}} = 300\,000 \cdot 1 \text{ mW} = 300 \text{ W}$. The second parameter, is the mechanical properties of the resonator : the dissipation processes must be minimized (factor Q/Ω_M), so as the mass M and the temperature T . For our experiment, it has been chosen to fabricate a cavity which presents, at one hand, state-of-the-art optical properties (a very high finesse and very low losses) but on the other hand, a relatively large mass ($\simeq 100$ mg), leading to a signal-to-noise ratio $S_x^{\text{rad}}/S_x^T \simeq 6 \cdot 10^{-2}$ at 4 K at an incident power $\bar{I}^{\text{in}} = 1 \text{ mW}$ which does not suffice to observe radiation-pressure effects. These calculations have been made with a single-mode description of the resonator. In reality, the resonator presents numerous vibrational modes which may lead to a modification of the mirror mechanical response $\chi[\Omega]$ due to interference

effects amongst various modes. We can thus expect a more favourable signal-to-noise ratio. Furthermore, a part of this thesis has been dedicated to the increase of the incident power \bar{I}^{in} from 1 mW to 10 mW in order to increase radiation-pressure effects by a factor 10.

1.5.2 Introducing Optomechanical Correlations

The observation of intensity quantum fluctuations would be a very easy task if the thermal noise of the mobile mirror was not predominant (if $S_x^{\text{rad}} > S_x^T$). One would simply need to measure the reflected phase quadrature δq_{out} . However, there is a problem posed by the Heisenberg inequality: the phase and the intensity of the light are two non-commutative conjugate observables and they can therefore not be measured simultaneously. In order to directly observe radiation-pressure effects, one should establish correlations between these two observables. By drawing inspiration from the atomic physics pump-probe experiments the group has developed a double-injection scheme: two different beams are used; one to excite the system (pump) and drive the mirror motion, and a second one to probe the position of the mirror without disturbing it. The realization of such a pump-probe experiment requires the development of a double injection scheme where two different laser beams are simultaneously resonant with the cavity. By coupling to the cavity an intense pump beam used to drive the mirror into motion and a weak probe beam one can directly measure radiation-pressure effects by establishing correlations between the reflected phase δq_{out}^m of the probe beam and the intensity of the pump beam δp_{out}^s where the indexes s and m stand for signal and meter (see Figure 1.6).

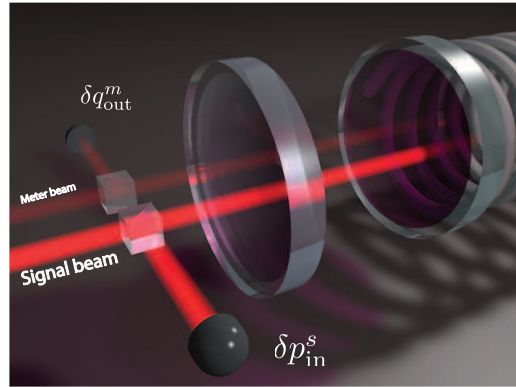


Figure 1.6: Pump-probe optomechanical correlations: The probe beam is used to measure the mirror displacement. Since $\delta p_{\text{in}}^s \simeq \delta p_{\text{out}}^s$ correlations between the probe output phase δq_{out}^m and the pump output intensity δp_{out}^s will provide a direct experimental demonstration of quantum radiation-pressure effects.

In particular, using equation (1.55), we find that if we neglect losses, the reflected intensity fluctuations reproduce the incident ones which are responsible for the displacement of the mirror:

$$\delta p_{\text{out}}^s = \delta p_{\text{in}}^s. \quad (1.78)$$

At the same time, the mirror displacement is imprinted onto the reflected phase of the probe beam. Using equation (1.56) we get:

$$\delta q_{\text{out}}^m[\Omega] = \delta q_{\text{in}}^m[\Omega] + \frac{128\mathcal{F}^2\bar{I}^{\text{in}}}{\lambda^2} \hbar\chi[\Omega]\delta p_{\text{in}}^s[\Omega], \quad (1.79)$$

where the radiation-pressure induced displacement, according to equation (1.68), is proportional

to the incident intensity fluctuations:

$$\delta x_{\text{rad}}[\Omega] = \frac{8\mathcal{F}\sqrt{\bar{I}_{\text{in}}}}{\lambda} \hbar\chi[\Omega] \delta p_{\text{in}}^s[\Omega]. \quad (1.80)$$

Quantum back-action effects are thus directly related to correlations between the incident pump intensity δp_{in}^s and the reflected probe phase δq_{out}^s . Furthermore, as we will see into the next section this scheme also permits to perform a quantum non demolition measurement of the pump beam intensity.

A very interesting aspect of the above experimental scheme is the Quantum Non Demolition (QND) [32–35] character of the measurement. In quantum mechanics, once the information on an observable is acquired it is not possible for the system to return to its original state; it is von Neumann projection postulate during the measurement process. A QND measurement permits to access the measurement of an observable without degrading the associated information. In order to qualify a measurement as a QND measurement, two criteria must be met [36]. First, the measurement procedure must not alter the observable, the noise imported by the measurement must be reported to the conjugated observable. Secondly, the issued measurement signal must contain the maximum information on the measured observable: strong correlations between the measurement apparatus and the measured observable must be present. Our double-injection scheme fulfils both criteria. The intensity of the pump beam is not modified when is it in resonance with the cavity. Furthermore, when the probe beam is also at resonance with the cavity the second criterion is satisfied. Indeed, at resonance the quantum correlations between the phase fluctuations of the reflected fields and the movable mirror displacement fluctuations are maximal.

1.5.3 Squeezing with a movable mirror cavity

However, there also exists an indirect way to experimentally demonstrate radiation-pressure effects by measuring the fluctuations of the cavity reflected field. Indeed, the optomechanical coupling induces a squeezing on the reflected field; certain quadratures will present a dispersion smaller than the standard quantum noise of the coherent state. This effect is presented in Figure 1.7. This effect can be understood with the help of equations (1.55) and (1.56) giving the reflected field quadratures. At low frequency ($\Omega \ll \Omega_{\text{cav}}$) and for a lossless cavity, they become:

$$\delta p_{\text{out}}[\Omega] = \delta p_{\text{in}}[\Omega], \quad (1.81)$$

$$\delta q_{\text{out}}[\Omega] = \delta q_{\text{in}}[\Omega] + \frac{128\mathcal{F}^2\bar{I}_{\text{in}}}{\lambda^2} \hbar\chi[\Omega] \delta p_{\text{in}}[\Omega]. \quad (1.82)$$

We will be interested in the injection of a coherent field into a movable mirror cavity represented in Figure 1.7 by a circular surface. We note that the unitarity of the input-output transformation implies the conservation of this surface. The projection of the surface on the horizontal axis gives the intensity fluctuations. The first equation then imposes the fact that at low frequency the amplitude fluctuations stay unaltered. On the other hand, the phase fluctuations increase as the radiation-pressure-induced displacement increases, as the second equation indicates. It corresponds to a widening of the angle under which the Wigner distribution is seen from the origin (see Figure 1.7). The distribution of quantum noise at the exit of the

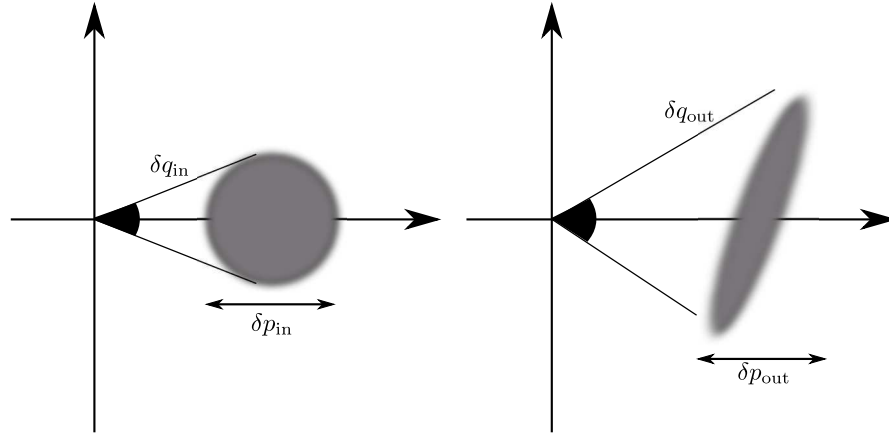


Figure 1.7: Phase-space representation of quantum noise of the incident (left) and reflected fields (right). The elliptical distribution of the reflected field indicates a squeezed state.

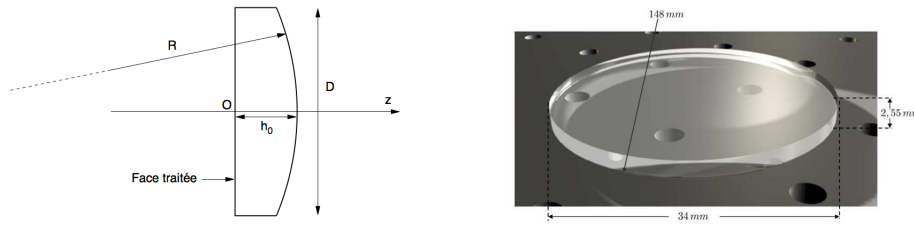


Figure 1.8: Geometry of the plano-convex mirror

cavity is elliptical with its long axis smaller than the original one; a squeezed state of the field is thus generated. We can finally note the analogy between the squeezing of the reflected field by optomechanical coupling and the Kerr effect by a non-linear medium in a cavity.

1.6 Experiment: basic elements

The group at the Laboratoire Kastler Brossel has developed a state-of-the-art experimental setup to perform ultra-sensitive displacement measurements. The main objective of this setup is to experimentally demonstrate radiation-pressure effects. It uses a measurement cavity, a Ti:Sa laser source, a spatial filtering cavity and a homodyne detection. All these parts will be detailed into the following sections.

1.6.1 Movable mirror cavity

The Fabry-Perot movable mirror cavity (FPM) is the core of our experiment. It is a cavity composed of a standard coupler and a specifically designed movable mirror whose displacement degree of freedom due to its internal vibrational modes. The design of the movable mirror is crucial as it has to combine very high optical quality with excellent mechanical properties. We choose fused silica as the best coatings cooling have been developed for this material and it has

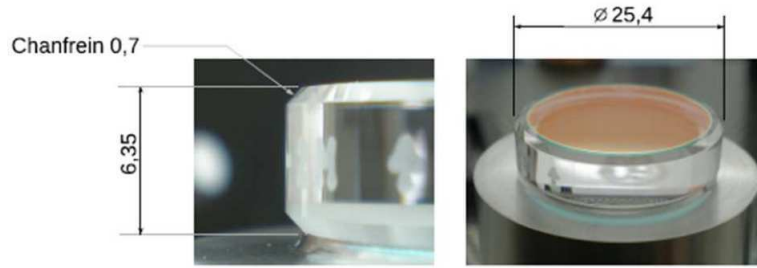


Figure 1.9: The cylindrical mirror

a very high intrinsic quality factor (up to 10^7) at room temperature. Figure 1.8 depicts the geometrical characteristics of the plano-convex mirror. It has a diameter $D = 34$ mm and a height $h_0 = 2.55$ mm. The convex side of the mirror has a radius of curvature $R = 148$ mm. The advantage of the plano-convex geometry of the substrate lies in the fact that it presents gaussian vibrational modes confined at the centre of the mirror whose waist, a few mm wide, is small compared to the mirror global size. These modes are then well isolated from the clamping and mechanical losses are reduced. The input mirror of the cavity (coupler) presents a cylindrical geometry (Figure 1.9) whose concave side has a radius of curvature $R = 1$ m. The substrates are then super-polished by REO or GSI and the optical coating is made by the Laboratoire de Matériaux Avancés (LMA) whose contribution is critical since they have the know-how of coating the dielectric layers on the substrates: the LMA mirrors generally present a transmission of a few ppm (part per million, i.e. 10^{-6}) with a very low absorption and scattering losses. The cavity moving end-mirror has a transmission $T_2 < 1$ ppm. The choice of the coupler transmission T comes from a trade-off between finesse ($T \ll 1$) and cavity losses P smaller than the coupler transmission ($T > P$) as shows equation (1.72). Typically, our cavities present losses P smaller than 10 ppm. For this reason, a coupler transmission of 20 ppm has been chosen in order build a cavity with a finesse $\mathcal{F} \simeq 300\,000$.

We have also seen that the cavity has a low-pass filtering effect to the fluctuations, which is characterized by its bandwidth Ω_{cav} . This cut-off frequency should be high enough not to limit the sensitivity to the mirror displacements. For the plano-convex geometry of the movable mirror, resonance frequencies of $\Omega/2\pi = 1$ MHz are expected, setting a down limit to the cavity bandwidth ($\Omega_{\text{cav}} > \Omega$). For a finesse $\mathcal{F} = 300\,000$, this limit would lead to a typical cavity length $L = 100\ \mu\text{m}$, which, in turn, along with the coupler radius of curvature, defines the optical waist in the cavity. Using equation (1.47) a waist $w_0 = 60\ \mu\text{m}$ is found.

A mechanical mounting system should also be designed taking into account two important factors. First, a good parallelism between the two mirrors is required for the cavity optical modes to be centered on the plano-convex mirror. This condition is necessary to obtain a good spatial overlap between the laser waist and the Gaussian mechanical modes which are confined to the centre of the mirror: a deviation of some millimetres of the laser beam away from the center of the movable mirror would lead to a read-out measurement insensitive to the mirror displacement. Second, the mirrors must be mounted in such a way that clamping losses are reduced. The cavity mounting design developed by the group is depicted in Figure 1.10. The mirrors are stacked into a tube closed by a thin, circular and elastic blade. The mounting is designed in such a way so that the resulting cavity is compact and rigid, minimizing residual

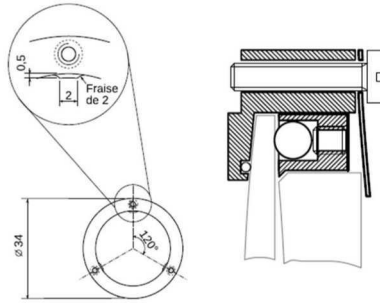


Figure 1.10: The mounting design of the movable mirror cavity.

vibrations. For this purpose, no piezoelectric actuator is integrated into the cavity and no active control of the length cavity is realized. Instead, it is the laser wavelength that is tuned, in order to keep the cavity on resonance. An adapter ring allows to adapt the diameter of the cylindrical mirror to that of the plano-convex. Given the importance of the spatial overlap between the optical and the mechanical modes, we integrated into the mounting design a centering system: three housing holes are located at 120 degrees from each other in the adapter ring of the input mirror, in which three steel balls are inserted and pushed by an adjusting screw, thus permitting the necessary tilt of the coupler.

Mounting and alignment of the cavity

Extreme caution must be taken while mounting the mirrors into the mounting system. The procedure must take place under a very clean air flow. We have at our disposal a specific class 1 laminar air flow under which all mirror manipulations take place. The operator must be equipped with a special uniform, including gloves, a mask and a hat in order to avoid any external pollution of the superpolished mirrors. The mounting procedure is as follows: first, the coupler is put on a cylinder with the coated surface facing upwards. The adaptation ring is then placed around the coupler. The plano-convex mirror is carefully deposited onto the adaptation ring, the polished surface facing downwards, towards the coupler. The external tube is then placed round the adaptation ring and the plano-convex mirror. Finally, the system is flipped in order to be able to close the tube with the thin blade.

Once the mirrors are mounted the system is almost air tight, protecting the fragile optical coating. It can then directly be mounted onto the experimental setup in a vacuum chamber. Once an incident beam is well coupled to the coupler, by carefully adjusting its incident angle, with the help of an infra-red camera, transverse modes can immediately be observed at the exit of the cavity. The cavity not being stabilized in temperature and the vacuum chamber being open, its optical length naturally changes and thus the cavity is naturally swept. By observing the transverse modes we try to focus the light to the centre of the plano-convex mirror. This is done by carefully tightening the screws to adjust the mirror parallelism and adjusting the incident beam angle. Once this alignment stage is optimized the temperature controller is turned on and the vacuum chamber is pumped down to $\sim 10^{-4}$ mbar. The second alignment step consists in modulating the laser frequency at 100 Hz and observing the cavity transmission via a photodiode. A Lorentzian Airy peak should be visualized with a digital oscilloscope. Using the micrometric screws of the mirrors that adjust the beam incident angle

we optimize the coupling between the beam and the cavity.

1.6.2 Laser source

In the previous section, we mentioned that in order to increase the stability of the cavity we have decided not to implement a piezoelectric actuator into the cavity in order to control the cavity length. Instead, a widely tunable laser is used. The measurement cavity (FPM) is a short cavity with a length, typically of the order of some hundreds of microns, which results in a Free Spectral Range (FSR) of a few hundreds of GHz. This means that the tunability of the laser should be at least equal to a cavity FSR. Furthermore, the laser source should be continuously tunable over a frequency range of some GHz, which corresponds to the interval between two transverse modes ν_{tr} . We therefore need a laser source that is continuously tunable over a frequency range of some GHz and capable of frequency jumps of some hundreds of GHz. In addition, a fast sweep of a few MHz of the laser frequency is necessary in order to visualize the FPM Airy peak. The laser frequency should also be stabilized to the frequency of a cavity resonance at one point. For this purpose, a fast control of the laser frequency should be set up. Finally, it is very important that the laser technical noises are negligible compared to the photon noise close to the analysis frequency.

All these requirements are met by a Titane:Sapphire laser constructed by the group and based on a model designed by François Biraben [37] in the 1980. The core of the laser is a ring cavity where the Titane:Sapphire crystal is pumped by a Verdi laser delivering a 18 W laser beam at 532 nm.

Figure 1.11 depicts the main elements of the laser. The direction of the light path into the cavity is imposed by a unidirectional system made of a Faraday rotator, which induces a polarisation rotation compensated by the out-of-plane mirrors M_4 , M_5 and M_6 . All mirrors have a high reflectivity for wavelengths of 810 nm except the exit mirror M_6 with a transmission of 4%. The Ti:Sa crystal has a very large gain spectrum compared to the interval between two longitudinal cavity modes, typically about 200 MHz. The laser cavity alone is thus highly multimode and a series of optical elements are added into the cavity in order to provide a monomodal operation of the laser and to be able to select the desired frequency:

- The Lyot filter is made of 4 parallel birefringent plates selecting a frequency range of a few hundreds of GHz. A motor is coupled to the Lyot filter in order to rotate the 4 plates and select the desired range.
- The thin etalon is a thin plate made of silica, acting as a Fabry-Perot cavity with a free spectral range of 150GHz. This etalon can continuously be tilted by means of a motor, thus controlling the optical path and consequently tuning the optical resonances of the laser.
- The thick etalon is made of two prisms facing each other in order to form Fabry-Perot cavity. Each prism presents a reflection coefficient of 30%. The cavity thickness is equal to 8 mm and its Free Spectral Range is 19 GHz. One of the prisms is mounted on a piezoelectric actuator in order to shift the cavity resonance comb at will. This piezoelectric actuator is also used in order to lock its resonance frequency at the laser frequency: the cavity length is modulated at 3 kHz via the piezoelectric actuator resulting in an intensity modulation of the laser beam. This modulation is detected and demodulated at

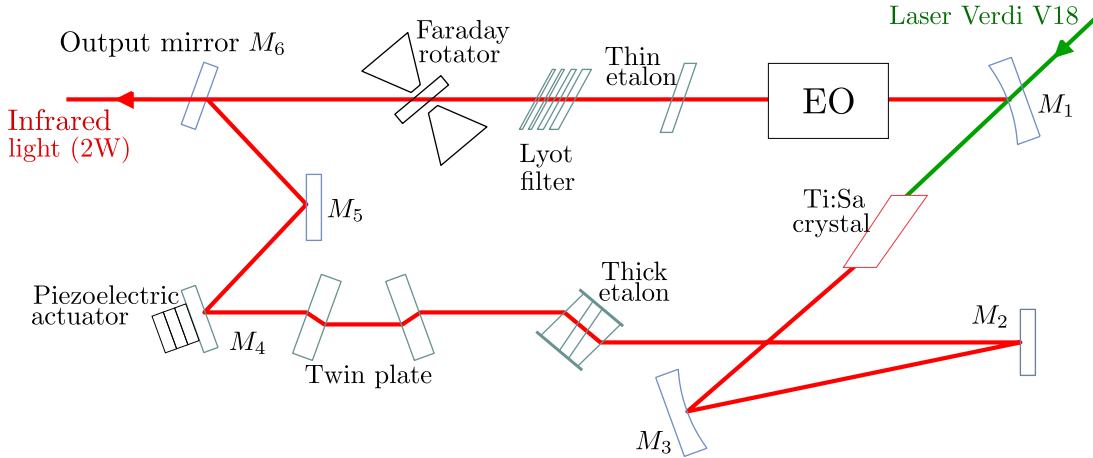


Figure 1.11: Ring cavity and the different elements in the Ti:Sa laser.

the same frequency creating an error signal used to lock the thick etalon for a maximum transmission.

The Ti:Sa crystal pumped by a 18 W Verdi laser combined with the three elements described above provide a monochromatic laser beam, tunable in the range from 790 to 850 nm. We can modify the laser frequency either continuously or by frequency jumps. To scan continuously the frequency, we use a twin plate composed of two symmetrical plates. A motor is used to tilt these plates and thus the laser wavelength. This system allows the tuning of the laser over a range of a few gigahertz. An internal Electro-Optical Modulator (EO) is also implemented into the ring cavity also altering the optical path. It can induce small and fast changes in the laser wavelength; this EO is used to lock the laser frequency to the measurement cavity (up to 1 MHz). Furthermore, a second piezoelectric actuator is implemented into the laser cavity, mounted onto the mirror M_4 , permitting to either sweep the laser frequency over some MHz or, in addition to the internal EO, to lock the laser wavelength at low frequencies (up to a few hundreds of Hz). Finally, in order to make frequency jumps, either the Lyot filter or the thin etalon is used. A commercial wavemeter (Bristol 182) is used to continuously monitor the laser wavelength. Finally, this system can provide an infrared laser beam of up to 2 W which is only limited by photon shot-noise at 1 MHz, for an available power of 1 mW.

1.6.3 Tunable double injection

Figure 1.12 depicts a simplified version of the experimental setup. It corresponds to the actual experimental setup before the implementation of our double injection scheme. The Ti:Sa delivers an infrared beam at 800 nm which is first spatially filtered by a mode cleaner cavity (Fabry-Perot Filtering cavity FPF) with a large bandwidth (Ω_{cav}) and then intensity-stabilized by an Electro-Optic Modulator. The beam is then split into two parts, each one corresponding to an arm of a Michelson interferometer; one arm being the meter beam and the other the local oscillator. Both beams, are recombined and the interference pattern is monitored by two photodiodes. This type of Michelson interferometer is called a homodyne detection and it will

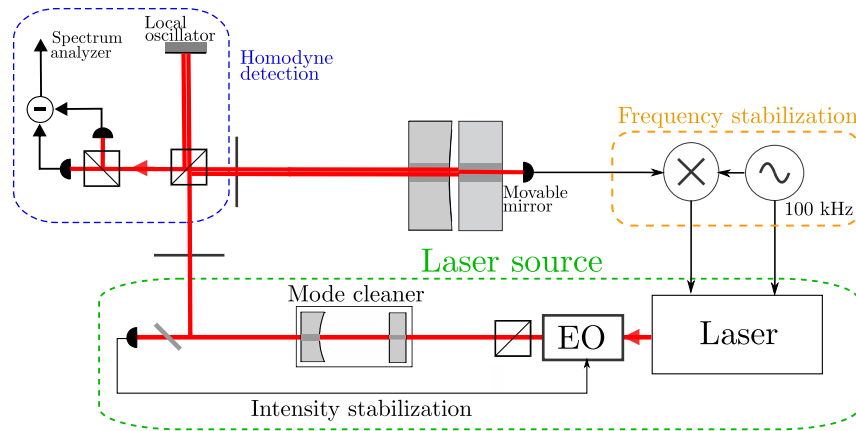


Figure 1.12: A simple injection scheme. The light emitted by the Ti:Sa is spatially filtered and intensity stabilized. Then, it is separated into two beams: the local oscillator and the measuring beam. The laser frequency is also locked on the cavity resonance.

be detailed in the next section.

In order to observe the quantum correlations between the intensity fluctuations and the displacements of the mirror, the group has developed a scheme to inject two laser beams into the FPM as in a standard pump-probe scheme: an intense pump beam is used to drive the mirror motion whereas a weaker probe beam monitors the position of the mirror.

Double injection optical setup

The development of such a scheme involves a number of precautions. First, the two beams must be well matched to the measurement cavity. The optical structure of both beams must be identical when they are coupled to the cavity. Their frequencies must also be tunable since the measurement cavity is rigid and may present birefringent effects. Second, an excellent optical isolation must be achieved in order to ensure that no optical contamination occurs to either of the reflected beams. Finally, such a scheme needs two separate detection systems: one to monitor the reflected intensity of the pump (a simple photodiode) and one to monitor the mirror displacement (homodyne detection) via the phase-shift of the probe.

Figure 1.13 depicts the optical setup of the double injection scheme. The beam goes through a system of a half-wave plate and a Polarizing Beam Splitter (PBS_1) in order to split it into two parts. The reflected part plays the role of the probe beam while the transmitted part is the pump beam. The pump beam first goes through a non-resonant Electro-Optic Modulator (EOM) which in combination with the beamsplitter PBS_2 forms an intensity modulator. Afterwards, the pump beam goes through an optical circulator formed by beamsplitters, PBS_2 , a half-wave plate and the Faraday rotator. This way the reflected pump beam can be monitored by the photodiode Phd_1 . A similar optical system is installed for the probe beam. After its reflection by beamsplitter PBS_1 it passes through a half-wave plate and PBS_4 in order to set the desired intensities for the probe beam and the Local Oscillator (detail on the homodyne detection will be given in section 1.6.5). In addition, there is a second optical circulator ensuring the monitoring of the reflected probe beam by the homodyne detection. The probe and the pump beams are recombined by PBS_3 . We then have two beams with orthogonal polarizations

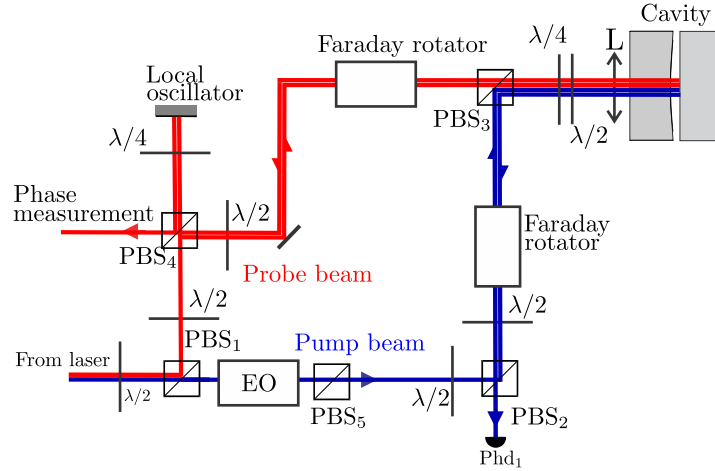


Figure 1.13: Double injection setup: the two cross-polarized beams are split by PBS₁ to form the probe (red) and pump (blue) beam. Both beams are first coupled to the measurement cavity and then reflected towards their detections.

propagating together. They both pass by two plates -one half-wave and one quarter-wave- in order to precisely adjust the polarizations of the two beams and to compensate eventual polarization rotations caused by the cavity. Before they are finally coupled to the cavity, they both pass by a system of two thin lenses used to match the cavity.

Once the beams are reflected by the cavity, they follow the inverse path. They are once again split by beamsplitter PBS₃ but as each beam propagates back to its own Faraday rotator their polarization is turned to 90° with respect to the beam polarization at first pass. This way, both the pump and the probe beams are simply transmitted by beamsplitters PBS₂ and PBS₄ respectively, allowing their detection.

Tunable double injection

The double injection of two beams with orthogonal polarizations into the same cavity comes with a major drawback: the cavity birefringence due to the dielectric coatings of the mirrors induces phase-shifts which are different for each polarization. The length, the free spectral range of the cavity and therefore the resonance frequency of each polarization will be different. Our cavities present birefringent effects which can correspond to several cavity bandwidths. It is thus necessary to be able to tune the frequency of each beam independently within a range of at least a few megahertz. For this purpose, a system of two Acousto-Optic Modulators (AOM) is used to change the frequency of the pump and the probe beam. This type of modulator is composed of a crystal which is coupled to a piezoelectric actuator. Once the crystal is excited by the piezoelectric a static wave is formed into the crystal and creates a diffraction grating. As the laser beam propagates through the crystal there is a momentum exchange between the field and the acoustic wave: the photons are diffracted and a frequency shift, corresponding to the number of the involved phonons, occurs. As we only need a frequency difference of a few MHz between the probe and the pump beams, both beams are sent into two identical double-pass configured AOM systems. One of them is driven by a constant frequency of 200 MHz, while the other is driven by a tunable VCO (between 190 and 210 MHz) offering the possibility of a

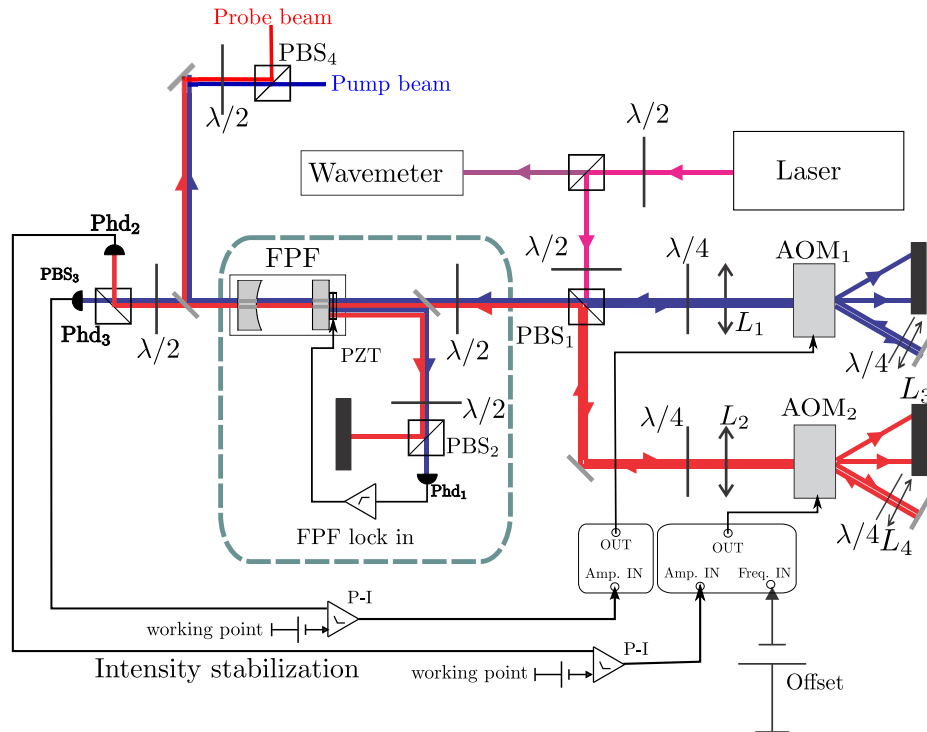


Figure 1.14: Tunable double injection: in order to cancel any birefringence effects of the measurement cavity at two double-pass acousto-optic modulators system is system in order to add a frequency difference between the two beams.

fine and fast tuning of the laser frequency without preventing any tilt noise on the beam. This two-AOM system is depicted in Figure 1.14. The laser beam is split by beamsplitter PBS_1 into two perpendicular polarizations, corresponding to the pump and the probe beam. Both double-pass system use an AOM (AA Opto-electronic, MT200-A0.5-800). A thin lens (L_1 and L_2) is carefully set in order to create an optical waist centered at the AOM, whose Rayleigh length is comparable to the AOM length. With the help of a diaphragm, we then select the first order of diffraction. A mirror placed at normal incidence is used to re-inject the beam into the AOM following exactly the inverse path. A second thin lens (L_3 and L_4) is placed in order to create an optical waist onto the mirror so that the properties of the reflected beam are identical to the incident one. Finally, a quarter-wave plate is used to form an optical circulator with the beamsplitter PBS_1 . AOM_1 is driven by a fixed-frequency Voltage Controlled Oscillator (VCO) AA MODA200 2W delivering a radiofrequency signal at 200 MHz, offering the possibility to alter the wave amplitude by a 0-5 V input. AOM_2 is driven by a variable-frequency VCO AA DRFA10Y, offering, in addition to the amplitude control, a frequency control (± 10 MHz) via a second 0-10 V input. Since this VCO does not deliver a high-power signal, necessary for the AOM proper operation, its output is sent to an amplifier AA AMPA-B-33, capable of delivering 2 W.

Mode cleaner

For the mode matching between the laser beam and the measurement cavity (FPM) to be optimal, the beam must present a perfect Gaussian profile. This is not the case since the Ti:Sa laser delivers an astigmatic Gaussian beam. In order to correct this, a Fabry-Perot Filtering cavity (FPF) is used. This is a 12-cm long cavity made of a plane input mirror and a plano-concave output mirror (radius of curvature $R = 1$ m) both having a 95% reflectivity; a cavity finesse of almost 100 is obtained. By maintaining the fundamental mode TEM_{00} of the cavity resonant with the laser, only the corresponding component of the beam is transmitted by the cavity while the other components will be reflected. A perfect Gaussian mode TEM_{00} is thus obtained. In order to keep the laser beam at resonance with the fundamental mode of the FPF cavity, the input mirror is mounted on a piezoelectric actuator and allows to adjust the cavity length (see Figure 1.13). The locking-loop uses a lock-in scheme that drives the actuator at a frequency of 4.5 kHz. This cavity length modulation is equivalent to a frequency modulation leading to an in-phase or out-of-phase intensity modulation, depending on the sign of the cavity detuning, which can be observed either in the transmitted or in the reflected field. In our case, the reflected field is monitored by photodiode Phd_1 . The resulted signal is then demodulated with a local oscillator at the same frequency creating an error signal which is used to drive the piezoelectric actuator via a feedback loop. In fact, since both cross-polarized beams are reflected by the cavity, a polarizing beamsplitter selects only one, whose intensity is sent to the photodiode. The cavity is then locked only on one of the two beams, which causes no problem as long as the two beams have strictly the same frequencies. However, due to the birefringent measurement cavity, the two beams are slightly detuned with respect to each other. In principle, if the birefringence is greater than the FPF bandwidth $\nu_{BP} = 5.6$ MHz, then one of the two beams will be filtered by the cavity. Since birefringent effects of only a few MHz are observed, this problem is bypassed limited to the loss of some optical power.

Intensity lock-in

The above tunable double injection setup can also be used also to stabilize the intensities of the beams using a standard P-I feedback controller. The schematic layout of such a stabilization is shown on Figure 1.14. The intensity of the beam, is detected at the output of the mode cleaner cavity, and the working point of the AOM is modified via a feedback loop so that the intensity of the laser beam is stabilized. In order to perform the feedback, the AOM working point has to be set at a value below the maximum of diffraction obtained for a control voltage of 5 V. Ideally, the optimal working point is 2.5 V to have the maximum dynamics for the feedback loop. However, we have observed that if the working point is lower than 5 Volts then the AOM adds high-frequency intensity noise to the beam. Therefore, such a noise eater can prove to be destructive especially for the pump beam which is supposed to be at photon noise, .

1.6.4 Frequency stabilization: the Pound-Drever-Hall technique

A Pound-Drever-Hall (PDH) technique [38] is used to stabilize the laser frequency resonant with respect to the movable mirror cavity resonance. It consists in observing the cavity response to a phase modulation of the incident field. The phase modulation is realized by a resonant electro-optic modulator at a given frequency Ω_{PM} , greater than the cavity bandwidth (see Figure 1.15). This phase modulation creates sidebands at Ω_{PM} with respect to the carrier.

When the light enters the cavity it becomes sensitive to the mirror displacement and the cavity detuning we are seeking to control. The carrier is then phase-shifted proportionally to the detuning. On the other hand, the sidebands, are very far from the cavity resonance and are simply reflected by the cavity. Consequently, a phase difference between the sidebands and the carrier occurs and the incident phase modulation becomes an amplitude modulation on the reflected field. The beating between the carrier and the sidebands has a slowly-varying envelope that constitutes the error signal. In order to extract the error signal the reflected field intensity is then demodulated at the frequency of the phase modulation.

The Pound-Drever-Hall error signal

We will see in this section how the Pound-Drever error signal is derived. The incident laser field α_0 is phase-modulated. It then becomes:

$$\alpha_{\text{in}}(t) = \alpha_0(t)e^{i\beta \cos(\Omega_{\text{PM}}t)}, \quad (1.83)$$

where β is the modulation amplitude. This expression can be developed with the help of the Bessel expansion $e^{iz \cos \theta} = \sum_{-\infty}^{\infty} i^n e^{in\theta} J_n(z)$. Assuming a small modulation depth β , the first-order expansion is:

$$\alpha_{\text{in}}(t) = \alpha_0(t) \left[J_0(\beta) + iJ_1(\beta)e^{i\Omega_{\text{PM}}t} - iJ_{-1}(\beta)e^{-i\Omega_{\text{PM}}t} \right]. \quad (1.84)$$

From the above equation, we clearly see that the incident field can be decomposed into a carrier frequency (term J_0) and two sidebands at frequencies $\pm\Omega_{\text{PM}}$ (terms $J_{\pm 1}$), in quadrature with respect to the carrier. We are now going to derive the error signal in the simple case where the carrier is detuned from the cavity by a quasi-constant phase-shift. Using expressions (4.1) and (4.2) describing the incident and reflected fields we deduce the reflection coefficient r_{Ψ} at frequency Ω as a function of the detuning Ψ :

$$r_{\Psi}[\Omega] = \frac{\gamma - P + i\Psi + i\Omega\tau}{\gamma - i\Psi - i\Omega\tau}. \quad (1.85)$$

By applying this static response to each term of equation (1.84) we obtain the expression of the cavity reflected field:

$$\alpha_{\text{out}}(t) = \alpha_0(t) \left\{ r_{\Psi}[0]J_0(\beta) + ir_{\Psi}[-\Omega_{\text{PM}}]J_1(\beta)e^{i\Omega_{\text{PM}}t} - ir_{\Psi}[\Omega_{\text{PM}}]J_{-1}(\beta)e^{-i\Omega_{\text{PM}}t} \right\}. \quad (1.86)$$

The output field intensity $I_{\text{out}} = |\alpha_{\text{out}}|^2$, detected by a photodiode, has a DC component, a component oscillating at frequency $\Omega_{\text{PM}}/2\pi$ and all the harmonics of this frequency coming

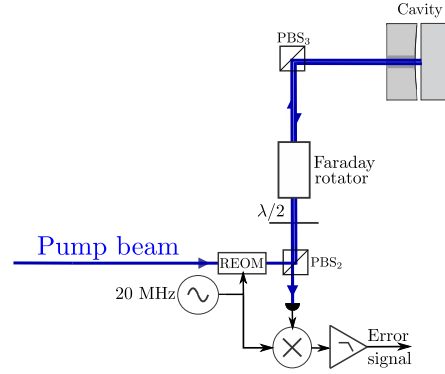


Figure 1.15: A Pound-Drever-Hall detection scheme: a resonant electro-optic modulator creates sidebands. The reflected intensity is then demodulated to yield the error signal.

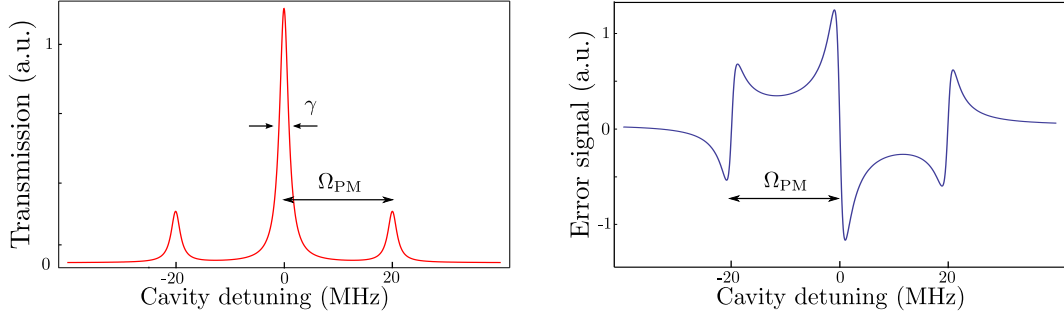


Figure 1.16: Left: sidebands at 20 MHz with respect to the carrier. Right: the corresponding Pound-Drever error signal. Both curves are calculated for a lossless cavity, with a bandwidth $\Omega_{\text{cav}} = 1$ MHz, for an incident field phase-modulated at 20 MHz.

from higher-order terms of the Bessel expansion. We are interested only in the Ω_{PM} part:

$$I_{\text{out}} \Big|_{\Omega_{\text{PM}}} = -2J_0 J_1 \bar{I}_{\text{in}} \left[\text{Im} \left[r_{\Psi}^*[0] \left(r_{\Psi}[-\Omega_{\text{PM}}] + r_{\Psi}[\Omega_{\text{PM}}] \right) \right] \cos(\Omega_{\text{PM}} t) + \text{Re} \left[r_{\Psi}^*[0] \left(r_{\Psi}[-\Omega_{\text{PM}}] - r_{\Psi}[\Omega_{\text{PM}}] \right) \right] \sin(\Omega_{\text{PM}} t) \right]. \quad (1.87)$$

The above signal will be demodulated at frequency Ω_{PM} : it is mixed with a reference signal oscillating at the same frequency, i.e. a local oscillator, and a low-pass filter is used to remove the generated harmonics, keeping only the slow-varying envelope of the reflected field. The result of this operation can provide either the amplitude of the first or the second term, or a combination of both, depending on the phase of the local oscillator. The term oscillating as $\sin(\Omega_{\text{PM}} t)$ has a zero slope at zero detuning. Hence, this part of the error signal is not useful to lock the cavity close to resonance. The phase of the local oscillator must thus be set in order to keep only the term oscillating as $\cos(\Omega_{\text{PM}} t)$. The error signal can then be written as:

$$V_{\text{err}}(\Psi) = \langle I_{\text{out}}(t) \cos(\Omega_{\text{PM}} t) \rangle \quad (1.88)$$

$$= -J_0 J_1 \bar{I}_{\text{in}} \text{Im} \left[r_{\Psi}^*[0] \left(r_{\Psi}[-\Omega_{\text{PM}}] + r_{\Psi}[\Omega_{\text{PM}}] \right) \right]. \quad (1.89)$$

When the frequency of the sidebands is greater than the cavity bandwidth Ω_{cav} and the detuning is small compared to the bandwidth, the latter equation can be simplified:

$$V_{\text{err}} \approx -J_0 J_1 \bar{I}_{\text{in}} \frac{\gamma \Psi}{\gamma^2 + \Psi^2}. \quad (1.90)$$

This equation shows that the error signal varies rapidly around zero, changing sign as the cavity working point passes from one side of the Airy peak to the other. Figure 1.16 depicts the transmission of a cavity swept around its resonance and the corresponding error signal. The error signal is always positive for red detunings (between the resonance and $-\Omega_{\text{PM}}$) and negative for its symmetrical part corresponding to blue detunings: the feedback loop will thus be able to locate the cavity resonance. Furthermore, the error signal is still non-zero even for a detuning much larger than the cavity bandwidth: the capture range is equal to $2\Omega_{\text{cav}}$.

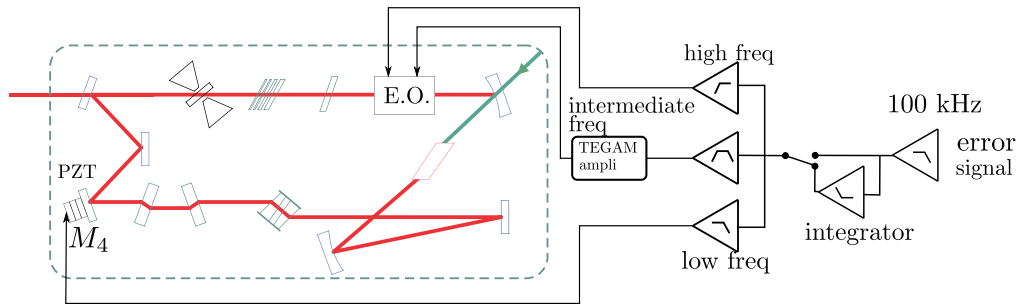


Figure 1.17: The laser lock-in. The error signal is split into a low-frequency, a high-frequency and an intermediate frequency component driving the piezoelectric actuator and the electro-optic modulator of the laser.

Pound-Drever-Hall implementation

We have decided to implement the phase modulator on the pump beam and not on the probe beam. This decision has been taken primarily due to eventual electronic saturation effects of the homodyne detection caused by the phase modulation. Figure 1.15 depicts the layout of this technique. A resonant phase modulator (model 4851 by New Focus) modulates the pump beam at 20MHz. The frequency modulation was chosen as a good compromise between the cavity bandwidth and the bandwidth of the photodiode monitoring the reflected pump field. The optical circulator, formed by beamsplitters PBS_2 and PBS_3 and the Faraday rotator, ensures the detection of the reflected field. Once the field is detected, the generated signal is amplified by a 30 dB amplifier (Nucléonides ALP64-10). The extraction of the error signal is then realized by a home-made demodulator circuit that consists of a low-pass filter (MiniCircuits PLP-21.4+), suppressing the phase-modulation harmonics, a frequency mixer (MiniCircuits SBL-1+), mixing the signal with the local oscillator, and a low-pass filter (MiniCircuits PLP-1.9+), suppressing the harmonics produced by the mixing procedure. Both the phase modulator and the local oscillator are driven by a double generator (Tektronix AFG3102) delivering two monochromatic sinusoidal signals with the same frequency but with an adjustable relative phase between them. This feature is very convenient in order to choose the correct quadrature of the demodulated signal.

The produced Pound-Drever error signal is then used in order to lock the laser frequency to the resonance of the measurement cavity. To this purpose, two optical elements of the laser cavity are mainly used as feedback transducers: the piezoelectric actuator mounted on mirror M_4 (see Figure 1.17) and the internal electro-optic modulator; each one is driven by a different spectral band of the error signal. As Figure 1.17 depicts, a series of filters (a high-pass, a low-pass and a band-pass) splits the error signal into three, well-distinguished, frequency bands: a slow one (up to 100 Hz), an intermediate one (between 100 Hz and some kHz) and a fast one (up to 10 kHz). The piezoelectric actuator, presenting a slow response but a great amplitude is used to compensate the slow drifts of the cavity. The intermediate component, via a low-noise, high-speed amplifier (TEGAM), drives the internal electro-optical modulator (entry +) while the fast component also drives directly the electro-optical modulator (entry -). The global error signal is also filtered by a low-pass filter with a cut-off frequency at 10 kHz adding a global slope of 10 dB/decade. Finally, once a stable lock-in is achieved, there is an additional integrator

stage, adding further low-frequency gain to low frequency component ensuring stability on long time scales, typically several hours.

1.6.5 Homodyne Detection

The double injection scheme consists in using two separate laser beams coupled to the measurement cavity. Both reflected beams are monitored by two separate detectors. For the pump beam we are interested in measuring its intensity, therefore a simple photodiode suffices. Usually, we use photodiodes which are coupled to a home-made pre-amplifier circuit. It is based on two stages, one providing the DC-component of the signal and another giving the high-frequency component. The high-frequency part of the amplifier presents a typical bandwidth of 50 MHz. A FND100 Si PIN photodiode EG&G is used, presenting a quantum efficiency of 90%.

We need to measure the phase of the probe beam which can be done by an interferometric scheme. The probe beam reflected by the movable mirror is thus fed into a homodyne detection [39] in order to detect its phase fluctuations. It is based on the mixing of the signal to be measured with another field used as a phase reference namely the local oscillator. By carefully locking the relative mean phase between the local oscillator and the reflected beam we are capable of measuring a relative phase variation between the two beams. It is thus possible to measure the fluctuations of any quadrature of the reflected field by accordingly choosing the phase of the local oscillator.

Principle of the homodyne detection

The optical setup of the homodyne detection is depicted on Figure 1.18. The incident beam, linearly polarized, is split in two parts thanks to a half-wave plate followed by a polarizing beam splitter PBS₅, creating the probe beam and the local oscillator. In practice, the local oscillator should be at least one order of magnitude more powerful than the probe beam. By setting the local oscillator at typically 10 mW the probe beam power may arbitrarily vary up to 1 mW. Each beam goes through a quarter-wave plate, oriented at 45°, turning accordingly their polarization two times as both beams realize a double-trip towards their respective mirrors and back. This results into a global polarization rotation of 90° for each beam which are then recombined at the fourth output of beam splitter PBS₅. At this point the two co-propagating beams are cross-polarized and thus no interference effects are observed. In order to combine the two beams, they are directed towards a system made of a half-wave plate, oriented at 22.5°, and a polarizing beam splitter which splits them into two parts of equal intensity. Interference effects can now be observed by directing each output port of the beam splitter towards a photodiode. By noting α_{out} the reflected field by the cavity and $\alpha_{OL}e^{i\phi}$ the field of the local oscillator, the fields $\alpha_1(t)$ and $\alpha_2(t)$ detected by photodiodes Phd₁ and Phd₂ are:

$$\begin{aligned}\alpha_1(t) &= \frac{1}{\sqrt{2}}[\alpha_{out}(t) + \alpha_{OL}(t)e^{i\phi}], \\ \alpha_2(t) &= \frac{1}{\sqrt{2}}[\alpha_{out}(t) - \alpha_{OL}(t)e^{i\phi}],\end{aligned}\tag{1.91}$$

where the mean fields amplitudes $\bar{\alpha}_{OL}$ and $\bar{\alpha}_{out}$ are assumed real, ϕ being the relative phase between the two fields. The two photocurrents produced by the two photodiodes are pre-

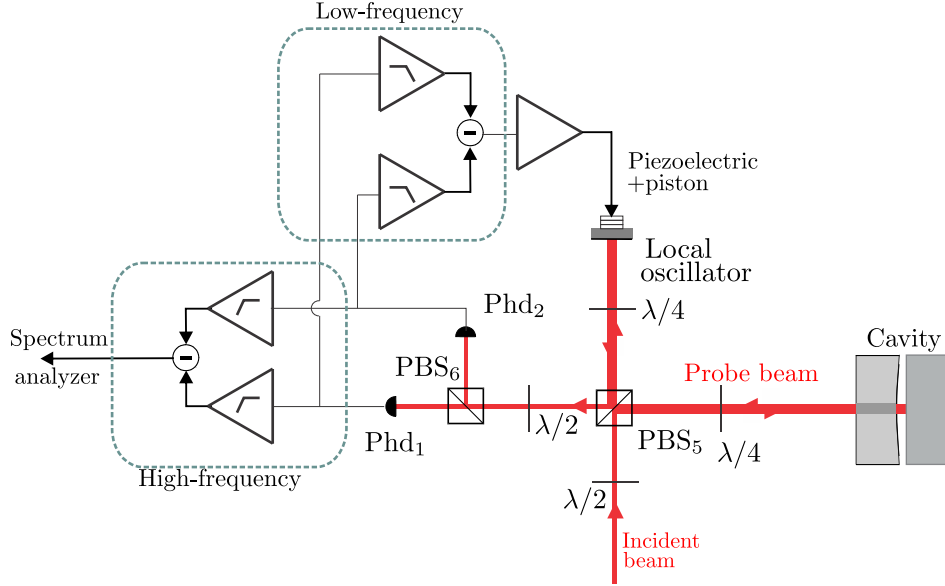


Figure 1.18: Homodyne detection: the incident beam is first split into the two parts by PBS₆. One forming the Local Oscillator and the other the probe beam. PBS₆ also serves to recombine the two beams before feeding them to the balanced detection. The A-B output of the detection is then split to a HF and LF component serving to observe the mirror motion and to stabilize the length of the Local Oscillator, respectively.

amplified and then subtracted. The signal $I_-(t)$ generated by this operation is:

$$I_-(t) = 2Re[\alpha_{\text{out}}\alpha_{\text{OL}}^*e^{-i\phi}]. \quad (1.92)$$

By linearizing this equation we get the fluctuations $\delta I_-(t)$ around the mean value $I_-(t)$. The mean value of the photocurrent difference $I_-(t)$ is given by:

$$\bar{I}_- = 2\bar{\alpha}_{\text{out}}\bar{\alpha}_{\text{OL}}\cos\phi, \quad (1.93)$$

and is directly related to the relative phase between the two fields:

$$\bar{I}_- = 2\sqrt{\bar{I}_{\text{out}}\bar{I}_{\text{OL}}}\cos\phi, \quad (1.94)$$

while the fluctuation $\delta I_-(t)$ are given by:

$$\begin{aligned} \delta I_-(t) = & \bar{\alpha}_{\text{OL}}[\delta\alpha_{\text{out}}(t)e^{-i\phi} + \delta\alpha_{\text{out}}^*(t)e^{i\phi}] \\ & + \bar{\alpha}_{\text{out}}[\delta\alpha_{\text{OL}}(t)e^{i\phi} + \delta\alpha_{\text{OL}}^*(t)e^{-i\phi}]. \end{aligned} \quad (1.95)$$

The fluctuations of I_- are then given by the sum of the fluctuations of the reflected field quadrature α_{out}^ϕ and the fluctuations of the local oscillator quadrature α_{OL}^ϕ mixed with the mean fields $\bar{\alpha}_{\text{OL}}$ and $\bar{\alpha}_{\text{out}}$ respectively. By setting the intensity of the local oscillator large compared to the intensity of the probe beam the second term of the latter equation can be neglected. The fluctuations of the probe beam are therefore imprinted onto the difference of

the two photocurrents produced by photodiodes Phd₁ and Phd₂. The noise spectrum $S_-[\Omega]$, as measured by a spectrum analyzer, is then proportional to the noise spectrum $S_{\text{out}}^\phi[\Omega]$ of quadrature α_{out}^ϕ :

$$S_-[\Omega] = \bar{I}_{\text{OL}} S_{\text{out}}^\phi[\Omega]. \quad (1.96)$$

The control of the relative phase ϕ between the two beams permits access to the noise spectrum of any quadrature of the field α_{out} . For instance, we can access the phase of the reflected beam when $\phi = \pi/2$ by locking the local oscillator at $\bar{I}_- = 0$.

Real homodyne detection

The previous calculation assumes an ideal detection. Experimental imperfections can add signal losses and lead to a measurement sensitivity deterioration. The quantum efficiency of the photodiodes, and more generally the losses induced by the optical elements attenuate the reflected field and couple it to vacuum fluctuations. The phase spectrum of the reflected field is then contaminated by the vacuum fluctuations:

$$S_-[\Omega] = \bar{I}_{\text{OL}}(\eta_{ph} S_{\text{out}}^\phi[\Omega] + 1 - \eta_{ph}), \quad (1.97)$$

where η_{ph} is the efficiency of the detection and $1 - \eta_{ph}$ represents losses. Losses have then a direct effect on the signal-to-noise ratio: for an efficiency smaller than 1, the noise measurement remains equal to photon phase noise but the contribution of the mirror displacement is reduced by a factor $\sqrt{\eta_{\text{OL}}}$ in amplitude. Likewise, an imperfect spatial overlap between the local oscillator and the probe beam can also deteriorate the measurement. Indeed, an imperfect spatial overlap leads to a reduced contrast in the measured interference between the two beams, given by:

$$\bar{I}_- = 2\sqrt{\eta_{\text{OL}}\bar{I}_{\text{OL}}\bar{I}_{\text{out}}}\cos\phi. \quad (1.98)$$

An imperfection to the spatial overlap is equivalent to optical losses: the signal is still reduced by a factor $\sqrt{\eta_{\text{OL}}}$.

1.6.6 Complete measurement sensitivity

With the description of the homodyne detection and the introduction of the overlap coefficient between the probe beam and the local oscillator we have completed the description of the main experimental imperfections of our experiment which limit its sensitivity: cavity losses $T + P$, coupler transmission T , mode matching of the measurement cavity η_{cav} , overlap η_{OL} and quantum efficiency of the homodyne detection photodiodes η_{ph} . The complete measurement sensitivity then becomes:

$$\delta x_{\text{shot}} = \frac{\lambda}{16\mathcal{F}\eta_{\text{cav}}\sqrt{\eta_{\text{OL}}\eta_{\text{ph}}}}\sqrt{\frac{T+P}{T}}\sqrt{\frac{1+(\Omega/\Omega_{\text{cav}})^2}{\bar{I}_{\text{in}}}}. \quad (1.99)$$

1.7 Position calibration

The homodyne detection readout is fed a Spectrum Analyzer that provides its power spectral density. It is then crucial to convert this signal in terms of displacements of the movable mirror.

We will finish this introductory chapter by presenting two different methods for the calibration the readout of the homodyne detection as a displacement. One uses a calibrated phase modulation which the other makes use of the Pound-Drever error signal. Let us first understand the nature of the measurement provided by the spectrum analyzer. The input electrical signal is filtered around frequency f over a given spectral range called the Resolution BandWidth ν_{RBW} . The analyzer also has an input impedance $R = 50 \Omega$ and makes a frequency analysis of the power $P(f)$ dissipated by R . Finally, the analyzer gives the corresponding power $P(f)$ in dBm. We can establish the relation between the power $P(f)$ provided by the apparatus and the component $V_{HD}(f)$ at frequency f of the voltage delivered by the homodyne detection. The dBm is defined as:

$$\text{dBm} = 10 \log \frac{P(f)}{P_0}, \quad (1.100)$$

where $P(f) = V_{DH}(f)^2 \nu_{RBW} / R$ and $P_0 = 1 \text{ mW}$. It follows that the corresponding amplitude measured by the spectrum analyser will be given by:

$$V_{DH}(f) = \frac{10^{P(f)/20}}{\sqrt{20} \nu_{RBW}}, \quad (1.101)$$

where the power $P(f)$ is expressed in dBm. The position calibration, which will be described below, consists in converting the amplitude $V(f)$ provided by the spectrum analyzer into displacement ($V/\sqrt{\text{Hz}} \rightarrow \text{m}/\sqrt{\text{Hz}}$). This conversion can easily be realized thanks to the well known fact that a length variation δx of a cavity is completely equivalent to a frequency variation $\delta \nu$ of the laser:

$$\frac{\delta \nu}{\nu} = \frac{\delta \lambda}{\lambda} = \frac{\delta x}{L}, \quad (1.102)$$

where ν is the laser frequency, λ the laser wavelength and L the cavity length.

1.7.1 Pound-Drever-Hall calibration

The Pound-Drever error signal can also be used to calibrate the mirror displacement. It is generally used in a frequency feedback loop, however it contains all the required information on the mirror displacement. It can be shown [40] that the error signal fluctuations δV_{err} can be written as the product of the detuning fluctuation around the optical resonance $\delta \Psi$ and the error signal static slope $dV_{\text{err}}/\delta \Psi$, corrected by the cavity filtering effects at high frequency:

$$\delta V_{\text{err}} = \frac{1}{1 + \Omega^2/\Omega_{\text{cav}}^2} \frac{dV_{\text{err}}}{d\Psi_{\Psi=0}} \delta \Psi [\Omega]. \quad (1.103)$$

By determining the static slope we can perform a position calibration. The error signal is visualized with a digital oscilloscope and -exactly as done for the optical characterization- its time axis is converted into a frequency axis. The slope value expressed in V/Hz ensures the first step of the calibration. It will permit the conversion from the amplitude given by the apparatus to a frequency ($V/\sqrt{\text{Hz}} \rightarrow \text{Hz}/\sqrt{\text{Hz}}$). The second step of the calibration consists in monitoring the high-frequency part of the Pound-Drever error signal and, thus, take a displacement acquisition. Since the spectrum analyser input has an input impedance of 50Ω , the numerical oscilloscope input impedance must be equally set to 50Ω so that both signals have the same electronic gains. We know that a mirror displacement δx results in a cavity detuning

equal to $\delta\Psi = 4\pi\delta x\lambda$. By combining this equation with equation (1.103) we determine the spectral density of the mirror displacement. We note finally that once the PDH calibration is done it suffices to compare every homodyne detection acquisition to it in order to calibrate the homodyne detection as well. The simplicity of this technique is evident: one simple thermal acquisition using the PDH signal is enough to calibrate the homodyne detection.

1.7.2 Calibration peaks

Thanks to its simplicity, the PDH technique has become our principal technique to calibrate the homodyne detection readout. We will now describe an alternative calibration than may be used instead. This calibration method is based on a frequency modulation of the laser used as a reference. By applying a frequency modulation to the laser and by observing the associated signal via the homodyne detection equation (1.102) will allow to transform this signal into the corresponding mirror displacement. The procedure consists of two steps: first, the frequency modulation must be calibrated and, afterwards, the effect of this modulation on the measurement cavity is observed by the homodyne detection.

The frequency modulation $\delta\nu_m$ performed with a signal generator driving the internal Electro Optic Modulator of the laser ring cavity via an amplification stage (fast amplifier Tegam). In order to calibrate the frequency modulation a cavity with a known bandwidth is used. For this purpose, the filtering cavity (FPF), with a bandwidth $\Omega_{BP}^{FPF} = 5.6$ MHz is very suitable. The filtering cavity will be used to transform the frequency modulation to an intensity modulation by simply detuning it. When the cavity is at resonance the frequency modulation has no effect on the output intensity as the slope of the Airy peak is zero. On the other hand, if it is detuned an intensity modulation is apparent on the cavity output. The frequency modulation can then be calibrated by simply monitoring the output laser beam while the cavity is locked on the side of the fringe. Its amplitude should be smaller than the cavity bandwidth Ω_{BP}^{FPF} . In this case it can be found [31] that the intensity modulation depth is given by:

$$\frac{\delta I[\Omega]}{\bar{I}} = \frac{\delta\nu_m[\Omega_m]}{\nu_{BP}^{FPF}}. \quad (1.104)$$

In practice, we ensure that the internal electro-optic modulator does not induce a residual intensity modulation by observing the output intensity while the cavity is at resonance. Afterwards, the cavity is detuned and maintained on the side of the Airy peak where the slope is maximal, by adding an offset to the control loop and both the modulation depth δI and the mean intensity \bar{I} are measured. Once the modulation peak is calibrated, its effect on the measurement can now be observed via the homodyne detection and used to calibrate the measured displacement (in meters). It suffices then to compare any signal V to the modulation peak V_m both observed by the homodyne detection. The amplitude V_m observed at frequency, Ω_m , corresponds to a well known frequency modulation. We thus write:

$$\frac{V_{DH}[\Omega_m]}{V_m[\Omega_m]} = \frac{\delta\nu_{DH}[\Omega_m]}{\delta\nu_m[\Omega_m]}, \quad (1.105)$$

allowing to calibrate the measured signal, initially expressed in volts, to hertz ($V/\sqrt{\text{Hz}} \rightarrow \text{Hz}/\sqrt{\text{Hz}}$). Finally, by combining equations (1.102), (1.104) and (1.105) the homodyne detection

readout is calibrated to meters ($\text{Hz}/\sqrt{\text{Hz}} \rightarrow \text{m}/\sqrt{\text{Hz}}$):

$$\delta x[\Omega_m] = L \frac{\delta \nu_m[\Omega_m]}{\nu} \frac{V_{DH}[\Omega_m]}{V_m[\Omega_m]}. \quad (1.106)$$

This method is of course applicable only at a single frequency, Ω_m . However, the bandwidth of our detection is large enough to be able to generalize the above technique to a span of a few megahertz. In fact, the only frequency dependence comes from cavity-filtering effects and, hence, equation (1.106) must include this correction by adding a factor $1/(1 + (\Omega/\Omega_{\text{cav}})^2)$.

Mechanical characterization

Once the displacement measurement is calibrated all the mechanical properties, the effective mass M_{eff} of the modes of the movable mirror can be computed by the thermal noise spectrum. A Lorentzian fit can determine both the center frequency, Ω_M and the width, Γ_M of the mode. Therefore, the quality factor of the mode can be straightforwardly calculated: $Q = \Omega_M/\Gamma_M$. Finally, the variance of the movement Δx^2 can also be determined by the Lorentzian fit and using the energy equipartition theorem

$$\frac{1}{2} M_{\text{eff}} \Delta x^2 = \frac{1}{2} k_B T, \quad (1.107)$$

the oscillator effective mass M_{eff} can be calculated. k_B is the Boltzmann constant and T the temperature.

1.8 Group past experimental results

The optomechanical coupling has been studied at the Laboratoire Kastler Brossel since 1995 and some remarkable experimental results have been obtained, often setting new standards and opening new horizons in this research domain. Some of these results will be briefly discussed here.

1.8.1 Thermal noise observation and measurement sensitivity

The first experimental results were obtained in the late 90's thanks to the experimental setup already described in Figure 1.12 allowing to perform a displacement measurement with a sensitivity limited by the phase noise of the incident probe beam. Here we will present the observed characteristics of thermal noise as well as the sensitivity achieved by the experimental setup. In order to measure the thermal noise of the mirror, the laser frequency is locked on the cavity resonance of the cavity, where the sensitivity is maximal, and the homodyne detection monitors the phase of the reflected beam. Figure 1.19(a) shows the reflected phase noise in and out of the cavity resonance. The phase noise of the reflected beam is a superposition of the thermal fluctuations of the mirror and of the phase noise of the incident beam (red curve in Figure 1.19(a)). The spectrum presents a series of peaks, each one corresponding to an acoustic mode of the mirror which behaves like a damped harmonic oscillator. Between the peaks the noise level is almost flat in frequency and corresponds to a thermal background due to the incoherent sum of the non-resonant thermal noise of all modes. The incident beam phase noise can be easily measured by performing the same measurement when the cavity is out-of-resonance and

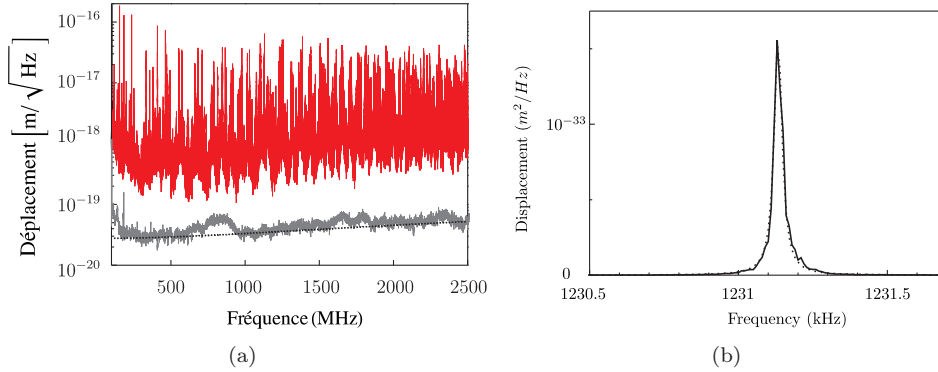


Figure 1.19: (a) Thermal noise spectrum between 100 kHz and 2.5 MHz (red). The grey curve is the experimental sensitivity limit caused by the phase noise of the probe beam while the black one corresponds to the theoretical limit. (b) Thermal noise spectrum around a mechanical resonance of the movable mirror.

the beam being only reflected by the cavity ($\delta q_{\text{in}} = \delta q_{\text{out}}$). The grey curve of 1.19(a) depicts this spectrum which corresponds to the experimental sensitivity limit. Finally, in black the expected theoretical sensitivity is depicted. It has been calculated using expression (1.99) taking into account the mode matching of the cavity ($\eta_{\text{cav}} = 98\%$), the overlap between the local oscillator and the probe beam ($\eta_{\text{LO}} = 94\%$), the photodiode quantum efficiency ($\eta_{\text{ph}} = 91\%$), the total cavity losses $T + P = 27$ ppm and the coupler transmission $T = 18$ ppm. At low frequency the theoretical sensitivity is equal to:

$$\delta x_{\text{shot}}[\Omega \ll \Omega_{\text{cav}}] = 2.7 \times 10^{-20} \text{ m}/\sqrt{\text{Hz}}. \quad (1.108)$$

At higher frequency the shot noise level increases due cavity filtering effects. For the presented spectra the power of the probe beam was set to $50 \mu\text{W}$ allowing to study the mirror thermal noise with a good sensitivity and the measured spectra have been calibrated using the technique presented in section 1.7.2. Finally, Figure 1.19(b) depicts the thermal noise around one specific vibrational mode resonance frequency. It has been acquired with a resolution of $\nu_{\text{RBW}} = 3$ Hz and has been averaged 80 times. By applying a Lorentzian fit we determine the resonance frequency $\Omega_M/2\pi = 1231.133$ kHz and a width $\Gamma_M/2\pi = 32$ Hz, corresponding to a mechanical quality factor $Q = \Omega_M/\Gamma_M = 38\,500$ and an effective mass $M_{\text{eff}} = 430$ mg.

1.8.2 Full mechanical characterization

The group has used dedicated software utilities in order to predict the mechanical characteristics (resonance frequency and effective mass) of the acoustic modes of the cylindrical mirrors. In particular, the software CYPRES written by François Bondu, has been used to identify the mechanical modes. They are described by 3 indexes: the circumferential order η , characterizing the angular symmetry of the mode, the parity ξ , taking a value equal to either 0 or 1 and indicating whether the sides of the mirror are vibrating in phase or out-of-phase, and the order number m which is related to the radial structure of the mode. Our experiment has provided an excellent agreement between the predicted mechanical modes and the observed ones. The setup is depicted in Figure 1.20(a). Its principle lies in the driving of the mirror on multiple points

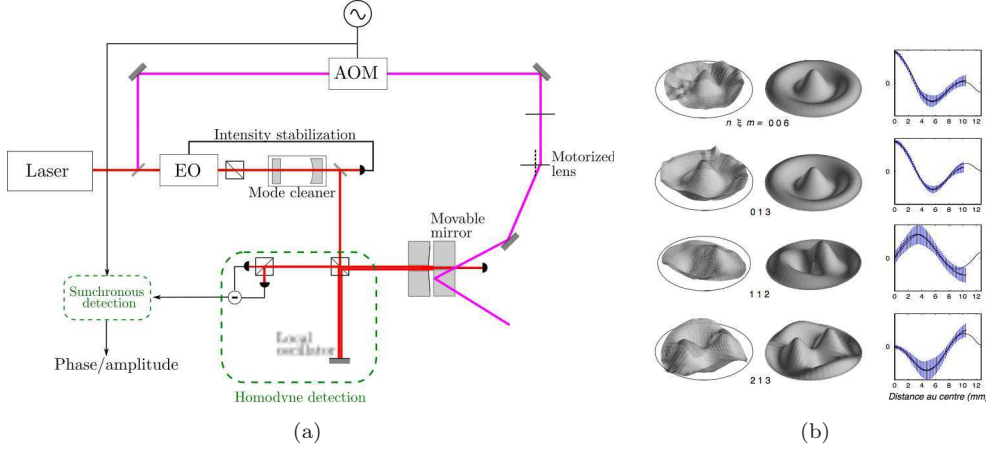


Figure 1.20: (a): The experimental setup used to measure the spatial profile of the mirror mechanical modes. The intensity of the auxiliary laser beam is modulated by an acousto-optic modulator. A motor-mounted lens is used to scan the surface of the movable mirror so that multiple points of the mechanical mode are excited. The signal acquired by the homodyne detection is then sent to a synchronous detection apparatus in order to extract the amplitude and the phase of the mirror response. (b) The spatial profiles of 4 mechanical mode of a cylindrical mirror (diameter 25.4 mm , thickness 6.35 mm). The left column depicts the profiles reconstitutes experimentally while the centered one presents the profiles calculated by CYPRES. The right column shows the theoretical and experimental radial function of the modes.

of its surface at the resonance frequency Ω_M of one particular mode. The resulting mirror displacement is proportional to the mode amplitude at the corresponding point. The excitation is produced by the radiation-pressure of an auxiliary beam whose intensity is modulated at frequency Ω_M by an acousto-optic modulator. The amplitude of the modulation is chosen so that the resulting displacement is some orders of magnitude greater than thermal noise. The mirror response for each point is then sampled and recorded with the help of a home-made lock-in detection providing the amplitude and the phase of the motion. The excitation point is then scanned over the surface of the mirror thanks to a lens mounted onto a computer-controlled, motorized translation stage. Monitoring the mirror response allows then to reconstruct the spatial profile of the mode. The results of this experiment are depicted in Figure 1.20(b) where an excellent theory-experiment agreement can be noticed. The group has also studied the time dependence of the thermal noise. It has been experimentally demonstrated [41] that the thermal noise of a mirror corresponds to a Brownian motion in the phase-space defined by the quadratures of the mirror displacement. The quadratures of the position $\delta x_M(t)$ of a mechanical mode are defined as the slowly-varying amplitudes of the two terms (sinus and cosinus) oscillating at frequency Ω_M :

$$\delta x_M(t) = X_1(t) \cos(\Omega_M t) + X_2(t) \sin(\Omega_M t), \quad (1.109)$$

where $X_1(t)$ and $X_2(t)$ are the two quadratures. A demodulation procedure, depicted in Figure 1.21(a), is implemented in order to extract the quadratures. A band-pass filter is used to filter the homodyne detection readout around frequency Ω_M and isolate the mode in which we are

interested. The output of the filter is then split into two parts; both are then mixed with two monochromatic signals, in quadrature in respect with each other and are filtered by a low-pass filter suppressing the mixing-generated harmonics. The signals are finally calibrated using the technique described previously (section 1.7.2). Figure 1.21(b) depicts the obtained results for the fundamental mode of a plano-convex movable mirror whose mechanical characteristics deduced from its thermal noise spectrum are: resonance frequency $\Omega_M/2\pi = 1858$ MHz, mass $M = 230$ mg and width $\Gamma_M/2\pi = 57$ Hz. The temporal evolution in phase-space, defined by the two quadratures X_1 and X_2 , is represented; it corresponds to a bounded random walk as expected for the Brownian motion of a harmonic oscillator.

1.8.3 Cold damping

Our research group was the first to experimentally demonstrate an active cooling effect on a mirror by using a feedback loop [42]. This technique is known as cold-damping: it consists in applying a viscous force to the mirror which increases the mirror dissipation processes without adding any thermal fluctuations. According to the fluctuation-dissipation theorem [23] this technique can lead to a temperature decrease of the mirror. In particular, a force $F_{fb}[\Omega]$ proportional to the velocity is applied to the mirror, using the real-time displacement measurement. The feedback actuation is applied on the movable mirror. Its displacement is then given by:

$$\delta x[\Omega] = \chi[\Omega](F_T[\Omega] + F_{fb}[\Omega]), \quad (1.110)$$

where F_T the Langevin force and $F_{fb} = i\Omega M \Gamma g \delta x[\Omega]$ is the force applied by the feedback loop, with g the dimensionless gain of the loop and $\Gamma_M = \Omega_M/Q$ is the damping of the mechanical mode. The mirror displacement becomes:

$$\delta x[\Omega] = \frac{1}{1/\chi[\Omega] - i\Omega M \Gamma g} F_T[\Omega]. \quad (1.111)$$

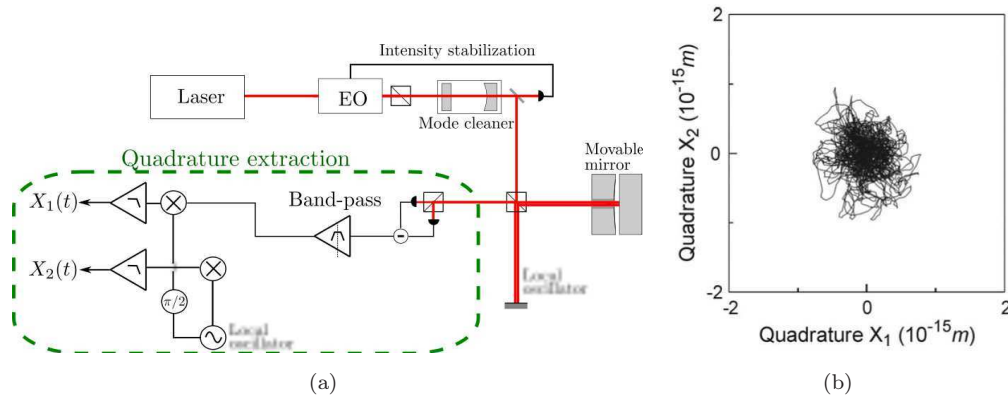


Figure 1.21: (a): the extraction of the movement quadratures. The homodyne detection read-out is first filtered around the frequency of analysis Ω_M . It is then split in two parts. One part is demodulated using a local oscillator at frequency Ω_M whereas the other one using a local oscillator in quadrature with respect to the first one. (b) Brownian noise trajectory of the mirror in the phase-space.

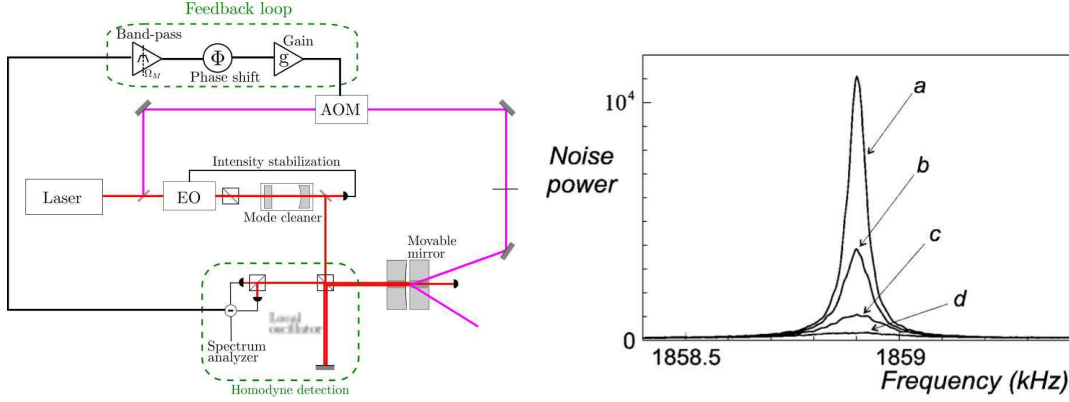


Figure 1.22: Left: the experimental setup used to cold-damp the moving mirror. Right: Thermal noise without cold-damping (a) and increasing gains of the feedback loop (b to d).

This expression shows that in presence of the feedback loop, the mirror displacement is still the response to the Langevin force but with an effective mechanical susceptibility χ_{fb} . If we consider, for simplicity, only one mode of the mirror, the effective mechanical susceptibility is:

$$\chi_{\text{fb}}[\Omega] = \frac{1}{M(\Omega_M^2 - \Omega^2 - i(1+g)\Gamma_M\Omega)}. \quad (1.112)$$

The feedback loop introduces a modification of the damping of the mechanical mode without changing the Langevin force characterizing thermal noise. When $g > 0$, the feedback widens the mechanical mode by a factor $(1+g)$. The displacement spectrum S_x remains Lorentzian, but its height and area decrease by a factor $(1+g)^2$ and $(1+g)$ respectively. The decrease of the mode area corresponds to a decrease of the displacement variance which, using the energy equipartition energy, can be interpreted as a mirror cooling effect. The temperature of the mechanical mode, in presence of the feedback, is:

$$T_{\text{fb}} = \frac{T}{1+g}. \quad (1.113)$$

The group has been able to experimentally demonstrate such a cooling effect, thanks to the experimental setup depicted on Figure 1.22(a). An auxiliary laser beam is used to apply an external radiation-pressure force on the movable mirror with an intensity controlled by an acousto-optic modulator driven by the feedback loop. The signal obtained by the homodyne detection is filtered by a band-pass filter at Ω_M to exclude other mechanical modes from the feedback loop. Once the signal is filtered, it is phase-shifted in order to set its phase in quadrature with respect to the displacement and obtain a signal proportional to the mirror velocity. A variable gain electronic stage completes the feedback loop. The results obtained with the plano-convex mirror are presented on Figure 1.22(b). A temperature reduction by a factor 30 has been achieved, the efficiency of the cooling feedback loop being essentially limited by the thermal noise background.

1.8.4 Back-action cancellation

Inspired by a theoretical study, also developed in our group [43], on the sensitivity limits of a gravitational-wave antenna based on a dual resonator, the group has demonstrated an anti-resonance effect between the fundamental mechanical mode and the mechanical background. The idea consists in forming a cavity composed of two almost identical movable mirrors and to measure the cavity length variation δL_{sig} caused by an external force applied to one of the mirrors, or an apparent length variation (a laser frequency variation or a gravitational wave in an interferometer). This measurement will contain the quantum phase noise of the incident probe beam as well as the position fluctuations of the two mirrors δx_e and δx_f both created by the back-action effect. At low frequency ($\Omega \ll \Omega_{\text{cav}}$) the phase fluctuations of the reflected field will be given by (equation (1.70)):

$$\delta q_{\text{out}}[\Omega] = \delta q_{\text{in}}[\Omega] + \frac{8\mathcal{F}}{\lambda} \left[\delta X_f[\Omega] - \delta X_e[\Omega] + \delta L_{\text{sig}}[\Omega] \right]. \quad (1.114)$$

In the framework of the linear response theory, the length fluctuations $\delta X_f - \delta X_e$ can be written using the corresponding mechanical susceptibilities $\chi_e[\Omega]$ and $\chi_f[\Omega]$:

$$\delta X_f[\Omega] - \delta X_e[\Omega] = \left(\chi_e[\Omega] + \chi_f[\Omega] \right) F_{\text{rad}}[\Omega], \quad (1.115)$$

where F_{rad} is the radiation-pressure force applied by the intracavity field to the mirrors which is equal in norm on both mirrors but with an opposite direction. The sensitivity limit $\delta L_{\text{min}}[\Omega]$ can be calculated the same way as done in section 1.4.1:

$$\delta L_{\text{min}}[\Omega] = \sqrt{\hbar |\chi_e[\Omega] + \chi_f[\Omega]|}. \quad (1.116)$$

Compared to equation (1.72) this time the sensitivity depends on the sum of the mirrors mechanical susceptibilities $\chi_f + \chi_e$. Since both resonators can be described as two different harmonic oscillators whose resonance frequencies Ω_f and Ω_e are close but slightly different, there will be an anti-resonance effect at frequency Ω_{ar} in the range $[\Omega_f, \Omega_e]$ corresponding to a destructive interference effect between the back-action applied to the two mirrors. Hence, at the anti-resonance frequency Ω_{ar} , the real parts of the two mechanical susceptibilities are exactly equal with an opposite sign. The latter equation then becomes:

$$\delta L_{\text{min}}[\Omega_{\text{ar}}] = \sqrt{\hbar |\text{Im}[\chi_e[\Omega_{\text{ar}}] + \chi_f[\Omega_{\text{ar}}]|}. \quad (1.117)$$

At the anti-resonance frequency, the sensitivity obtained is then greater than the Standard Quantum Limit for a single mirror. The back-action cancellation can also be taken advantage of in order to measure a small force. The idea is to use a two-movable-mirror cavity where an external force is only applied one of the two mirrors. The force will be transduced into a measurable displacement $\delta X_{\text{sig}} = \chi_f[\Omega] F_{\text{sig}}[\Omega]$, where χ_f is the transducer mechanical susceptibility. The maximum sensitivity of the displacement measurement δX_{sig} leads to a Standard Quantum Limit for the force measurement given by:

$$\delta F_{\text{sQL}}[\Omega] = \sqrt{\frac{\hbar}{|\chi_f[\Omega]|}}. \quad (1.118)$$

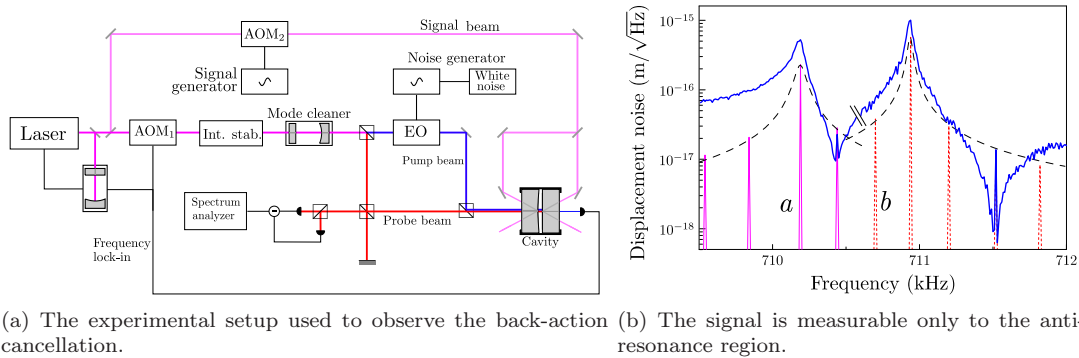


Figure 1.23: Back-action cancellation.

Since, the radiation-pressure effects are now proportional to the sum of both susceptibilities $\chi_f + \chi_e$ the existence of an anti-resonance will lead to a better sensitivity to the applied force associated to the smallest measurable displacement:

$$\delta F_{\min}[\Omega] = \frac{\sqrt{\hbar}|\chi_f[\Omega] + \chi_e[\Omega]|}{|\chi_f[\Omega]|}, \quad (1.119)$$

which can be much better than δF_{SQL} . The group has been able to experimentally demonstrate such a sensitivity improvement using a high-finesse cavity formed by two cylindrical mirrors. Since, the two mirrors are almost identical, their mechanical resonances are similar: in the thermal noise spectrum they appear as doublets. Figure 1.23(a) depicts the experimental setup used to demonstrate this effect. Close to a doublet we can neglect the contribution of the thermal background and consider the cavity as a system of two harmonic oscillators. Since the mirror displacement is dominated by thermal noise, a non-resonant, electro-optic modulator has been used in order to simulate a quantum intensity noise at a level much higher than thermal noise. The electro-optic modulator was driven by a white noise filtered in a frequency band of 600 kHz round the analysis frequency. The signal δF_{sig} to be measured was created by modulating the signal beam with an acousto-optic modulator. The signal beam then excites one of the two mirrors, applying a corresponding radiation-pressure force resulting into a length variation. The result of this measurement is presented in Figure 1.23(b). The applied weak force is only measurable only round the anti-resonance frequency Ω_{AR}

1.9 Optomechanics worldwide

The LKB group has been active in optomechanics research for more than 15 years and it is widely considered to be one of the pioneers of the field, providing both the theoretical framework but also solid experimental results. At the same time, other major research groups have emerged, pushing even further the barriers of optomechanics by creating optomechanical systems capable of observing quantum effects that until very recently were only predicted by theory. Indeed, over 40 groups worldwide are now active in the optomechanics research domain with systems presenting masses that span from picograms to kilograms and resonance frequencies from some Hz to some GHz. In figure 1.9 we present some important optomechanical

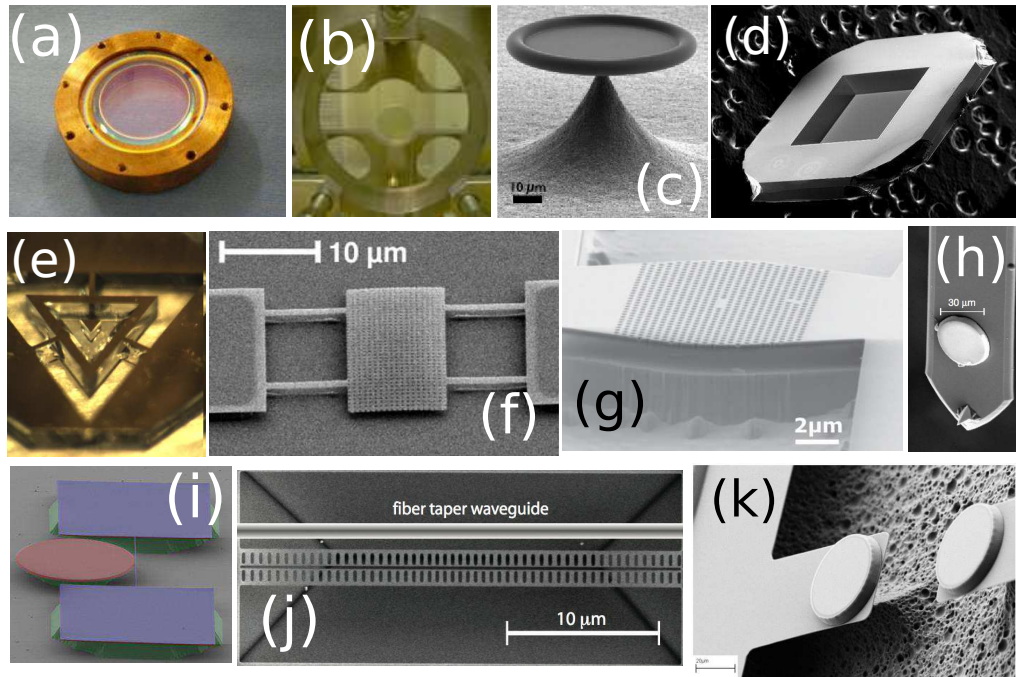


Figure 1.24: Some optomechanical systems: (a), (b) gram-scale movable mirrors used in Paris and in MIT respectively. (c) Micro-toroids used in EPFL but also in MPQ-Paris and in Queensland. (d) A commercial SiN membrane used in Yale. (e), (f) A high-Q micropillar and a low-mass membrane both developed in Paris. (h), (k) Micromirrors used in Vienna and Santa Barbara. (i) an hybrid, on-chip optomechanical transducer developed in EPFL. (g), (j) A new generation of photonic crystal where optical and mechanical coexist developed in EPFL and Caltech.

systems.

As mentioned earlier, our group has developed gram-scale, plano-convex resonators (a) presenting high finesse and a high Q [41]. The group of Nergis Mavalvala at MIT (b) also uses gram-scale suspended mirrors [44, 45] to explore radiation-pressure induced effects. Our group is currently developing a photonic crystal membrane (f) in collaboration with the Laboratory for Photonics and Nanostructures [46, 47] presenting an ultra-low mass (\sim pg) and a high-Q micropillar (e) in collaboration with the ONERA and the LMA [48]. At the same time, other types of micromirrors have been developed by the groups of Markus Aspelmeyer in Vienna [49] and Dirk Bouwmeester in Santa Barbara [50]. In parallel, Tobias Kippenberg in the EPFL has introduced and developed microresonators (d) presenting Whispering Gallery Modes (WGM) [51, 52] while similar systems are used by Ivan Favero's group at MPQ-Paris [53] and Warwick Bowen at the University of Queensland [54]. In the group of Kippenberg they have also managed to develop an integrated, on-chip transducer where a nanomechanical beam is coupled to disk-shaped optical resonator [55]. Jack Harris at Yale has introduced the “membrane-in-the-middle” technique using commercial SiN membranes (d) in order to explore the dispersive optomechanical coupling [56]. Finally, the co-existence of vibrational and optical modes occurs in a new generation of photonic crystal membranes (g, j) developed by the LPN/EPFL [57] and by the group of Oskar Painter at Caltech [58, 59].

This thesis is particularly focused onto the experimental observation of the quantum radiation-pressure shot-noise and other groups have offered significant contribution towards this end. Kjetil Børkje *et al.* in the group of Jack Harris have offered a proposition to distinguish quantum from classical noise [60] while other closely related results have also been by other groups. Laurent *et al.* [61] have shown experimental evidence of a negative back-action in interferometric measurements. Classically-induced optomechanical correlation have been used by Marino *et al.* [62] to observe a classical ponderomotive squeezing effects while some other works have presented equally significant results related to back-action evasion and quantum-noise cancellation measurements [63–65]. Finally, very recently Purdy *et al.* [66] succeeded in providing a first direct evidence of a quantum radiation-pressure effect using a membrane-in-the-middle.

Radiation pressure effects

IN our experiment, thermal noise completely dominates over noises of fundamental nature, notably the radiation pressure noise we want to observe. A possible way to suppress thermal effects would be to perform the experiment at low temperatures. According to equation (1.77) this would indeed lead to a more favourable signal-to-noise ratio. However, a major experimental drawback is the fact that at low temperature the silica resonator loses its good mechanical behaviour: its quality factor drastically decays down to factors of the orders of 1000 [67], compared to values in the 10^6 range at ambient temperature. Consequently, the problems expected at low temperature led us to find alternative ways to observe radiation pressure effects at ambient temperature.

In this chapter we will describe how a classical simulation of a quantum intensity noise has been used in order to obtain a favourable signal-to-noise ratio and detect radiation pressure effects at ambient temperature. A non-resonant EO has been used in order to classically modulate the pump beam and to induce a mirror displacement more important than the thermal motion. Under these conditions, classical optomechanical correlations have been observed by monitoring, at the same time, the intensity of the pump beam and the phase of the probe beam. A second experiment will also be described, where the same classical intensity modulation was again applied but now at a level smaller than the thermal noise. In this case, an averaging technique used to extract pump-probe correlations has been demonstrated.

We present in the following the experimental details concerning in particular the addition of the classical pump noise, and we present the results obtained in the two regimes of huge and weak radiation pressure effects. We then briefly describe the limitations and conditions in order to observe quantum radiation pressure effects, defining the strategy to observe quantum correlations at room temperature. Finally, we present another experiment, based on the same classical pump noise, where a signal amplification is observed due to radiation-pressure effects in a detuned cavity.

2.1 Optomechanical classical correlations

The double injection setup was conceived and installed in order to experimentally observe the quantum back-action effect in interferometric measurements. The use of a classical intensity modulation to excite the mirror on a higher level than thermal noise is a necessary, intermediate step towards quantum correlations, as it allows us to test the capabilities of the double injection scheme and to better understand the experimental imperfections limiting its performance such as optical or electrical interferences. The main elements of the double injection have already been discussed in the previous chapter. The only adjustment to the existing experimental setup is the implementation of an electro-optic (EO) modulator on the pump beam. A careful study

was also needed in order to produce a noise signal which, in turn, would drive the EO modulator and create an intensity modulation exhibiting the same statistical properties as the quantum intensity noise. Both of these aspects will be presented below.

The basic principle of this experiment is to apply such a classical intensity modulation to the pump beam so that the intracavity pump beam drives the movable mirror. Since the measurement cavity presents a very high-finesse, an incident power of 1 mW will correspond to an intracavity power of a few hundreds of watts, making radiation-pressure effects visible. Afterwards, a much weaker probe beam will also be coupled to the cavity in order to measure the induced mirror displacements. The experimental demonstration of these effects needs a near flawless mode matching between both beams and the cavity, and a good overlap between the movable mirror mechanical modes and the cavity optical modes. Both of these criteria are expected to be met. It is strictly the same experiment we want to perform to observe quantum fluctuations, the only difference being the use hereafter of a classical intensity noise produced by the non-resonant EO modulator. The same technical problems exist in both experiments and it is a very crucial intermediate stage towards quantum correlations.

2.1.1 Implementing the modulator

The complete experimental setup used to perform this experiment is depicted in figure 2.2, where the only addition is a non-resonant electro-optic modulator (GSÄNGER LM 202) used to modulate the phase of the pump beam. It is inserted between the polarizing beam splitter (PBS_2) which separates the initial beam into two perpendicular polarizations, thus creating the cross-polarized probe and pump beams, and the resonant electro-optic modulator (REO) used for the Pound-Drever error signal. The axes of the modulator are oriented at 45° compared to the pump beam polarization, and at its output there is an integrated PBS transforming the polarization modulation into an intensity modulation while at the same time it ensures that the REO input polarization is the proper one. The non-resonant electro-optic modulator creates a polarization modulation which is transformed to an intensity modulation via a PBS placed at the output of the electro-optic. The non-resonant electro-optic modulators are, in principle, driven using a high-tension modulation. In our case, a low-noise, high-speed TEGAM amplifier is used, producing a ± 200 V output voltage with a 4 MHz bandwidth. This way, the impedance matching at 50Ω , in order to maximize the power transfer and avoid electrical interference, is impossible. Hence, an electromagnetic radiation is emitted which may

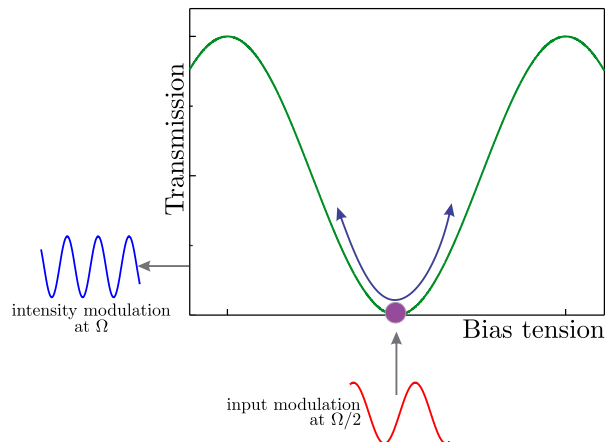


Figure 2.1: The non-resonant electro-optic modulator emits an electromagnetic parasitic signal at the very same frequency which is captured by the homodyne detection. By applying a modulation Ω at its minimum transmission an intensity modulation at $\Omega/2$ is generated, thus decoupling the signal from the parasite.

be fully captured by the photodiodes of the homodyne detection, making the physical signal unobservable. In order to eliminate this problem the non-linear transfer function of the EO is exploited.

As a matter of fact, its transfer function has a sinusoidal form presenting maxima and minima. Its working point (bias) will define either a linear (maximum slope) or a non linear (zero slope) response. When a working point is set to a maxima/minima the transmitted intensity is proportional to the square of the incident voltage applied to the electro-optic modulator. The double frequency of the input modulation is thus generated. When desired to modulate the beam intensity at a frequency Ω , the bias is set to a maxima/minima point and a tension modulation at $\Omega/2$ is applied. Consequently, the light intensity is modulated at Ω whereas the electromagnetic parasites are emitted at $\Omega/2$ (figure 2.1). The parasites are, thus, decoupled from the signal to be measured. We note, however, that this method will create a supplementary difficulty when measuring the mechanical response of the mobile mirror using a network analyzer. The latter is not capable of modulating at a frequency $\Omega/2$ and monitoring at frequency Ω . We will confront with this problem later on. Once the electromagnetic parasites are eliminated the optical parasites will have to be dealt with as well.

2.1.2 Optical isolation

The observation of the optomechanical correlations consists in monitoring the intensity of a pump beam and the phase shift of a probe beam, both injected into the moving mirror cavity. This requires a double injection system with a perfect optical isolation. If part of the pump beam contaminates the probe beam, or inversely, it creates fake correlations. To check for the optical isolation, a careful experimental protocol is applied. The laser frequency is swept around optical resonance of the moving mirror cavity. The Pound-Drever phase modulation on the REO is switched on in order to visualize on a digital oscilloscope the PDH error signal. A first adjustment can be made by monitoring the effect of the probe beam to the error signal generated by the pump beam. If the optical isolation is nearly perfect, the pump beam is not contaminated by the probe beam and, thus, the photodiode Ph_1 only detects the pump beam; the error signal then stays identical with or without probe beam. On the other hand, if an important optical contamination is present, the beating between the two will be detected by the photodiode, it will be demodulated and it will be finally be visible on the error signal. By carefully adjusting the half-wave and quarter-wave plates we align the pump beam incident polarization to one of the cavity axes. In practice, this way we maximize the transmitted Airy peak -the birefringence effect is small but evident- and at the same time we ensure that the reflected beam polarization matches the one of the incident beam; it is therefore reflected towards the photodiode Ph_1 without contaminating the probe beam. A second, equally delicate, adjustment consists in modulating the intensity of the pump beam at a given frequency $\Omega/2\pi$ (typically 1 MHz). The A+B output of the homodyne detection is then monitored with a spectrum analyzer. Again, using both plates we minimize the corresponding modulation peak in order to suppress the residual optical parasite. A rejection up to -35 dB has been obtained. This adjustment is realized when the laser frequency is out of cavity resonance. We have observed that when light is resonant with the cavity the polarization of the reflected beams slightly changes, leading to an optical contamination. The second stage of the optical isolation adjustment consists in locking the laser frequency to the movable mirror cavity and monitoring with the spectrum analyzer the beating between both beams either at the output of the homodyne detection or

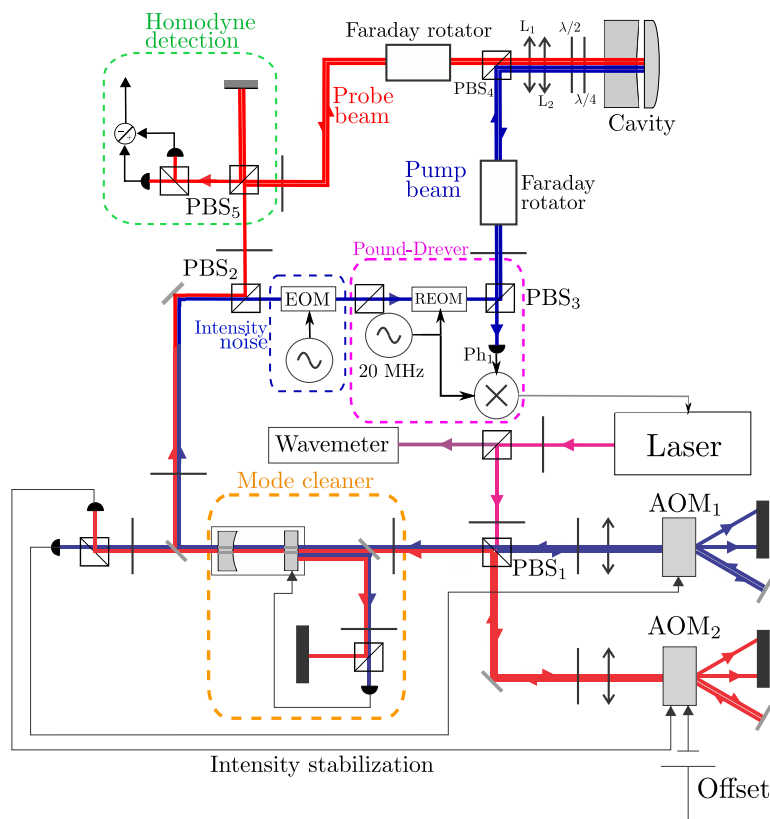


Figure 2.2: The experimental setup used for the experimental observation of radiation pressure effects using a classical intensity modulation to mimic quantum noise. It depicts all major components of the double injection: the laser source, the mode cleaner, the Pound-Drever-Hall technique, the moving mirror cavity and the homodyne detection. In addition, a non-resonant electro-optic modulator (EOM) has been implemented in order to modulate the intensity of the probe beam. A classical modulation excites the mirror via the pump beam and the probe beam measures the phase shift induced by the resulting mirror displacement.

on the photodiode Ph₁. The two plates are then carefully adjusted. We shall note that this procedure is very delicate: the plates must be rotated by some fractions of a degree. To this purpose, both plates are mounted on a high-precision rotation mount.

2.1.3 Construction of a classical intensity noise

The remaining step in order to perform the optomechanical classical correlations experiment is to define the waveform which will drive the non-resonant, electro-optic modulator and properly mimic the statistical properties of quantum intensity noise. To this purpose, we have programmed an arbitrary signal generator. We have seen, in the previous chapter that quantum intensity fluctuations do not present any frequency dependence; it is a white Gaussian noise. However, it is not necessary to generate a broadband signal to simulate such a noise. Indeed, through the detection process, any noise is filtered by the bandpass filter of the measurement apparatus. In our case, the span ν_{span} and the central frequency of the spectrum analyzer, de-

fine the frequency window of interest. The central frequency is set by the resonance frequency $\Omega_M/2\pi$ of the movable mirror, i.e. 1 MHz, and the frequency span is set to be a few linewidths, i.e. 1 kHz. In order to mimic, in the best possible way, the statistical properties of a quantum noise with a classical noise, it suffices to generate a signal with a carrier frequency $\Omega_M/2\pi$ of the form

$$u(t) = A(t) \cos(\Omega_M t + \phi(t)), \quad (2.1)$$

where the amplitude, $A(t)$, and phase, $\phi(t)$, are independently and randomly modulated with a maximum modulation frequency slightly larger than ν_{span} . The amplitude $A(t)$ should present Gaussian statistics while the phase $\phi(t)$ is uniformly distributed. Equivalently, $u(t)$ may be written:

$$u(t) = V_1 \cos(\Omega t) + V_2 \sin(\Omega t), \quad (2.2)$$

where V_1 and V_2 are the slowly-varying noise quadratures. Equations (2.1) and (2.2) offer two natural ways for generating the noise $u(t)$: either by using a synthesizer generating a sine wave whose amplitude and phase are modulated with two random signals, or by summing two phase-locked sine waves at 90° , whose amplitudes are both modulated with two random signals. In both cases, one has to precalculate and play two random signals altogether synchronized with each other and with the carrier at Ω_M to obtain a pseudo-random noise $u(t)$ that can be repeated reproducibly. It is convenient to use the phase-space representation defined by the signal quadratures V_1 and V_2 as a visual criterion for the produced optomechanical correlations between the pump and the probe beam. Since the generated quadratures present Gaussian statistics the corresponding phase-space representation will also be a centered Gaussian distribution. A good quality noise is a function $u(t)$ that achieves a random walk with a reasonably good mapping of the phase-space.

2.1.3.1 Hardware

The difficulty in generating such an intensity noise lies in the fact that both the phase and the amplitude of the signal must be controlled simultaneously. Or, equivalently, both independent envelopes have to modulate two carriers at exactly the same frequency, $\Omega/2\pi$, and they have to be strictly in quadrature. To achieve this, a synthetic work combining the available hardware and the most convenient programming language was done. Most arbitrary function generators offer the possibility of uploading a point array, a function or a modulation pattern. The two most important parameters of the candidate hardware we are interested in are the scan speed of the array, determining the spectral range of the noise in the Fourier space, the width of the sidebands and the array memory depth determining the filling level of phase-space. We have tested various configurations, including two identical Stanford DS345 arbitrary function generators and a Marconi generator. Both solutions presented serious drawbacks: the Stanford generators provided a poor memory while the phase modulation provided by the Marconi generator added extra phase noise to the generated signal, thus making it not reproducible. At the same time, neither solution provided a centered random walk. We therefore concluded in the use of two dual-channel Tektronix AFG3102 generators.

It is the same generator we are using to generate the Pound-Drever-Hall error signal (see section 1.6.4). The advantage of these generators is that they provide two independent signals having exactly the same carrier frequency, with an adjustable relative phase between them. Furthermore, they can work in an arbitrary modulation mode where the generated signal am-

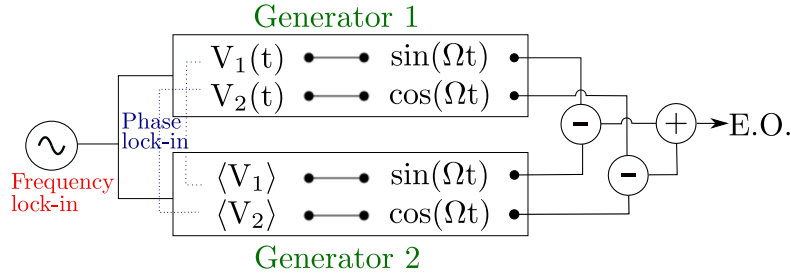


Figure 2.3: The cabling scheme of the two arbitrary waveform generators in order to generate a random walk mapping all four quadrants of the phase-space $\{V_1, V_2\}$.

plitude is modulated by a user-defined function. In fact, this generator suits particularly well our purposes, i.e. the generation of a classical intensity noise: both quadratures V_1 and V_2 can directly be uploaded in the internal memory as two 4000-long point arrays with 8-bit resolution. Each quadrature will modulate the amplitude of the sine wave generated by each channel whose phase is strictly locked at $\pi/2$ so that the two output signals are in quadrature. In the following, the two outputs of the generator are added using a standard Mini-Circuits power splitter. Nevertheless, this solution came with some drawbacks, the most important one being the fact that the generator only accepts amplitude modulation values comprised between 0% and 100% where $V_1, V_2 > 0$. Therefore, the slowly-varying envelopes V_1 and V_2 of the generated signal will present only positive values, leading to random walk confined only in the positive quadrant of the phase-space. To solve this problem, we generated both envelopes with non-null mean value, great compared to the variance of the envelope. A second, identical, arbitrary generator was used to generate two supplementary signals at the same frequency, Ω , with an amplitude equal to the mean value of the generated envelopes, $\langle V_1 \rangle$ and $\langle V_2 \rangle$. With a *Mini-Circuit* splitter we subtract the corresponding signals and we obtain a signal of the form:

$$u(t) = (V_1(t) - \langle V_1 \rangle) \cos(\Omega t) + (V_2(t) - \langle V_2 \rangle) \sin(\Omega t), \quad (2.3)$$

which is a signal covering all four quadrants of the phase-space. In other words, the random walk is first biased and, then, the splitter subtracts the mean values and re-centers it before being injected to the intensity modulator. Figure 2.3 depicts the corresponding connections of the two generators. Furthermore, extra attention was paid in the definition of the relative phase between both carrier signals since it randomly changes every time the generator configuration is altered. The relative phase has to be manually aligned to each generator ensuring that both outputs of each generator are in quadrature. Finally, another imperfection of this scheme is the limited size of the array of points accepted by the generator, leading to a mediocre Gaussian statistics as we will see later (see figure 2.5).

2.1.3.2 Software

We decided to compute the classical noise, offering total control over the statistical properties of the resulting pseudo-random signal. Given its simplicity to establish a communication between the computer and the Tektronix AFG3102 generator, the programming language LabVIEW was chosen to compute and upload the intensity quadratures. The first step is to write an algorithm that generates a filtered array of normally-distributed random numbers, whose dimension and

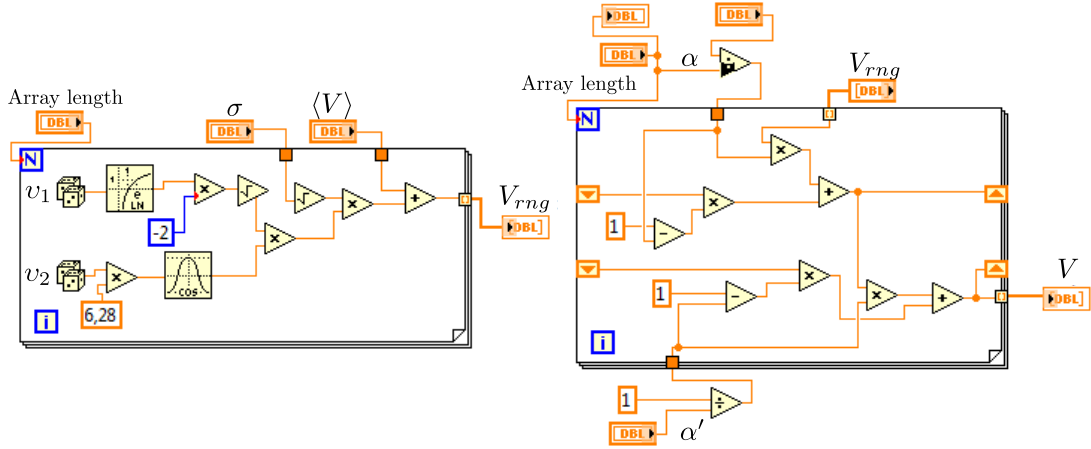


Figure 2.4: Left: LabVIEW realization of the Box-Muller transformation (equation (2.4)). Right: the double Lorentzian filter applied to the random number distribution.

filtering properties are user-defined. The second step is to upload this array to the internal memory of the generator. Since LabVIEW cannot generate by default a random number array with a normal distribution, we applied the pseudo-random number sampling method known as the Box-Muller method [68]. This method provides a Gaussian distribution by applying to the uniformly-distributed random number array in $]0, 1]$ the following:

$$(v_1, v_2) \mapsto \langle V \rangle + \sigma \cos(2\pi v_1) \sqrt{-2 \ln(v_2)}. \quad (2.4)$$

The result is a Gaussian distribution with a mean value $\langle V \rangle$ and a variance σ . The second stage of the algorithm involves the filtering of the generated noise in order to obtain an apparent random walk in the phase-space. For this, Lorentzian-type filtering was chosen, similar to the effect of the mirrors response at mechanical resonance on the Langevin force. The corresponding operation is then a convolution between the random-number array and the temporal response of the filter, which is a simple decreasing exponential: $n \mapsto e^{-n \ln a}$, where a is the width of the filter. The latter convolution operation can be simply written under the form of the following recurrence relation:

$$V[n+1] = aV[n] + (1-a)V_{rng}[n+1], \quad (2.5)$$

where V_{rng} is the random-array generated by the transformation (2.4). In fact, in order to eliminate all high-frequency components of the random walk, and thus make it more visible in the phase-space, the above filter is applied twice. Figure 2.4 depicts the LabVIEW realization of the pseudo-algorithms (2.4) and (2.5). The third, and final, stage of the software consists of a communication routine, inspired by the National Instruments Driver, used to upload the filtered, random arrays into the memory of the generator. We should note that the generated signal is indexed by a dimensionless integer. The time axis is defined afterwards by the generator itself, which plays the sequence at a given sampling rate. The modulation depth and the sampling rate are set manually.

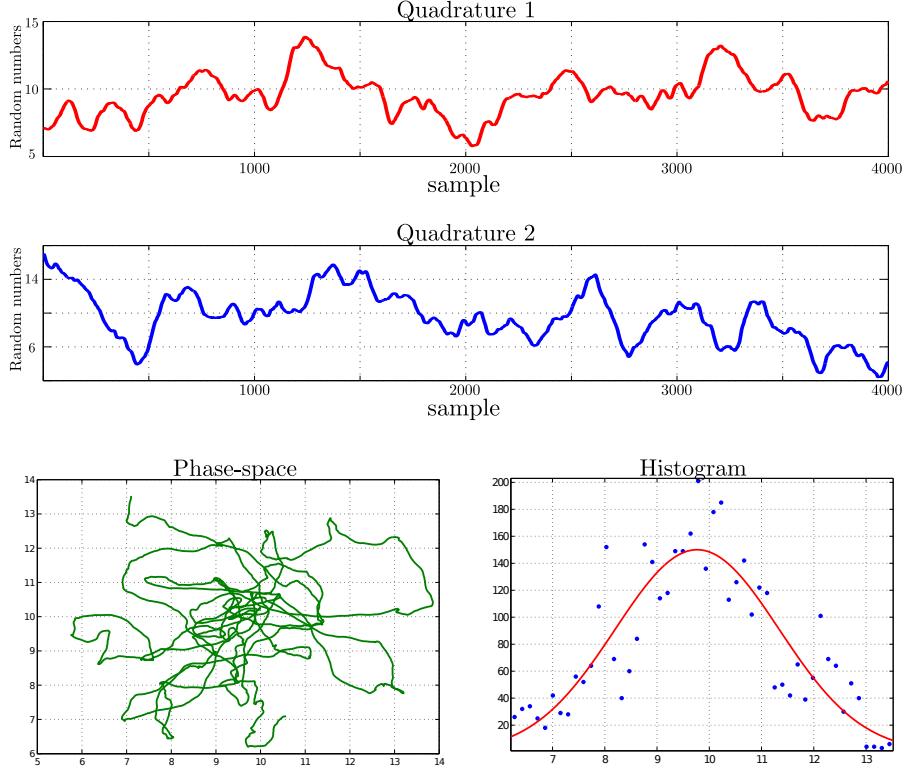


Figure 2.5: An example of the LabVIEW routines output shown in figure 2.4. The two upper graphs depict the two generated quadratures. The corresponding random-walk in the phase-space is depicted in the down-left graph, while the histogram of one quadrature is shown in the down-right corner. A Gaussian fit has been applied to the latter.

Finally figure 2.5 depicts an example of two generated quadratures V_1 and V_2 containing 4000 points, the corresponding random walk in phase-space $\{V_1, V_2\}$ and an histogram of one quadrature. We finally note the poor Gaussian statistics, due to the generator-limited number of sample points (4000) which is clearly visible in the Gaussian fit of the histogram.

At the beginning of this chapter, we have discussed the necessity of using the non-linear transfer function of the non-resonant electro-optic modulator in order to decouple the signal-to-be-measured from the electromagnetic parasite captured by the homodyne detection. The generated signal will, therefore, undergo another transformation induced by the working point of the electro-optic modulator, set at its minimum transmission. The resonance of the EO is then quadratic and, hence, the signal which will eventually drive the modulator will be proportional to the squared signal provided by the generator: $\propto A^2(t) [\cos(2\Omega t + 2\phi(t))]$. In other words, it will undergo the following transformation $(A'(t), \phi'(t)) \mapsto (A^2(t), 2\phi(t))$ and, therefore, the generated signal oscillating at half-frequency $\Omega/2$ (see equation 2.1) will become:

$$u'(t) = u_1(t) \cos(\Omega t) + u_2(t) \sin(\Omega t), \quad (2.6)$$

where the quadratures are now given by: $u_1(t) = \frac{V_1^2(t) - V_2^2(t)}{2}$ and $u_2(t) = V_1 V_2$. We can immediately note that these quadratures are no longer independent from each other. Further-

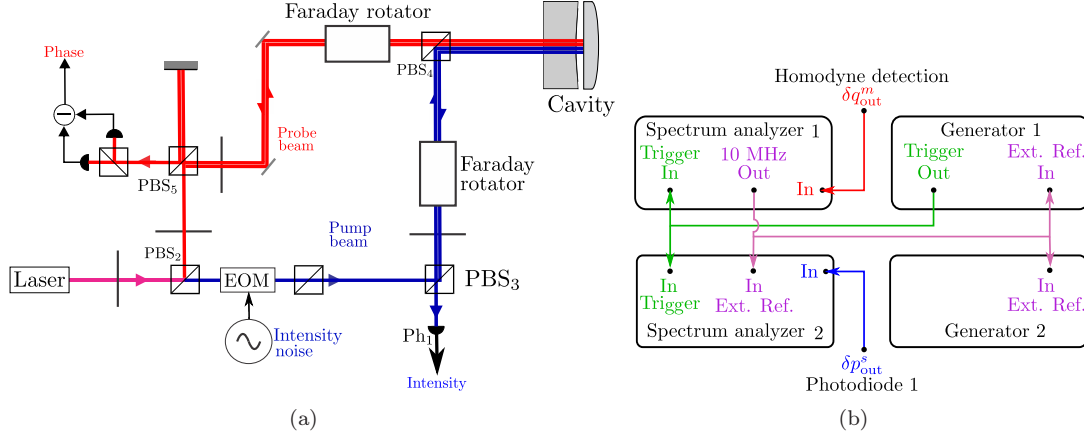


Figure 2.6: (a) A simplified experimental setup of the double injection, conceived to demonstrate correlations between the intensity of the pump beam and the phase of the much weaker probe. (b) The synchronization and triggering scheme among the spectrum analyzers and the arbitrary generators: the 10-MHz reference of spectrum analyzer 1 is used to synchronize the three other apparatus, while the generator 1 triggers the acquisition by the two analyzers.

more, by calculating the Jacobian associated to this transformation, one can easily find that the probability law governing these quadratures is:

$$P_{(u_1, u_2)} = \frac{1}{4\pi\sigma^2\sqrt{u_1^2 + u_2^2}} e^{-\frac{\sqrt{u_1^2 + u_2^2}}{\sigma^2}}, \quad (2.7)$$

which is not a Gaussian distribution. Instead, it represents a distribution with an accumulation of points close to the center occurs. We then conclude that even though we have successfully constructed a classical noise mimicking the statistical properties of quantum noise very well, these properties are partly lost due to the half-frequency drive of the electro-optic modulator. Nevertheless, we have decided to use this “non-Gaussian” classical noise to perform the experiment.

2.1.4 Experimental results

We will now present the experimental results obtained [69]. Optomechanical correlations have been demonstrated for various configurations: at and out of mechanical resonance and for different levels of the intensity modulation. In the following, we will present the results obtained out of mechanical resonance, for an amplitude of modulation higher or lower than the thermal noise. The measurement cavity used to perform this experiment was composed by a plano-convex movable mirror (ref. 3022/12) and a cylindrical coupling mirror (ref. 07125/1). Its fundamental vibrational mode is at $\Omega_M/1/2\pi = 1.1$ MHz, with a quality factor $Q=500\,000$, an effective mass $M_{\text{eff}} = 500$ mg and an optical finesse $\mathcal{F} = 330\,000$.

2.1.4.1 Experimental protocol

The experiment consists in establishing optomechanical correlations between the measured intensity fluctuations of the pump beam $\delta p_{\text{out}}^p = \delta p_{\text{in}}^p$ (for a lossless cavity) and the phase fluctuations δq_{out}^s of the reflected probe beam. Equivalently, we are seeking optomechanical correlations between the intensity fluctuations of the pump beam and the position fluctuations of the movable mirror (see section 1.5.2). The experimental setup is drawn in figure 2.2. The non-resonant, electro-optic modulator is driven by the Gaussian noise generator described in the previous section and modulates the pump beam through a high-speed, high-voltage, low-noise TEGAM 2340 amplifier, driven by custom-made pre-amplifiers designed to change the bias voltage of the signal, and is set in such a way so that the modulator transmission is minimal. The output of the homodyne detection and the high-frequency (HF) output of the photodiode Ph₁ are both monitored by two identical spectrum analyzers Agilent MXA 9020. Analyzer 1 and 2 then measure the reflected phase and intensity fluctuations, respectively. Both analyzers are set in I/Q mode. They demodulate the input signal in real time and, thus, give immediate access to the desired quadratures. The principle of the I/Q mode of the MXA spectrum analyzer is similar to the demodulation procedure depicted in figure 1.21. Two parameters are defined: the central frequency $\Omega/2\pi$ at which the signal is demodulated and a spectral range (span) $\Delta\Omega$, which defines the frequency window around the central frequency. The signal measured by the analyzer is then filtered around the central frequency on the defined spectral range. Afterwards, it is mixed with a local oscillator at the same frequency, generated by the analyzer, and filtered at low frequency in order to suppress the generated harmonics. A sweep time can also be defined which is related to the defined spectral resolution ν_{RBW} of the analyzer. It is imperative for the acquisition of the two read-out signals to start simultaneously as they are compared point by point. For this purpose, both spectrum analyzers are triggered by one of the arbitrary generators via an external input of the analyzers. Furthermore, it is also necessary that the demodulation process of the two analyzers is realized at exactly the same frequency, which should of course coincide with the frequency delivered by the two generators. Three of the apparatuses are synchronized by the same 10-MHz reference frequency provided by analyzer 1. The corresponding configuration is drawn in figure 2.6(b). The first step is to execute the LabVIEW program in order to generate the intensity noise and upload the corresponding random arrays in both generators. We then manually define the carrier frequency Ω_{ref} of the signals delivered by the generators. The sweep speed of the arrays is also manually set, defining the spectral range of the intensity modulation. This range is then measured by the spectrum analyzer; the frequency span of the I/Q demodulation of both analyzers is set to match the spectral width of the pseudo-random noise. If the analyzer integrates a signal larger than the intensity noise spectral range then we will also measure the thermal motion of the mirror resulting in a degradation of the measured pump-probe correlations. If the span is smaller, we miss a part of the useful signal and this results in a loss of resolution and a longer acquisition time. Finally, the laser frequency is locked on the optical resonance of the measurement cavity and the sequence of acquisitions is started. Both spectrum analyzers provide the pairs of quadratures under the form of point-files, which can be processed by a computer. We thus obtain the temporal evolution of the pump beam intensity noise and the probe beam phase fluctuations. We will finally draw the corresponding trajectories into phase-space and also compute the correlation coefficient.

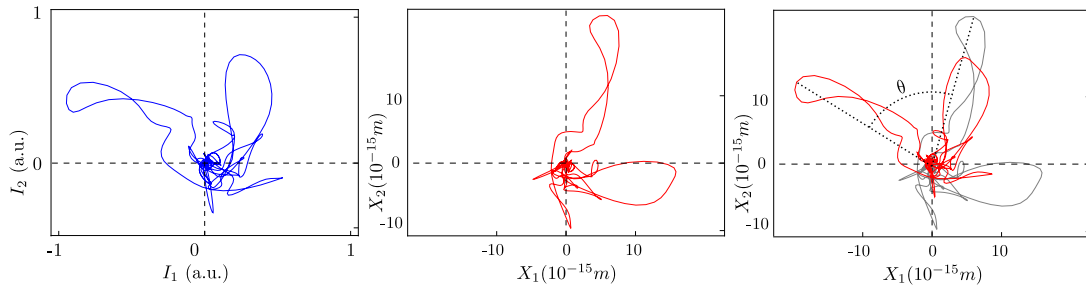


Figure 2.7: Optomechanical correlations obtained out of mechanical resonance. Right: Classical intensity noise depicted in phase-space as measured by photodiode Ph₁. Center: Mirror motion measured by the homodyne detection. We notice an arbitrary rotation with respect to the intensity noise caused by the detection chain. A signal-to-noise ratio $S_x^{\text{rad}}/S_x^T = 6000$ is obtained. Left: Mirror motion, phase-shifted by an angle $\theta = 74.6^\circ$.

2.1.4.2 Out of mechanical resonance

The experimental results presented here were obtained by applying the classical intensity noise at frequency $\Omega_M/2\pi = 1123$ kHz, 1 kHz away from the mechanical fundamental resonance of the mirror. The sweep speed was set to 200 ms corresponding to a measured spectral range of the intensity noise of 400 Hz. Therefore, the I/Q mode of the analyzers was also set at a frequency $\Omega_M/2\pi$ and at a span frequency $\nu_{\text{span}} = 400$ Hz. The pump beam was set at a power of 500 μW , whereas the probe beam at 150 μW . Let us note that even though, in this case, the probe and pump powers are of the same order of magnitude, the probe beam radiation-pressure fluctuations are negligible compared to the applied, classical modulation. Figure 2.7 depicts the correlations obtained for the above parameters. On the left, the phase-space trajectory of the intensity noise is drawn, as measured by the photodiode Ph₁, while in the middle the corresponding motion of the mirror is depicted as measured by the homodyne detection. This configuration corresponds to a signal to noise ratio $S_x^{\text{rad}}/S_x^T = 6000$. The correlations between the intensity and the motion of the mirror are evident in this figure; the phase-space trajectories are almost identical. We also notice that the trajectories are following a pseudo-random walk, exploring all four quadrants of the phase-space. Except for the Gaussian statistics, the classical intensity noise is then acceptable for a proof-of-principle. Nevertheless, the only difference is a global rotation between the two trajectories which is attributed to the detection chain which induces a supplementary dephasing to the quadratures measurement.

In order to quantify these optomechanical correlations we will define the correlation coefficient between the two observables, the reflected phase δq_{out}^m and the reflected intensity δp_{in}^s :

$$C_{s-m} = \frac{\langle \delta p_{\text{in}}^s \delta q_{\text{out}}^m \rangle}{\Delta p_{\text{in}}^s \Delta q_{\text{out}}^m}, \quad (2.8)$$

where $\langle \dots \rangle$ represents the temporal mean value and ΔX the variance of variable X. C_{s-m} is then a dimensionless quantity whose value lies in the $[-1, 1]$ range. C_{s-m} is equal to 1 or -1 when δp_{in}^s and δq_{out}^m are perfectly correlated and tends to 0 if δp_{in}^s and δq_{out}^m are independent. It can also be expressed in terms of the measured pump intensity $\delta I(t)$ and the mirror displacement

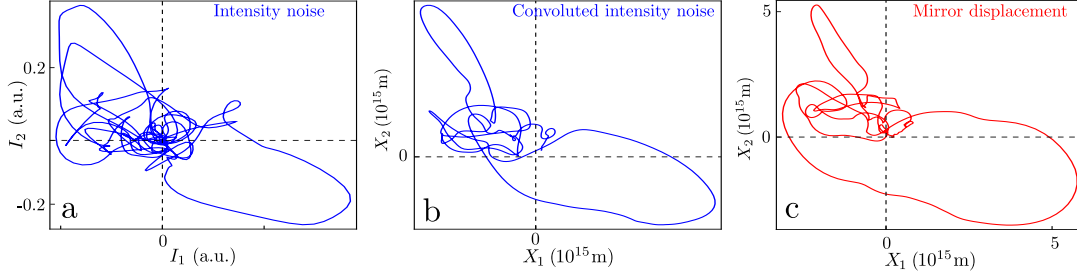


Figure 2.8: Optomechanical correlations obtained in mechanical resonance. (a) The classical intensity noise depicted in the phase-space as measured by photodiode Ph₁. (b) The simulated mirror response and (c) the mirror response as measured by the homodyne detection. A correlation coefficient $|\mathcal{C}_{\delta I-\delta x}|^2 = 0.97$ between trajectories depicted in b and c is found.

$\delta x(t)$:

$$\mathcal{C}_{\delta I-\delta x} = \frac{\langle \delta I(t) \delta x(t) \rangle}{\Delta I(t) \Delta x(t)} = \lim_{T \rightarrow \infty} \frac{\frac{1}{T} \int_0^T dt \delta I(t) \delta x(t)}{\left(\frac{1}{T} \int_0^T dt \delta I^2(t) \right)^{\frac{1}{2}} \left(\frac{1}{T} \int_0^T dt \delta x^2(t) \right)^{\frac{1}{2}}}, \quad (2.9)$$

where we have also written the correlation coefficient as the mean value averaged over the measurement time T and $\langle \dots \rangle$ indicates the expected value of the bracketed function as defined by: $\langle X \rangle = \lim_{T \rightarrow \infty} \frac{1}{2T} \int_{-T}^T X(t) dt$. In practice, in order to take advantage of the measured quadratures directly provided by the spectrum analyzer we chose to represent the two measured noises by two complex variables $I = I_1 + iI_2$ and $X = X_1 + iX_2$. These complex variables directly describe the phase-space trajectory. The correlation function (2.9) then becomes:

$$\mathcal{C}_{\delta I-\delta x} = \frac{\langle X(t) I^*(t) \rangle}{\sqrt{|X(t)|^2 |I(t)|^2}} = \lim_{T \rightarrow \infty} \frac{\frac{1}{T} \int_0^T dt X(t) I^*(t)}{\left(\frac{1}{T} \int_0^T dt |I(t)|^2(t) \right)^{\frac{1}{2}} \left(\frac{1}{T} \int_0^T dt |X(t)|^2(t) \right)^{\frac{1}{2}}}. \quad (2.10)$$

This coefficient is complex: $\mathcal{C}_{\delta I-\delta x} = |\mathcal{C}_{\delta I-\delta x}| e^{i\theta}$. The modulus determines the level of the correlations while the angle gives the relative position between the two variables. For perfect correlations, its modulus should be equal to 1. For the trajectories of figure 2.7 we find a correlation amplitude $|\mathcal{C}_{\delta I-\delta x}|^2 = 0.98$ and an angle $\theta = 74, 6^\circ$ (see the right part of figure 2.7).

2.1.4.3 At mechanical resonance

We have also tried to demonstrate optomechanical correlations by applying the classical intensity noise in a frequency band around the fundamental resonance of the plano-convex, movable mirror. The acquisition protocol is strictly the same as the one described in the previous section. Figure 2.8 depicts the phase-space trajectories of the applied intensity noise as measured by photodiode Ph₁ (subfigure a) and the resulted mirror displacement provided by the homodyne detection (subfigure b). By comparing figures a and c we note that there is a global resemblance between the two trajectories. Nevertheless, some details of the induced displacement are lost. This signal loss is emphasized by calculating the correlation function using equation (2.10): $|\mathcal{C}_{\delta I-\delta x}|^2 = 0.4$. The reason for this “signal loss” is the fact that the mirror mechanical response acts as a low-pass filter to the intensity fluctuations [24], thus filtering the high-frequency com-

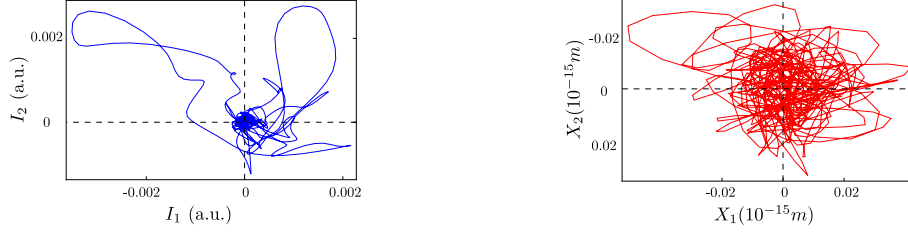


Figure 2.9: Optomechanical intensity (left)-phase (right) correlations for a signal-to-noise ratio $S_x^{\text{rad}}/S_x^T = 0.1$. The mirror displacement is mainly dominated by thermal noise.

ponents of the applied intensity noise. In order to reveal the real optomechanical correlations it suffices to write the temporal evolution $X(t)$ of the mirror displacement quadrature $X(t)$ as the convolution product:

$$X(t) = 2\hbar k \int_0^{+\infty} \chi(\tau) I(t - \tau) d\tau \quad (2.11)$$

and, in the following, to calculate the correlation function whose denominator can be written as:

$$\langle X(t + \tau) I^*(\tau) \rangle = 2\hbar k \int_0^{+\infty} \chi(\tau') \langle I(t + \tau - \tau') I^*(t) \rangle d\tau', \quad (2.12)$$

where $\chi(t)$ denotes the mirror susceptibility given by [24]: $\chi(t) = 1/(2M\Omega_M)e^{-\Gamma t/2}$. By thus simulating the mirror response $X(t)$, by performing the convolution between the mechanical susceptibility $\chi(t)$ and the intensity noise measured by photodiode Ph₁, we retrace in phase-space the trajectory corresponding to the filtered intensity noise (see figure 2.8b). We observe that the resulted, simulated response is almost identical to the mirror displacement measured by the homodyne detection (figure 2.8c). Finally we can calculate the corrected correlation function which gives $|\mathcal{C}_{\delta I - \delta x}|^2 = 0.97$.

Optomechanical correlations with a weak intensity noise

Finally, in figure 2.9 the optomechanical correlations for signal-to-noise ratio smaller than 1 ($S_x^{\text{rad}}/S_x^T = 0.1$) are depicted. In this case, the correlation coefficient is found to be $\mathcal{C}_{\delta I - \delta x} \simeq 0.1$. The mirror displacement is dominated by thermal noise and the big lobe on the top-left corner is barely distinguishable. In the next section, we will describe an averaging method in order to suppress thermal contribution to the mirror displacement and extract optomechanical correlations between the intensity fluctuations and the radiation-pressure-induced displacements even at room temperature when S_x^{rad}/S_x^T is much lower than unity.

2.1.5 Optomechanical correlations in the thermal regime: averaging

We have demonstrated that the double injection scheme is suitable for the detection of radiation pressure effects. However, the measured effects were induced by a large-amplitude, classical intensity modulation leading to a signal-to-noise ratio $S_x^{\text{rad}}/S_x^T = 6000$. As seen in figure 2.9, it is evident that the mechanical and optical characteristics of our system do not permit

to directly observe quantum intensity fluctuations. The read-out of the homodyne detection contains indistinguishably both the thermal motion of the mirror and the radiation pressure induced motion. However, the thermal contribution completely dominates the quantum effect of radiation pressure. In this section we describe the averaging method we have implemented to extract radiation pressure effects in the thermal regime where $S_x^{rad} \ll S_x^T$.

The idea relies on the incoherence of thermal noise: thermal noise can be suppressed by sufficient averaging. This averaging can be realized by data-treatment. In particular, when the correlation experiment is performed two quantities are measured: the probe beam reflected phase, δq_{out}^s , and the pump output intensity, δI_{out}^m . Equation (1.56) gives the expression of the output reflected phase. By neglecting cavity filtering effects ($\Omega_{cav} \gg \Omega$) and losses ($P \simeq 0$), we obtain:

$$\delta q_{out}^m = \delta q_{in}^m + \frac{16\mathcal{F}\sqrt{\bar{I}_{in}}}{\lambda}(\delta x_T + \delta x_{rad}). \quad (2.13)$$

The radiation-pressure induced displacement, δx_{rad} , given by equation 1.68, is proportional to the incident intensity fluctuations driving the mirror δp_{in}^s , and, in our case, is only induced by the pump beam:

$$\delta x_{rad}[\Omega] = \frac{8\mathcal{F}\sqrt{\bar{I}_{in}}}{\lambda} \hbar\chi[\Omega] \delta p_{in}^s[\Omega]. \quad (2.14)$$

and, since, $\delta p_{in}^s = \delta p_{out}^s$ the correlation function \mathcal{C}_{m-s} , given by equation (2.9), can be given by calculating the following time-averaged term:

$$\langle \delta q_{out}^m \delta p_{out}^s \rangle = \underbrace{\langle \delta q_{in}^m \delta p_{out}^s \rangle}_{\rightarrow 0} + \frac{16\mathcal{F}\sqrt{\bar{I}_{in}}}{\lambda} \underbrace{\langle \delta x_T \delta p_{out}^s \rangle}_{\rightarrow 0} + \frac{128\mathcal{F}^2\bar{I}_{in}}{\lambda} \hbar\chi[\Omega] \langle (\delta p_{out}^s)^2 \rangle, \quad (2.15)$$

where $\langle \dots \rangle$ symbolizes a temporal averaging. Since thermal noise δx_T and the incident phase noise δq_{in}^m have a null mean value and are completely uncorrelated to the reflected intensity fluctuations δp_{out}^s , the first two terms of the latter equation also present a null mean value and, therefore, their contribution are then negligible once averaged over a sufficiently long time. However, the equation also contains a third, quadratic term presenting a strictly non-zero mean value, containing the information on the radiation pressure-induced displacement. Therefore, in principle, this method can permit the extraction of real quantum intensity noise even in the thermal regime. Let us first present a simple experimental demonstration of this technique.

2.1.5.1 Experimental demonstration

The experimental protocol followed is strictly the same as the one described in sections 2.1.4.1 and 2.1.4.2, the only difference being the amplitude of the classical intensity noise induced to the pump beam via the EOM. The intensity modulation depth has been set in order for the resulted mirror displacement to be lower than the thermal noise contribution: the signal-to-noise ratio is now equal to 3×10^{-2} . Both spectrum analyzers are set in I/Q mode, and provide the demodulated quadratures of the signals. The center frequency is set at $\Omega/2\pi=1123$ kHz, with a spectral range $\nu_{span} = 400$ Hz. The arbitrary point array modulating the intensity of the pump beam is played with a periodicity of 200 ms. 500 different cycles of the arbitrary signal have been repeated. At every cycle, the phase of the probe beam and the intensity of the pump beam were acquired by the spectrum analyzers and uploaded to the computer. Figure

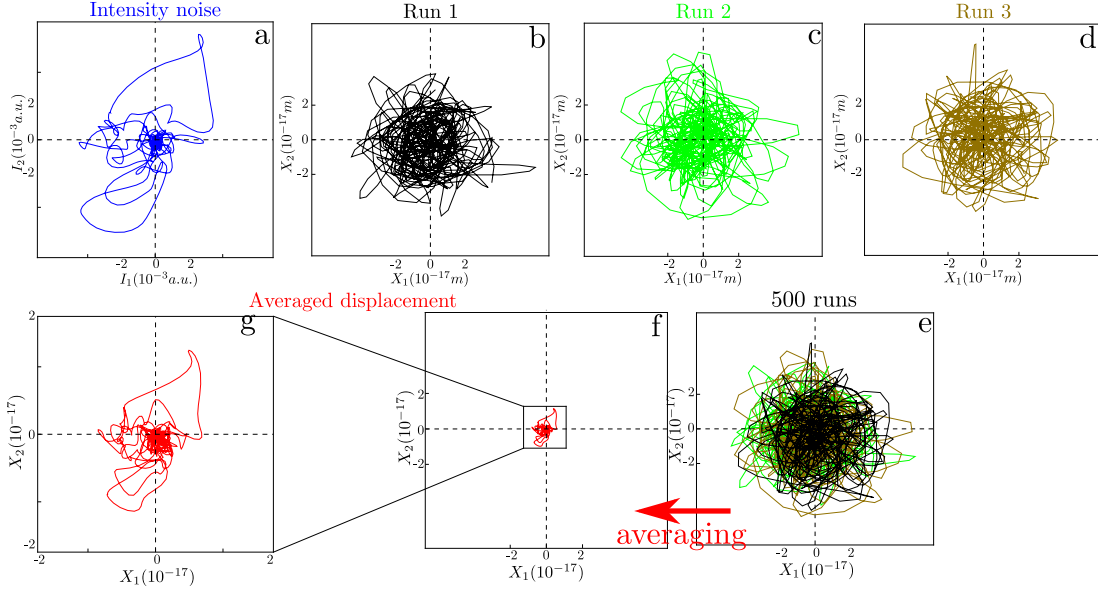


Figure 2.10: Extraction of the optomechanical correlations in the thermal regime. The classical intensity noise is repeated 500 times (in blue) and the phase of the reflected beam is acquired. On each individual run, thermal noise completely covers the radiation-pressure induced displacement (runs 1, 2, 3). However, on the averaged curve deduced from these 500 runs the imprint of the classical intensity noise is revealed (red).

2.11(c) depicts the results of this experiment. The intensity noise of the pump beam is drawn in blue, on the top-left corner. We have also included in the figure three different measurements of the phase quadrature δq_{out}^m . While the intensity noise remains strictly constant at each cycle, we notice that this is not the case for the corresponding mirror displacement. Indeed, as the mirror motion is dominated by thermal noise, at each cycle the measured signal is different; an expected characteristic of the mirror Brownian motion (2.11(c) runs 1, 2 and 3). However, if the data of these 500 runs are averaged, radiation pressure-induced displacements are revealed as depicted in figure 2.11(c). A straightforward way to deduce the signal-to-noise ratio is to compare the dispersions of the averaged and the non-averaged displacement measurements, which in this case is found to be $S_x^{\text{rad}}/S_x^T = 2.9 \times 10^{-2}$.

2.1.6 Averaging restrictions

While the method applied to experimentally demonstrate the classical optomechanical correlations has proven to be very practical and illustrative, it can not be used for real quantum optomechanical correlations. Evidently, quantum intensity fluctuations are a non-repetitive white noise that can not be drawn in the phase-space in order to acquire some useful information on the intensity-phase correlations. Instead, a purely statistical study of the resulted correlation function must be done in order to acquire a desired precision to a realistically small amount of averaging time. Of course, a good precision -even if it is combined in good agreement with the theoretical predictions- does not suffice to rigorously prove the existence of the quan-

tum measurement back-action effect: it would be a merely indirect observations of these effects. However, it is known that the spectral density of intensity fluctuations scale linearly with the incident power ($S_I \sim I_{\text{in}}$, see equation (1.23)) while it can be easily shown that classical noises, such as thermal noise, scale with the square of the incident power. This fundamental difference between quantum and classical noises must be experimentally proven in order to obtain a solid demonstration of the quantum intensity fluctuations of a coherent field. Indeed, as we will see in the next section, the expected value of the correlation function scales linearly with the spectral density of the incident intensity noise ($\mathbb{E}[C_{s-m}] \propto S_p^{\text{in}}$). This linear dependence allows to prove that the observed optomechanical correlations indeed reflect the existence of the measurement quantum back-action.

In the following section, we will quantify the time evolution of the correlation function by studying its statistical properties and we will also present an experimental demonstration using the same classical intensity modulation used earlier.

2.1.6.1 Averaging time

In [70] the sufficient averaging time needed to demonstrate the radiation pressure effects was quantitatively determined with the assumption that the mechanical response is flat within the detection apparatus bandwidths. Here we propose to extend this approach by considering the peaked nature of the mechanical response. Therefore, the mirror displacement can be written as the convolution between its Lorentzian impulse response $\chi(t)$ and the force applied to the mirror $F_{\text{ext}} = F_{\text{th}}(t) + F_{\text{rad}}(t)$:

$$\begin{aligned} \delta x(t) &= \chi(t) \star F_{\text{ext}}(t) \\ &= \int_{-\infty}^{\infty} d\tau \chi(t - \tau) F_{\text{ext}}(\tau). \end{aligned} \quad (2.16)$$

The impulse response of the mirror is given by [43]:

$$\chi(t) = \frac{1}{2M\Omega_M} \theta(t) e^{-\Gamma_M t/2}, \quad (2.17)$$

where M , Ω_M and Γ_M are the effective mass, the resonance frequency and width of the mechanical resonance. For causality reasons, the Heaviside step-function $\theta(t)$ is also included.

Let us now repeat that when the optomechanical correlation experiment is performed we have access to two observables: the reflected phase fluctuations of the probe beam δq_{out}^m and the reflected intensity fluctuations of the pump beam δp_{out}^s . These observables are coupled to their respective detection apparatus which can be described by their respective response functions H_q^{out} and H_p^{out} [19], and can be written:

$$\delta \tilde{p}_{\text{out}}^s(t) = \delta p_{\text{out}}^s(t) \star H_p^{\text{out}}(t) = \int_{-\infty}^{+\infty} \delta p_{\text{out}}^s(\tau) H_p^{\text{out}}(t - \tau) d\tau, \quad (2.18)$$

$$\delta \tilde{q}_{\text{out}}^m(t) = \delta q_{\text{out}}^m(t) \star H_q^{\text{out}}(t) = \int_{-\infty}^{+\infty} \delta q_{\text{out}}^m(\tau) H_q^{\text{out}}(t - \tau) d\tau. \quad (2.19)$$

The correlation function \mathcal{C}_{m-s} , according to equation 2.15, can be calculated by¹ :

$$\mathcal{C}_{m-s} \propto \langle \delta \tilde{q}_{\text{out}}^m \delta \tilde{p}_{\text{out}}^s \rangle_T = \underbrace{\frac{1}{T} \int_0^T \tilde{\beta}(t) \delta \tilde{p}_{\text{out}}^s(t) dt}_A + \underbrace{\frac{1}{T} \int_0^T \delta \tilde{x}_{\text{rad}}(t) \delta \tilde{p}_{\text{out}}^s(t) dt}_B, \quad (2.20)$$

where, for simplicity reasons, we have introduced the measurement noise $\tilde{\beta}(t)$:

$$\tilde{\beta}(t) = \left[\delta q_m^{\text{in}}(t) + \frac{16\mathcal{F}\sqrt{\bar{I}_{\text{in}}}}{\lambda} \delta x_T(t) \right] \star H_q^{\text{out}}(t). \quad (2.21)$$

The above expression shows that the correlation function consists of two terms: a noise term $A = \langle \tilde{\beta} \delta \tilde{p}_{\text{out}}^s \rangle_T$ corresponding to the measured probe phase fluctuations which are independent from the radiation pressure driving force, and a signal term $B = \langle \delta \tilde{x}_{\text{rad}} \delta \tilde{p}_{\text{out}}^s \rangle_T$, that we seek to experimentally observe. To do so, the measurement time T needs to be such that the dispersion on the signal term is small compared to the correlation expected value:

$$\sigma(\langle \delta \tilde{q}_{\text{out}}^m \delta \tilde{p}_{\text{out}}^s \rangle_T) \ll \mathbb{E}[\langle \delta \tilde{q}_{\text{out}}^m \delta \tilde{p}_{\text{out}}^s \rangle_T]. \quad (2.22)$$

As already explained, the measurement shot noise δq_m^{in} and the thermal noise δx_T are both white noises, statistically independent from the signal intensity fluctuations δp_{out}^s ; it is straightforward to show that the mean value of the product $\delta p_{\text{out}}^s \beta$ is null. Therefore, the mean value of the signal term B can easily be shown equal to:

$$\mathbb{E}[\mathcal{C}_{m-s}] \propto \mathbb{E}[B] = \frac{256\mathcal{F}^2 \hbar \bar{I}_{\text{in}}}{\lambda^2 T} \int_0^T dt \langle \delta \tilde{p}_s^{\text{out}} \star \chi(t) \delta \tilde{p}_s^{\text{out}} \rangle = \frac{256\mathcal{F}^2 \hbar \bar{I}_{\text{in}}}{\lambda^2} \frac{S_p^{\text{out}}}{T} \int_0^T dt \chi(0), \quad (2.23)$$

To determine the correlation dispersion, we start from its definition,

$$\sigma^2(\mathcal{C}_{m-s}(T)) = \mathbb{E}[\mathcal{C}_{m-s}^2(T)] - \mathbb{E}^2[\mathcal{C}_{m-s}(T)], \quad (2.24)$$

where, using equation (2.20), the second-order moment of the correlation function reads:

$$\mathbb{E}[\mathcal{C}_{m-s}^2(T)] = \mathbb{E}[A^2] + \mathbb{E}[B^2], \quad (2.25)$$

the cross term contribution in $\mathbb{E}[\mathcal{C}_{m-s}^2(T)]$ being zero-valued since featuring odd moments of uncorrelated noises β and δp_{out}^s . The correlation variance is therefore the sum of two terms $\mathbb{E}[A^2]$ and $\sigma^2(B)$ arising from the random nature of both the noise and signal. Let us start by calculating the term $\mathbb{E}[A^2]$. It writes:

$$A = \frac{1}{T} \int_0^T dt \delta \tilde{q}_{\text{in}}^m(t) \delta \tilde{p}_{\text{out}}^s(t) + \frac{16\mathcal{F}\sqrt{\bar{I}_{\text{in}}}}{\lambda T} \int_0^T dt H_q^{\text{out}}(t) \star \chi(t) \star F_T(t) \delta \tilde{p}_{\text{out}}^s(t). \quad (2.26)$$

Assuming the mechanical response to be sharp compared to the detection filter enables us to approximate the latter using a Dirac delta function, $H_q^{\text{out}}(t) \simeq \delta(t)$. Hence, we have $H_q^{\text{out}}(t) \star$

¹We have noted $\langle X(t) \rangle_T = \int_0^T X(t) dt$.

$\chi(t) \simeq \chi(t)$, the noise contribution to the correlation variance therefore being:

$$\begin{aligned} \mathbb{E}[A^2] &= \frac{1}{T^2} \iint_{[0,T]} dt dt' \langle \delta \tilde{q}_{\text{in}}^m(t) \delta \tilde{q}_{\text{in}}^m(t') \rangle \langle \delta \tilde{p}_{\text{out}}^s(t) \delta \tilde{p}_{\text{out}}^s(t') \rangle \\ &+ \frac{256 \mathcal{F}^2 \bar{I}_{\text{in}}}{\lambda^2 T^2} \iint_{[0,T]} dt dt' \langle \chi(t) \star F_T(t) \chi(t') \star F_T(t') \rangle \langle \delta \tilde{p}_{\text{out}}^s(t) \delta \tilde{p}_{\text{out}}^s(t') \rangle. \end{aligned} \quad (2.27)$$

All noises δq_{in}^m , δp_{out}^s , and F_T being assumed to be gaussian white noises, and using the Wiener-Khinchin theorem, the latter equation simplifies as:

$$\begin{aligned} \mathbb{E}[A^2] &= \frac{S_p^{\text{in}} S_p^{\text{out}}}{T^2} \iint_{[0,T]} dt dt' \mathcal{K}[H_q^{\text{out}}](t, t') \mathcal{K}[H_p^{\text{out}}](t, t') \\ &+ \frac{256 \mathcal{F}^2 \bar{I}_{\text{in}}}{\lambda^2 T^2} \frac{S_F^T S_p^{\text{out}}}{T^2} \iint_{[0,T]} dt dt' \mathcal{K}[\chi](t, t') \mathcal{K}[H_p^{\text{out}}](t, t'), \end{aligned} \quad (2.28)$$

where \mathcal{K} is the bi-valuated function $\mathcal{K} : H \mapsto \int_{-\infty}^{+\infty} d\tau H(t-\tau)H(t'-\tau)$. For simplicity, we also assume the acquisition of the quantum intensity fluctuations to be performed using a bandwidth large compared to the mechanical damping rate ($H_p^{\text{out}}(t) \simeq \delta(t)$), the latter equation becoming therefore:

$$\mathbb{E}[A^2] = \sigma^2(A) = \frac{256 \mathcal{F}^2 \bar{I}_{\text{in}}}{\lambda^2} \frac{S_F^T S_p^{\text{out}}}{T^2} \int_0^T dt \mathcal{K}[\chi](t, t). \quad (2.29)$$

Equation (2.29) shows that the contribution of the first term in equation (2.28) vanishes: this is due to the assumption that both H_q^{out} and H_p^{out} are Dirac-type: this results in an ‘‘instantaneous’’ convergence towards its (zeroed) expected value, which practically is much faster than the quantities involving the mechanical response. Moreover, this term is experimentally small as compared to the remaining one (Eq. 2.28), as the thermal noise is resolved with a resolution exceeding 30 dB in our experiment. The second contribution to the correlation measurement imprecision (equation (2.25)) arises from the random nature of the driving quantum radiation pressure force:

$$F_{\text{rad}}(t) = \frac{8\hbar \mathcal{F} \sqrt{\bar{I}_{\text{in}}}}{\lambda} \delta p_{\text{in}}^s(t). \quad (2.30)$$

Assuming the cavity losses to be zero, this term reads:

$$\mathbb{E}(B^2) = \left(\frac{256 \mathcal{F}^2 \hbar \bar{I}_{\text{in}}}{\lambda T} \right)^2 \iint_{[0,T]} dt dt' \langle \chi(t) \star \delta p_{\text{out}}^s(t) \chi(t') \star \delta p_{\text{out}}^s(t') \delta p_{\text{out}}^s(t) \delta p_{\text{out}}^s(t') \rangle. \quad (2.31)$$

The integral in the above equation requires determining the fourth moment of δp_{out}^s . This can be done by means of Wick theorem [71], since δp_{out}^s has a Gaussian distribution. One can write:

$$\begin{aligned} \langle \delta p_{\text{out}}^s(\tau_1) \delta p_{\text{out}}^s(\tau_2) \delta p_{\text{out}}^s(\tau_3) \delta p_{\text{out}}^s(\tau_4) \rangle &= \langle \delta p_{\text{out}}^s(\tau_1) \delta p_{\text{out}}^s(\tau_2) \rangle \langle \delta p_{\text{out}}^s(\tau_3) \delta p_{\text{out}}^s(\tau_4) \rangle \\ &+ \langle \delta p_{\text{out}}^s(\tau_1) \delta p_{\text{out}}^s(\tau_4) \rangle \langle \delta p_{\text{out}}^s(\tau_2) \delta p_{\text{out}}^s(\tau_3) \rangle \\ &+ \langle \delta p_{\text{out}}^s(\tau_1) \delta p_{\text{out}}^s(\tau_3) \rangle \langle \delta p_{\text{out}}^s(\tau_2) \delta p_{\text{out}}^s(\tau_4) \rangle. \end{aligned} \quad (2.32)$$

Using this expression together with equation (2.31), we obtain:

$$\begin{aligned} \mathbb{E}(B^2) &= \left(\frac{256\mathcal{F}^2\hbar\bar{I}_{\text{in}}}{\lambda} \right)^2 \left(\frac{S_p^{\text{out}}}{T} \right)^2 \iint_{[0,T]^2} dt dt' \\ &\iint_{[-\infty,+\infty]^2} d\tau d\tau' \chi(t-\tau)\chi(t'-\tau') \left(\delta(t-t')\delta(\tau-\tau') + \delta(t-\tau)\delta(t'-\tau') + \delta(t-\tau')\delta(\tau-t') \right), \end{aligned} \quad (2.33)$$

where we use that δp_{out}^s is a white noise, $\langle \delta p_{\text{out}}^s(t)\delta p_{\text{out}}^s(t') \rangle = S_p^{\text{out}}\delta(t-t')$. The above expression can be easily simplified such that one finally obtains:

$$\mathbb{E}(B^2) = \left(\frac{256\mathcal{F}^2\hbar\bar{I}_{\text{in}}}{\lambda} \right)^2 \left(\frac{S_p^{\text{out}}}{T} \right)^2 \left[2 \int_0^T dt \mathcal{K}[\chi](t, t) + \iint_{[0,T]^2} dt dt' \chi^2(0) \right]. \quad (2.34)$$

By identifying the squared mean value of the correlation function into the second term of the latter equation one gets:

$$\sigma^2(B) = \left(\frac{256\mathcal{F}^2\hbar\bar{I}_{\text{in}}}{\lambda} \right)^2 \left(\frac{S_p^{\text{out}}}{T} \right)^2 2 \int_0^T dt \mathcal{K}[\chi](t, t). \quad (2.35)$$

The correlation variance finally becomes:

$$\sigma(\mathcal{C}_{s-m}(T)) = \left[\frac{256\mathcal{F}^2\hbar\bar{I}_{\text{in}}}{\lambda} \frac{S_p^{\text{out}}}{T} \sqrt{2} + \frac{16\mathcal{F}\sqrt{\bar{I}_{\text{in}}}}{\lambda} \frac{\sqrt{S_F^T S_p^{\text{out}}}}{T} \right] \times \left[\int_0^T dt \mathcal{K}[\chi](t, t) \right]^{1/2}. \quad (2.36)$$

Finally, by comparing the calculated mean value to the dispersion of the correlation function one gets the precision of the acquired correlations:

$$p = \frac{\sigma(\mathcal{C}_{s-m})}{\mathbb{E}[\mathcal{C}_{s-m}]} = \left(1 + \sqrt{\frac{S_x^T}{S_x^{\text{rad}}}} \right) \times \frac{\left[\int_0^T dt \mathcal{K}[\chi](t, t) \right]^{1/2}}{\int_0^T dt \chi(0)}. \quad (2.37)$$

We assume that thermal effects are much greater than radiation-pressure effects, such that $S_x^T \gg S_x^{\text{rad}}$; by calculating the associated integrals we get:

$$p \approx \sqrt{\frac{1}{\Gamma_M T} \frac{S_x^T}{S_x^{\text{rad}}}} \Rightarrow T = \frac{1}{p^2} \frac{1}{\Gamma_M} \frac{S_x^T}{S_x^{\text{rad}}}. \quad (2.38)$$

This equation is relatively simple and verifies basic physical intuitions. First, the precision of the measurement increases with the averaging time. This averaging time is furthermore directly proportional to the signal-to-noise ratio between thermal and radiation-pressure noise. Also, a given precision may be acquired more rapidly if the typical bandwidth of the measurement -here defined by the width of the mechanical mode Γ_M - is large. Consequently, when working at mechanical resonance a good compromise between the signal-to-noise ratio and the width of the mechanical resonance should be found in order to make the measurement experimentally feasible. Ideally, for this purpose, it would be preferable to widen the mechanical mode without

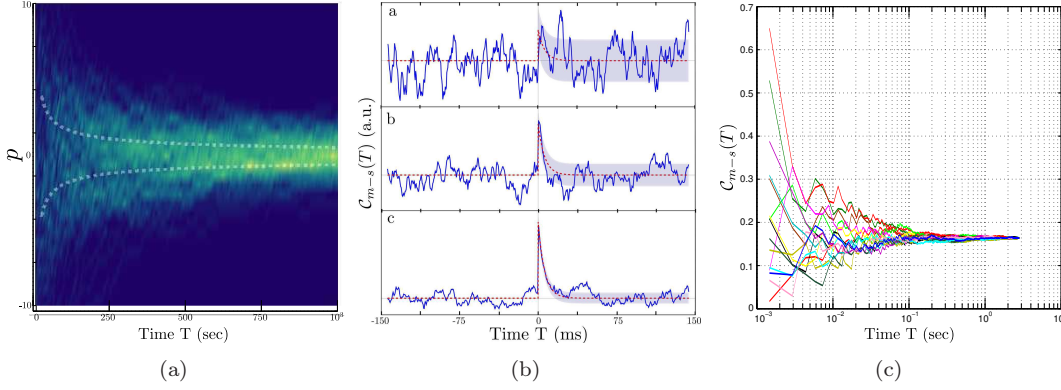


Figure 2.11: (a) Imprecision over the measurement of the optomechanical correlations as a function of the measurement time by simulating the mechanical response to a radiation pressure noise covered by thermal movement. (b) Averaging optomechanical correlations: simulated expected value of the optomechanical correlations along three different acquisition time, $T = 700$ ms (a), $T = 7$ s (b), and $T = 70$ s (c). The dashed red lines correspond to the expected value of the optomechanical correlations. The blue zones corresponds to the theoretical imprecision (c) Time evolution of the optomechanical correlation function for multiple, 2.8-s long independent acquisitions, by accumulating the product $\delta\phi_{\text{out}}^m \delta I_{\text{out}}^s$ normalized by the product $\Delta\phi_{\text{out}}^m \Delta I_{\text{out}}^s$. At long times ($t \rightarrow +\infty$) each acquisition converges towards the value $C_{s-m} \simeq 0.16$.

degrading the signal-to-noise ratio. In fact, this ideal case is very well approximated in our experiment. In particular, our mirrors present a thermal background which presents a better mechanical response than the fundamental mechanical resonance. This is why, for our system it is preferable to perform the optomechanical correlation measurement out of mechanical resonance where not only the signal-to-noise ratio is optimal but also much greater measurement bandwidths can be acquired; some kilohertz instead of some hertz.

Before moving on to the out-of-resonance case we will verify the above statistical model by means of a computer simulation. We have assumed a signal-to-noise ratio $S_x^{\text{rad}}/S_x^T = 10^{-2}$ and a mechanical damping rate equal to $\Gamma_M/2\pi = 50$ Hz. We have simulated the mechanical response to a radiation pressure noise buried into the thermal noise over 100 independent, 1-s long runs. These runs were used to establish the corresponding optomechanical correlations whose statistical dispersion is depicted in 2.11(a). The dispersion histogram whose density plot is drawn is very well fitted by equation (2.38) -the dashed grey line, also drawn to the figure- verifying our statistical model. Let us note that our model assumes only synchronous correlations; a null delay time $\tau = t_1 - t_2 = 0$ for the calculation of the optomechanical correlations is assumed, where t_i is the corresponding time of each quadrature. However, it can easily be generalized for any non-zero delay time and, in fact, it can be shown [72] that the imprecision on the optomechanical correlations presents an exponential dependence on the delay time τ :

$$p = \left[\frac{\sigma(C_{s-m})}{\mathbb{E}[C_{s-m}]} \right]^2 = \left(1 + \frac{P}{T} \right) \frac{S_x^T}{S_x^{\text{rad}}} \frac{e^{\Gamma_M \tau}}{\Gamma_M T}. \quad (2.39)$$

The latter equation shows that it takes longer to measure slower components of the optomechanical correlations. This is due to the fact that the expected value of the correlation function

decreases exponentially with the delay time. This behaviour is illustrated in figure 2.11(b). The upper figure is acquired within a measurement time equal to $T = 220 \text{ } 1/\Gamma_M$, which is insufficient in order to extract quantum optomechanical correlations from the thermal floor. The middle figure corresponds to an intermediation acquisition time $T = 2200\Gamma_M$, which guarantees a measurement resolution better than 20 standard deviations for the synchronous correlations, but does not enable resolving the correlations over more than a mechanical coherence. The third figure shows that acquiring the correlations for $T = 22000 \text{ } 1/\Gamma_M$ ensures a good resolution over a few mechanical coherences. As radiation pressure response of optomechanical systems is improved by decreasing the mechanical damping rate, this eventually poses an important problem. As an example, let us consider detecting the correlations with a resolution bandwidth $\nu_{\text{RBW}} \simeq 1/\tau \leq \Gamma_M/2\pi$ in experimental conditions where quantum radiation pressure effects are four orders of magnitude smaller than thermal noise $S_x^{\text{rad}} = 5 \times 10^{-4} S_x^T$, while the linewidth of the mechanical resonator is equal to $\Gamma_{rmM}/2\pi = 1 \text{ Hz}$. In this case, the extraction of optomechanical correlations would require an acquisition time greater than $T = 370 \text{ hours}$, a duration upon which stable experimental operation needs to be guaranteed.

Out-of-resonance case

The above general calculation of the needed averaging time can be easily simplified for the out-of-resonance case the difference being that, given the flat mechanical response out of resonance, the phase shift induced by the mechanical resonance to the measured fluctuations may be ignored. Therefore, the characteristic time constants of the measurement are only defined by the apparatus filters $H(t)$ which, in this case, may be approximated by a Lorentzian-type filter:

$$H(t) = \theta(t) \frac{\Gamma_{\text{span}}}{2} e^{-\Gamma_{\text{span}} t/2}. \quad (2.40)$$

The steps of this calculation are identical to the one presented above. It is thoroughly described here [70], giving a very similar result in the out-of resonance case. It can similarly be found that the expected value of the correlation function is equal to:

$$\mathbb{E}[\mathcal{C}_{s-m}] \propto \mathbb{E}[B] = \frac{16\hbar\mathcal{F}^2}{\lambda M \Omega_M^2} \Gamma_{\text{span}} S_p^{\text{out}}. \quad (2.41)$$

The imprecision on the correlation function is found to be equal to:

$$\sigma^2(A) = \frac{2S_p^{\text{out}S_\beta}}{16T^2} (\Gamma_{\text{span}} T + e^{-\Gamma_{\text{span}} T} - 1), \quad (2.42)$$

while as the Langevin force dominates the mirror motion: $\sigma(A) \gg \sigma(B)$. We finally get for the correlation function imprecision:

$$p = \frac{\sigma(\mathcal{C}_{s-m})}{\mathbb{E}[\mathcal{C}_{s-m}]} = \sqrt{\frac{S_x^T}{S_x^{\text{rad}}}} \frac{\sqrt{2}(\Gamma_{\text{span}} T + e^{-\Gamma_{\text{span}} T} - 1)^{1/2}}{\Gamma_{\text{span}} T}. \quad (2.43)$$

By assuming an acquisition time much greater than the time constant of the measurement $\tau_{\text{span}} = 2/\Gamma_{\text{span}}$ one may reduce the latter equation to an expression resembling equation

(2.38):

$$T = \frac{\tau_{\text{span}}}{p^2} \times \frac{S_x^T}{S_x^{\text{rad}}}. \quad (2.44)$$

If one then wants to measure optomechanical correlations with a precision of 10%, a signal-to-noise ratio $S_x^{\text{rad}}/S_x^T = 10^{-2}$, and a measurement bandwidth of 10 kHz it would take him only a few seconds, making the averaging idea, particularly interesting in the out-of-resonance case.

We will finish this section with an experimental demonstration of the above arguments using the same classical intensity noise as earlier. Figure 2.11(c) shows the time-evolution of the normalised correlation function $\mathcal{C}_{m-s}(T)$ for multiple acquisitions, each one realized under the same experimental conditions; the same 200-ms long intensity noise is applied repeatedly for a total duration of 2.8 s. We observe that all acquisitions presented in this figure converge towards a non-zero, asymptomatic value $\mathcal{C}_{m-s}(T) = 0.16$.

2.2 Backaction amplification

In the introductory chapter we have discussed the sensitivity limits in the moving mirror displacement measurement. We have shown the existence of the quantum fundamental limit associated to this measurement, the so-called Standard Quantum Limit (equation 1.72). Our research group has published various theoretical articles describing these limits. One of these studies shows how the mirror dynamics are modified in the case of a detuned Fabry-Perot cavity [73]. In the previous section of this manuscript, we have already described that in a such detuned cavity a coupling between the displacement of the moving mirror and the intra-cavity intensity -and consequently the radiation-pressure force applied onto the mirror- occurs. Pioneering experiments have been carried out by the group, exploiting such effects in order to cool down the moving mirror via radiation pressure [74], [75]. Another interesting aspect of this coupling is that it can be used in order to beat the quantum limits associated to the displacement measurement.

Let us assume we want to measure an extremely weak classical signal, an apparent length variation induced by a gravitational wave for example. It has been shown, that in a detuned cavity, the mirror motion becomes sensitive to the signal and, depending on the cavity working point, a signal amplification can occur. During this thesis, an experimental demonstration of this effect has been achieved [29].

2.2.1 Sensitivity improvement in a detuned cavity

Let us assume a single-ended Fabry-Perot cavity of length L , composed by a perfectly reflecting, movable mirror and a fixed slightly transmitting coupler mirror, as depicted in figure 2.12. We want to measure a small cavity length variation X_{sig} produced by an external phenomenon. This signal may be caused by a gravitational wave, a weak force applied to the movable mirror or, equivalently, a laser frequency modulation. It is superimposed to the actual displacement

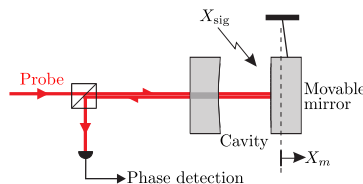


Figure 2.12: Principle of an apparent length variation signal X_{sig} through the detection of the probe beam phase.

of the movable mirror X_m induced by the radiation pressure noise of the intracavity field. The cavity detuning then reads:

$$\psi(t) = 2kL [2\pi] = \psi_0 + 2k[X_m(t) + X_{\text{sig}}(t)]. \quad (2.45)$$

We have already written down the general input-output field transformation for a cavity with a non-zero detuning $\psi \neq 0$ (see equations (4.5) and (4.6)). The force fluctuations that the movable mirror undergoes are related to the intracavity intensity fluctuations:

$$\delta F_{\text{rad}}[\Omega] = 2\hbar k \delta I[\Omega] = 2\hbar k \bar{\alpha} \delta p[\Omega]. \quad (2.46)$$

We can now relate the radiation-pressure fluctuations to the phase, intensity and position fluctuations:

$$\delta F_{\text{rad}}[\Omega] = \delta F_{\text{rad}}^{\text{intra}} + \delta F_{\text{rad}}^m + \delta F_{\text{rad}}^{\text{sig}}, \quad (2.47)$$

where:

$$\begin{aligned} \delta F_{\text{rad}}^{\text{intra}} &= 2\hbar k \bar{\alpha} \frac{1}{\Delta} \sqrt{\frac{2\gamma}{\gamma^2 + \bar{\psi}^2}} \left((\gamma^2 + \bar{\psi}^2 - i\gamma\Omega\tau) \delta p_{\text{in}}[\Omega] - i\bar{\psi}\Omega\tau \delta q_{\text{in}}[\Omega] \right), \\ \delta F_{\text{rad}}^m &= -8\hbar k^2 \bar{\alpha}^2 \frac{\bar{\psi}}{\Delta} \delta X_m[\Omega] \\ \delta F_{\text{rad}}^{\text{sig}} &= -8\hbar k^2 \bar{\alpha}^2 \frac{\bar{\psi}}{\Delta} \delta X_{\text{sig}}[\Omega]. \end{aligned} \quad (2.48)$$

The first force $\delta F_{\text{rad}}^{\text{intra}}$ corresponds to the radiation-pressure force induced by the quantum fluctuations of the incident field: the quantum back-action of the measurement. The second force δF_{rad}^m depends on the position fluctuations of the mirror and is responsible for the dynamical modification of the resonator mechanical properties. It is similar to the active feedback force F_{fb} we have introduced in section 1.8.3 which may induce a modification of the effective damping of the mirror as well. When the mirror displacement is dominated by the thermal noise, the force F_{fb} may be used for example cool the resonator. Similarly, the dynamical back-action can be used to the same end. One may qualitatively interpret this optomechanical effect by an analogy to the Stokes and anti-Stokes processes: the optomechanical coupling lies in the fact that the mirror displacement is coupled to the intra-cavity intensity. In particular, as we have seen, the displacement is essential internal vibrational modes oscillating at a frequency Ω_M modulating, in turn, the amplitude of the intra-cavity intensity. In the frequency domain, this modulation creates two sidebands $\omega_0 + \Omega_M$ (anti-Stokes) and $\omega_0 - \Omega_M$ (Stokes). Once one of this sidebands is resonant with the cavity the Stokes/anti-Stokes process takes place either amplifying or cooling the mirror. Experimental demonstrations of this using radiation pressure to cool a resonator have been realized in our group [74] and elsewhere [76], [56]. In fact, these two processes take place at the same time, once both sidebands are in the bandwidth of the cavity. The resulting dissipative effect is then a competition of the two.

Naturally, one gets a better cooling efficiency by excluding the Stokes process or, in other words by setting the corresponding sideband out of resonance. This can be achieved when the cavity bandwidth Ω_{cav} is great compared to the mechanical resonance Ω_M and the experience can be performed in the resolved sideband regime [77], [78], [79]. At low frequency ($\Omega \ll \Omega_{\text{cav}}$)

this force can be written:

$$F_{\text{rad}}^{\text{m}} \simeq 4\hbar k \frac{d\bar{I}}{d\psi} \delta X_{\text{m}}(t), \quad (2.49)$$

introducing an additional restoring force, often called ponderomotive force or an optical spring, modifying the resonator spring constant or, equivalently, the resonance frequency. It corresponds to the so-called dynamical back-action which changes the mechanical response of the mirror, its mechanical susceptibility χ being modified to an effective susceptibility χ_{eff} given by:

$$\chi_{\text{eff}}^{-1}[\Omega] = \chi^{-1}[\Omega] + 8\hbar k^2 \bar{I} \frac{\bar{\psi}}{\Delta}. \quad (2.50)$$

The third force $F_{\text{rad}}^{\text{sig}}$ in equation (2.48) is the force induced by the signal. According to (2.48) and (5.9), it induces a mirror displacement $X_{\text{m}}^{\text{sig}} = \chi_{\text{eff}} F_{\text{rad}}^{\text{sig}}$ proportional to the signal X_{sig} , leading to a total length variation due to the signal:

$$X_{\text{m}}^{\text{sig}}[\Omega] + X_{\text{sig}}[\Omega] = \frac{\chi_{\text{eff}}[\Omega]}{\chi[\Omega]} X_{\text{sig}}[\Omega]. \quad (2.51)$$

Depending on the ratio between the initial and effective susceptibilities, one then gets either an amplification or a compensation of the signal by the mirror motion. We now derive the phase of the field reflected by the cavity, using the usual definition of the phase quadrature $q[\Omega]$ for any field operator a ,

$$|\bar{a}| q[\Omega] = i (\bar{a} a^\dagger[\Omega] - \bar{a}^* a[\Omega]). \quad (2.52)$$

Assuming for simplicity that the frequencies Ω of interest are much smaller than the cavity bandwidth $\Omega_{\text{cav}} = \gamma/\tau$, equations (4.5) show that the phase q^{out} of the reflected field simply reproduces the cavity length variations $X_{\text{m}} + X_{\text{sig}}$ (including radiation-pressure noise), with an additional noise term related to the incident phase fluctuations q^{in} ,

$$q^{\text{out}}[\Omega] = q^{\text{in}}[\Omega] + 2\xi (X_{\text{m}}[\Omega] + X_{\text{sig}}[\Omega]), \quad (2.53)$$

where $\xi = 4k\gamma |\bar{a}^{\text{in}}| / (\gamma^2 + \bar{\psi}^2)$. One finally gets the spectrum $S_q^{\text{out}}[\Omega]$ of the measured phase quadrature as

$$\frac{S_q^{\text{out}}}{4\xi^2} = \frac{1}{4\xi^2} + \hbar^2 \xi^2 |\chi_{\text{eff}}|^2 + \left| \frac{\chi_{\text{eff}}}{\chi} \right|^2 S_x^{\text{sig}}, \quad (2.54)$$

where $S_x^{\text{sig}}[\Omega]$ is the spectrum of the signal X_{sig} . The first two terms in equation (2.54) are the usual quantum shot noise and radiation-pressure noise: they exactly correspond to the ones obtained for a resonant cavity with a mirror having a mechanical susceptibility χ_{eff} . Their sum can be rewritten as $|\hbar\chi_{\text{eff}}| \frac{\zeta^{-1} + \zeta}{2}$, which only depends on the dimensionless optomechanical parameter $\zeta = 2\hbar\xi^2 |\chi_{\text{eff}}|$. At any frequency Ω , the sum is minimal and equal to the standard quantum limit $|\hbar\chi_{\text{eff}}[\Omega]|$ when $\zeta[\Omega] = 1$. Last term in equation (2.54) reflects the signal, but with an amplification factor $|\chi_{\text{eff}}/\chi|^2$ similar to the one already found in equation (2.51). In absence of dynamical radiation-pressure effects ($X_{\text{m}}^{\text{sig}} = 0$) as in the case of a resonant cavity, this factor simply disappears and the second term in equation (2.54) reduces to S_x^{sig} . It is then clear that dynamical back-action not only changes the mechanical behavior of the moving mirror from χ to χ_{eff} , but also enables an amplification of the signal in proportion to the factor $|\chi_{\text{eff}}/\chi|^2$. Equation (2.54) therefore shows that a high amplification factor together with an

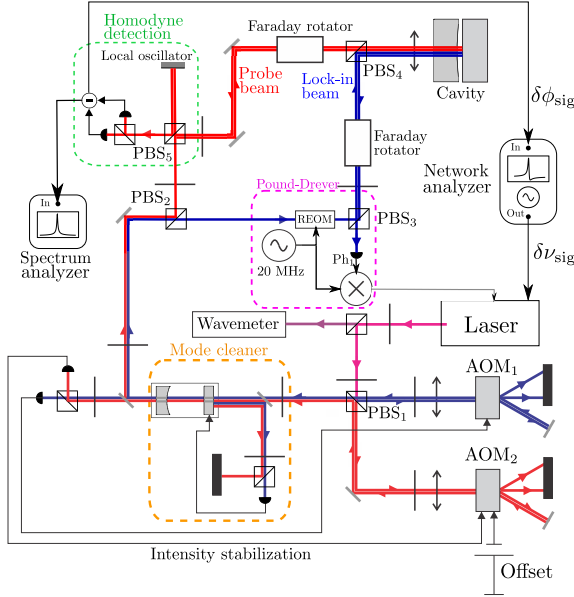


Figure 2.13: The experimental setup used to observe the amplification of an apparent length variation signal by a dynamical backaction effect in a detuned cavity. A network analyzer provides a signal $\delta\nu_{\text{sig}}$ at a given frequency while measuring the corresponding response of the cavity via the homodyne detection output δq_{out} . The pump beam is used to lock the laser frequency to the measurement cavity. The probe beam is detuned thanks to the acousto-optic modulator AOM_2 and measures the position of the mirror.

optomechanical parameter $\zeta \simeq 1$ may afford a significant increase of the measurement sensitivity beyond the SQL $|\hbar\chi_{\text{eff}}|$.

2.2.2 Experimental protocol and results

As for previously discussed optomechanics experiment, we use a Fabry-Perot cavity with a plano-convex movable mirror. The references of the mirrors used are: PC 3021/13 for the plano-convex and 07125/3 for the cylindrical coupler. The resulting cavity presents a quality factor $Q = 762\,000$ with a resonance frequency at $\Omega_M/2\pi \simeq 1.128$ MHz, an effective mass $M_{\text{eff}} = 72$ mg and an optical finesse $\mathcal{F} = 110\,000$. The principle of the experiment is to observe the optomechanical effect produced by an apparent length variation in a detuned cavity. The length variation X_{sig} is a frequency modulation of the laser source induced by the electro-optic modulator, placed inside the laser ring-cavity. In order to measure the cavity response to the signal a network analyzer is used. A network analyzer provides a monochromatic signal at a well-defined frequency while measuring the system response at the same frequency. It can perform user-defined frequency sweeps making the measurement of a function transfer a straightforward procedure. In our case, the signal is the laser frequency modulation and the response is provided by the read-out of the homodyne detection δq_{out} . We use again the double-injection scheme adjusted this time to the purposes of this experiment. The probe beam is coupled to the measurement cavity in order to measure the position of the movable mirror. The pump beam is also coupled to the cavity, but presents a low power as it is only used to lock the cavity. We then alter the frequency of the probe beam in order to detune the cavity. The detuning is done with the help of the acousto-optic modulator coupled to the probe beam by changing the radio-frequency carrier driving the modulator. The experimental setup is depicted in figure 2.13. An important experimental change, compared to the optomechanical correlations experiment described earlier, is the incident power of the two beams, notably because the effect we want to observe is proportional to the power. It is then preferable to perform the experiment

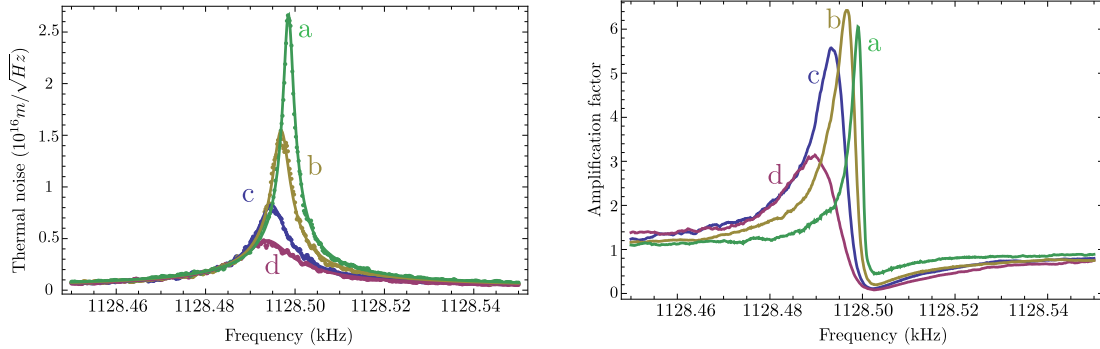


Figure 2.14: Left: Thermal noise spectra measured by the homodyne detection, providing the effective susceptibility χ_{eff} of the mirror for different detunings of the probe beam (4 mW): $\bar{\psi}/\gamma = -3.64$ (a), -2.97 (b), -2.03 (c), -1.87 (d). Right: for the same cavity detunings the optomechanical amplification factor provided by the network analyzer.

with a powerful probe beam. The upper limit for the probe power is mainly imposed by one factor: the saturation limit of the homodyne detection photodiode, which is approximately 30 mW. A proper behaviour of the homodyne detection is ensured when the local oscillator power is large compared to the probe power. This led us to set the probe power at 5 mW and the local oscillator at 25 mW. On the other hand, for the lock-in of the measurement cavity, a weak pump beam suffices; it is set at 200 μW . The small transmission of the measurement cavity can be used to set the working point of the cavity. As the cavity is coupled to two cross-polarized beams, a polarizing plate is placed at the exit of the cavity in order to select only the transmitted power from the probe. The intensity transmitted by the cavity is directly related to the cavity detuning: the bandwidth of the measurement cavity is known ($\Omega_{\text{cav}}/2\pi = 1.4$) MHz and the transmitted intensity is calibrated by modulating the laser frequency at 100 Hz, to visualise the Airy peak on a digital oscilloscope. One can deduce the absolute detuning value $\bar{\psi}/\gamma$. The experimental protocol is as follows. We first select the detuning of the probe beam with respect to the cavity resonance, and we monitor the mirror thermal noise by sending the homodyne detection signal to a spectrum analyzer. This step allows one to determine the effective mechanical response χ_{eff} induced by dynamical back-action. Then, using a network analyzer, the modulation of the laser frequency is turned on and swept around the mirror mechanical resonance. The modulation power is set about 25 dB above thermal noise at the mechanical resonance frequency so that thermal noise can be neglected. The resulting phase modulation of the reflected probe beam is monitored by the network analyzer. We finally turn the probe beam off, and we measure the mirror thermal noise immediately after, using the Pound-Drever-Hall signal. This last step is essential in order to accurately determine the intrinsic mechanical response χ of the moving mirror (obtained with the locking beam at resonance), which may be slightly frequency-shifted from one measurement to the other due to slow thermal drifts -typically 0.1 Hz per minute. We present in figure 2.14 the experimental results. On the left thermal noise, for different detunings, is depicted, as measured by the homodyne detection. We observe that the mechanical resonance frequency is red-shifted, translating the fact that the optical spring constant is lowered when the cavity is driven away from resonance. We furthermore notice a change in the mechanical oscillator damping effect cooling down the mirror: the

thermal noise widens as the detuning increases. On the right, the resulting phase modulation power S_q^{out} is drawn. It is measured by the network analyzer when the signal modulation X_{sig} is swept around the mechanical resonance frequency Ω_M . Curves (a) to (c), obtained for various negative detunings $\bar{\psi}$, are normalized to the phase modulation obtained far from the mechanical resonance (measured 1 kHz above Ω_M). They thus represent the amplification factor $|\chi_{\text{eff}}/\chi|^2$ appearing in eq. (2.54), as can be seen from the inset which compares the experimental result to the expected amplification factor deduced from the measured susceptibilities χ_{eff} and χ . A clear amplification is observed near the effective mechanical resonance of χ_{eff} , which is downshifted from Ω_M as expected from eq. (5.9), whereas one gets an attenuation at the mechanical resonance Ω_M where χ is maximum. Note that similar results are obtained for positive cavity detunings, corresponding to the amplification regime of the mirror-cavity system rather than to the cooling one, but the proximity of the parametric instability makes the results less stable. Nevertheless, we have reached a very large signal amplification effect, with an amplification factor larger than 6 for curve *c*: back-action effects induce a motion $X_m^{(\text{sig})}$ of the mirror in phase with the signal X_{sig} , and with an amplitude larger than the signal itself. Finally, we have determined the sensitivity increase associated to the signal amplification we have observed. However, our experiment is dominated by thermal noise and thus quantum noise cannot be measured experimentally. For this reason, in our calculation, thermal noise was completely neglected. We have considered the case at which the greatest amplification factor is achieved:

$\bar{\psi}/\gamma = -2.97$ and all associated parameters have been experimentally determined. Figure 2.15a depicts the results. Curves b and c depict the Standard Quantum Limits $|\hbar\chi|$ and $|\hbar\chi_{\text{eff}}|$ for two oscillators with a mechanical susceptibility χ and χ_{eff} , respectively. It is clear on curve a, characterized by an signal amplification factor 6, that the measurement sensitivity beats the quantum limits associated to both the oscillator with a susceptibility χ_{eff} and χ . The sensitivity is optimal at a frequency close to Ω_{eff} , where an amelioration of almost 9 dB for the resonator χ_{eff} is seen.

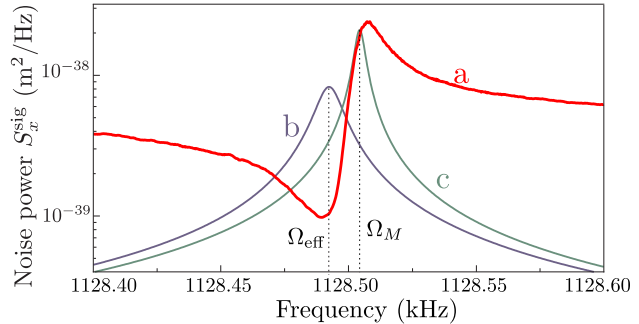


Figure 2.15: The calculated sensitivity on a detuned cavity using our experimental parameters. A sensitivity better than the associated SQL can be achieved.

Development of the experimental setup

IN the previous chapter we have described a technique to demonstrate quantum radiation pressure effects. We have showed that potentially our experiment would be capable of doing so at low temperature. As it is not possible for us to perform the experiment at low temperature, we have started an effort in order to perform it at ambient temperature. This is the subject of this chapter. The detection has been upgraded by constructing a balanced detection to monitor the intensity fluctuations, directly providing the quantum noise of the incident pump beam. Also, the homodyne detection photodiodes have been replaced with new ones with better quantum efficiency. Furthermore, in order to achieve a more favourable signal-to-noise ratio S_x^{rad}/S_x^T , it has been decided to increase the incident power by a factor of 10. Since our Ti:Sa laser source provides a quantum-noise limited beam up to 1 mW, this implies the construction of a second mode-cleaner cavity to further filter the laser classical noise at a power of 10 mW. The implementation of the new mode-cleaner cavity also led us to change the laser frequency stabilization scheme. As we will discuss later on, this cavity inserted between the laser source and the FPM makes the laser stabilization very difficult. In an attempt to solve this experimental drawback, various solutions have been explored during this thesis: a feed-forward technique, the use of an acousto-optic modulator implemented after the mode-cleaner to lock the laser frequency to the measurement cavity and the construction of a new measurement cavity in which a piezoelectric actuator is implemented. In this chapter, these experimental upgrades of our setup will be detailed.

3.1 Balanced detection

Until now, the reflected intensity was monitored by a single photodiode. We have decided to replace the photodiode with a balanced detection system. Such a system is depicted in figure 3.1. It consists of two perfectly identical photodiodes, a polarizing beam splitter and an electronic circuit working either as a sum or as a differential amplifier. The incoming light is first separated into two parts of equal optical power, each one being detected by a photodiode. The photocurrents produced by the photodiodes are then either added or subtracted using the electronic circuit at the output of the photodiodes. The advantage of this system is that it is able to suppress classical noises. Indeed, once the beam splitter

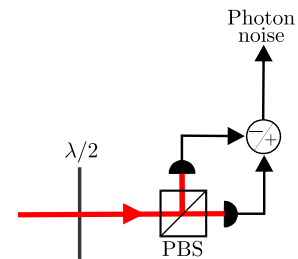


Figure 3.1: Balanced detection.

divides the incoming light in two parts of equal power, classical noises are correlated in each other whereas quantum noises are completely uncorrelated. Consequently subtracting the two photocurrents will lead to a suppression of the sole incident optical, classical noise. Therefore, a balanced detection system can be very useful when one wants to observe incident quantum noise but its construction presents several difficulties. The electronic noise of the two photodiodes will not be suppressed by the subtraction operation since they are uncorrelated to each other and thus it will contribute to the measured signal. Under this view, electronic noise resembles quantum noise and, therefore, one cannot distinguish the two noises. This can be controlled by carefully designing the photodiodes so that they present a favourable signal-to-noise ratio at the desirable power and frequency. Another technical difficulty is the perfect matching of the detector. The spectral response of the two photodiodes must be exactly the same. This is not easy to realize since the spectral response can depend on numerous factors: the photodiodes themselves, the actual wiring of the electronic circuit amplifying the photocurrent, the electronic components of the circuit, for instance the resistors or the operational amplifiers, the imperfections of the beam splitter and many more. Any detection imbalance may result in a degradation of the detection efficiency.

3.1.1 Designing the photodetectors

Typically, a photodiode consists of a sensitive surface -usually a PIN semiconductor structure- converting a photon to an electron: once a photon flux strikes the diode a photocurrent is produced, with the same statistical properties as the incident light. This structure is usually mounted on an electronic circuit which transforms the produced photocurrent to a voltage which is amplified using some stages of operational amplifiers. A similar scheme has been used for our custom-made photodiodes.

A photodiode is characterized by its electronic noise, and therefore the threshold above which a signal can be detected, its bandwidth, its saturation level, its quantum efficiency and its dark noise. The quantum efficiency and the dark noise solely depend on the PIN structure itself; they then have to be carefully chosen. However, all other properties are set by the design of the electronic circuit.

Electronic noise

The electronic circuit will be a source of electronic noise, mostly from thermal noise in the resistors. It is known as Johnson noise and has no spectral dependence; it is a white noise, given by equation:

$$V_j = \sqrt{4k_B T R \nu_{BW}}, \quad (3.1)$$

where R is the resistor value, k_B the Boltzmann constant, T the temperature and ν_{BW} the detection bandwidth. The origin of this noise is the random process of the electrons passing through the resistor. It is actually the electronic equivalent to the optical shot noise. There are other contributions as well to the electronic noise such as the dark noise and the amplifier noise. We will consider that both of these noises are negligible compared to Johnson noise. It is Johnson noise that will set a limit to the photodiode sensitivity. The Johnson noise generated by the photodiode amplifier is to be compared to the generated photocurrent to set the corresponding signal-to-noise ratio. In fact, usually this quantity is expressed using the Noise Equivalent Power (NEP) parameter giving the floor noise of the photodiode ensemble or,

alternatively, the optical power that produces a unity signal-to-noise ratio at the output of the detector. The balanced detection will replace the photodiode which monitors the light reflected by the measurement cavity. Typical input powers range from 1 mW to 10 mW. Considering that the reflection coefficient \mathcal{R}_0 may reach values down to 10%, depending on the optical characteristics of the measurement cavity, reflected power of at least 100 μW will be injected to the balanced detector. This means that the detector must be sensitive enough to detect an input power of at least 100 μW .

Bandwidth

The bandwidth of a photodetector is an important parameter. It depends on the active components of the electronic circuit. The signal we want to monitor correspond to the displacements of a mirror, which vibrates at relatively low frequencies, around 1 MHz. However, the detector should be fast enough in order to be able to derive a Pound-Drever error signal. Until now, a phase modulation at 20 MHz was applied to the laser beam. We have decided, however to increase the phase modulation frequency to 50 MHz in order to increase as well the capture range of the laser feedback loop. Therefore, the photodiode bandwidth is set by the Pound-Drever phase modulation and must be at least 50 MHz.

Quantum efficiency

An ideal photodetector would transform each photon into an electron. The quantum efficiency η would be 1 in this case. However, in a real detector, each photon has a non-zero probability not to be detected and the quantum efficiency corresponds to the fraction of photons converted into electrons. It depends on the properties of the detector material. In order to measure it, one should measure the output voltage V of the photodiode versus the incidence power P . The photocurrent is given by:

$$I(t) = \eta \frac{P(t)e}{h\nu}, \quad (3.2)$$

where e is the electron charge, h the Planck constant and ν the photon frequency.

Saturation

Finally, there is a saturation level of the detector above which the photocurrent of the detector no longer increases. Photodiodes are usually polarized by a bias voltage in order to increase their power tolerance. The photocurrent produced is transformed into a voltage via the load resistor R_{load} connected to the output of the photodiode. Once the load voltage becomes comparable to the bias voltage the photodiode no longer behave normally, presenting saturation effects. As already stated above, the detector is supposed to detect signals of up to 10 mW, so the load resistor should be chosen accordingly.

3.1.2 Constructing the detector

To sum up, the major qualities of a good photodiode is its excellent quantum efficiency, a spectral response large enough in order to efficiently detect both the mirror displacements and the Pound-Drever error signal, a low NEP and a high saturation level. We will now describe all the construction stages in order to fulfil all the above requirements.

Mounting setup

A compact and rigid system, inspired by the one used for the homodyne detection [80] has been constructed in order to mount the photodiodes. The photodiodes are packaged into an aluminium box assuring their best isolation from parasitic electromagnetic captures. All detector elements are fixed onto a 18 times 15-cm² dural plate. A lens $f=100$ mm is used to focus the light onto the sensitive surface of the photodiodes. A system of a half-wave plate and a polarizing beam splitter (PBS) is used afterwards; the half-wave plate is mounted onto a turning mount system setting the light power detected by each photodiode. The beam splitter is mounted onto a micrometric screw system permitting to rotate it around the 3 axes. The aluminium boxes harbouring the photodiodes are mounted onto two micrometric translation stages permitting to align the photodiodes on the light beam. The orientation of these boxes is set to 45° compared to the beam orientation. The photodiode will reflect a small portion of the light, this configuration permits the re-injection of the reflected light using a simple mirror. This can improve the quantum efficiency by a few percents. The whole rigidity of the mounting system provides an excellent ground contact of the ensemble and, consequently, eliminates any high-frequency electronic parasite. Finally, the output of the photodiodes is sent to the electronic circuit performing the subtraction.

Si PIN photodiode

For the PIN structure we chose the *Hamamatsu* S5971 Si PIN photodiode. It has an effective area of 1.2 mm diameter. It has a very low terminal capacitance ($C_t = 2$ pF), its bandwidth is high enough for our purpose (100 MHz) and it presents a sensitivity peak at a wavelength of 900 nm -very close to our Ti:Sa typical wavelength. At 830 nm its photo-sensitivity is equal to 0.6 A/W. Its floor noise (NEP) is equal to $7.4 \cdot 10^{-15}$ W/ $\sqrt{\text{Hz}}$. These numbers only represent the Si PIN photodiode. The photodiode will be used with a 70 V bias in order to reduce its time response and to be able to increase as much as possible the value of its load resistor reducing its Johnson noise.

The pre-amplifiers

The pre-amplifier is separated in two parts: one for the low-frequency signals (DC) and one for the high-frequency (HF) ones. The separation of the two signals is realized by a simple RC filter consisting of a capacity $C = 1$ nF placed at the entry of the HF stage and two resistors in series with the photodiode ($R_{\text{load}} = 910 \Omega$ and $R'_{\text{load}} = 100 \Omega$). The cut-off frequency of this low-pass filter is $f_c = 144$ kHz.

The HF part has two different amplification stages. The first one of an inverting amplifier having a feedback resistor $R_{\text{fb}} = 2.7$ k Ω . The operational amplifier we used for this stage is the fast (gain bandwidth product=1.6 GHz), low noise (4.8 nV/ $\sqrt{\text{Hz}}$) OPA657. The choice of the feedback resistor, R_{fb} , and the photodiode load resistor, R_{load} is very critical for the good operation of the pre-amplifier: it will determine at the same time the Johnson noise level, the gain and the bandwidth of the amplification stage. Moreover, the load resistor will set the saturation level of the photodiode. The voltage created across the load resistor by the photocurrent may compromise the polarization of the photodiode if it reaches values comparable to the bias voltage (70 V). Therefore, the choice of the load and feedback resistor will result from a compromise between the proper operation of the PIN diode and the generated Johnson

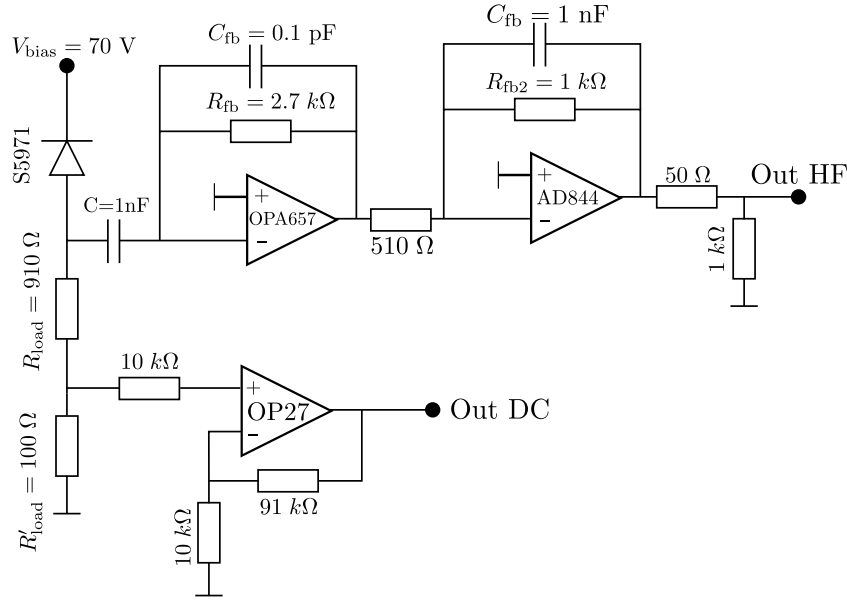


Figure 3.2: The pre-amplifier circuit used to transform and amplify the photocurrent. It is made of mainly three parts. A RC circuit separates a DC and a high-frequency component. The HF part is more critical and has a high-speed, low-noise operational amplifier and two amplification stages.

noise. There is also a feedback capacitance, $C_f = 0.1$ pF used to render the spectral response of the amplification stage flat at high frequencies. In particular, the amplifier typically presents resonances at high frequencies (~ 60 MHz); the amplification stage thus plays the role of a low-pass filter with a cut-off frequency carefully chosen to suppress the apparent resonance. A second amplification stage is added in order to amplify a bit more the signal at the expense of a bandwidth reduction. We used the standard operation amplifier AD844 cabled in an inverting mode as well, presenting a gain $g = 2$. The bandwidth of this amplification stage depending on the choice of the feedback resistor, we chose a $R_{f2} = 500\Omega$ in order to obtain a bandwidth of 50 MHz. It is this part of the photodiode pre-amplifier that will provide both the 1-MHz intensity fluctuations and the 50-MHz Pound-Drever signal. Considering the importance of the high-frequency stage, in order to assure its low-noise operation, some design precautions were taken. We have tried to minimize the cabling from the PIN photodiode to the HF stage in order to avoid any parasitic noise capture. For the same reason, a ground plane on the other side of the electronic plate has been realized. The DC part is also very critical, since it will be used to observe the reflected absorptive Airy peak. More importantly, it is the DC signal of each photodiode upon which we will rely in order to balance the detection. Since no particular requirements for this stage are necessary -slow signals, up to some hundreds of kHz, no low noise requirements- we chose the most common operation amplifier OP27. It is designed in order to operate in non-inverting amplifier mode where the feedback resistors are chosen to have a gain $g=10$. No special precaution has been taken when designing the DC part of the circuit. Figures 3.4(b) and 3.3 show the performance of the custom-made photodiodes. The incident power versus the output voltage of the DC part is plotted in figure 3.4(b). Equation 3.2 can

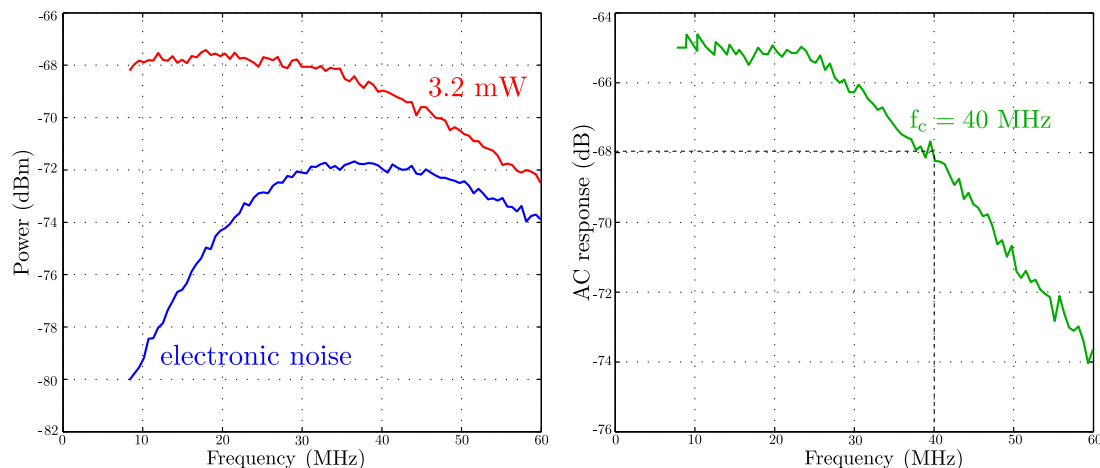


Figure 3.3: The achieved bandwidth of the photodiodes. For an input power of 3.2 mW, a 40-MHz bandwidth is achieved.

be used to derive the quantum efficiency of the photodiode. By adjusting a linear fit to the measured value we find a quantum efficiency $\eta = 93\%$. Figure 3.3 shows the spectral response of the HF part of the photodiodes, by measuring the electronic noise generated by the circuit and then, the output voltage generated by a 3.2 mW input laser beam. The electronic noise is then subtracted from the signal in order to find the spectral response of the electronic circuit. A relatively flat spectral response is observed, presenting a cut-off frequency close to 50 MHz for a power of 3.2 mW. Finally, by doing a study of the high-frequency response dependence on the incident power one can measure the detection threshold where the signal-to-noise ratio is unity. We simply simulate the function of a balanced detector by using a post-data processing: the classical noise is subtracted from the measured signal. It suffices to perform an electronic noise measurement, to monitor the photodiode light response varying the incident power and, finally, to subtract from each measurement the electronic noise. Figure 3.4(a) shows the result of this study. We observe a threshold of $100 \mu W$ where the measured signal is equal to the electronic noise.

We have managed to construct custom-made photodiodes presenting a quantum efficiency $\eta = 93\%$, a bandwidth of 50 MHz and a threshold of $100 \mu W$. Even though the two photodiodes are constructed using the same components it is however not guaranteed that the detector is perfectly balanced.

3.1.3 Balancing of the detector

The procedure followed is thoroughly described in [80]. Practically, we first balance in the best possible way the DC part of the photodiodes. We consider, only by observing the DC output, that each photodiode detects the same light power. Afterwards, by looking the HF response difference between the two photodiodes at a given frequency (1 MHz for instance) we adjust accordingly the feedback resistor R_f of one photodiode in order to balance them.

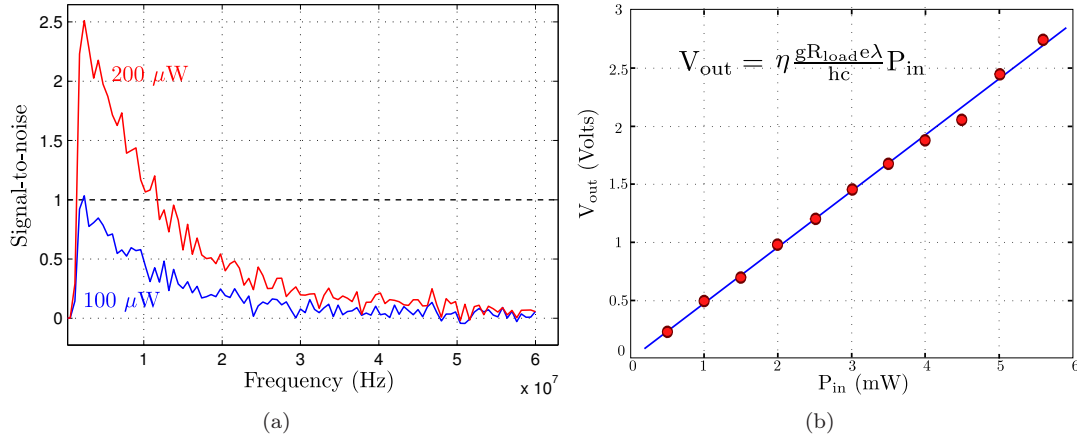


Figure 3.4: (a) The obtained noise floor obtained at power 100 μW and 200 μW over a spectral range of 6 MHz. At low frequency (<1 MHz) a unity signal-to-noise ratio is obtained at 100 μW . (b) The output voltage as a function of input power; the slope gives the quantum efficiency, $\eta = 93\%$.

DC

To balance the DC part of the photodiodes an artificial imbalance of the detections is induced by rotating accordingly the half-wave plate. This imbalance is then detected by the following procedure: by changing the incident power we monitor both DC outputs, V_1 and V_2 , of the photodiodes in order to determine their relative difference $R_1 = (V_1 - V_2)/V_1$. We repeat this process a second time inverting this time the position of the photodiodes. The corresponding relative gain differences can be found to be:

$$R_1 = 2\varepsilon + \frac{\delta g}{g}, \quad (3.3)$$

$$R_2 = -2\varepsilon + \frac{\delta g}{g}, \quad (3.4)$$

where ε is the optical imbalance and δg the gain imbalance. The gain g is considered to be equal to 10. Using the above system of equations the electronic gain imbalance can be measured; it is equal to $g/2(R_1 + R_2)$.

HF

Once the DC output is balanced, the half-wave plate is used to perfectly balance the detector. By observing a monochromatic modulation applied to the light at 1 MHz via an acousto-optic modulator (AOM), we measure the modulation level with the help of a spectrum analyzer and we adjust the feedback resistor R_f of one photodiode accordingly. Finally, a modulation sweep (0-10 MHz) is applied again via the AOM. The sweep is essentially limited by the AOM bandwidth. Nevertheless, since we want to measure a signal at a frequency of a few MHz, this sweep suffices. The AOM is driven via a network analyzer which is monitoring at the same time the response of the balanced detector. The internal potentiometer of the subtraction circuit is then adjusted accordingly in order to compensate any residual gain imbalance of the HF part.

3.2 Mode cleaner cavity

A coherent state is also known as "classical light" since it is the quantum state that resembles the most to the properties of the classical harmonic oscillator; an ideal laser source is described by such a model. According to it, the quantum noises present in a coherent source pose fundamental limits to the performance of such a laser source, the so-called Quantum Noise Limits. A real laser however presents extra classical noises -usually at low frequencies- which usually completely covers these limits. The laser source of our experimental setup can provide quantum-noise limited light power up to 1 mW, to the analysis frequency (~ 1 MHz). A way to increase the signal-to-noise ratio to observe radiation pressure effects would be to increase the incident power which is limited by the noise properties of the light source. Therefore, since the Ti:Sa presents classical intensity fluctuations completely dominating the quantum fluctuations we are trying to observe, the increase of the incident power is not an option. A standard method of noise reduction is the use of a Fabry-Perot cavity with a small bandwidth. Once the incident laser beam is resonant with a FP cavity it acts like a low-pass filter that reflects all spectral components of the light fluctuations at frequencies larger than its bandwidth. The smallest the bandwidth is, the more efficient the filtering of the classical intensity fluctuations. We have then envisioned to construct a new mode-cleaner cavity and obtain a quantum-noise limited light beam of 10 mW, at 1 MHz. By increasing then the incident power by a factor of 10 we may expect a resulting signal-to-noise ratio $S_x^{\text{rad}}/S_x^T = 10^{-2}$. For reasons that will be made clear later on, two different filtering cavities were tested. We will start this section by describing some alternatives methods to optically calibrate a cavity and we will continue by describing the efforts made to construct such a cavity and efficiently lock the laser on its optical resonance.

3.2.1 Optical calibration

Optical characterization of the cavity

We will now describe various methods in order to determine the optical characteristics of the measurement cavity: its length, its bandwidth and its finesse.

Free Spectral Range measurement

It is known that a Fabry-Perot cavity presents multiple optical modes that may be observed using a CCD camera or even a standard webcam placed at the exit of the cavity. In particular, by scanning the laser wavelength, a repetitive pattern of resonances (a frequency comb) can be observed. This comb consists of the fundamental mode (TEM_{00}) and an infinite number of transverse modes (TEM_{pq}); figure 3.5(a) presents the fundamental mode and 4 transverse modes. The interval between two longitudinal modes TEM_{00} is called the Free Spectral Range of the cavity and is directly related to its length. The Free Spectral Range is given by:

$$\nu_{ISL} = \frac{c}{2L_0}, \quad (3.5)$$

where L_0 is the cavity length. Since the laser wavelength is monitored by a wavemeter, we measure the wavelength of two successive longitudinal modes and we deduce the interval $\Delta\lambda$ is

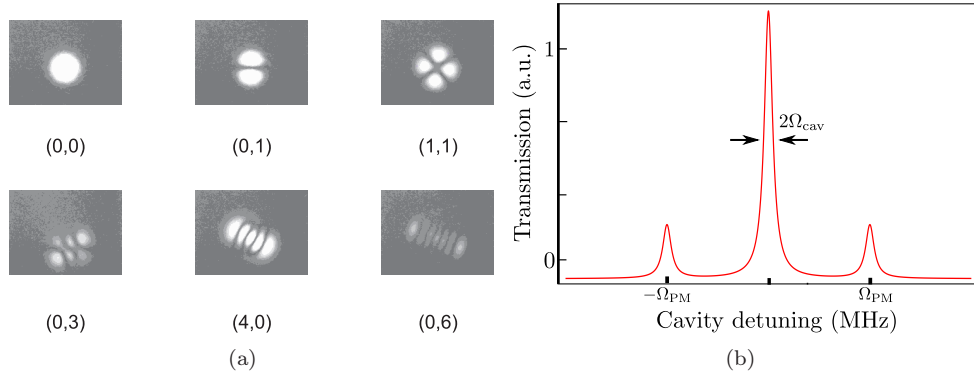


Figure 3.5: (a) The fundamental mode and the first transverse modes of a high-finesse cavity. Each mode TEM_{pq} is identified by two indexes (p,q) each one indicating the number of nodes in the horizontal and vertical directions. (b) The sidebands of the Pound-Drever-Hall phase modulation permit to calibrate the measured cavity bandwidth.

deduced. The Free Spectral Range then becomes:

$$\nu_{ISL} = c \frac{\Delta\lambda}{\lambda^2}. \quad (3.6)$$

Finally, the cavity length can be determined using equation (3.5). The spectral range between two transverse mode depends not only on the cavity length, but also on the radius of curvature R of the coupling mirror. By assuming a radius of curvature much larger than the cavity length, the transverse spectral range, ν_{tr} is given by:

$$\nu_{tr} = \frac{\nu_{ISL}}{\pi} \sqrt{\frac{L_0}{R}} = \frac{c}{2\pi\sqrt{RL_0}}. \quad (3.7)$$

This way a rough estimation of both the cavity length and the radius of curvature can be made.

Bandwidth and finesse

There are a couple of methods to measure the cavity bandwidth. One of them consists in sweeping the cavity length of the laser frequency and visualizing the Airy peak with a numerical oscilloscope. A fit of the Lorentzian curve then gives its Half-Width at Half-Maximum (HWHM). This technique however requires to calibrate the horizontal scale of the curve. We can take advantage of the presence of a Pound-Drever-Hall setup implemented in our experiment. As we have seen earlier, the Pound-Drever-Hall technique consists in modulating the phase of the incident beam at a frequency Ω_{PM} . The phase modulation manifests itself with the presence of two sidebands at $\pm\Omega_{PM}$ that can be observed in the transmission of the measurement cavity (see figure 3.5(b)). This can be done using a digital oscilloscope while scanning the piezoelectric actuator of the laser cavity at 100 Hz. We can thus use these sidebands to calibrate the time axis of the oscilloscope. The finesse of the cavity can now be directly calculated. It is defined

as the ratio between the free spectral range and the bandwidth of the cavity:

$$\mathcal{F} = \frac{\nu_{ISL}}{2\nu_{BW}} \quad (3.8)$$

Cavity ringdown effects I

As already explained, the new mode-cleaner cavity is designed to have a very small bandwidth in order to filter the classical noise of the laser at the lowest frequency possible. To measure the FWHM of the cavity which is related directly the optical length of the cavity must be swept, by modulating either the laser frequency or the cavity length itself via a piezoelectric actuator glued to one of the mirrors of the cavity. This sweep is usually done at 100 Hz. It is slow enough so that the piezoelectric actuator has a mechanical response with an amplitude corresponding to a few tens of MHz, sufficient to visualize both sidebands on the same frequency window. At the same time, it must be fast enough so that the cavity resonance does not drift away from the frequency window.

For small cavity bandwidths, the sweep time of the cavity can lead to ringdown effects related to the photons time life into the cavity. These effects result in a distortion of the Airy peak Lorentzian shape [81]. When confronted with this problem, the frequency modulation must be decreased, noting that environmental vibrations will set a lower limit to the modulation frequency. In such a case this method cannot be applied: at high sweep frequency ringdown effects are visible whereas at low frequencies the Airy peak will completely be distorted due to vibrations. Into this section we will show how to use the distorted Airy peak to determine with high precision the cavity finesse. We will use the equations established in the first chapter for a lossless cavity. Moreover, the cavity length is swept with a constant speed v . We can then write down the usual equation for the intracavity field and transmitted field (equation (4.1)).

$$\tau \frac{d\alpha(t)}{dt} = \sqrt{\gamma} \alpha_{in}(t) + (i\Psi(t) - \gamma) \alpha(t), \quad (3.9)$$

$$\alpha_{tr} = \sqrt{\gamma} \alpha(t), \quad (3.10)$$

where we have considered the case of a symmetrical cavity where both mirrors present the same transmission. In this case $T = P = \gamma$. It is the usual input-output transformation we have found in the first chapter. The phase shift $\Psi(t)$ now has two contributions: the phase shift induced by the beam propagation into the cavity $\Psi_0(t)$ and the phase shift induced by the motion of the mirror:

$$\Psi(t) = 2kL(t) = 2k(L_0 + vt) = \Psi_0 + 2\Omega_v t, \quad (3.11)$$

with $\Psi_0 = 2\omega_0 L_0/c$ and $\Omega_v = \omega_0 v/c$. It follows for the transmitted field that:

$$\tau \frac{d\alpha_{tr}(t)}{dt} = \gamma \alpha_{in}(t) + (i\Psi(t) - \gamma) \alpha_{tr}(t). \quad (3.12)$$

This is a first-order differential equation whose solution is given by:

$$\alpha_{tr}(t) = \frac{\gamma}{\tau} \alpha_{in} \int_0^\infty e^{(-\gamma + i\Psi(t-v/2))v/\tau} dv. \quad (3.13)$$

It is convenient to express the above equation with the help of the complementary error function,

erfc, by making use of the identity:

$$\int_0^{\infty} e^{-\gamma v - v^2/4\beta} dv = \sqrt{\pi\beta} e^{\beta\gamma^2} \operatorname{erfc}(\gamma\sqrt{\beta}). \quad (3.14)$$

The transmitted intensity then becomes:

$$I_{\text{tr}} \propto e^{-\Psi(t)/(2\Omega_v\tau_{\text{cav}})} \left| \operatorname{erfc} \left(\frac{\gamma - i\Psi(t)}{2\sqrt{i\Omega_v\tau}} \right) \right|^2, \quad (3.15)$$

where $\tau_{\text{cav}} = \tau/2\gamma$. We remind that τ is the beam characteristic time for a photon to realize one cavity round-trip: $\tau = 2L_0/c$.

Equation 3.15 may prove very useful to characterize a high-finesse, low-bandwidth cavity presenting a large photon lifetime. When such a cavity is rapidly swept, the photons do not have enough time to escape the cavity while new ones enter it. Consequently, interference effects between “old” and “new” photons occur as they have travelled different optical paths. These effects occur under the form of rebounds effects visible at the one side of the Airy peak. We will describe an experimental demonstration of this in the following.

Cavity ringdown effects II

Another technique that might be useful is the optical analogue of the ringdown technique applied to measure the quality factor Q of a mechanical oscillator. Usually, the resonator is coupled to an actuator driven at its resonance frequency while its motion is monitored. The excitation is then abruptly turned off and its relaxation motion is observed, the quality factor Q being deduced from the exponential decay of the excitation. An analogue scheme can be applied to an optical cavity in order to measure its finesse \mathcal{F} . Practically, the cavity frequency bandwidth is determined by directly measuring the lifetime of the photons in the cavity. When the cavity is locked at resonance an intensity modulation with a great depth ($\delta I/I = 100\%$) is applied to the light beam. To achieve this the AOM is driven by a TTL signal (0V- 5V) at a frequency $\Omega/2\pi > \Omega_{\text{cav}}/2\pi$. The cavity transmission is actually flashing thanks to the large capture range of the Pound-Drever error signal the cavity is relocked automatically. By observing the transmitted light with a photodiode and a numerical oscilloscope we can visualize the photons coming out of the cavity and thus their life time into the cavity. Attention must be paid to the bandwidth of the photodiode, that has to be large compared to the cavity bandwidth, in order to ensure that we are not observing the photodiode response instead of the photon lifetime. This technique is known as optical ring-down. The calculation of the transmitted field when switching off the incident field is straightforward. Considering that there is no incident field and no loss ($\alpha_v = \alpha_{\text{in}} = 0$) equations 4.1 and 1.33 give for the transmitted intensity:

$$I_{\text{tr}}(t) = e^{-4\pi\nu_{BP}t}, \quad (3.16)$$

where ν_{BP} is the frequency bandwidth of the cavity. The finesse can then be calculated by measuring the FSR of the cavity.

Cavity frequency response

As equation (4.2) suggests, a Fabry-Perot cavity behaves as a first-order low-pass optical filter for the light, characterised by a cavity bandwidth Ω_{cav} . Every low-pass filter is characterized by its cut-off frequency which can be deduced from the corresponding spectral response diagram, the Bode diagram. To do so, the light intensity is modulated via an AOM or an EOM and the cavity response is monitored at its output. In practice, we use a network analyzer driving an AOM which is driven by a voltage between 0 V (corresponding to 0% transmission) and 5 V (100% transmission). A home-made preamplifier is used in order to add a 5 V DC voltage to the network analyzer modulation output and then set the AOM at half-transmission. The cavity is then locked to the optical resonance and the cavity transmitted power is fed to the network analyzer input. The analyser executes a frequency sweep and directly provides the Bode diagram of the cavity.

3.2.2 High-finesse filtering cavity

The measurement Fabry-Perot cavity is a compact and rigid cavity, which provides no possibility to dynamically control its length. Therefore, in order to stabilize the experiment the laser frequency is locked to the cavity vibrations. On the other hand, this is not the case for the filtering cavity. The mirrors of the cavity are both coupled to piezoelectric actuators permitting to change the cavity length and therefore to lock the cavity on the laser frequency. Furthermore, the filtering cavity is placed between the laser and the measurement cavity. Consequently, the filtering cavity must be able to compensate the measurement cavity vibrations that are imprinted onto the laser frequency. The output of the filtering cavity (FPF) will be coupled to the measurement cavity (FPM) which will be locked to the laser. The laser frequency will then follow the length variations of the filtering cavity resulting in a frequency jitter with an amplitude of some hundreds of kHz. The FPF must then be able to compensate this frequency noise. Otherwise extra intensity noise will be induced to the output beam. The filtering cavity already mounted in the experimental setup (see Figure 2.2) has a very large frequency bandwidth (~ 4 MHz). This is why the effect is less apparent. On the other hand, if a small-bandwidth cavity is used, this frequency jitter can be very destructive. The worst-case scenario would be the complete impossibility of locking the high-finesse filtering cavity to the laser. The FPF cavity stabilization loop will then be a very important parameter. It will be realized with a standard PDH technique. There are two factors determining the performance of cavity stabilization: the cavity finesse and the bandwidth. A high-finesse cavity will be more sensitive to environmental vibrations, optical bistability effects can occur, and consequently the feedback loop will be more difficult to realize. At the same time, the narrower the bandwidth the more difficult it is to stabilize the cavity. The cavity we want to construct combines both characteristics. It must present a narrow bandwidth and, since the cavity length is limited to the available space on the optical table, a high-finesse. The right trade-off between these parameters have to be found in order to render the cavity stabilizations the most robust possible.

The above considerations resulted in the construction of two different cavities, both with very similar mounting systems but with different mirror qualities in order to find a different compromise between the optical finesse and the frequency bandwidth. The mode cleaner is conceived to be a symmetrical cavity ($T_1 = T_2$) so that all light is transmitted at optical resonance as equation 1.46 shows. Both cavities consist of one plane mirror mounted on a

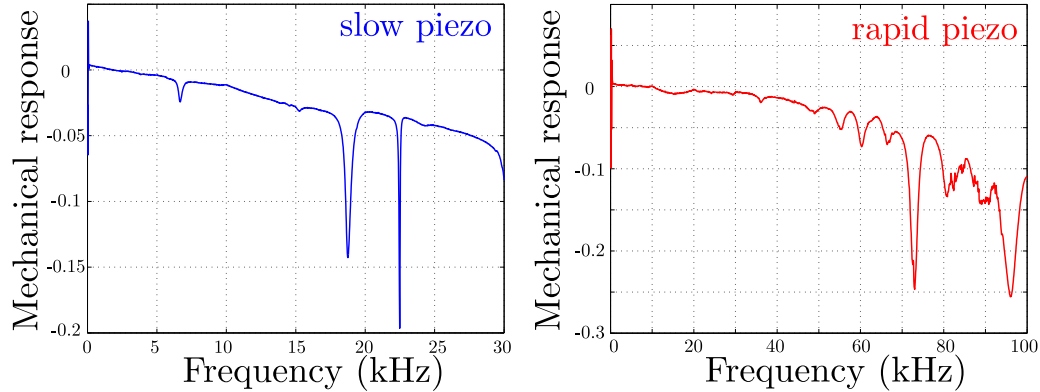


Figure 3.6: The mechanical resonances present to the filtering cavity mounting system: rapid piezoelectric actuator+clamp (left) and slow piezoelectric actuator (right).

stack of piezoelectric actuators (total length of 1 cm). The stack presents a large displacement travelling ($\sim 30 \mu\text{m}$), it is destined to work at low frequencies (some Hz) and to compensate the slow drifts of the cavity. The second mirror is a plano-concave mirror, presenting an IR coating on the curved surface, with a radius-of-curvature equal to 1 m. It is fixed on a small 1-mm thick piezoelectric actuator with a small displacement amplitude ($3 \mu\text{m}$) which will operate at high frequencies ($\sim 10 \text{ kHz}$). The mirrors have relatively small dimensions: a diameter of 7.75 mm and a thickness of 4 mm. This way, the mirrors will be lighter and therefore the cavity lock-in can be faster. All components were glued to the clamps of the cavity using a standard cyanoacrylide super glue. Special care has been taken in order to fully insulate the piezoelectric surface in order to avoid any contacts between the high voltage and the ground. Figure 3.6 depicts the mechanical system residual resonances which define the feedback loop bandwidth; no feedback at the mechanical resonances must be present otherwise, unavoidable resonances will occur, preventing proper operation of the cavity lock-in. We observe that the first resonances occur at 7 kHz and 50 kHz for the slow and rapid actuators respectively, high enough in order to realize an effective feedback loop.

The cavity is relatively long to ensure a small bandwidth. The alignment procedure can then be somewhat tricky. The cavity is very sensitive to the smallest mirror tilt. For a mirror with a radius curvature of 1 m, a tilt of 10^{-3} rad ($\simeq 0.06^\circ$) is equivalent to a beam offset of 1 mm with respect to the center of the mirror already making the alignment procedure impossible. The mirrors and the piezoelectric actuator being simply glued to the clamps it is certain that the two mirrors will not be parallel to each other. Small change to the orientation of the incident beam will be futile; either resonant modes will occur to the edge of the mirror inducing further losses or it will be absolutely impossible to find a cavity axis. The mirrors have thus to be perfectly parallel to each other. To do so, we have adapted a tilting system of the mirror based on either small springs mounted through the clamp screws or a elastic ring bringing in contact the clamp and the cavity tube. Both systems permit the tilting of the mirror by simply tightening or untightening accordingly the screws. In practice, we first ensure that the beam orientation is perfectly aligned to the cavity tube while both mirrors are unmounted. Then we mount the cavity end mirror. Normally the light should be reflected perfectly at the centre of the mirror. We tighten accordingly the screws until the reflection beam coincides with the

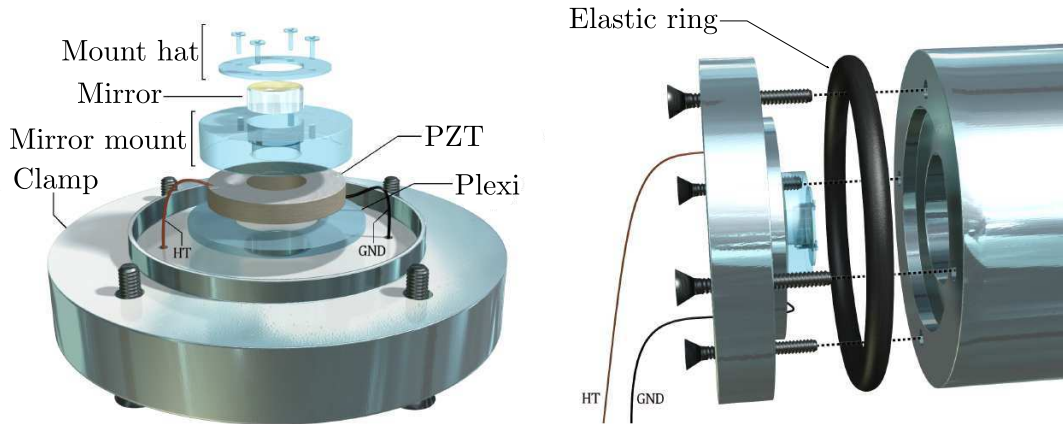


Figure 3.7: Left: the mirror is mounted into a plexiglas recipient which is glued onto a well-insulated, small and fast piezoelectric actuator. Right: the cavity clamps are mounted to the cavity cylinder via an elastic ring permitting to slightly tilt the mirror by tightening or untightening the screws.

incident one. Finally, we repeat the same procedure with the coupling mirror. Then a CDD camera may be used in order to observe the output of the cavity. Given the cavity small free spectral range, a fairly good alignment suffices in order to observe optical modes flashing at the output of the cavity as its residual vibrations naturally sweep its length. Fine adjustments of the beam orientation are made using the two mirrors in front of the cavity, to obtain a perfect coupling between the light and the cavity.

Cavity 1

The mirrors used for the first tested cavity were fabricated by *ATFilms* and present a transmission of 100 ppm with losses guaranteed lower than 10 ppm. The expected finesse with the combination of these mirrors is $\sim 30\,000$. Both mirrors are mounted on an invar cylinder which determines the cavity length. The tube length is 20 cm which means that the expected bandwidth of the cavity is 1 kHz. Once the alignment protocol is performed we can proceed to the characterization of the cavity. As expected, this cavity presents dynamical ringdown effects to the right side of the Airy peak preventing standard optical calibration by comparison of the width of the resonance to the Pound-Drever sidebands. Figure 3.8 shows the cavity transmission for various sweep speeds. The cavity finesse can be determined by simply determining the ratio of the first two maxima I_1/I_2 of the oscillations and their corresponding time interval $\Delta t = t_2 - t_1$. For each measurement the theoretical fit has been applied using equation (3.15). Each measurement gives a finesse value around 24 000. In order to take all measurements into consideration one can draw the Δt evolution versus I_1/I_2 . According to [81] this dependence is approximately linear, with a slope directly giving the optical finesse of the cavity. Figure 3.9(a) shows this evolution. The linear fit gives $\mathcal{F} = 24000$, resulting in a bandwidth $\nu_{BP} = 20$ kHz. The alternative calibration methods have also been applied in order to verify the bandwidth measurement, both giving a value close to 20 kHz. The newly constructed balanced detection was used to observe the beam photon noise exiting the cavity. The measurement consists in comparing the sum and the difference of the two photocurrents. The balanced detection in

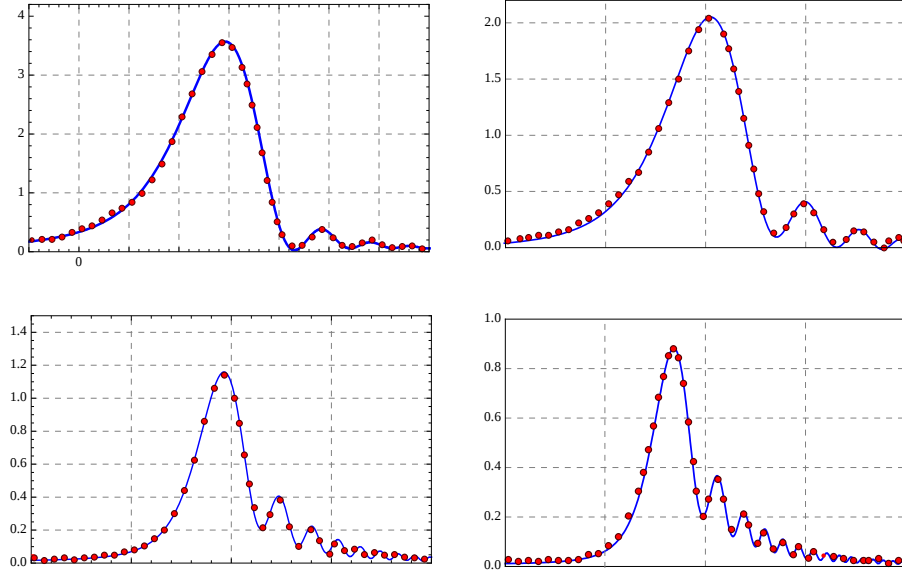


Figure 3.8: The cavity transmission for various sweep velocities 10 Hz, 50 Hz, 110 Hz and 200 Hz. We observe the ring-down effect at the right side of the Airy peak under the form of successive rebounds. The position and amplitude of these rebounds give access to the bandwidth of the cavity. We have made use of equation 3.15 to fit the measurements. They correspond to a finesse of 24 000 and to mirror velocities of $2.3 \mu\text{s}$, $1.6 \mu\text{m/s}$, $0.57 \mu\text{m/s}$ and $0.16 \mu\text{m/s}$.

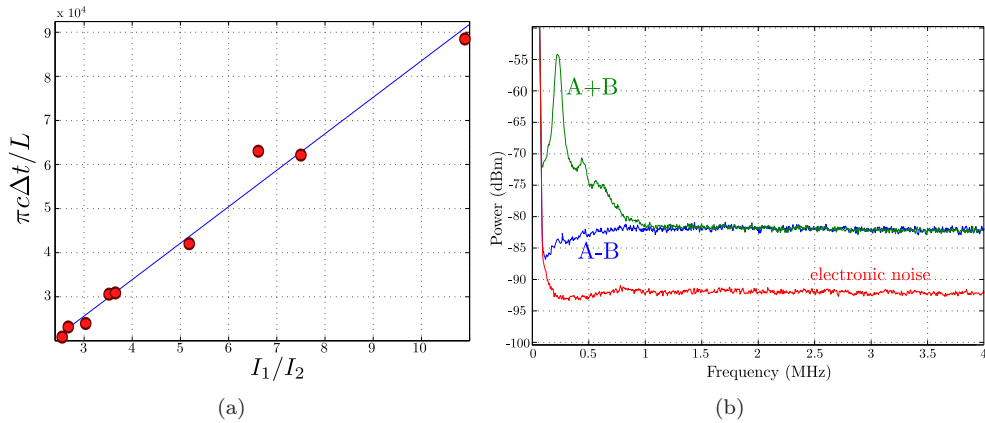


Figure 3.9: (a) For various velocity sweeps the time interval between two maxima is plotted as a function of their ratio. A linear approximation [81] of this dependence may provide an estimation of the finesse of the cavity. (b) A+B and A-B output of the balanced detection for an input power of 20 mW.

the difference mode will naturally suppress all classical noise leaving only quantum noise. By switching to the summing mode, and comparing it to the difference one, we can determine if the light is quantum-noise limited at the frequencies we are interested in. Figure 3.9(b) shows the balanced detector output for a beam at a 20-mW optical power. We observe the low-frequency

classical laser noise up to 1 MHz. The low-frequency modulation peak corresponds to a feedback loop oscillation. At frequencies greater than 1 MHz, no classical noise is evident, indicating that the beam is quantum-noise limited at 20 mW above 1 MHz.

The main objective is accomplished with this filtering cavity: a quantum noise limited laser beam at 1 MHz, with a power well above 10 mW, is obtained. At the same time, this cavity presents a transmission coefficient which is surprisingly low, $T = 15\%$, while the cavity is supposed to transmit all incident light. This normally poses no problem as it suffices to increase the input power in order to have enough power at the cavity output. However, optical bistability effects pose an input threshold power above which the cavity lock-in becomes impossible. For this cavity, the maximum power at its output is 15 mW. This power is more than the 10 mW we plan to inject into the measurement cavity. However, if additional optical losses, occurring during the beam propagation caused while the beam is propagated towards the cavity, are taken into account, 15 mW is not enough. Two things may explain this disappointing result: either the cavity is not really symmetric or optical losses are greater than expected. In order to determine this the mode matching and the reflection coefficient are necessary. It will then suffice to use equation 1.46, 1.30 1.41 to completely characterise the cavity. A mode matching $\nu_{cav} = 95\%$ and a reflection coefficient $\mathcal{R}_0 = 50\%$ are obtained. We then get for the transmissions of the two mirrors $T_1 = 950$ ppm $T_2 = 2000$ ppm. The losses are estimated to $P = 350$ ppm. Evidently, the purchased mirrors were not sufficiently balanced resulting to a low transmission.

Cavity 2

We have also tested a second Fabry-Perot cavity. In the past, the Ti:Sa laser was frequency stabilized with the help of a reference cavity (FPE) [31] which became practically useless once the measurement cavity was locked to the laser source via a Pound-Drever technique. This reference cavity presents an announced bandwidth $\nu_{BP} = 200$ kHz, that might sufficiently filter the laser beam for our needs. The mirrors of the FPE were unmounted from their previous mounting system and remounted onto an invar tube of length $L=30$ cm. The configuration is strictly the same as the first cavity. The mirrors used were purchased from Research Electro Optics and present a theoretical transmission of 2000 ppm each. The expected finesse is $\mathcal{F} = 1600$ and the expected bandwidth is $\nu_{BP} = 200$ kHz. For this cavity no dynamical ringdown effects were apparent. The standard calibration technique could then be applied by comparing the Airy peak width to the sidebands, in this case at 12 MHz. The Lorentzian fit in figure 3.10(a) gives a value of 1500 for the finesse, which for a cavity length $L=30$ cm gives a bandwidth of 100 kHz. In addition, we have checked the above value by measuring directly the cavity bandwidth and by performing ringdown technique described earlier (see figures 3.10(b) and 3.11(a) respectively). Finally, as seen in figure 3.11(b), with this cavity, we also obtain a quantum-noise limited laser beam at 10 mW, at 1 MHz. This cavity presents a transmission $T = 70\%$ and a reflection coefficient $\mathcal{R}_0 = 77\%$. For a mode matching $\nu_{cav} = 95\%$ we get mirror transmission $T_1 = 1000$ ppm and $T_2 = 2000$ ppm.

The first objective is largely accomplished. We have at our disposal two different cavities providing a quantum-noise limited beam of 10 mW. We will try a comparison between the two. Cavity 1 presents a bandwidth almost one order of magnitude narrower than cavity 2 (20 kHz over 100 kHz). Naturally, the narrow cavity comes with a much larger finesse (20 000 over 2 000). It is clear that the first cavity will present more locking difficulties. Even if cavity 1 filters much better the Ti:Sa classical noise, at the same time it presents major drawbacks. The

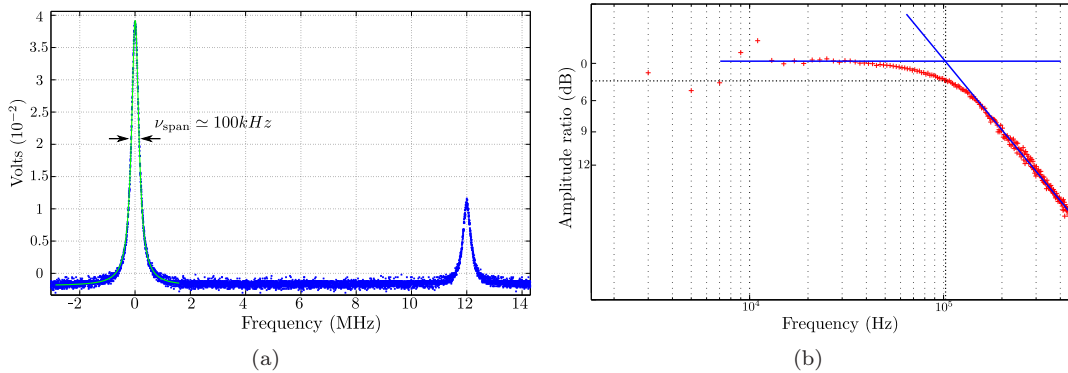


Figure 3.10: (a) The Airy peak of the second filtering cavity in transmission. We observe the carrier and the Pound-Drever sideband at 12 MHz. A lorentzian fit of the Airy peak gives the bandwidth of the cavity. (b) Direct measurement of the cavity response to an intensity modulation applied via an acousto-optic modulator. We obtain a standard low-pass filter behaviour with a cut-off frequency at approximately 100 kHz.

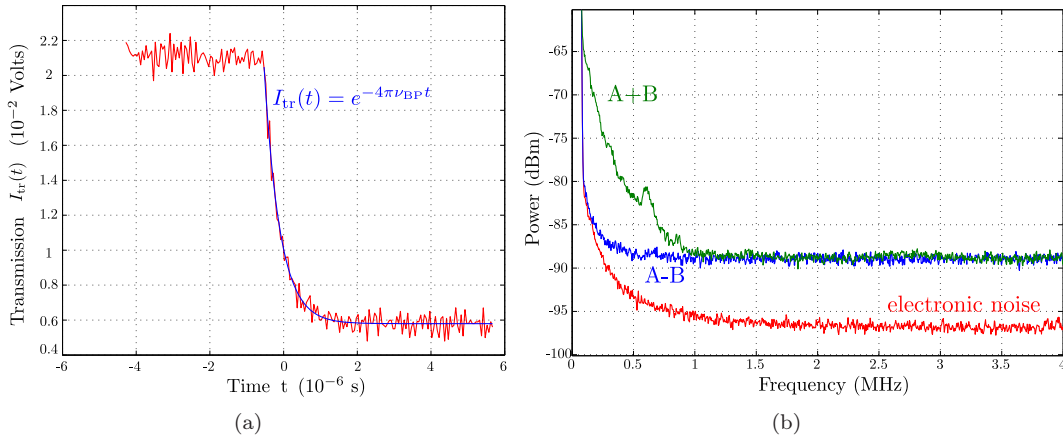


Figure 3.11: (a) Optical ringdown: direct photon lifetime measurement by abruptly turning off the light power. The exponential decay characteristic time directly gives the bandwidth of the cavity. (b) A+B and A-B output of the balanced detector for an input power of 13 mW.

very low transmission coefficient (15% versus 70% for cavity 2) is an important inconvenience. The lock-in of the filtering cavity alone is very much possible but it is extremely sensitive to vibrations. So sensitive that when working on the optical table -while the cavity is locked- extreme care has to be taken: violent manipulations cannot be tolerated by the cavity. This is a natural consequence since this cavity has a very high-finesse and a very narrow bandwidth. For the sake of experimental easiness we have chosen the 100 kHz cavity.

3.2.3 Cavity lock-in

To lock the cavity, a Pound-Drever method was used. The main advantage of the PDH technique is its large capture range defined by the sidebands created by the phase modulation. It is

preferable to obtain a capture range as large as possible. There is a limit however imposed by the cavity bandwidth. If the bandwidth Ω_{BP} is very small compared to the phase modulation frequency Ω_{PM} the error signal in the frequency range between the cavity bandwidth and the sidebands drops to zero and the capture range is lost. For this reason, the 20 kHz cavity was locked using a Pound-Drever signal generated at 3 MHz using a non resonant electro-optic modulator while this was done for the 100 kHz cavity using a resonant modulator at 12 MHz.

The electro-optic is placed before the two mirrors used to inject the light into the cavity. The second one presents a transmission coefficient equal to 10%. A portion of the reflected light from the cavity is then captured by a custom-made rapid photodiode, with an HF output (up to 50 MHz) and a DC output (up to some kHz). The high-frequency output of the photodiode is then used to detect the 3 MHz or 12 MHz modulation and to create the error signal, using a home-made demodulator. The servo-loop used to lock the cavity to the laser frequency drive both piezoelectric actuators of the cavity. For this the error signal is split into two channels, a HF channel and a LF channel, using a simple RC passive filter. The cut-off frequency is typically a few hertz. This way a slow and a rapid component are defined. The LF channel drives the stack of piezoelectric actuators and can compensate cavity drifts with frequencies up to some Hz and the fast channel drives the small piezoelectric actuator and is used to compensate the fluctuations up to some dozens of kHz, only limited by the resonance frequency of the piezoelectric actuator.

Proportional-Integral gain electric circuit

The group has developed a custom-made Proportional-Integral (PI) gain electrical circuit composed of two integrator stages where all necessary separation filters are already implemented. Inspired by this concept we have adapted the existing electric circuits in order to better suit for a double-channel, servo-loop cavity (or laser) lock-in. We have constructed a similar circuit for the high-finesse filtering cavity. A simplified version of the PI circuit is drawn on Figure 3.12. The error signal is injected into the input of the circuit via a 50Ω impedance. It first passes through an inversion stage of amplification with a gain $g=5$. The second stage adds a proportional or an integrator gain; a switch permits allows to choose between both modes. The proportional gain helps to find a good gain configuration before switching the integrator on. Once the integrator is turned on the amplification stage behaves as an active low pass filter, its spectral response presenting a 6 dB/octave slope (G1). It is a global gain. The error signal is the split into a slow and a rapid one. A simple RC circuit acts like a passive low-pass filter, with a cut-off frequency $f_c = 1 \text{ Hz}$. The high-frequency part then goes through another amplification stage. It is essentially another integrator stage with a switch permitting to short-circuit the feedback capacity and transform the amplification stage from a simple proportional gain mode to an integrator mode. The feedback resistor, always active, allows the stage to act in proportional mode up to a certain frequency defined by the cut-off frequency $f_c = 1/(2\pi RC)$. The global circuit response up to f_c is a combination of the two amplification stages and always presents a 6 dB per octave slope. On the other hand, at high frequencies ($f > f_c$) both stages behave as pure integrators resulting in a 12 dB/octave slope. This concept provides a high gain at low frequencies. Typically, it is desirable for the slow part to act at frequencies up to 10 Hz while the fast part is active from 10 Hz up to a limit frequency defined by the piezoelectric resonance. The 6/12 dB point is thus defined by the frequency resonance of the piezoelectric actuator. The high-frequency part of the error signal fed back to the system must be sufficiently

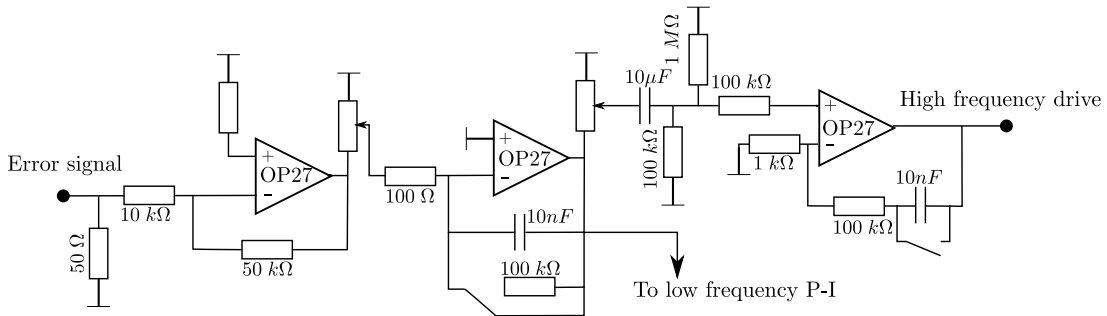


Figure 3.12: The proportional-integral gain circuit (simplified version). The error signal is first proportionally amplified. A second stage follows which may operate as a pure, global integrator. A passive RC filter then separates the error signal in two components. The rapid component goes through a second integrator stage thus attributing to the circuit response a 6/12 dB slope. The low-frequency component is sent to a similar integrator stage.

dumbed in order not to excite the piezoelectric resonance. The final part of the circuit consists of two supplementary amplification stages. One acts either as an inverting or non-inverting amplifier permitting to change the global phase by π . The other is simply a summing amplifier; it adds to the output signal a supplementary modulation signal called "modulation in", used either to modulate the piezoelectric actuator and visualize the cavity Airy peak or to test the response of the servo-loop. The slow part of the circuit is strictly identical to the fast one; the only difference being that it acts on a slower frequency range. The network analyzer was used to perform some diagnostic tests of the circuit. The output of the analyzer is injected into the circuit via the *modulation in* input. The output signal is monitored by the analyzer while it is also re-injected at the input of the circuit. We can thus test if the circuit compensates the injected perturbation. Two tests were performed, one for each channel. Figure 3.13 depicts the Bode diagram for the slow and rapid part. The perturbation is re-injected into the circuit, the gain is progressively increased while the network analyzer is sweeping its response. Figure 3.13 shows the Bode diagram for the fast channel. By progressively increasing the rapid gain we obtain a better noise rejection up to 50 dB. After that the oscillation regime is achieved (black curve). The second stage integrator acts as a low-pass filter as well. This is why an apparent performance degradation occurs at high frequencies.

3.2.4 Implementation of the filtering cavity

To implement the cavity into the experimental setup efforts were made to make as few changes as possible. The filtering cavity being relatively long, the displacement of the old filtering cavity was imperative. This would mean that both the measurement and the filtering cavities would have to be rematched. The implementation of the cavity is drawn in figure 3.14(b). The mirror reflecting the light towards the pump beam AOM of the double injection (3.14(b)) is replaced with a polarizing beam splitter (PBS1). The beam reflected by PBS1 is injected in the double-pass setup of AOM2 and thanks to a $\lambda/4$, when the beam comes back to PBS1 it has a polarization perpendicular and is therefore transmitted towards the new mode cleaner. Two mirrors are used to align the laser beam to the cavity. Just before the first mirror the

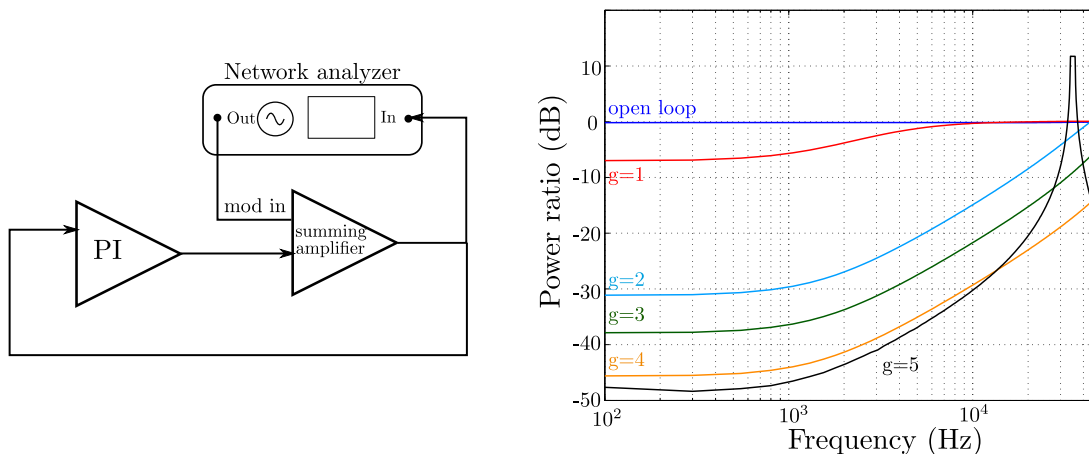


Figure 3.13: The Bode diagram of the home-made PI circuit showing a 50 dB compensation as the feedback loop gain is increased (yellow).

resonant EOM is mounted on a micrometric stage adjusting its height and its lateral position. The reflection of the cavity is partly transmitted by mirror M and is monitored by a fast photodiode. A system of two lenses is used to match the laser beam to the cavity. The cavity has a length of 30 cm and the plane concave mirror has a radius of curvature of 1 m. By applying equation 1.47 we find that a waist of $300 \mu\text{m}$ has to be placed onto the plane cavity of the mirror. The standard procedure to match a cavity consists in using two thin lenses. Given an initial waist size and position on the table, it usually requires 2 thin lenses to obtain a new waist with the right size and position. In order to do our calculations and estimate the focal values and position of the two thin lenses a beam profiler (THORLABS) was used to measure the waist after the thin lens L. The waist meter gave a waist, w_0 , of $100 \mu\text{m}$ 12 cm after the thin lens. We used this value in order to estimate the system of thin lenses to match the incident beam and the cavity. In practice, there are a lot of error sources affecting the precision of the waist measurement: the estimation of the position of the measured waist may present an imprecision of at least 1 cm, the accuracy of the announced focal of the thin lens can also be an important error to the final calculation. For this, while we initially choose the lenses based on a theoretical calculation we match the cavity empirically. We apply a large sweep to the stack piezoelectric of the cavity in order to visualize a full Free Spectral Range with the digital oscilloscope. Then, by playing with the alignment mirrors M_x and M_y we deduce what changes have to be made in order to increase the mode-matching coefficient n_{cav} . If odd modes are apparent it means that the M_y alignment is not optimal. On the other hand, if even modes are apparent it means that the beam waist does not have the right size or z-position. In this case the optimization implies the change of the lens position. A mode matching of 95% was obtained for this cavity. All losses essentially are in the TEM_{02} mode, which means that the waist of the beam is not optimal. However, 95% of mode matching for a filtering cavity is very satisfying.

The position of the new cavity was blocking the probe beam propagation. The two mirrors injecting the light into the old filtering cavity had to be moved. Efforts were made to displace the mirrors in such a manner so that the beam optical path stays unaltered. However, once the

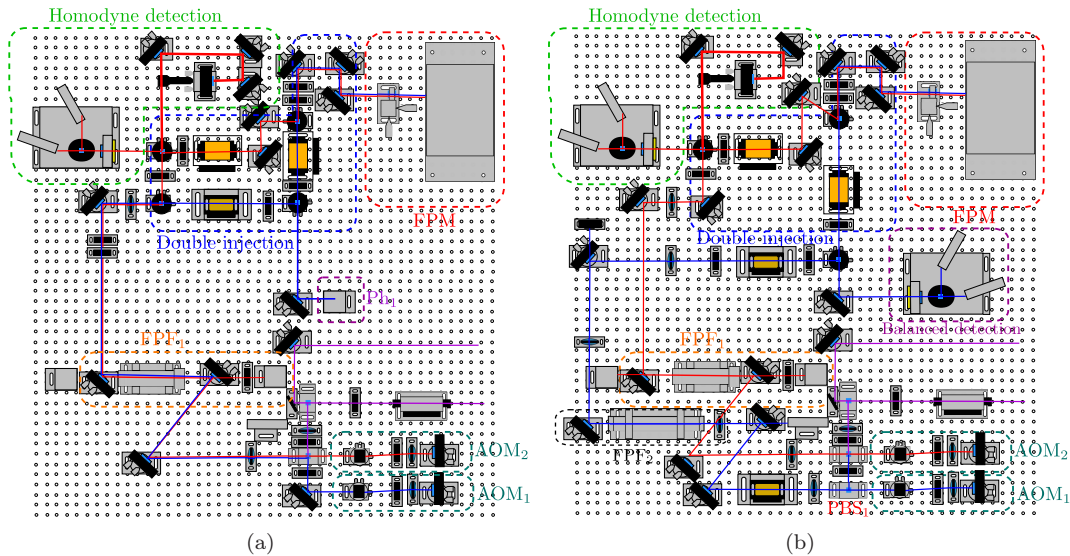


Figure 3.14: A realistic representation of the optical table before (a) and after (b) the implementation of the high-finesse filtering cavity.

alignment procedure was done the cavity was matched by placing a thin lens with focal $f=200$ mm at a distance $d=25$ cm from the previous waist situated into the AOM of the pump beam ($w_0 = 120 \mu\text{m}$). We obtained a mode matching of 95%.

Once both cavities were functional (aligned and matched), we checked the mode matching of the measurement cavity. Indeed, the implementation of the new filtering cavity proved very destructive for the mode matching of the measurement cavity: we measured a $n_{\text{cav}} = 80\%$. Given the importance of the mode matching of the measurement cavity -an imperfect mode matching deteriorates the sensitivity- an improvement was imperative. The measurement cavity has a very large free spectral range making the matching procedure difficult since all resonant modes cannot be visualized at the same time. Instead the laser frequency has to be tuned back and forth to visualize the transverse modes. In practice, once the estimated thin lenses are placed and the cavity is aligned we observe on the oscilloscope the first two transverse mode (TEM_{01} and TEM_{02}). Normally, the 01 should be very small whereas an important portion of the light should be coupled to the 02 mode, demonstrating a bad location of the waist. We adjust the position of the waist by moving the thin lens and we repeat the process until a good matching is obtained. In our case, each beam having a slightly different optical path, a different system of thin lenses on each beam path helps for the mode matching of the filtering cavity. Finally, we obtain a mode matching of 98% for both beams.

3.2.5 Difficulties met while implementing the high-finesse filtering cavity

The principle of a feedback stabilization loop is to modulate the laser frequency for instance around the resonance of the cavity. This modulation will be transformed into an intensity modulation which will be detected and demodulated in order to generate an error signal which is

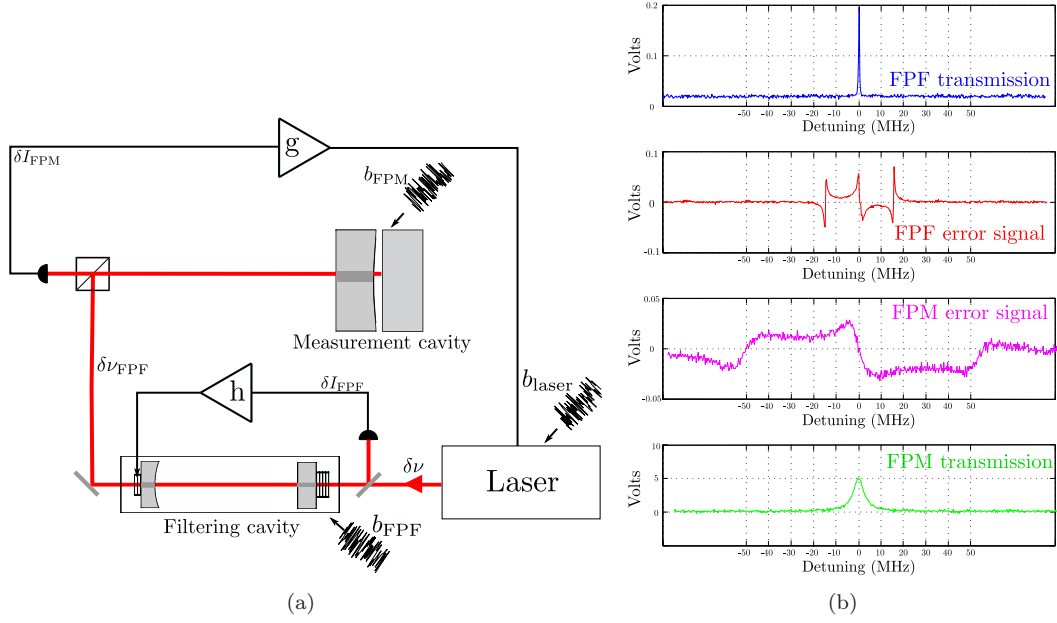


Figure 3.15: (a) The problem posed by the implementation of the high-finesse filtering cavity. The measurement cavity vibrations b_{laser} are imprinted into the laser frequency vibrations $\delta \nu$. These vibrations result into a corresponding detuning $\delta \nu_{\text{FPF}}$ of the filtering cavity. (b) The transmission of both cavities with their corresponding error signals.

essentially a derivative of the Airy peak whose amplitude is proportional to the cavity detuning and whose phase varies by π around the maximum of the peak. In our case, two different cavities -measurement and filtering cavity- are coupled in series and both of them require a feedback loop in order to be stabilized at the same time. For the current experimental setup, the feedback loops we tested and their configuration are depicted in figure 3.15(a). We denote b_{laser} , b_{FPF} and b_{FPM} the equivalent frequency noise of the laser, the filtering cavity and the measurement cavity respectively. The laser frequency undergoes a global feedback loop resulting in a frequency noise $\delta \nu$ equal to:

$$\delta \nu = b_{\text{laser}} - g \delta I_{\text{FPM}}, \quad (3.17)$$

where δI_{FPM} is the detected intensity modulation, g is the feedback loop gain and b_{laser} the residual laser noise. In the ideal case where no filtering cavity is present and the feedback loop gain tends to infinity ($g \rightarrow \infty$) the laser frequency jitter would only include the measurement cavity vibrations: $\delta \nu = -b_{\text{FPM}}$. Since the term δI_{FPM} is proportional to the residual fluctuations of the measurement cavity, it is obvious that these fluctuations are imprinted to the laser frequency fluctuations $\delta \nu$. On the other hand, the filtering cavity is stabilized locally thanks to the two piezoelectric actuators mounted on its mirrors which controls its length:

$$\delta \nu_{\text{FPF}} = b_{\text{FPF}} - h(\delta \nu - \delta \nu_{\text{FPF}}), \quad (3.18)$$

h being the local loop gain. This equation implies that the local feedback loop of the filtering cavity must be able to compensate both its residual vibrations and the measurement cavity vibrations. In particular, the residual jitter of the Ti:Sa laser is $b_{\text{laser}} \simeq 10$ kHz. Both filtering and measurement cavities present a high-finesse (2000 and 100 000 respectively) so they are expected to be more sensitive to environmental vibrations than the laser cavity. A rough estimation of their residual vibrations can be done empirically, by manually controlling the laser frequency on their optical resonance and observing the rapid fluctuations around it. By comparing these fluctuations to the known bandwidth of each cavity one can estimate the residual jitter. In our experiment, we can manually maintain the laser frequency within the bandwidth of the cavities. Therefore, we can assume that the filtering cavity noise is $b_{\text{FPM}} \simeq 50$ kHz while the measurement cavity noise is $b_{\text{FPM}} \simeq 1$ MHz.

Until now we have used a filtering cavity whose bandwidth is comparable to the one of the measurement cavity. In particular, the mode-cleaner bandwidth is $\Omega_{\text{FPP}}/2\pi \simeq 4$ MHz while the measurement cavity has $\Omega_{\text{FPP}}/2\pi \simeq 1$ MHz. When the measurement cavity servo-loop is working, a non-zero “jitter” of some dozens of kHz is not compensated. As the mode-cleaner is large compared to the measurement cavity this jitter is negligible and the $\delta\nu$ term in equation 3.18 may be neglected. However, as figure 3.15(b) illustrates, this is not the case for the new high-finesse filtering cavity with a bandwidth of 100 kHz.

Therefore, the high-finesse cavity having a very low bandwidth cannot compensate the frequency jitter induced to the laser once the measurement cavity is locked. In particular, the filtering always stays in the capture range of the lock in technique, largely thanks to the large Pound-Drever error signal capture range and the good feedback loop quality at low frequencies driving the stack piezoelectric actuator. On the other hand, the small, rapid piezoelectric actuator cannot compensate the rapid measurement cavity vibrations which have very large amplitudes compared to the mode cleaner bandwidth. This is actually the reason for having tested two different cavities. We were first confronted to this problem while testing cavity 1 ($\nu_{BP} = 20$ kHz). The impossibility of locking both cavities at the same time led us to cavity 2, the larger frequency bandwidth ($\nu_{BP} = 100$ kHz) of which might make this effect smaller. Unfortunately, this was not enough. Neither of the high-finesse filtering cavities could be locked at the same time with the measurement cavity. To solve this problem, several solutions were suggested: a feed-forward loop in order to help the local feedback loop to properly stabilize the filtering cavity, the construction of new measurement cavity in which a rapid piezoelectric actuator is implemented and the use of an acousto-optic modulator to make the two loop completely independent.

3.2.6 Feed-forward stabilization

The first idea we had in order to solve this problem was to apply a feed-forward stabilization technique whose principle is depicted in Figure 3.16. It consists essentially in using the error signal of the measurement cavity (derived by the Pound-Drever-Hall scheme, both to drive the laser frequency and also to inject it into the feedback loop used to stabilize the high-finesse filtering cavity. If the feed-forward is made with the right amplitude and phase, the feed-

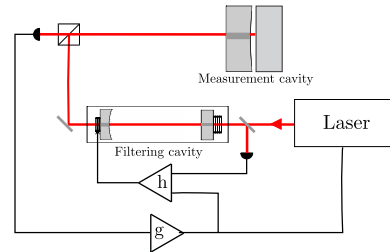


Figure 3.16: Principle of the feed-forward stabilization technique.

back of the filtering cavity only has to compensate its residual noise b_{FPF} and not the noise b_{FPM} of the measurement cavity. An additional experimental difficulty is due to the fact that pump beam is used to create the error signal of the measurement cavity. For this, we have decided to use the homodyne detection to generate the error signal. We will start this section by describing the changes made to the homodyne detection.

3.2.6.1 Homodyne detection changes

The changes realized to the homodyne detection were made at two levels: the photodiodes and the summing/subtracting circuit.

Photodiodes

First, having realized that the homodyne detection photodiodes (FND100) presented a mediocre quantum efficiency mainly due to time deterioration -we have measured it to be 73%- we have decided to replace them with new ones. Since we have already constructed new photodiode amplifiers for the balanced detection, we simply adjusted the existing electronics for the homodyne detection. We have then constructed a second set of photodiodes to replace the old ones. However, the photodiodes requirements for the homodyne detection are somewhat different. The homodyne detection consists of the Local Oscillator whose power is relatively high (~ 10 mW). Therefore, there is no need for the homodyne detection to possess very sensitive photodiodes since each photodiode will receive typically ~ 6 mW of light power. The only requirement is to ensure that the saturation level is high enough. We have then chosen to use a simplified version of the balanced detector photodiodes. The same Hamamatsu Si PIN S5971 were used presenting a quantum efficiency of 93% as well as the same low-noise, rapid OPA067 operational amplifiers. Two visible differences exist to the new photodiodes as opposed to the balanced detector ones. First, the second amplification stage of the RF part no longer exists since the signal is already strong enough at this stage. This change also dramatically increases the bandwidth of the photodiode since the operational amplifier AD844 is the one who essentially limits the bandwidth. In particular for the new photodiodes we obtain bandwidths of over 100 MHz. A Pound-Drever error signal may then be easily obtained. The second change consists in the careful choice of the load and feedback resistors R_{load} and R_{fb} in Figure 3.17(a) depicting the photodiodes electronic design. We have chosen these values in order to obtain saturation levels well over 10 mW. The balancing procedure described above for the balanced detection was applied to the new homodyne detection as well.

Pound-Drever-Hall error signal generation

The generation of the error signal using the probe beam and the homodyne detection raises some questions and problems. First of all, the actual electronics accompanying the optical detection provide the possibility to acquire either the intensity quadrature or the phase quadrature of the light via a commutator switching the circuit to either a summing or differential mode. In order to generate a Pound-Drever error signal and at the same time to detect the mirror displacements the electronic circuit must be adapted in order to obtain at the same time both the subtraction and the addition of the two signals. A new electronic circuit was thus designed. Figure 3.17(b) shows the drawing of the electric circuit. It consists of two parallel amplification stages, one cabled as a summing amplifier and the other one as a differential amplifier, both

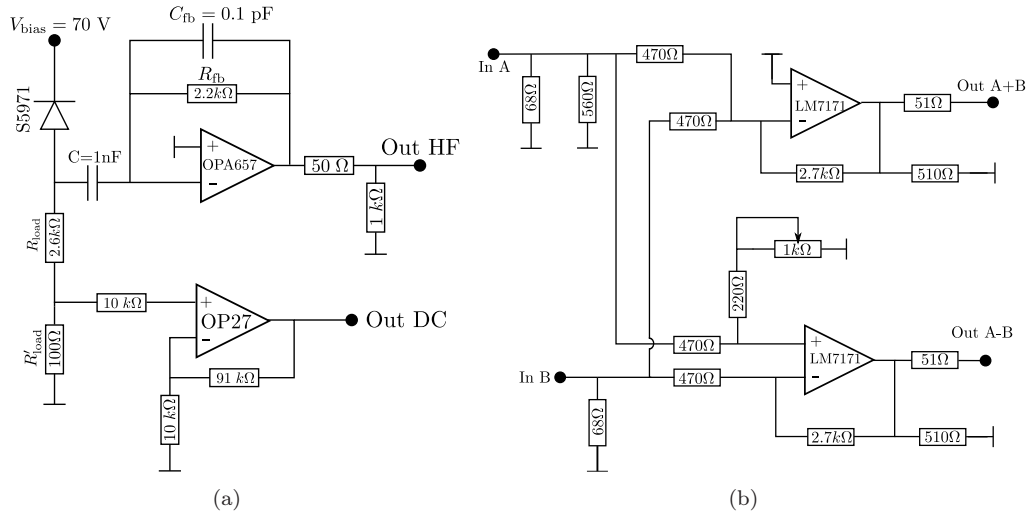


Figure 3.17: (a) The pre-amplifier circuit used for the homodyne detection photodiodes. (b) The electronic design of the circuit providing the addition and the subtraction of two signals A and B at the same time.

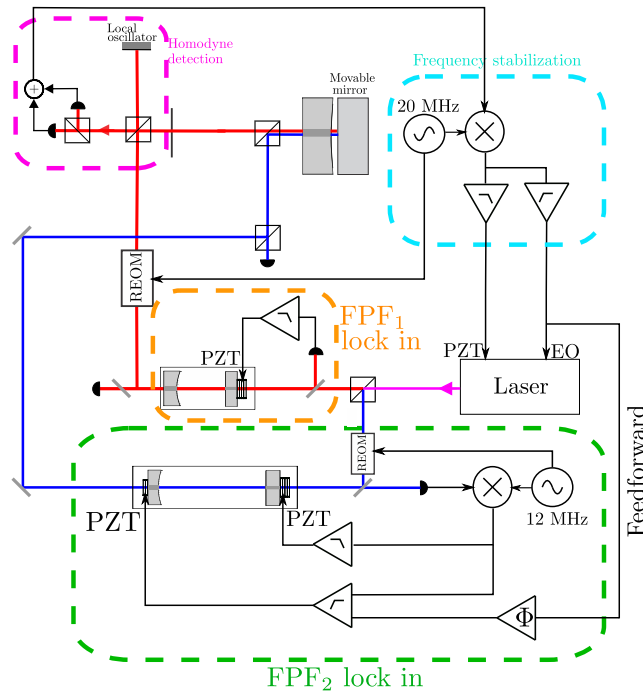
having a gain equal to 5. The operational amplifier used is the high speed LM7171 presenting a unity gain at 200 MHz. As explained in the first chapter the A+B stage provides the intensity of the input beam while the A-B provides the phase. The A+B signal will be demodulated in order to provide the error signal while the A-B will directly provide the displacements of the mirror.

The resonant electro-optic modulator used to create the sidebands of the input field is placed before the input beam separating into the Local Oscillator and the probe beam. Therefore, the Local Oscillator is also phase-modulated. The presence of a local oscillator in the homodyne detection adds a small difficulty to the Pound-Drever technique. In principle, even though the local oscillator is phase modulated the error signal should not be affected at all. However, we have observed that once the experiment is locked, the fluctuations, visible on the error signal used to lock the local oscillator length, were imprinted onto the Pound-Drever signal of the measurement cavity. In fact, this should be expected: the local oscillator movement should be detected by the Pound-Drever-Hall technique. Indeed, the local oscillator carrier interferes with the sidebands of the probe beam making the error signal sensitive to the local oscillator movement. This is an important imperfection if this error signal is used to lock the pump beam as we have described in the previous chapter how the movable mirror displacement contaminates the intensity quadrature of the pump beam.

Experimental procedure

In order to correctly realize the feed-forward loop, the signal must be properly phase-shifted and possess the correct amplitude. When we want to modulate the frequency of the laser and visualize the Airy peak of the measurement cavity, we do so by applying a 100-Hz sweep to the piezoelectric actuator of the laser ring cavity. In addition, a phase shifter is used in a feed-forward scheme to help locking the filtering cavity while the measurement cavity is swept. We decided to use the same phase-shifter in order to assist the lock-in of the new high-finesse

Figure 3.18: Experimental demonstration of the feed-forward stabilization technique helping the stabilization of the high-finesse filtering cavity. The probe beam is used to generate a Pound-Drever error signal for the measurement cavity. First, the probe beam frequency is locked to the resonance of the measurement cavity. The rapid output of the FPM servo-loop is then injected in the auxiliary input of the filtering cavity loop via a home-made phase-shifter with an independent gain.



filtering cavity. This phase-shifter, however, is built especially for a monochromatic signal at 100 Hz. As it is time-consuming and not straightforward to design a wideband phase shifter we decided to use this circuit unchanged for our purposes; the feed-forward will not be perfect but still sufficient to lock the cavity.

The corresponding experimental setup is drawn in Figure 3.18. The old filtering cavity is locked onto the laser frequency via a lock-in technique described in the introductory chapter. A 50-MHz resonant electro-optic modulator is installed in the probe beam. The A+B output of the homodyne detection monitors the intensity of the probe beam which is demodulated to provide the error signal of the measurement cavity. The error signal is then split into a LF channel and a RF channel, driving, respectively, the piezoelectric actuator and the internal electro-optic modulator of the laser. The high-finesse filtering cavity also presents two piezoelectric actuators used to modify the cavity length. To realize the feed-forward loop, the output of the servo-controller, controlling the electro-optic modulator, is sent via the 100-Hz phase-shifter to the auxiliary input of the rapid piezoelectric actuator servo-controller. Once the resonant electro-optic modulator (50 MHz) is installed and all cavities are aligned, we visualize on a digital oscilloscope the error signals of both cavities (see figure 3.15(b)). A typical locking sequence of all cavities is presented in Figure 3.19. The high-finesse filtering cavity lock-in is independent from the measurement lock in cavity so that the experimental protocol may be started by locking the measurement cavity (FPM - third and fourth graphs). During the first 28 seconds, the measurement cavity is not locked but stays in its capture range. When the feedback loop gain is turned on the laser frequency immediately is stabilized in the measurement cavity resonance. After 30 seconds, the loop gain of the filtering cavity (two upper graphs) is also turned on. Immediately, the loop is working well but the frequency jitter of the laser induced by the measurement cavity lock-in is not compensated and the filtering cavity does not

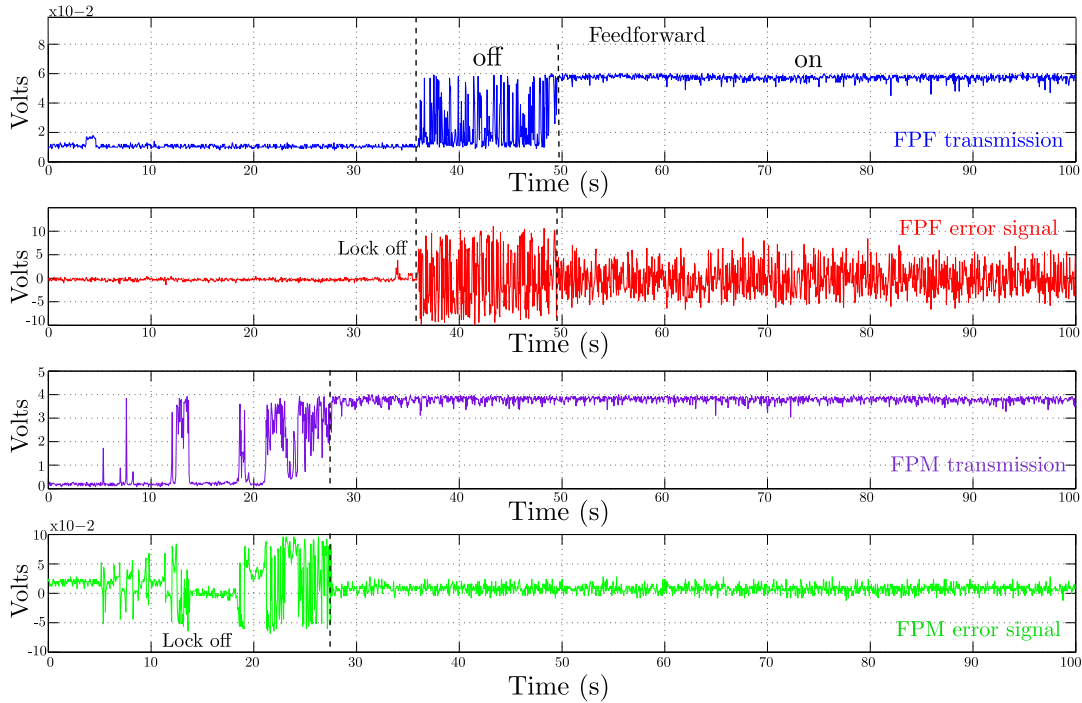


Figure 3.19: Experimental demonstration of the feed-forward technique. A lock sequence of 100 seconds is displayed. First the measurement cavity is locked (FPM). When locking the filtering cavity (feed-forward is in off position) -using the great capture range of the Pound-Drever error signal we observe the great amplitude of the laser jitter which is not compensated by the FPF servo-loop. Finally, the feed-forward gain is turned on and the filtering cavity transmission is stabilized.

stay at resonance. Instead, we may observe these vibrations both on the error signal (red) and the transmission of the cavity (blue). Finally, after 50 seconds, the feed-forward gain is also turned on. The working point of the cavity then stays at maximum transmission. Nevertheless, even if the fluctuations visible on the error signal are compensated by a factor almost 2, there are still some residual fluctuations due to the fact that the phase-shifter we have used is not ideal for our purpose. Indeed, the optimal configuration we have found for the phase-shifter corresponds to a phase-shift equal to π meaning that the phase-shifter is working simply as inverting amplifier only compensating other inverting amplifier found in the feedback loops. We thus have not exhausted the potential of this technique. This gave us motivation to test an acousto-optic modulator in order to stabilize the laser frequency onto the measurement cavity.

3.2.7 Use of an Acousto-Optic Modulator

In modern table-top, optics experiments, an acousto-optic modulator may be used for a number of applications such as laser beam deviation, intensity modulation or frequency shift of the beam. In the first chapter we have described the use of two acousto-optic modulators as an essential part of our double-injection setup. They are used to induce a static frequency shift between the intense and the probe beam, thus compensating eventual birefringence effects of

the measurement cavity. We can take advantage of the same experimental scheme in order to stabilize the laser frequency of a laser beam onto the resonance of a cavity by dynamically altering the RF modulation driving the acousto-optic modulator. Then, by implementing the acousto-optic after the high-finesse mode-cleaner cavity all cavities would become operational at the same time.

Two main advantages come with this technique. First, the high-finesse cavity would obviously no longer have stabilization issues and the feed-forward scheme, significantly raising the experimental difficulty, would no longer be necessary. Second, the acousto-optic presents a fast spectral response which would permit a feedback bandwidth in principle up to the MHz, in principle. On the other hand, it presents quite small frequency-shift capabilities. Therefore, for slow drifts with great amplitude this system is not convenient and should be replaced with a transducer with a low-frequency response but with great amplitude displacement, such as a piezoelectric stack.

The major experimental difficulty when using an acousto-optic for this purpose is the cancellation of any possible pointing noise that would lead to a beam misalignment or an eventual classical intensity noise. It is well known that this device shifts the laser frequency by diffracting the laser field ω_0 on the acoustic standing wave (Ω_{RF}) in the crystal. This frequency-shift comes with a deviation of the laser beam axis which can prove very problematic when the beam is later coupled to a Fabry-Perot cavity. A double-pass configuration can be used to overcome this problem [82]. In particular, after the beam has passed for the first time through the acousto-optic, it must be re-injected exactly the same way. For this purpose it should be directed to a retro-reflector optical system, sending the beam back to exactly the exact inverse path.

A way to do this would be to place a spherical mirror whose radius of curvature coincides with the distance between the mirror and the modulator, so that the diffracted beam is perpendicularly reflected by the mirror. However, a spherical mirror alters the optical properties of the field as it acts on it as a lens. It would thus be preferable to use a flat mirror in order to symmetrically reflect the laser beam. We have decided to proceed with a different type of retro-reflector. A cat's eye configuration is made of a thin lens and a plane mirror. The thin lens serves two equally important purposes: first, in the geometrical optics framework, by placing the lens to a distance equal to its focal length it directs the beam perpendicularly to the plane mirror so that the latter reflects it to the inverse direction. Second, the lens creates a beam waist w'_0 onto the plane mirror so that the reflected beam is symmetrical to the incident one. We define the coupling efficiency between the incident and diffracted light as their power ratio. For the efficiency to be optimal, the incident field must present an optical waist w_0 into the modulator crystal whose corresponding Rayleigh length z_R is comparable to the crystal length l so that the beam wavefronts are perpendicularly coupled to the diffraction grating. Furthermore, it is known that when the light is injected at a particular angle θ_B then it is said that the modulator operates in the Bragg regime where only one diffraction order is produced while all others are eliminated by destructive interference effects, thus increasing the efficiency. The principle of a double-pass acousto-optic modulator system with a cat eye retro-reflector is depicted in figure 3.20(a).

The mounting protocol of such a system applied to this experiment is the following. A thin lens is placed prior to the modulator creating a waist (with a Rayleigh length which is comparable to the modulator length), in the position where the modulator will be placed. The size and position of the waist is measured with the ThorLabs scanning slit beam profiler

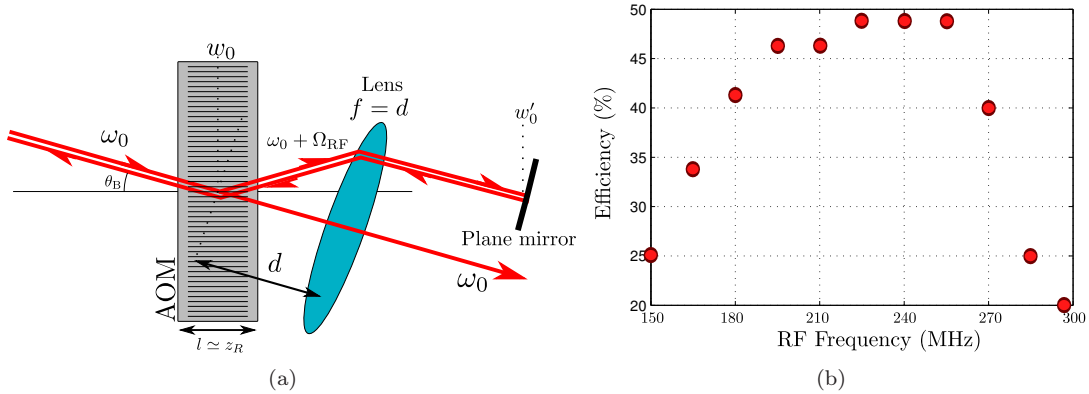


Figure 3.20: (a) Principle of the double-pass modulator system using a cat eye as a retro-reflector. (b) The coupling efficiency of this scheme to our experimental setup. An efficiency of up to 50% is achieved over a bandwidth of 20 MHz.

(BP104-IR). The modulator is mounted on a Newport 3-axis system in order to orient it so that the simple-pass efficiency is maximal. Typically, values up to 70% may be achieved. Once only zeroth and first diffraction orders are visible at the output of the modulator a thin lens is placed at a distance equal to its focal length with respect from the waist position.

The lens is mounted on a $x - y$ translation stage as the position and orientation of the lens is critical to the double-pass scheme. First, with the modulator turned off, by observing the very weak lens reflection, we ensure that the 0th diffraction order passes through the center of the lens so that it is not deflected. Afterwards, the modulator is turned on, we project the two diffraction orders a few meters away with a mirror. We then observe the deviation between both 0th and 1st orders and we adjust the z position of the lens so that the beams are perfectly parallel. This way, the first geometrical criterion is fulfilled. Finally, we measure the waist position with the beam profiler in order to set the plane mirror position. This last step is less critical since, thanks to the cat eye configuration the Rayleigh length of the beam after the thin lens is large and, consequently, the spot size varies slightly. As a first alignment test, we observe if both reflected 0th and 1st orders a) co-propagate and b) are both well-aligned to the downstream Fabry-Perot cavity (either the measurement or the filtering cavity).

We can also quantify the coupling efficiency of the double-pass scheme by measuring the ratio between input and output powers as a function of the RF frequency driving the modulator. Figure 3.20(b) depicts this efficiency. A double-pass efficiency up to 50% is achieved with a bandwidth of several tens of MHz. Knowing that the measurement cavity vibrations are equivalent to less than 1 MHz, this graph shows that any experimental imperfections of the double-pass configuration, leading to a pointing noise, will be negligible compared to the needed frequency-shift.

Experimental implementation

The double-injection scheme, already described in the first chapter of this thesis, contained two double-pass modulator systems with only a plane mirror as a retro-reflector. Nevertheless, the implementation of the above system after the high-finesse, filtering cavity involved important

changes in both optical and electronic aspects of the experiment. Figure 3.21(a) depicts the changes made on the optical table. A polarizing beam splitter is placed at the output of the high-finesse, filtering cavity replacing the mirror (see figure 3.14(b)). In combination with a quarter-wave plate it forms an optical circulator preventing the light to return to filtering cavity. A half-wave plate is placed between the cavity and the beam splitter in order to send the desirable power to the double-pass modulator. Typically, we have 50 mW of optical power at the output of the cavity, which is largely sufficient to obtain a frequency-controlled pump beam up to 10 mW, even when taking into account losses induced by various elements, mostly by the AOM efficiency.

The beam is then directed towards the acousto-optic modulator implemented in a double-pass configuration, as described above. We have used two thin lenses; one to create a waist into the modulator and another to create a waist on the plane mirror.

The implementation changes to the experiment feedback stabilization loops were important. The new, high-finesse cavity is stabilized by using as feedback transducers the two piezoelectric actuators on which are mounted its two mirrors, as done in the feed-forward scheme described earlier. However, it is obvious that the electro-optic of the laser ring-cavity can no longer be used for the measurement cavity stabilization. Therefore, a natural choice is to use the high-finesse as a reference cavity (FPE) on which the frequency laser is locked. The low-frequency fluctuations will be compensated by the laser cavity piezoelectric actuator via the high-finesse filtering cavity length while the high-frequency fluctuations will be compensated by the AOM.

We use the Pound-Drever error signal to realize a double servo-loop, driving the internal, piezoelectric actuator of the laser at low frequency and the laser electro-optic modulator at high frequency (see figure 3.21(b)). The LF and RF channels of the servo-loop are realized using two identical NewFocus P-I servo-controllers (LB-1005). Two passive low-pass and high-pass filters split the error signal in two parts each one used to drive the piezoelectric actuator and the electro-optic modulator; both with a cut-off frequency $f_c = 1$ Hz. The low-frequency output of the servo controllers drives the stacked piezoelectric-actuator via a home-made, high-voltage amplifier (1000 V) while the high-frequency drives the electro-optic modulator via a home-made pre-amplifier (pre-ampli TEGAM) and a high-speed low-noise amplifier (TEGAM 2340). At the input of the pre-amplifier a passive high-pass filter ($f_c = 1$ Hz) is installed in order to damp any DC component sent to the electro-optic modulator since it is not designed to be driven a low frequency. Also, at the output of the pre-amplifier a low-pass filter ($f_c = 300$ kHz) is used to damp the high-frequency white noise generated by the latter.

Since the electro-optic modulator is used to lock the laser frequency to the new mode-cleaner cavity, each beam -the pump and the probe- need a separate double-pass-configured acousto-optic modulator in order to stabilize its own frequency to the measurement cavity resonance. Furthermore, it is important that both modulators induce identical and fast frequency-shifts to the beams while simultaneously they are frequency-shifted (cavity birefringence) so that both resonate at the same time with the cavity. For this purpose, the output of the high-frequency servo-controller is split in two parts, each one passing through a home-made TEGAM pre-amplifier serving to add an independent gain and offset to each part. It is very crucial to ensure the output of the servo-controller contains no DC component which would lead to a stabilization imbalance between the beams. For this, a high-pass filter is coupled to the output of the controller.

Both outputs of the pre-amplifiers present an offset of 2.5 V; for such a voltage the cat's eye retro-reflector of the double-pass modulator is configured in order for it to work in the flat

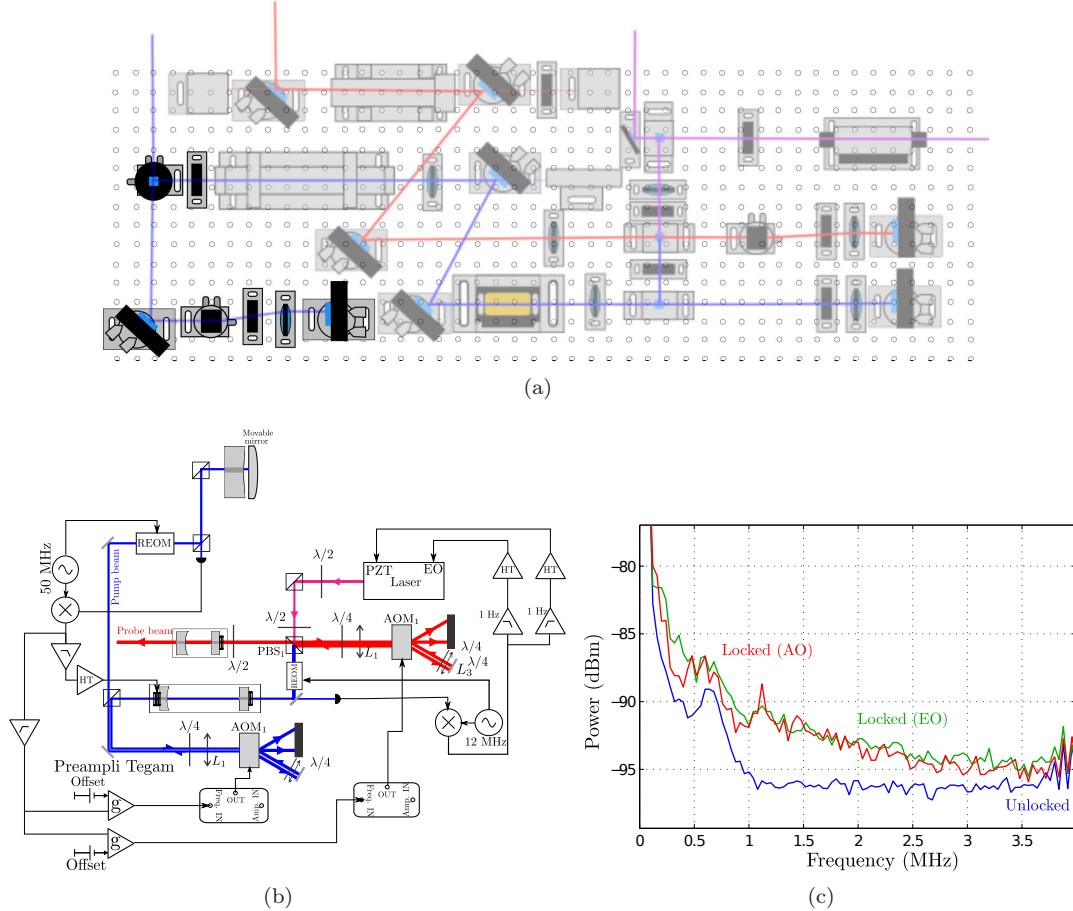


Figure 3.21: (a) A realistic figure depicting the optical elements placements after setting up the double-pass modulator after the high-finesse filtering cavity. (b) Experimental setup for the two main feedback loops: the laser frequency is locked on the high-finesse filtering cavity via a Pound-Drever technique at 12 MHz. The pump beam is used to generate an error signal for the measurement cavity. The low-frequency component of the error signal drives the stacked piezoelectric actuator altering the cavity length and consequently the laser frequency. The high-frequency component drives simultaneously the two double-pass-configured acousto-optic modulators. (c) The pump reflected intensity noise out of resonance (blue) and at resonance, locked using the electro-optic modulator (green) and the acousto-optic modulator (red). Both techniques give the same results.

regime of curve 3.20(b). The gain of the pre-amplifier driving the pump beam is randomly set since the servo-controller controls the gain of the loop. On the other hand, the pre-amplifier gain and offset of the probe beam is carefully set to obtain the right frequency offset and gain for both beams. Again, a low-pass passive filter ($f_c = 300$ Hz) is coupled to the output of both pre-amplifiers damping any high-speed classical noise that could interfere at the analysis frequency

(~ 1 MHz). Finally, the output of each pre-amplifier is sent to two commercial variable-frequency Voltage-Controlled -Oscillators (VCO, models AA Opto-Electronic (DRFA10Y-B-)) in order to control the frequency of the RF drive. The amplitude of the RF wave is set by a double Tektronix generator providing two DC signals with a 5V amplitude. Finally, the acousto-optic modulators are also AA Opto-Electronic-made (models MT200-A0.5-800).

However, this scheme of electronic circuits has some imperfections: the gain of the two parallel servo-loops is identical resulting to a frequency jitter between the two beams over a range of 500 kHz. This jitter can be observed by the beating of the two beams either on the homodyne or on the balanced detection. Figure 3.22 depicts this beating. While both beams are locked to the measurement cavity we observe the reflected intensity readout on a spectrum analyzer. By creating an optical contamination of the pump beam by the probe beam the beating becomes apparent. The beating is in fact the frequency difference between the two beams; since this frequency difference is not constant the beating is not monochromatic but it rather dynamically jitters taking a lorentzian-like form while the measurement is averaged by the spectrum analyzer (see figure 3.22). Special care must be taken with respect to this imperfection since if this beating contaminates the chosen frequency analysis window it could completely mask the optomechanical correlation signal.

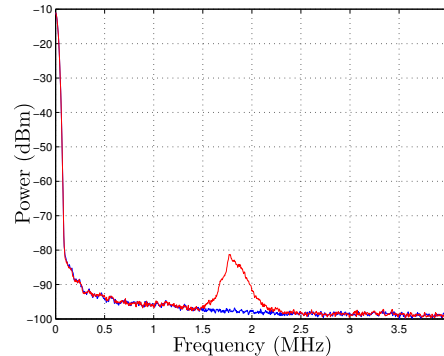


Figure 3.22: The beating between the two beams as observed by the balanced detection (red). In blue is the output of the balanced detection when the optical contamination is eliminated.

In practice, the $\lambda/2$ and $\lambda/4$ plates, placed in front of the measurement cavity are well configured in order to eliminate any optical contamination. Nevertheless, as the measurement cavity interacts with the incident fields, it slightly rotates the reflected polarizations of the fields in a dynamical manner, resulting in the appearance of this beating. During an experiment one must frequently check if this parasitic beating is present. In practice, there is no need for the probe beam to be completely resonant with the measurement cavity. One can slightly detune the probe beam and yet only lose less than 3 dB of measurement sensitivity. By then detuning the probe the beating can be tuned, away from the frequency analysis window.

In order to test the capabilities of this new experimental scheme and to ensure that no additional classical intensity noise is induced on the pump beam we have performed the following test. First, the high-finesse mode cleaner as well as the acousto-optic modulator were removed from the optical table. This way, we could simply lock the laser frequency on the measurement cavity by monitoring at the same time the reflected and incident intensity noise in and out of resonance, using the balanced and homodyne detections, respectively. The corresponding intensity noise graphs are depicted in figure 3.21(c). The blue graph (a) depicts the pump incident intensity noise at 4 mW out of resonance, which is equivalent to 10 mW of light power coupled to the measurement cavity (the reflection coefficient being $\mathcal{R}_0 = 60\%$). It should be compared to the reflected intensity noise when the laser frequency is locked to the measurement cavity with either the electro-optic or the acousto-optic modulator, curves b and c, respectively. Ideally, all three measurements should give the same result, if no additional, classical noise is present. However this is not the case: a 5 dB noise excess is visible near the analysis frequency at 1 MHz. It is present in both configurations, indicating that there is not a pointing noise

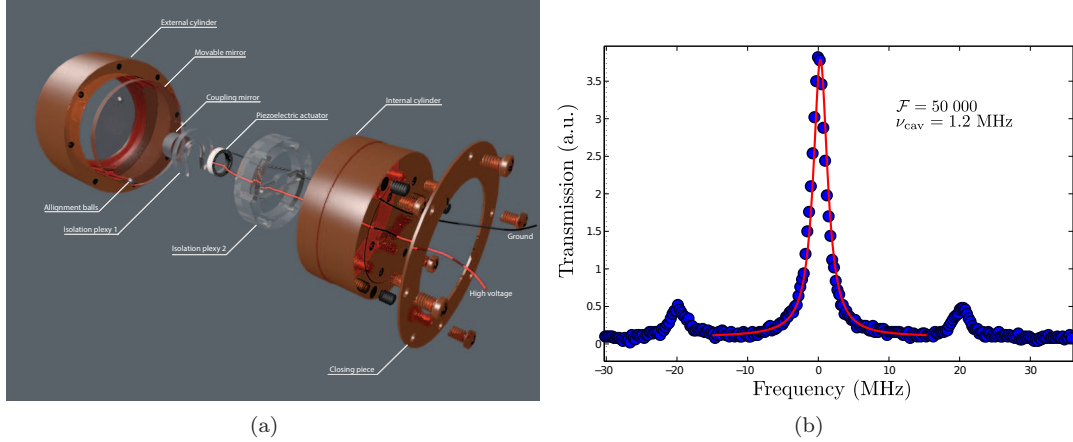


Figure 3.23: (a) The new measurement cavity. The 20-ppm transmission ATFilm coupler is glued onto a piezoelectric actuator. (b) The Airy peak of the cavity corresponding to a finesse $\mathcal{F} = 50\,000$.

induced by the acousto-optic modulator. At the same time, a beam splitter is used to direct a fraction of the incident field towards the balanced detector of the homodyne detection, where no difference was observed between the in and out of resonance incident intensity noises, also indicating that the excess noise is not induced by the laser source but by the measurement cavity. The contamination effect of the reflected intensity by the motion of the movable mirror is indeed observed.

3.2.8 Piezoelectric-implemented measurement cavity

In parallel to the above efforts in increasing the incident power we have also constructed a new measurement cavity whose coupler is mounted onto a piezoelectric actuator. Even though the diagnostics to explore the experimental limitations of this cavity were not conclusive, we will give a brief description of the cavity in case of future use.

Until now, the design of the measurement cavity is a rigid and compact cavity, in order to reduce the sensitivity to environmental vibrations. Nevertheless, the possibility of implementing a piezoelectric actuator has been taken into consideration. The design inspired by the current measurement cavity is depicted in figure 1.10 and has been modified in order to receive a piezoelectric actuator. Since the goal was to use the actuator as a high-frequency transducer for the feedback loop we have chosen to use fast, small ring actuators sold by Physik Instrumente with an internal diameter of 7 mm, an external diameter of 8 mm and a width of 1 mm. The idea was to couple this fast actuator to a small, low-weight coupling mirror coupler which would replace the heavier, cylindrical mirror used in the current cavity. For this, we have purchased from ATFilms a dielectric coating with a 20 ppm transmission coated on a silica substrate presenting a diameter of 7.75 mm, a thickness of 4 mm and a radius of curvature of 1 m.

For the design of this cavity great care was given to how the small ATFilm mirror would be mounted. For this we have designed two different parts: one where the mirror had to be glued onto it and another that came with a little screw clamping the mirror at its side. Both of them are made from plexiglass in order to provide an electrical insulation and at the same to be

light enough for the correct compensation of the high-frequency vibrations. The development of this cavity only reached the alignment stage where a cavity with a finesse of $\mathcal{F} = 50\,000$ was obtained. Further characterization tests, notably stabilization tests, were dropped due to lack of time. Figure 3.23(a) depicts the design of the cavity while figure 3.23(b) shows the obtained finesse using the plano-convex movable mirror.

Contamination feedback loop

WE have demonstrated in the second chapter a robust averaging technique capable of extracting optomechanical correlations in the thermal regime. However, as we will see in the following, the pump beam optical contamination of the intensity quadrature (equation 4.9) by the motion of the mirror is susceptible to cover the quantum back-action signal we are seeking to experimentally demonstrate, if the quality of the cavity locking is not sufficiently good. This effect sets a severe limitation to the optomechanical correlations experiment. We will start this chapter by presenting a quantitative description of the contamination effect on the measured correlations and by giving an efficiency criterion on the quality of the feedback loop stabilization. The success of the experimental observation of the quantum back-action depends on whether this particularly demanding criterion is met. In the opposite case, the observed correlations will have a classical origin. We will then explain the strategy chosen to surpass this experimental problem. In particular, we will describe the efforts made towards the development of a novel detection method enabling the accurate tracking of the cavity detuning, based on the derivation of an error signal directly related to the contamination effect on the pump beam. We will establish a model of this technique and a comparison with the Pound-Drever-Hall locking technique will also be attempted. We will compare the robustness of this novel technique to the Pound-Drever-Hall scheme, enabling a significant advance towards demonstrating the quantum optomechanical correlations and more generally optomechanically-induced quantum optics. We will finally present the experimental implementation in our setup and the characterization of the feedback loop realized.

4.1 Contamination effect in a detuned cavity

The averaging time is not the only issue one has to deal with when detecting optomechanical correlations. There is in fact a contamination effect of the reflected intensity quadrature of the pump beam, deteriorating the efficiency of phase-intensity optomechanical correlations. We have already seen in the first chapter that when taking the optical losses of the cavity into account, the intensity of the reflected field presents a Lorentzian dip near an optical resonance ($\bar{\Psi} \simeq 0$). This corresponds to a non-unity reflection coefficient with a minimum \mathcal{R}_0 at resonance. The first effect is a decrease of the optomechanical correlations due to a lower intracavity intensity and the contamination of the pump beam by the vacuum fluctuations. This can be easily handled by increasing the input power as long as \mathcal{R}_0 corresponds to a few dBs of attenuation as it is the case for our cavity. However, due to experimental imperfections, the condition of “perfect optical resonance” is in practice never met: the laser frequency is never perfectly stabilized to the cavity optical resonance. In fact, even when the main locking loop is locked, a frequency noise still exists which results to a corresponding jitter of the cavity working

point around the optical resonance. As depicted on Figure 4.1, the working point of the system will spend some time on the side of the Lorentzian dip where the intracavity intensity is sensitive to the mirror displacement due to a non-zero derivative $d\mathcal{R}/d\psi \neq 0$. In other words, a coupling between the output intensity fluctuations and the phase/position fluctuations occurs. This coupling does not exist when the cavity is perfectly resonant where ($d\mathcal{R}/d\psi = 0$) (equations (1.53) and (1.55)). In the following, we will quantify this effect by generalizing the calculation already made in the first chapter by taking this time a non-zero detuning, $\bar{\psi} \neq 0$. A detuned cavity modifies the relations between the phase and intensity quadratures. Let us start by recalling the typical input-output transformation equations of a coherent field interacting with a single-ended, lossy Fabry-Perot cavity:

$$\tau \frac{d\alpha}{dt} = \sqrt{T}\alpha_{\text{in}} + \sqrt{P}\alpha_{\text{v}} + (i\psi - \gamma)\alpha(t), \quad (4.1)$$

$$\alpha_{\text{out}}(t) = \sqrt{T}\alpha(t) - \alpha_{\text{in}}(t), \quad (4.2)$$

from which, as before, the steady state amplitudes can be deduced:

$$\bar{\alpha} = \frac{\sqrt{T}}{\gamma - i\psi} \bar{\alpha}_{\text{in}}, \quad \bar{\alpha}_{\text{out}} = \frac{\gamma - P + i\psi}{\gamma - i\psi} \bar{\alpha}_{\text{in}}. \quad (4.3)$$

Compared to the in-resonance case, the incident and reflected mean fields $\bar{\alpha}_{\text{in}}$ and $\bar{\alpha}_{\text{out}}$ are phase-shifted with respect to the mean intra-cavity field $\bar{\alpha}$ which, for simplicity reasons, is considered to be real ($\bar{\alpha} = |\bar{\alpha}|$). In the non-zero detuning case, the incident and reflected mean fields are given by $\bar{\alpha}_{\text{out}} = |\bar{\alpha}_{\text{in}}|e^{-i\theta_{\text{in}}}$ and $\bar{\alpha}_{\text{out}} = |\bar{\alpha}_{\text{in}}|e^{-i\theta_{\text{out}}}$. By combing these equations with equation (4.3), one can write down their relative phases:

$$e^{-i\theta_{\text{in}}} = \frac{\gamma - i\psi}{\sqrt{\gamma^2 + \psi^2}}, \quad e^{-i\theta_{\text{out}}} = \frac{\gamma - P + i\psi}{\sqrt{(\gamma - P)^2 + \psi^2}}. \quad (4.4)$$

These phase-shifts make the calculation of the reflected quadrature more complex since they have to be taken into account when writing down the corresponding fluctuations. The fluctuations of the incident and reflected field in the out-of-resonance case may be written:

$$(\gamma - i\psi - i\Omega\tau)\delta\alpha[\Omega] = \sqrt{T}\delta\alpha_{\text{in}}[\Omega] + \sqrt{P}\delta\alpha_{\text{v}}[\Omega] + 2i\bar{\alpha}k\delta x[\Omega], \quad (4.5)$$

$$\delta\alpha_{\text{out}}[\Omega] = \sqrt{T}\delta\alpha[\Omega] - \delta\alpha_{\text{in}}[\Omega]. \quad (4.6)$$

Equation (1.10) defines any quadrature in function of its rotation in the phase-space. We can thus write down the fluctuations δp_{out} , $\delta\alpha_{\text{in}}$, $\delta\alpha_{\text{v}}$ of the reflected intensity, the incident intensity

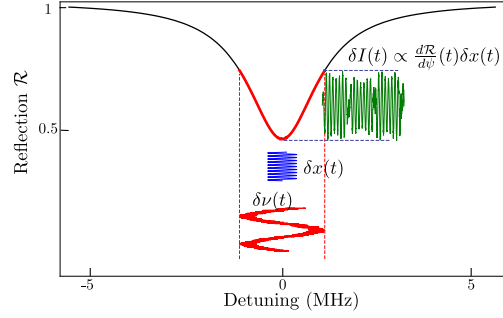


Figure 4.1: The side-of-the-fringe standard technique to measure the mirror motion via the reflected intensity: if the intense beam is not perfectly at resonance with the cavity, it becomes sensible to the mirror position.

and the vacuum, respectively:

$$\begin{aligned}\delta p_{\text{out}}[\Omega] &= e^{i\theta_{\text{out}}}\delta\alpha_{\text{out}}[\Omega] + e^{-i\theta_{\text{in}}}\delta\alpha_{\text{out}}^*[\Omega], \\ \delta\alpha_{\text{in}}[\Omega] &= \frac{1}{2}e^{-i\theta_{\text{in}}}(\delta p_{\text{in}}[\Omega] + i\delta q_{\text{in}}[\Omega]), \\ \delta\alpha_{\text{v}}[\Omega] &= \frac{1}{2}(\delta p_{\text{v}}[\Omega] + i\delta q_{\text{v}}[\Omega]).\end{aligned}\tag{4.7}$$

We are particularly interested in calculating the reflected intensity fluctuations δp_{out} . The result is a very long expression; we will focus only on the term that involves the mirror motion δx :

$$\delta p_{\text{out}}^x = -4k\bar{\alpha}\frac{\sqrt{T\bar{\psi}}(-P + i\Omega\tau)}{\Delta\sqrt{(\gamma - P)^2 + \bar{\psi}^2}}\delta x[\Omega],\tag{4.8}$$

where $\Delta = (\gamma - i\Omega\tau)^2 + \bar{\psi}^2$. By neglecting cavity-filtering effects ($\Omega_{\text{cav}} \gg \Omega$) and for a small detuning $\bar{\psi} \ll \gamma$, this can be reduced to the following simple expression:

$$\delta p_{\text{out}}^x[\Omega] \simeq 2k\frac{1}{\sqrt{\bar{I}_{\text{out}}}}\frac{d\bar{I}_{\text{out}}}{d\bar{\psi}}\delta x[\Omega].\tag{4.9}$$

Indeed, we find that the reflected intensity, once the cavity is detuned, is sensitive on the movable mirror displacements: there is a contamination effect of the intensity quadrature by the mirror displacement which is proportional to the slope of the Airy peak. Therefore, the reflected signal intensity presents not only the incident intensity fluctuations responsible for quantum correlations. This inevitably leads to fake correlations as both the pump intensity and probe phase simply display the effect of thermal noise. The thermal correlation coefficient $\mathcal{C}_{\delta_{\text{out}}^s - \delta x_T}$ no longer vanishes by time-averaging and may become comparable to the quantum correlations $\mathcal{C}_{\delta p_{\text{out}}^s - \delta x_{\text{rad}}}$.

4.2 Contamination effect on optomechanical correlations

We will continue this chapter by quantifying the effect of the contamination on the optomechanical correlation function. The displacement of the movable mirror results from two independent forces: the Langevin force F_T , resulting in a thermal motion δx_T , and the radiation-pressure force F_{rad} , resulting in a displacement $\delta x_{\text{rad}}[\Omega] = \chi[\Omega]F_{\text{rad}}[\Omega]$. We will consider that only the intense pump beam contributes to the radiation-pressure force which is then given by:

$$F_{\text{rad}}[\Omega] = 2\hbar\bar{\alpha}_s\delta p_s[\Omega],\tag{4.10}$$

where the fluctuations of the intensity quadrature δp_s are derived by equations (4.5) and (4.7):

$$\begin{aligned}\delta p_s[\Omega] &= \sqrt{T}\left[(\gamma - i\Omega\tau)\cos\theta_{\text{in}} + \bar{\psi}\sin\theta_{\text{in}}\right]\delta p_{\text{in}}^s[\Omega] \\ &+ \sqrt{T}\left[(\gamma - i\Omega\tau)\sin\theta_{\text{in}} - \bar{\psi}\cos\theta_{\text{in}}\right]\delta q_{\text{in}}^s[\Omega] \\ &+ \sqrt{P}(\gamma - i\Omega\tau)\delta p_{\text{v}}^s[\Omega] - \bar{\psi}\sqrt{P}\delta q_{\text{v}}^s[\Omega].\end{aligned}\tag{4.11}$$

We will now write the correlation function $\mathcal{C}_{s-m}[\Omega]$ under the form:

$$\mathcal{C}_{s-m}[\Omega] = \mathcal{C}_{\text{opto}}[\Omega] + \mathcal{C}_{x-x}[\Omega], \quad (4.12)$$

where we have noted $\mathcal{C}_{\text{opto}}[\Omega]$ the term corresponding to the quantum optomechanical correlations and $\mathcal{C}_{x-x}[\Omega]$ the term corresponding to the classical correlations caused by the intensity-phase quadrature coupling of the pump beam. Using the Wiener-Khinchin theorem, we may write the spectrum of the correlation function:

$$2\pi\delta(\Omega + \Omega')\mathcal{C}_{s-m}[\Omega] = \langle \delta p_{\text{out}}^s[\Omega] \delta q_{\text{out}}^m[\Omega'] \rangle. \quad (4.13)$$

Likewise, for two terms of the correlation function we write:

$$\begin{aligned} 2\pi\delta(\Omega + \Omega')\mathcal{C}_{\text{opto}}[\Omega] &= \frac{4\sqrt{T}}{\gamma - i\Omega\tau} k\bar{\alpha}_m \langle (\delta p_{\text{out}}^s[\Omega] - \delta p_{\text{out}}^{s,x}[\Omega]) \delta x_{\text{rad}}[\Omega'] \rangle, \\ 2\pi\delta(\Omega + \Omega')\mathcal{C}_{x-x}[\Omega] &= \frac{4\sqrt{T}}{\gamma - i\Omega\tau} k\bar{\alpha}_m \langle \delta p_{\text{out}}^{s,x}[\Omega] \delta x[\Omega'] \rangle. \end{aligned} \quad (4.14)$$

At low frequency ($\Omega \ll \Omega_{\text{cav}}$) the two terms of the correlation function can be written as follows:

$$\begin{aligned} \mathcal{C}_{\text{opto}}[\Omega] &= \frac{8\hbar k^2 T \bar{\alpha}_s \bar{\alpha}_m}{\gamma^2} \chi^*[\Omega] S_{\text{in}}^{p,s}[\Omega] \\ \mathcal{C}_{x-x}[\Omega] &= \frac{8k^2 \sqrt{T} \bar{\alpha}_m}{\gamma^2} \frac{d\bar{I}_{\text{out}}^s}{d\psi} S_x[\Omega]. \end{aligned} \quad (4.15)$$

The ratio between these two terms can give us a tolerance condition of the cavity detuning $\bar{\psi}$ on the optomechanical correlations. By considering a quantum-noise-limited incident beam ($S_{\text{in}}^{p,s} = 1$) this ratio becomes:

$$\left| \frac{\mathcal{C}_{x-x}[\Omega]}{\mathcal{C}_{\text{opto}}[\Omega]} \right|^2 = \frac{16\pi^2}{\bar{I}_{\text{out}}^s} \left(\frac{d\bar{I}_{\text{out}}^s}{d\psi} \right)^2 \left(\frac{S_x[\Omega]}{\lambda^2} \right) \left(\frac{S_x[\Omega]}{S_x^{\text{rad}}[\Omega]} \right). \quad (4.16)$$

The above expression shows us that the contamination effect on the optomechanical correlations essentially depend on three parameters. First, it is proportional to the Airy peak slope defining the sensitivity of the reflected beam to the mirror displacement. Second, it is also proportional to the noise spectrum of the mirror displacement. Third, it is inversely proportional to the signal-to-noise ratio between radiation-pressure effects and thermal noise. Hence, it is possible to experimentally observe optomechanical correlations if the above ratio is *sufficiently* small, i.e. if it is smaller than the desired measurement precision ε . Consequently, there is a critical value of the cavity detuning $\bar{\psi}_\varepsilon$ for which the optomechanical correlations are masked by the contamination:

$$\frac{\bar{\psi}_\varepsilon}{\gamma} = \frac{\sqrt{\mathcal{R}_0}}{8\mathcal{F}\sqrt{\bar{I}_{\text{in}}}} \frac{\gamma^2}{TP} \left(\frac{S_x[\Omega]}{\lambda^2} \right)^{-\frac{1}{2}} \left(\frac{S_x[\Omega]}{S_x^{\text{rad}}[\Omega]} \right)^{-\frac{1}{2}} \varepsilon, \quad (4.17)$$

where \mathcal{R}_0 is the reflection coefficient as defined in equation (1.40).

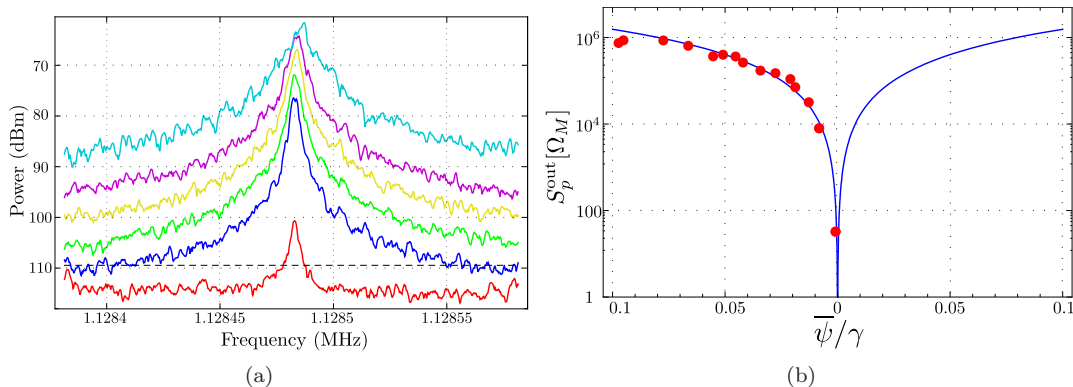


Figure 4.2: (a) Intensity spectrum noise around the mechanical resonance frequency $\Omega_M/2\pi = 1.1287$ MHz of the movable mirror for different cavity detunings. From bottom to top these graphs correspond to detunings -0.0009γ , -0.0082γ , -0.0128γ , -0.021γ , -0.042γ and -0.097γ . The power of the pump beam was set at 1 mW. The contamination effect increases as the cavity is further detuned. (b) Evolution of the contamination noise level as a function of the aforementioned detunings at the mechanical resonance frequency Ω_M . The red dots correspond to the experimental measurements of graph (a), while the continuous blue line corresponds to the theoretical model described by equation (4.9)

4.3 Characterization of the contamination effect

Here we will present the experimental evidence and characterization of the contamination effect of the intensity quadrature by the motion of the mirror. This effect immediately manifests itself under the form of an excess noise on the reflected intensity noise spectrum of the pump beam; see Figure 3.21(c) for instance, where a 5 dB excess noise is visible compared to the quantum intensity noise: this noise is induced by the thermal motion of the mirror, and can be easily compared to the motion measured by the homodyne detection.

To quantify this effect, we have performed a calibration of the contamination as a function of the cavity working point. This experiment has been carried out using only the pump beam locked to the measurement cavity using the Pound-Drever error signal. By adding an offset to this signal the working point of the cavity is slightly detuned. This detuning is calibrated by comparing the voltage offset to the error signal peak-to-peak amplitude [40]. For different offsets, the pump beam frequency is stabilized onto the measurement cavity and the corresponding contamination effect on the intensity quadrature is measured using the same photodiode as for the Pound-Drever error signal. We have explored only the blue side of the resonance, as in the red side the cavity quickly presents parametric instability effects [74], making the measurements unexploitable.

Figure 4.2(a) presents the successive spectra of the reflected intensity S_I^{out} measured by the spectrum analyzer for cavity detunings from 0 to $-\gamma/10$ and for an incident power of 1 mW. The contamination is observed over a large frequency band around the mechanical resonance. Thermal noise is larger and a clear signature of the contamination can be observed. The further the cavity is detuned away from its resonance the greater the contamination becomes. Indeed, as equation (4.9) implies, the amplitude of the contamination level should be proportional to

the Airy peak slope, which is zero at resonance and maximum at the peak half-maximum. We have thus tried to check this prediction by plotting the contamination level, given by the measured intensity quadrature spectrum S_p^{out} at the mechanical resonance frequency Ω_M , as a function of the cavity detuning. This noise power is measured by the spectrum analyzer; the intensity quadrature δp is recovered using $\delta I = \bar{\alpha} \delta p$. The mean intensity is deduced by the corresponding detuning: as the cavity bandwidth is known, for a given detuning the intensity can be deduced by the in-resonance intensity.

The measurements were done for an input power of the pump beam of 1 mW and are depicted on Figure 4.2(b) in red dots. The blue continuous line corresponds to the theoretical fit using equation (4.9). This fit is plotted using the optical and mechanical calibrations of the measurement cavity composed of mirrors 3021/13 and 07125/3, giving a bandwidth $\nu_{\text{cav}} = 0.9$ MHz, which corresponds to a finesse $\mathcal{F} = 167\,000$ and a cavity length $L = 500 \mu\text{m}$, and a mass $M = 170$ mg. We note that the experimental measurements are in very good agreement with the theoretical model proving that the excess noise we observe is indeed a contamination effect as modeled in section 4.1. Figure 4.2(b) shows the strong dependence of the contamination with the cavity detuning. In particular, around the optical resonance, the contamination first varies very strongly before converging to a constant value as the cavity is further detuned. It is clear that this effect sets an important limitation to the observation of the quantum correlations. It is also clear that the Pound-Drever-Hall error signal does not provide the necessary cavity detuning resolution for the feedback loop to sufficiently stabilize the measurement cavity. In order to overcome this experimental difficulty, a robust technique is needed in order to monitor the detuning while the cavity is locked. This efforts will be described in the following sections.

4.4 A lock-in scheme

For the experiments described until now in this manuscript, the Pound-Drever-Hall scheme is used to stabilize the laser frequency to the cavity resonance. While it is a robust stabilization technique, we used to use another standard stabilization technique, applied to a wide range of experiments: the lock-in (LI) technique. The derivation of the error signal is quite similar to the Pound-Drever scheme, presenting however some important disadvantages. Whereas its implementation in table-top optics experiments is quite simple and permits to perform a lock-in either on the maxima or on the side of a fringe, it presents a capture range limited by the width of the fringe and the bandwidth is limited by the reference modulation ($\nu_{BP} < \nu_{\text{ref}}$). During this manuscript we attribute the name ‘‘Lock-in’’ (LI) to this technique.

The implementation of the LI scheme is depicted on Figure 4.4(a). The system is probed via a frequency modulation $\delta\nu_{\text{ref}}$. It may be induced by either modulating the frequency of the laser or the cavity length via an integrated piezoelectric actuator for example. Once the laser beam is coupled to the cavity, the reference modulation is superimposed to the residual cavity noise and is later transformed into an intensity modulation at the same frequency $\Omega_{\text{ref}}/2\pi$ as the reference modulation, which can be detected by a photodiode at the output of the cavity.

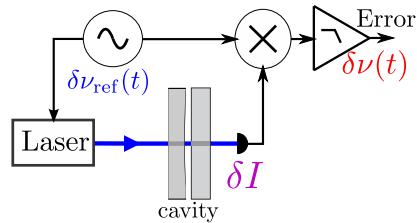


Figure 4.3: Principle of a lock-in scheme applied for a Fabry-Perot cavity.

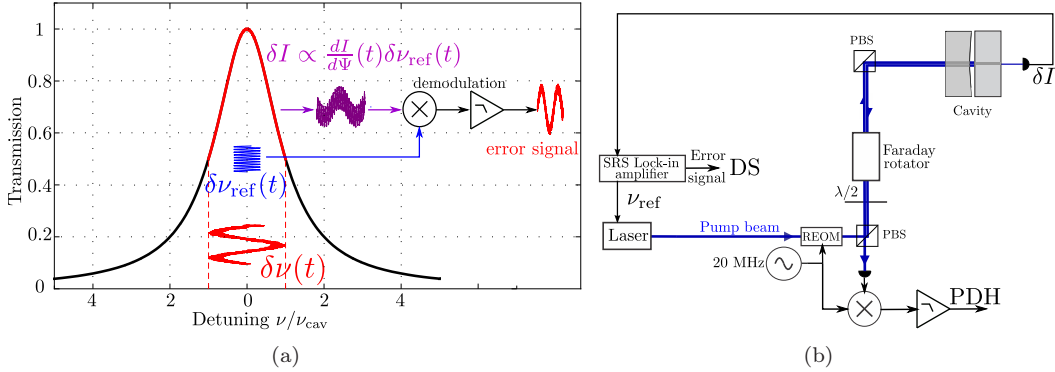


Figure 4.4: (a) Error signal derivation using a typical lock-in scheme: a phase- or frequency-modulation ν_{ref} , by modulating either by the frequency of the laser beam or the length of the cavity. This modulation is added to the residual cavity noise and is in turn transformed at the output of the cavity to an intensity modulation, proportional to the Airy peak slope and to the cavity's residual noise. The intensity modulation presents a slowly-varying envelope containing the information of the cavity detuning and is then detected and demodulated in order to obtain a corresponding error signal. (b) Typical lock-in scheme used in our experimental setup: the reference modulation frequency is induced to the laser electro-optic modulator, while the intensity modulation is monitored by a photodiode at the output of the cavity.

The intensity modulation is proportional to the Airy peak slope. Therefore, its amplitude varies proportionally to the detuning amplitude. Moreover, the modulation is in-phase, on the left side of the peak, and in opposite phase on the right side.

By demodulating this signal at frequency Ω_{ref} , one can obtain an error signal providing an information on the cavity residual noise $\delta\nu$ we are trying to compensate. In principle, this technique seems identical to the Pound-Drever scheme: in both cases, a reference modulation is coupled to the cavity and later transformed to an intensity modulation. In fact, the major difference is the frequency of the reference modulation compared to the cavity bandwidth. Indeed, if the reference modulation is much greater than the cavity bandwidth ($\delta\nu_{\text{ref}} \gg \nu_{\text{cav}}$), it will be filtered by the cavity and no signal will be transmitted by the cavity. In this case, one should observe the cavity response to the modulation on the beam reflected by the cavity. There lies the main difference between the two schemes and this is actually why the Pound-Drever signal is derived on the reflected beam; the sidebands created by the phase modulation are outside the cavity's bandwidth and are thus completely reflected (see Figure 3.5(b)). In general, the Pound-Drever makes use of a reference modulation frequency much greater than the cavity bandwidth ($\nu_{\text{ref}} \gg \nu_{\text{cav}}$) in order to obtain the largest possible capture range and to be able to measure high-frequency signals, of the order of ν_{cav} and even greater. This major difference may radically change the performance of the feedback loop notably its bandwidth which is set by the reference modulation. Such a lock-in feedback loop, will act only to frequencies up to $\nu_{\text{ref}} \ll \nu_{\text{cav}}$; the reference modulation may be interpreted as the detection sampling rate defining a cut-off frequency above which the loop becomes ineffective. In our experimental setup, the measurement cavity presents typical bandwidth of 1 MHz and therefore a lock-in scheme can efficiently act up to frequencies of some hundreds of kHz, whereas a Pound-Drever signal may use a reference modulation up to 50 MHz, as in our experiment.

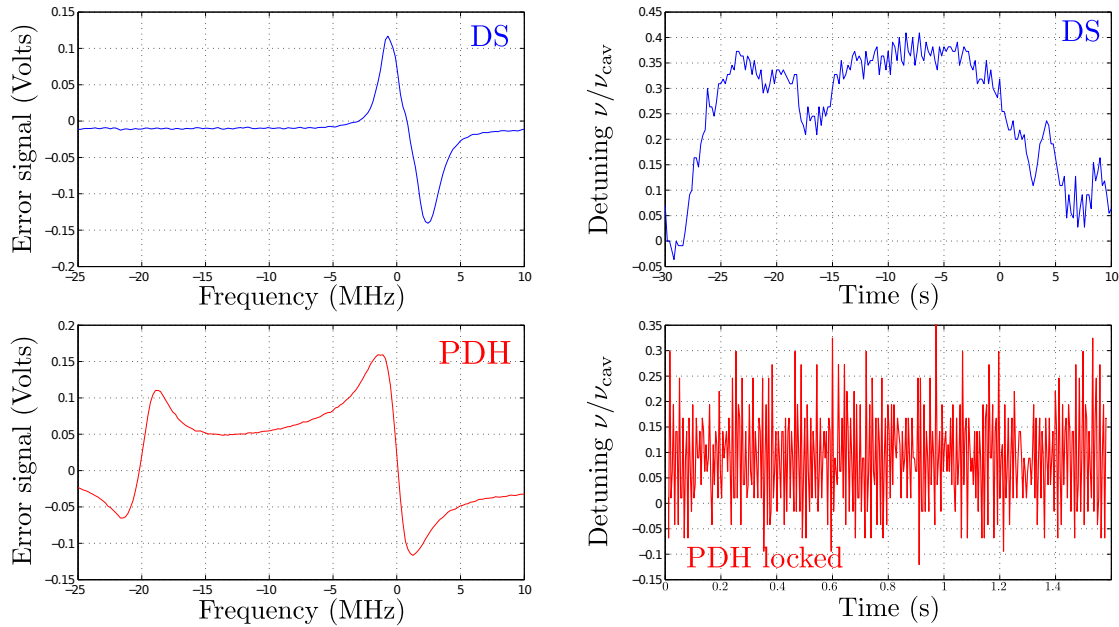


Figure 4.5: The two error signals obtained by two different techniques: lock-in (blue) and Pound-Drever (red), while the cavity is swept (left) and locked (right) using the PDH error signal.

The implementation of the LI scheme in our experimental setup is depicted on Figure 4.4(b). We will now present a simple demonstration of this technique. The idea is to derive two independent error signals using the two schemes described: one used to lock the measurement cavity and the other one to monitor eventual drifts or lock-in imperfections not compensated by the feedback loop. The Pound-Drever locking is implemented as described in the introductory chapter: the feedback loop is realized by directly driving the laser frequency. The lock-in error signal is derived using a digital lock-in amplifier (Stanford Research Systems SR810) also providing the reference modulation driving the electro-optic modulator of the laser cavity which is set at 100 kHz; the bandwidth of the PDH loop is limited well below this frequency so that the reference is not compensated. The intensity modulation is finally detected by a photodiode placed at the exit of the measurement cavity which uses the few ppm of the movable mirror transmission. Figure 4.4 presents both error signals while the cavity is swept and locked on the Pound-Drever signal. When the cavity is locked, the contrast between the two signals is evident: while the Pound-Drever signal rapidly oscillated around a near-zero value, the lock-in signal, due to its low bandwidth, presents only components much slower than the Pound-Drever error signal. On the other hand, it clearly shows that at low frequencies the cavity drifts over almost half a cavity linewidth ($\sim 0.4 \nu_{cav}$), demonstrating the lower efficiency of the stabilizing feedback loop.

There are several experimental reasons for the Pound-Drever inefficiency, the most important of which being that the Pound-Drever-Hall error signal is sensitive to any possible, parasitic intensity modulation of the pump beam. Indeed, for the creation of the sidebands, the resonant electro-optics modulators used are known to also generate an unwanted residual amplitude

modulation (RAM) rejection at the drive frequency which eventually sets a direct limit to the sensitivity of the error signal. The sources of this amplitude modulation are not completely understood although some are well-known: parasitical reflections and temperature variations of the modulator signal, or even spatial inhomogeneities of the light field coupled to the modulator [83]. Furthermore, once the light field is phase-modulated, it travels a round-trip trajectory towards the measurement cavity and finally to the balanced detector, passing through various optical elements. The laser beam propagates through the various optical elements at normal incidence. Even though the optical elements have an anti-reflecting coating, parasitical reflections do exist randomly forming low-finesse, Fabry-Perot cavities which result in an additional intensity modulation. Finally, it is also known that the polarization of the incident beam should also be horizontal with respect to the crystal's normal axes. For this a polariser is placed in the input and the output of the modulator. However, while for different incident polarizations we have observed a strong dependence on the phase modulation efficiency, no evident change has been observed on the derived error signal; we attribute this to the simultaneous incidence of amplitude modulation making its elimination experimentally complex.

The lock-in scheme allowed to experimentally demonstrate the low-frequency drifts of the cavity even though the feedback loop was on. In the following, we would like to use a combination of the two error signals, the Pound-Drever and the lock-in signal. However, the LI signal not only presents a low sensitivity, mainly due to the extremely low transmission of the measurement cavity, but also possible parasitic offsets. In the next section, we will then describe a novel technique using a contamination measurement to perform a truly independent detuning effect, that may lead to the pump beam phase-intensity quadrature decoupling.

4.5 Contamination-based lock-in

The idea is to create an artificial contamination on the intensity quadrature δp_{out}^s which may be detected in order to deduce the cavity detuning $\bar{\psi}(t)$. Indeed, as we have shown in a section 4.1, the unavoidable optical losses P (e.g. scattering, absorption, etc...) in a high-finesse Fabry-Perot cavity couple the reflected intensity quadrature to the mirror displacements δx , with a slope proportional to the cavity detuning $\bar{\psi}$. By considering that the contamination effect is much greater than then intensity shot noise ($S_{p_{\text{out}}^{s,x}} \gg 1$) we may assume the intensity read out only contains the term $\delta p_{\text{out}}^{s,x}$ given by equation (4.9):

$$\delta p_{\text{out}}^{s,x}[\Omega] \simeq -4k\bar{\alpha}_s \frac{\sqrt{T}(-P + i\Omega\tau)\bar{\psi}}{\Delta\sqrt{(\gamma - P)^2 + \bar{\psi}^2}} \delta x[\Omega]. \quad (4.18)$$

We also assume that the detuning is small compared to the cavity losses ($\bar{\psi} \ll \gamma, P$). The last expression then becomes:

$$\delta p_{\text{out}}^{s,x}[\Omega] \simeq -4k\bar{\alpha}_s \frac{\sqrt{T}(-P + i\Omega\tau)\bar{\psi}}{\Delta|\gamma - P|} \delta x[\Omega]. \quad (4.19)$$

Let us now introduce an external excitation applied onto the movable mirror at frequency $\Omega_d/2\pi$:

$$F_{\text{ext}}(t) = F_0 e^{i\Omega_d t}, \quad (4.20)$$

inducing a mirror displacement

$$\delta x_0[\Omega] = \chi[\Omega] F_0 \delta(\Omega - \Omega_d). \quad (4.21)$$

If the motion of the mirror is driven at its mechanical frequency $\Omega_d = \Omega_M$, the reflected intensity quadrature becomes:

$$\delta p_{\text{out}}^{s,x}[\Omega] \simeq -4k\bar{\alpha}_s \frac{\sqrt{T}}{|\gamma - P|} \frac{-P + i\Omega_M\tau}{\Delta} \frac{i}{M\Gamma_M\Omega_M} F_0 \delta(\Omega - \Omega_M) \bar{\psi}. \quad (4.22)$$

By using the following expression:

$$\delta I_{\text{out}}^s[\Omega] = \bar{I}_{\text{out}}^s \delta p_s^{\text{out}}[\Omega], \quad (4.23)$$

between the measured intensity and its associated quadrature, and by demodulating the output intensity $\delta I_{s,x}^{\text{out}}$ at frequency Ω_M with a phase ϕ , one gets the following error signal:

$$V_{\text{err}} = \text{Re} \left[-4k\sqrt{I_s^{\text{out}}\bar{\alpha}_s} \frac{\sqrt{T}}{|\gamma - P|} \frac{-P + i\Omega\tau}{\Delta} \frac{i}{M\Gamma_M\Omega_M} F_0 \bar{\psi} e^{-i\phi} \right]. \quad (4.24)$$

In order to further simplify the above expression, we will assume the demodulation frequency smaller than the cavity bandwidth and neglect any cavity-filtering effects ($\Omega_M \ll \Omega_{\text{cav}}$). The error signal then becomes:

$$V_{\text{err}}(t) \simeq -4k\sqrt{I_s^{\text{out}}\bar{\alpha}_s} \frac{T}{|\gamma - P|} \frac{F_0}{M\Gamma_M\Omega_M} \frac{[(\gamma - P)^2 + \bar{\psi}^2]^{1/2}}{(\gamma^2 + \bar{\psi}^2)^2} \bar{\psi} P \sin \phi. \quad (4.25)$$

The last expression gives the resulting signal after detection and demodulation of the reflected intensity at frequency Ω_M . Let us notice, that the demodulation angle ϕ of the local oscillator, if the movable mirror is driven at its mechanical resonance, must be set at $\pi/2$ as the mechanical response is quadrature with the driving. Finally, if we consider the case of small detunings ($\bar{\psi} \ll \gamma$), equation (4.25) shows that the error signal is directly proportional to the cavity detuning ($V_{\text{err}} \propto \bar{\psi}$). Therefore, in the linear regime, a direct measurement of the cavity detuning may be performed using this technique. It is now very interesting to compare this novel scheme to the traditional Pound-Drever-Hall technique by examining its experimental limitations.

4.5.1 Experimental realization

The idea of the contamination feedback loop is to create an error signal by performing a direct measurement of the contamination effect on the reflected intensity quadrature. Several options exist in order to drive the mirror at a given frequency. The most common one would be to use a piezoelectric actuator coupled to the movable mirror in order to modulate the cavity length. For reasons stated in the first chapter, this solution is not considered for our experiment (rigid, compact measurement cavity to reduce environmental vibrations, etc...). Second, a laser phase modulation may also be used to induce an apparent cavity length variation. However, since it is desirable to completely decouple the mirror driving from the double injection scheme of our setup, it has been decided to drive the mirror with an external radiation-pressure force. A

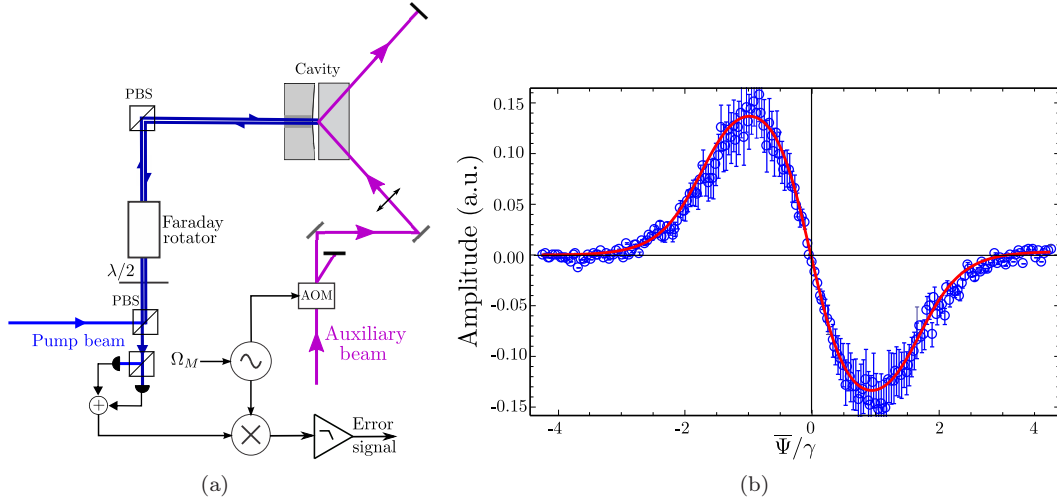


Figure 4.6: (a) Experimental setup used to create an error signal based on a contamination measurement: an acousto-optic modulator modulates the intensity of the beam at a frequency $\Omega_m \sim 1$ MHz, which in turn induces a mirror motion at the same frequency, creating a contamination signal at the reflected intensity quadrature of the pump beam. This signal is finally demodulated, providing the corresponding error signal. (b) Error signal derived using the configuration in (a). Blue dots are the experimental measurements with their error bars while the continuous red line is the theoretical fit using equation (4.24).

system composed of a half-wave plate and a polarizing beam splitter is installed at the output of the laser in order to split the beam into two parts: one is used to feed the double-injection experimental setup and the other one to create an auxiliary beam that may be used to directly drive the movable mirror of the measurement cavity with radiation pressure. The Ti:Sa laser provides 2 W of laser power at optimal operation. As only some hundreds of milliwatts are necessary to feed the double injection, about 1 W is still available for the auxiliary beam. In fact, the optical setup is similar to the one used to create an active feedback loop and to cool down the movable mirror (1.22(a)). The auxiliary beam is first intensity-modulated by an acousto-optic modulator. It operates in the Bragg regime where we can reach a coupling efficiency, and thus a modulation depth $\delta I/I$, up to 80%. The zeroth-order diffraction is reflected upon the back-end of the movable mirror as depicted on Figure 4.6(a). We use an acousto-optic modulator sold by AA opto-electronics (MT200-A0,5-800) driven by RF driver (AMPA-B). For the alignment, a system of two mirrors and a thin lens -roughly focusing the beam onto the end mirror- is used. The measurement cavity is placed inside a vacuum chamber (ST300 ^4He cryostat) presenting optical front and rear access; the rear access is used to inject the auxiliary beam and drive the movable mirror with radiation pressure. Two precautions must be taken while aligning the auxiliary beam. First, for the mirror drive to be maximum, it is important for overlap between the auxiliary beam and the mirror mechanical mode to be optimized.

Second, efforts must be made so that the auxiliary beam is coupled to the movable mirror under a non-zero angle to prevent any coupling with cavity. Indeed, since the cavity presents a very high finesse ($\sim 10^5$), even a low mode-matching of the high-power beam with the cavity would eventually damage the dielectric coating of the mirrors. Since the cavity is placed several

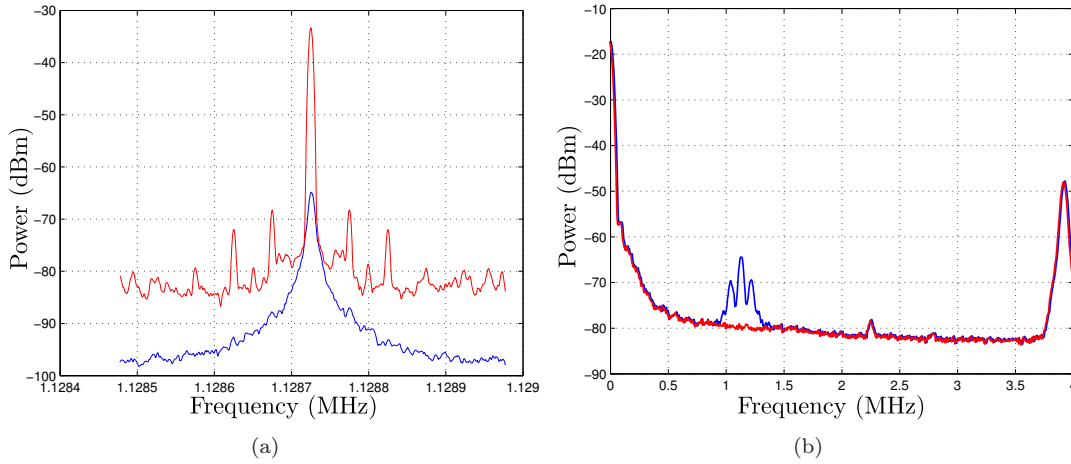


Figure 4.7: (a) Resulted coherent drive of the movable mirror, measured by the homodyne detection, with the auxiliary beam at a power $P_{\text{aux}} = 200$ mW and a modulation depth of 50%. A signal 40 dB above the maxima of the thermal resonance is achieved. The thermal spectrum depicted on blue has been acquired using a resolution bandwidth of $\nu_{\text{RBW}} = 4$ Hz. (b) Effect of the coherent drive on the reflected intensity spectrum: the low-frequency classical laser noise is convoluted with the mirror motion creating sidebands at a range of approximately 400 kHz.

centimetres away from the rear access -which is only 1-cm large- of the cryostat, the possible manipulation of the laser beam in order to properly align it is limited. Nevertheless, a fairly good alignment is possible achieving a mechanical response 40 dB above the thermal noise at the mechanical resonance Ω_M (see Figure 4.7(a)). The driving level achieved on Figure 4.7(a) is obtained with relatively poor optical characteristics of the auxiliary beam: 200 mW of incident power and a modulation depth of 50%. It may be optimized by increasing the auxiliary beam power up to 1 W and increasing the modulation depth by an optimization of the coupling between the beam and the acousto-optic modulator.

The corresponding displacement peak may be observed on the homodyne detection output when the probe beam is coupled to the cavity but also at the output of the balanced detection of the pump beam since its intensity is contaminated by the mirror motion. The A+B output of the balanced detection is then sent to a home-made demodulator consisting of a low-pass filter (MiniCircuits PLP 1.9 MHz), a frequency mixer (MiniCircuits SBL-1) and a second low-pass filter presenting a cut-off frequency $f_c = 300$ kHz (MiniCircuits LPFBOR-300 kHz). The corresponding error signal is depicted on Figure 4.6(b). The blue circles correspond to the experimental points provided by a digital oscilloscope. The red continuous line is the theoretical fit done using equation (4.24) where we have used the optical and mechanical parameters of the cavity measured independently. As Figure 4.6(b) indicates, this signal qualifies as an error signal as it presents a steep slope within the bandwidth of the cavity and changes sign around zero-point. We note that, as the error bars associated to the experimental points suggest, the sensitivity of the detuning measurement is maximal very close to resonance. Indeed, as the cavity is further detuned, either to the blue or to the red side, the reflected intensity becomes more contaminated by the mirror thermal motion, thereby deteriorating the signal-to-noise ratio of the measurement. Let us note that this detection is also sensitive to the thermal noise of the mirror; in particular the contamination lock-in error signal also contains the mirror

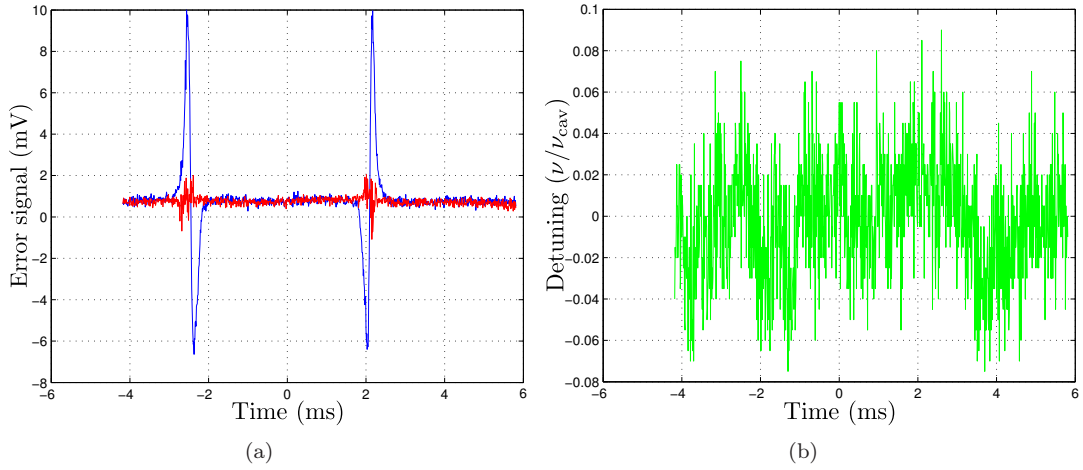


Figure 4.8: (a) The lock-in error signal with the mirror excitation turned off (blue) and on (red). (b) The error signal while the laser frequency is stabilized onto the measurement cavity.

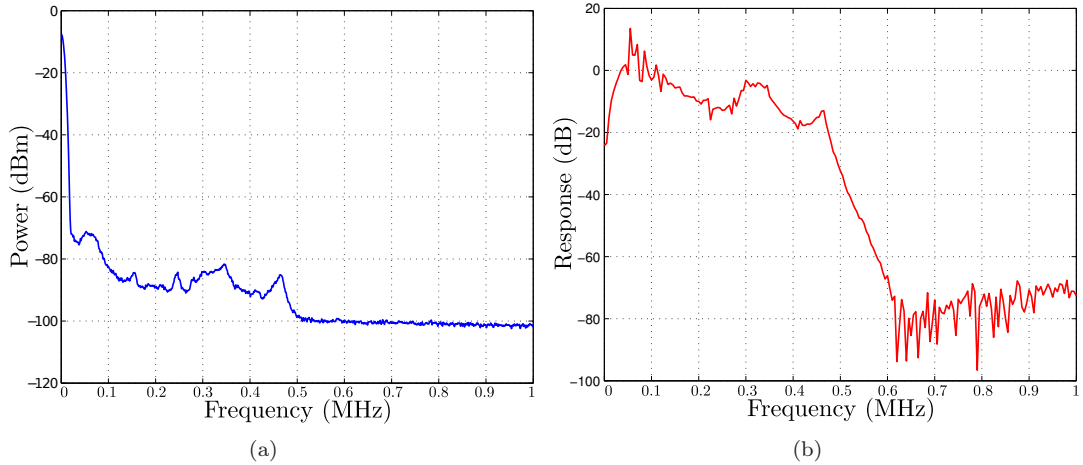


Figure 4.9: (a) The spectrum of the lock-in error signal with the feedback loop turned on and (b) the response of the loop to a coherent perturbation.

displacement $X_\phi(t)$. This is directly verified by observing the resulted error signal without the coherent drive of the mirror. In this case the thermal noise is demodulated at the resonance frequency Ω_M as Figure 4.8(a) shows. While sweeping the cavity around its resonance the auxiliary beam is turned off and the corresponding contamination error signal is observed with a digital oscilloscope. While the auxiliary beam is off, the red curve shows that the demodulated quadrature X_ϕ is clearly visible while the pump beam interacts with the cavity. On the other hand, as soon as the mirror is driven, a nice error signal is derived. In the following, we have used the contamination lock-in error signal also to lock the laser frequency onto the cavity. The stabilized error signal is depicted on Figure 4.8(b). Its peak-to-peak amplitude (calibrated in the cavity-bandwidth units) gives a rough estimation on the stability of the loop. The cavity detuning is better than 6%.

The movable mirror is coupled to a thermal bath characterized by a temperature T . The

fundamental gaussian mode of the plano-convex movable mirror indeed drifts some Hz in a time interval of 30 minutes. Any temperature variation, due to the mirror heating by the coupled laser field, lead to a drift of the mechanical resonances of the mirror. As we can see in Figure 4.7(a), the mirror is driven to its fundamental high-Q, mechanical resonance. Its width being 1 Hz, any drift results in a decrease of the response to the drive, as well as in a phase-shift of the local oscillator used for the demodulation. Both variations are of multiplicative nature and, as we will see later on, have no impact on the offset of the error signal but only change the global gain of the servo-loop. We have written a LabVIEW script in order to automate the drive frequency adjustment. For that purpose, we have interfaced the generator driving the acousto-optic modulator and the spectrum analyzer coupled to the output of the homodyne detection, measuring the reflected phase of the probe beam. The sequence is as follows: every 5 minutes an amplitude measurement of the excitation modulation peak on the intensity quadrature is realized by the spectrum analyzer. Then, if the amplitude difference between two successive measurements is greater than 1 dB, a frequency measurement of the modulation peak is realized and the program sends the corresponding command to the generator. In practice, after 30 minutes of experimental operation, the mirror reaches an equilibrium and frequency adjustment of the drive is no longer necessary.

This scheme provides an extreme stability on a time scale of one hour. We have finally measured the spectrum of the error signal while the feedback loop is turned on. The corresponding spectrum is depicted on Figure 4.9(a), where we observe that the bandwidth of the loop reaches 500 kHz as we systematically couple low-pass filters to the lock-box outputs at some hundreds of kilohertz. Finally, with a network analyzer, we have measured the response of the feedback loop to a monochromatic external perturbation up to 1 MHz. The perturbation was induced by a frequency modulation produced by the electro-optic modulator of the laser cavity. The spectrum of the error signal is thus reproduced while the bandwidth of the loop is also evident as depicted on Figure 4.9(b). Let us note that this Bode diagram is made while the laser frequency is stabilized and the feedback loop is closed. The open-loop diagram is also necessary in order to quantify the feedback quality. In order to realize the open-loop measurement, it would be necessary to manually - or at low frequency- keep the laser frequency onto the cavity resonance. However, the residual vibrations of the cavity overwhelm the measured signal making the open-loop Bode diagram impossible to measure.

4.5.1.1 Low-frequency measurement of a signal

We have finally tested the low-frequency sensitivity of the contamination lock-in error signal. For this the double-injection scheme is used. Both beams are coupled to the measurement cavity. As Figure 4.10(a) shows, a laser beam, drawn in blue, is used to create the error signal which is then used to stabilize the laser frequency via a double-pass acousto-optic modulator. At the same time, a signal beam is also coupled to the cavity and is used to induce a low-frequency displacement of the movable mirror. Let us note that even if it is not depicted on the figure, the signal beam is also coupled to a double-pass AOM used to lock its frequency but also to modulate its intensity. The VCO that drives the AOM is driven by a 100-Hz pulse generated by a function generator. Therefore, the intensity of the signal beam is modulated at 100 Hz with a modulation depth of 100%. Even though the AOM of the signal beam is placed before the filtering cavity, when the beam is turned for 10 ms it stays in the capture range of the cavity's lock-in loop. The 100% depth intensity modulation passes the filtering

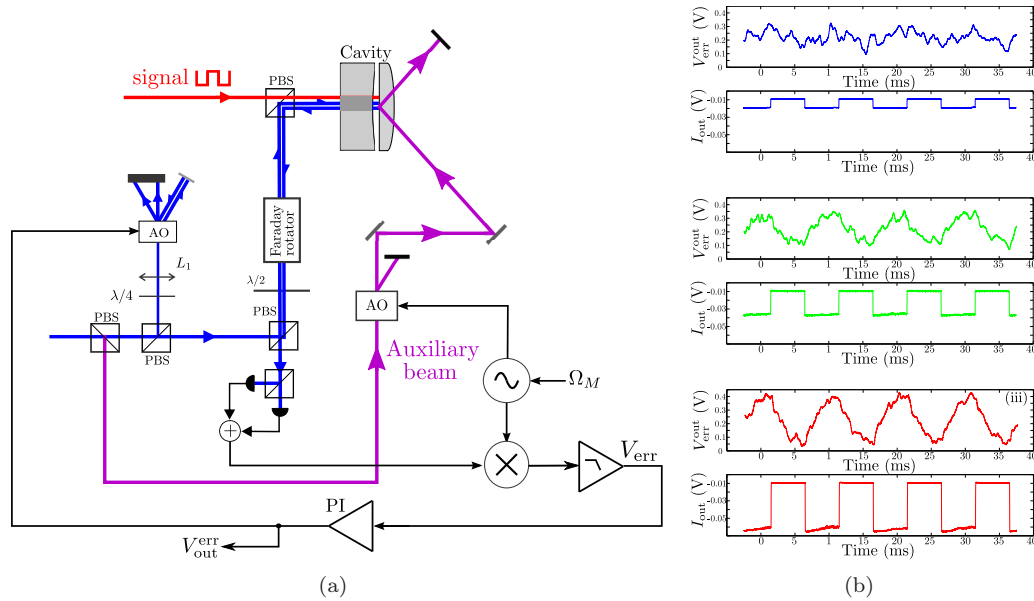


Figure 4.10: (a) The intense (blue) beam is used to create the contamination error signal. The laser frequency is locked to the cavity using a double-pass AOM. A signal, beam (red) is also coupled to the measurement cavity inducing a low-frequency displacement. The signal beam is intensity-modulated (modulation depth of 100%). The induced displacement is measured by the contamination error signal and compensated by the feedback loop. The feedback signal driving the AOM is visualized with a digital oscilloscope. For simplicity reasons, the optical path of the signal beam is not shown. (b) Derivation of the resulting displacement measurement for different signal beam powers.

cavity undisturbed. An attenuator serves then to set the power of the signal beam sent into the measurement cavity.

Since for a closed loop the error signal is zero, the readout of the resulted displacement is performed by observing the output voltage which drives the AO modulators to compensate the perturbation. The error signal beam (blue) is set to 1.5 mW while the power of the signal -red- beam is swept from some μW s up to some hundreds of μW s. The DC output of the homodyne detection also monitors the reflected intensity of the signal beam. Figure 4.10(b) shows the measured displacements for three different input powers of the signal beam. Each subfigure contains two curves. The top one corresponds to the output of the feedback loop $V_{\text{out}}^{\text{err}}(t)$ compensating the induced displacement. The second one is the intensity modulation of the signal beam measured by the homodyne detection.

In order to calibrate the resulted displacements, a ramp is used to drive the laser frequency via the AOM and sweep the cavity. The Airy peak -or the error signal- is then simultaneously visualized along with the ramp on a digital oscilloscope. One can then compare the ramp to the cavity linewidth and derive the corresponding displacement. subfigures (i) to (iii) show the measured displacement as the input power is increased. In subfigure(i) the displacement is barely visible as it is lost within the residual vibrations of the cavity, while subfigure(iii) shows a situation where the low-frequency displacement is clearly visible on the correction signal. The

resulted low-frequency displacement is found to be $\Delta x_{\min} \simeq 10^{-13}$ m.

4.5.2 Experimental limits

What we proposed earlier is to replace the phase-modulator by directly inducing a mirror displacement. Even though the analogies between the two schemes are visible, we will show that there exist important differences which may potentially lead to significant improvements on the limits of the cavity detuning measurements, up to several orders of magnitude. As we have discussed earlier, two categories of limits could potentially affect the sensitivity of any detection method in general. On one hand, the slope fluctuations, the fluctuations of the transfer function which are of multiplicative nature (such as low-frequency intensity fluctuations). These fluctuations result in a finite accuracy for the measurement. On the other hand, some noises always add to the measured signal, and imply sensitivity limits for the measurement (such as a residual amplitude modulation caused by the phase modulator for instance).

4.5.2.1 Slope fluctuations

Equation (4.24) shows that $V_{\text{err}}(t)$ appears as the product of a gain function $G(p_i)$ (where p_i denotes the different parameters defining G) with the detuning $\bar{\psi}$. It is thereby clear that any gain variation could not be distinguished from a detuning variation. Mathematically, this is equivalent to write that the increases of V_{err} along G and $\bar{\psi}$ respectively are identical:

$$(dV_{\text{err}})_{p_i} = (dV_{\text{err}})_{\bar{\psi}} \Rightarrow G\delta\bar{\psi} = \delta G\bar{\psi}. \quad (4.26)$$

The above equation implies that a relative increase of the gain function G results in an apparent relative increase of the measured detuning, $\delta\bar{\psi}/\bar{\psi} = \delta G/G$, such that the direct effect of gain variation is a finite accuracy over the detuning determination. Two potential sources of slope fluctuations are identified in our experimental setup: the thermal noise also detected by the demodulation procedure and the frequency drifts of the mechanical resonance due to the heating of the mirror. We will now quantitatively estimate the effect of these two parameters.

Thermal noise

The principle of the demodulation procedure used to extract the quadratures of the mirror motion is depicted on 4.6(a). Naturally, one important source of slope fluctuations arises from the thermal noise detected when measuring the mirror displacement. Thermal noise then has to be taken into account when writing the displacement $\delta x[\Omega]$ in equation (4.22):

$$\delta I_s^{\text{out}}[\Omega] \simeq 4k\bar{\alpha}_s \sqrt{\bar{I}_s^{\text{out}}} \frac{\sqrt{TP}}{\gamma^2|\gamma - P|} \times \bar{\psi} \times \chi[\Omega] (F_0\delta(\Omega - \Omega_d) + F_T[\Omega]). \quad (4.27)$$

This additional term results in a slowly varying noise term $X_\phi(t)$ which corresponds to a thermally-driven motion of the mirror [24], which must be included in the expression of the demodulated signal:

$$V_{\text{err}}(\bar{\psi}) = 4k\bar{\alpha}_s \sqrt{\bar{I}_s^{\text{out}}} \frac{\sqrt{TP}}{\gamma^2|\gamma - P|} \left\{ F_0 \text{Re} \left(\frac{i}{M\Omega_M\Gamma_M} e^{i\phi} \right) + X_\phi(t) \right\} \bar{\psi}. \quad (4.28)$$

This noise term is, in turn, responsible for a statistical dispersion of the slope $\Delta V_{\text{err}}(\bar{\psi})$ given by:

$$\Delta V_{\text{err}}(\bar{\psi}) = 4k\bar{\alpha}_s \sqrt{\bar{I}_s^{\text{out}}} \frac{\sqrt{TP}}{\gamma^2|\gamma - P|} \Delta X_\phi \bar{\psi}, \quad (4.29)$$

with $\Delta X_\phi = (k_B T / M \Omega_M^2)^{1/2}$ for a demodulation bandwidth large compared to Γ_M [24]. Using equation (4.26), we can finally give the uncertainty caused by thermal noise (for $\phi = \pi/2$):

$$\frac{\delta \bar{\psi}}{\bar{\psi}} = \frac{\Delta V_{\text{err}}(\bar{\psi})}{V_{\text{err}}(\bar{\psi})} = \frac{\delta x_T}{\delta x_0}, \quad (4.30)$$

where $\delta x_T = \Delta X_\phi$ denotes the thermal induced motion variance and $\delta x_0 = F_0 / M \Omega_M \Gamma_M$ the coherent oscillation amplitude. Practically, the mechanical mode is driven more than 40 dB above thermal noise as is depicted on Figure 4.7(a). We note that in order to compare the two measured amplitudes, one must take into account the resolution bandwidth ν_{RBW} of the thermal noise measurement. In this case, the thermal noise acquisition was made with a $\nu_{\text{RBW}} = 100$ Hz. The monochromatic drive is then almost 500. In reality, the mechanical susceptibility is not purely Lorentzian: the multimode nature of the mirror results in a so-called thermal background, which can be considered as being frequency-independent around a specific resonance. Demodulating over a large bandwidth can make this background contribution comparable or even larger than the one of the mechanical resonance in $\Delta V_{\text{err}}(\bar{\psi})$. A larger driving amplitude will then be necessary in order to compensate the additional noise induced by such a large demodulation bandwidth.

Mechanical frequency drifts

Another important source of slope fluctuations arises from the mechanical frequency drifts $\delta \Omega_M$, which are mostly due to the fluctuations of mirror temperature due to the laser-induced heating. Their effect on $V_{\text{err}}(\bar{\psi})$ can be written as follows:

$$\begin{aligned} \delta V_{\text{err}}(\bar{\psi}) &= 4k\bar{\alpha}_s \sqrt{\bar{I}_s^{\text{out}}} \frac{\sqrt{TP}}{\gamma^2|\gamma - P|} F_0 \text{Re} \left(\frac{\partial \chi}{\partial \Omega_M} [\Omega_M] e^{i\phi} \right) \bar{\psi} \delta \Omega_M \\ &= -4k\bar{\alpha}_s \sqrt{\bar{I}_s^{\text{out}}} \frac{\sqrt{TP}}{\gamma^2|\gamma - P|} F_0 \frac{\Gamma_M \delta \Omega_M}{M (\Omega_M \Gamma_M)^2} \bar{\psi}. \end{aligned} \quad (4.31)$$

The resulting equivalent detuning fluctuations are therefore given by:

$$\frac{\delta \bar{\psi}}{\bar{\psi}} = -\frac{\delta \Omega_M}{\Omega_M}. \quad (4.32)$$

For $\Omega_M / 2\pi$ in the MHz-range, the effect of a few Hertz drift will hence be negligible. Note that the above expression applies as long as the frequency drift is small compared to the resonance width $\delta \Omega_M \ll \Gamma_M$. However, in our system, we use an ultra-low dissipation mechanical mode ($\Gamma_M / 2\pi \simeq 1$ Hz) and the drift effects may be significant.

4.5.2.2 Detection noise

The detection noise is more critical than the slope noise, as it sets a lower detection floor. Taking it into account leads us to include a supplementary noise term in equation 4.22:

$$\delta I_s^{\text{out}}[\Omega] = \delta I_{\text{shot}}[\Omega] + 4k\bar{\alpha}_s \sqrt{\bar{I}_s^{\text{out}}} \frac{\sqrt{TP}}{\gamma^2|\gamma - P|} \bar{\psi} \delta x[\Omega]. \quad (4.33)$$

In our experiment, the reflected intensity detected is quantum-noise-limited. Therefore we may write the spectrum of the reflected intensity fluctuations as follows:

$$S_{I_s}^{\text{out}}[\Omega] = \bar{I}_s^{\text{out}} + \left(4k\bar{\alpha}_s \sqrt{\bar{I}_s^{\text{out}}} \frac{\sqrt{TP}}{\gamma^2|\gamma - P|} \right)^2 \bar{\psi}^2 S_x[\Omega]. \quad (4.34)$$

Assuming the movable mirror is coherently driven at frequency $\Omega_d = \Omega_M$, and integrating the above equation along the demodulation bandwidth ν_{DS} , one obtains:

$$\langle V_{\text{err}}(\bar{\psi})^2 \rangle = \bar{I}_s^{\text{out}} \nu_{\text{DS}} + \left(4k\bar{\alpha}_s \sqrt{\bar{I}_s^{\text{out}}} \frac{\sqrt{TP}}{\gamma^2|\gamma - P|} \right)^2 \bar{\psi}^2 \delta x_0^2, \quad (4.35)$$

where we noted $\delta x_0 = (F_0/M\Omega_M\Gamma_M)$. The quantum intensity noise thereby implies a detection limit $\bar{\psi}_{\text{min}}$ given by:

$$\frac{\bar{\psi}_{\text{min}}}{\gamma} = \frac{1}{4k\sqrt{\bar{I}_s^{\text{in}}}} \times \frac{\gamma^2(\gamma - P)}{TP\delta x_0} \times \sqrt{\nu_{\text{DS}}}. \quad (4.36)$$

For a detection bandwidth $\nu_{\text{DS}} = 1$ kHz, an input power $\bar{I}_s^{\text{in}} = 1$ mW, a wavelength $\lambda = 800$ nm, a finesse $\mathcal{F} = \pi/\gamma = 300\,000$, external losses $P = 0.4\gamma$, and a driven amplitude $\delta x_0 = 0.1$ pm, we find $\bar{\psi}_{\text{min}}/\gamma \simeq 2 \times 10^{-7}$, which corresponds to a drift resolution on the order of 100 mHz for a cavity bandwidth in the MHz-range.

4.5.3 Comparison with the Pound-Drever scheme

An interesting question is the quantitative comparison of the lock-in optomechanical detection with the PDH technique, the latter being thoroughly described in section 1.6.4 and [40]. Its core principle consists in detecting the intensity of the field reflected by the cavity, at the frequency Ω_{PDH} of the sidebands applied to the incident light using a phase modulator. In the ideal case, the phase-modulated incident field writes:

$$\alpha^{\text{in}}(t) = \bar{\alpha}^{\text{in}} e^{i\beta \cos \Omega_{\text{PM}} t}, \quad (4.37)$$

with β denoting the phase modulation depth. However, commercial, birefringent medium-based phase modulators do not provide a pure phase modulation, the light amplitude being unavoidably slightly modulated as well at the frequency of phase modulation (RAM):

$$\alpha^{\text{in}}(t) = \bar{\alpha}^{\text{in}} \times (1 - \beta' - \beta' \cos \Omega_{\text{PM}} t) e^{i\beta \cos \Omega_{\text{PM}} t}, \quad (4.38)$$

where β' denotes the rejection depth. The field reflected by the cavity $\alpha^{\text{out}}(t)$ can be thereby written as [40]:

$$\begin{aligned} \frac{\alpha^{\text{out}}(t)}{\bar{\alpha}^{\text{in}}} &= (1 - \beta') \times (J_0 r_\psi[0] + iJ_1 r_\psi[-\Omega_{\text{PM}}]e^{i\beta \cos \Omega_{\text{PM}}t} + iJ_1 r_\psi[\Omega_{\text{PM}}]e^{-i\beta \cos \Omega_{\text{PM}}t}) \\ &\quad - \frac{\beta'}{2} e^{i\beta \cos \Omega_{\text{PM}}t} (J_0 r_\psi[0] + iJ_1 r_\psi[-\Omega_{\text{PM}}]e^{i\beta \cos \Omega_{\text{PM}}t} + iJ_1 r_\psi[\Omega_{\text{PM}}]e^{-i\beta \cos \Omega_{\text{PM}}t}) \\ &\quad - \frac{\beta'}{2} e^{-i\beta \cos \Omega_{\text{PM}}t} (J_0 r_\psi[0] + iJ_1 r_\psi[-\Omega_{\text{PM}}]e^{i\beta \cos \Omega_{\text{PM}}t} + iJ_1 r_\psi[\Omega_{\text{PM}}]e^{-i\beta \cos \Omega_{\text{PM}}t}), \end{aligned} \quad (4.39)$$

where $J_0 = J_0(\beta)$ and $J_1 = J_1(\beta)$ denote the zeroth- and first-order Bessel functions respectively. Keeping only the reflected intensity terms oscillating at frequency Ω_{PM} , and neglecting the second-order terms in J_1 and β' , the above expression yields:

$$\begin{aligned} I_{\Omega_{\text{PM}}}^{\text{out}}(t) &= -2(1 - \beta')J_0J_1\bar{I}^{\text{in}} (\text{Im}\{r_\psi^*[0](r_\psi[-\Omega_{\text{PM}}] + r_\psi[\Omega_{\text{PM}}])\} \cos \Omega_{\text{PM}}t \\ &\quad + \text{Re}\{r_\psi^*[0](r_\psi[-\Omega_{\text{PM}}] + r_\psi[\Omega_{\text{PM}}])\} \sin \Omega_{\text{PM}}t) \\ &\quad - J_0^2\beta'\bar{I}^{\text{in}}|r_\psi[0]|^2 \cos \Omega_{\text{PM}}t. \end{aligned} \quad (4.40)$$

Demodulating at frequency Ω_{PM} and low-pass filtering the reflected intensity, we obtain (assuming $\bar{\psi} \ll \gamma$):

$$V_{\text{err}}(\psi) \simeq (1 - \beta')J_0J_1\bar{I}^{\text{in}} \times \frac{2T}{\gamma^2} \bar{\psi} - J_0^2\beta'\bar{I}^{\text{in}}\mathcal{R}_0, \quad (4.41)$$

with $\mathcal{R}_0 = (T-P)^2/(T+P)^2$ the cavity reflection coefficient at the optical resonance. The above equation shows that the obtained signal is the sum of two terms. The first term, proportional to the detuning, corresponds to the contribution which identifies to the signal expected in the ideal, pure phase-modulation case (though with a slope reduced by a factor $1/(1 - \beta')$ due to reduced carrier intensity). The second term is independent from the detuning: as a phase-modulation converts the phase fluctuations of the incident light into intensity variations, an intensity-modulation converts the intensity changes into an intensity variation as well. In absence of any intensity fluctuation, this second term simply results in an offset in the error signal, without any further consequence on the detuning sensitivity. Instead, in presence of intensity fluctuations $\delta\bar{I}^{\text{in}}$, this corresponds to an additive noise, limiting thereby the sensitivity to a lower limit $\bar{\psi}_{\text{min}}$ given by:

$$\bar{\psi}_{\text{min}}/\gamma = \frac{J_0\beta'\mathcal{R}_0\gamma}{2TJ_1} \times \frac{\delta\bar{I}^{\text{in}}}{\bar{I}^{\text{in}}}. \quad (4.42)$$

For the above cavity parameters, and with an intensity noise depth $\delta\bar{I}^{\text{in}}/\bar{I}^{\text{in}} = 1\%$ (typically reached using a standard stabilization scheme [24]), a phase-modulation depth of 1 rad (corresponding to the optimum parameter [40]), and a rejection depth $\beta' \simeq 0.01$ (corresponding to a residual intensity-modulation depth of -40 dB [83]) we find that the Pound-Drever detuning sensitivity is limited to the level of $\bar{\psi}_{\text{min}}/\gamma \simeq 3 \times 10^{-5}$, which is 2 orders of magnitude above the sensitivity reached with the lock-in optomechanical detection method.

Towards quantum correlations at ambient temperature

The main effect preventing us from observing quantum optomechanical correlations at room temperature is the contamination of both beams by thermal noise. The thermal motion of the mirror is obviously seen by the probe beam and when the cavity is not perfectly tuned at resonance this motion is also imprinted on the intense beam. This creates fake correlations which completely mask the quantum radiation pressure noise. This effect, as we will show in this chapter, leads to a demanding criterion on the stability of the measurement cavity. In chapter 3, we described the improvement of our laser source in order to provide a quantum-noise limited laser light up to 10 mW at 1 MHz. This increases the radiation-pressure effects by one order of magnitude, leading to a corresponding increase of the signal-to-noise ratio between radiation pressure and thermal noise. Furthermore, we have developed a novel and robust technique in order to perform a direct measurement of the contamination. This signal can be used to either dynamically control the cavity detuning and then the contamination level in a feedback loop or to perform a feed-forward technique by post-selecting useful data. We will present in this chapter the efforts made towards this direction. We will begin by providing a quantitative description of the multi-modal character of the plano-convex movable mirror in order to show that, in our case, it is preferable to choose a analysis frequency without any mechanical resonance of the mirror. We will then expand the stability tolerance criterion (equation 4.16) to the out-of resonance case. Finally, we will discuss the choice of the frequency analysis and the development of an experiment that may allow the observation of radiation-pressure effects in the near future.

5.1 Multi-modal response of the movable mirror

Radiation pressure and thermal noise both present very similar effects on a harmonic oscillator such as our movable mirror. They both come from the response of the resonator to an external force. However, the multi-modal character of the mirror displacement sets a fundamental difference between both. Indeed, whereas the same radiation-pressure force is applied to all vibrational modes of the mirror. Thermal noise can be described as the sum of all the responses of the modes to uncorrelated Langevin forces. This difference is the reason why a spectral dependence of the mirror mechanical response occurs. It can be shown [24] that the intra-cavity field induces a deformation on the surface of the movable which is equivalent to an effective, one-dimensional displacement of the mirror $x(t)$. In particular, this displacement is given by the overlap integral between the mirror deformation and the incident laser beam, with

an optical waist w_0 situated on the mirror:

$$x(t) = \langle u(t), v_0^2 \rangle, \quad (5.1)$$

where $v(r) = \sqrt{2/\pi w_0^2} e^{-r^2/w_0^2}$ is the spatial profile of the coupled light field and $u(t)$ is the projection of the mirror deformation on the propagation direction of the field. An effective mechanical susceptibility χ_{eff} can be introduced to describe the mirror motion induced both by thermal and radiation pressure effects. The mirror motion x is:

$$x[\Omega] = \chi_{\text{eff}}[\Omega](F_{\text{rad}}[\Omega] + F_T[\Omega]), \quad (5.2)$$

where the effective susceptibility is given by the sum of the mechanical susceptibilities over all modes weighted by the overlap between the light field and the modes profiles u_n :

$$\chi_{\text{eff}}[\Omega] = \sum_n \langle u_n, v_0^2 \rangle \chi_n[\Omega]. \quad (5.3)$$

The susceptibility of each mode is given by equation (??):

$$\chi_n[\Omega] = \frac{1}{M_n[\Omega_n^2 - \Omega^2 - i\Omega_n^2 \phi_n^2[\Omega]]}, \quad (5.4)$$

with M_n the mass of the n^{th} mode and $\phi_n[\Omega] = \Omega/(\Omega_n Q_n)$ the corresponding loss angle. The radiation-pressure force is a global force applied to all modes given by:

$$F_{\text{rad}}[\Omega] = 2\hbar k I[\Omega], \quad (5.5)$$

whereas the overall Langevin force F_T is the incoherent sum of all the uncorrelated Langevin forces F_T^n for modes n given by:

$$F_T[\Omega] = \sum_n \langle u(t), v_0^2 \rangle \frac{\chi[\Omega]}{\chi_{\text{eff}}[\Omega]} F_{T,n}[\Omega]. \quad (5.6)$$

As in the mono-modal treatment presented in the first chapter, the spectrum of the Langevin force is related to the dissipative part of the susceptibility (i.e. the imaginary part) and can then be written as (equivalently to equation 1.74):

$$S_{T,n}^{\text{eff}} = -\frac{2k_B T}{\Omega} \text{Im}\left(\frac{1}{\chi_{\text{eff}}[\Omega]}\right). \quad (5.7)$$

The spectrum of the radiation-pressure force will be given by equation (1.69). We are specifically interested in the signal-to-noise ratio, in the case of multi-modal motion of the mirror $S_x^{\text{rad}}/S_{T,n}^{\text{eff}}$, which is given by:

$$\frac{S_x^{\text{rad}}}{S_{T,n}^{\text{eff}}} = 32 \frac{\hbar^2 \mathcal{F}^2 \bar{I}_{\text{in}}}{\lambda k_B T} \frac{-\Omega}{\text{Im}[1/\chi_{\text{eff}}[\Omega]]}. \quad (5.8)$$

For the mono-modal case the second term becomes equal to $1/(M\Omega\phi)$ and does not depend on the frequency. The latter equation reduces to equation (1.77). However, in the multi-modal case the signal-to-noise ratio has a strong frequency dependence as the effective susceptibility is a quite complex function. The calculation of the effective mechanical susceptibility is an

extremely complicated task: first, a perfect knowledge of all vibrational modes is needed and, second, the numerical calculation of such a sum is straightforward. Nevertheless, there exists an alternative method [84], [85], [86], which, combined with the fluctuation-dissipation theorem, gives the static effective susceptibility by calculating the mirror deformation to a constant force. This approach gives a low frequency susceptibility equal to [87]:

$$\chi_{\text{eff}}[0] = \frac{1 - \sigma^2}{\sqrt{2\pi}(1 - i\phi_0)Ew_0}, \quad (5.9)$$

where σ is the Poisson coefficient, E the Young module of the material and ϕ_0 the loss angle .

5.1.1 Thermal background effect on the response

We will briefly describe the mechanical background effect on the mechanical response. We can distinguish three different cases: at the mechanical resonance Ω_n , at lower and at higher frequency.

The mechanical resonance corresponds to the orthogonal normal modes of the mirror. For a small displacement, the linear response theory applies and they can be considered completely independent from one another. Moreover, it can be shown that [70] the response of the mirror is the superposition of the response of the resonant mode alone and the response of the mechanical background of the low frequency of all near-resonant modes. In particular, one may write down the ratio between the mirror response at resonance and at low frequency:

$$\left| \frac{\chi_n^{\text{eff}}[\Omega_n]}{\chi_n^{\text{eff}}[\Omega = 0]} \right|^2 \simeq \frac{2\pi E^2 w_0^2}{(1 - \sigma^2)^2 (M_n^{\text{eff}})^2 \Omega_n^4 \phi_n^2}, \quad (5.10)$$

where we have supposed that $\phi_0 \ll 1$ and $M_n^{\text{eff}} = M_n / \langle u_n, v_0^2 \rangle$. Using $E = 7.3 \times 10^{10}$ Pa and $\sigma = 0.17$ we find numerically a ratio of 10^6 , indicating that near a mechanical resonance the motion is mainly ruled by the resonant mode. The signal-to-noise ratio at resonance is:

$$\frac{S_x^{\text{rad}}[\Omega \simeq 0]}{S_x^T[\Omega \simeq 0]} = \frac{32\hbar^2 \mathcal{F}^2 \bar{I}_{\text{in}}}{\lambda^2 k_B T} \frac{1}{M_n^{\text{eff}} \Omega_n \phi_n}. \quad (5.11)$$

Far from resonance, i.e. at low frequency, or in between two resonances, the effective susceptibility χ_{eff} is ruled by the mechanical background. A good estimation of the mechanical susceptibility is then given by equation (5.9). The corresponding signal-to-noise ratio is obtained by combining equations (5.8) and (5.9):

$$\frac{S_x^{\text{rad}}[\Omega \simeq 0]}{S_x^T[\Omega \simeq 0]} = \frac{32\hbar^2 \mathcal{F}^2 \bar{I}_{\text{in}}}{\lambda^2 k_B T} \frac{(1 - \sigma^2)^2 \Omega}{\sqrt{2\pi} E w_0 \phi_0}. \quad (5.12)$$

By comparing the two equations above, for the parameters of the fundamental gaussian mode with $M_1 = 153$ mg, $\Omega_1/2\pi = 1.1$ MHz and $\phi_0 = \phi_1$, we find a a signal-to-noise ratio 500 times better out of resonance than at resonance; at low-frequency the thermal background responds more than 20 dB better to radiation pressure better than the independent vibrational mode. Finally, we note that just above the mechanical resonance, destructive interference effects between the vibrational mode and the mechanical background occur, leading to an anti-resonance on the mirror response. This effect, already described in section 1.8.4, leads to

dips in the signal-to-noise ratio at the antiresonance frequency. It can be shown that in the anti-resonance the mirror responds up to several dozens of dB less.

5.2 Measurement of the mirror response to a radiation-pressure force

By taking into account the frequency dependence of the multi-modal mechanical response, the choice of the most favourable analysis frequency band for the optomechanical correlations is an open question which must be addressed experimentally. As done for the classical optomechanical correlations experiment (see chapter 5), the idea is to apply a radiation-pressure force onto the movable mirror via the pump beam and observe the mechanical response via the phase-shift of the probe beam. In the following, we will describe the experimental scheme that may allow to demonstrate the signal-to-noise S_x^{rad}/S_x^T spectral dependence and to choose the analysis frequency band on which we will attempt to perform the quantum correlations experiment.

5.2.1 Experimental setup

The core of the experimental setup for this kind of measurement is of course the double-injection scheme, already described in the first chapter. We have seen that our setup can provide two different ways to drive the movable mirror: either using the auxiliary beam or the pump beam. For the classical correlations we wish to observe, it is preferable to use the pump beam. Indeed, it is crucial for the overlap between the probe beam and the excitation point to be optimal. This can be done more easily using the pump beam as the double-injection configuration ensures a perfect alignment of both beams. On the other hand, no such guarantee exists for the auxiliary beam. Experimentally, it is then difficult to ensure that the incident beam really probes the excitation point. Furthermore, the fact that the pump beam is coupled to an ultra high-finesse cavity ($\mathcal{F} \sim 10^5$) can prove to be favourable as with an incident beam of 1 mW the intra-cavity field can reach up to several Watts, making radiation-pressure effects greater; whereas the auxiliary beam can reach at best 1 Watt.

In order to create a modulation, two possible solutions can be taken into consideration. As we have done for the classical correlations, the electro-optical modulator can be used. However, we have described, that the radio-frequency parasite emitted by the high voltage driving the EOM considerably complicates the measurement (see section 2.1.1). A first attempt has been made by driving the EOM at the half-frequency $\Omega/2$. The non-linear response of the modulator then provides an intensity modulation at frequency Ω (see figure 2.1). The frequency of the output of the network analyzer has to be divided by 2. It is actually the electronic circuit used to extract the quadratures of the mirror motion as depicted in figure 1.20(a) [24]. It consists of a Voltage Controlled Oscillator controlled by a Phase Locking Loop (PLL). The major drawback of this scheme is that the capture range of the lock-in is limited to some kHz. When the input modulation is out of this range, the circuit must be manually tuned by means of a potentiometer in order for it to become operational. However, the automatization of the measurement is severely compromised as every few minutes one has to tune the electronic circuit.

We have then chosen to reduce the complexity of the setup by using the acousto-optic modulator used to lock the frequency of the pump beam on the measurement cavity (see

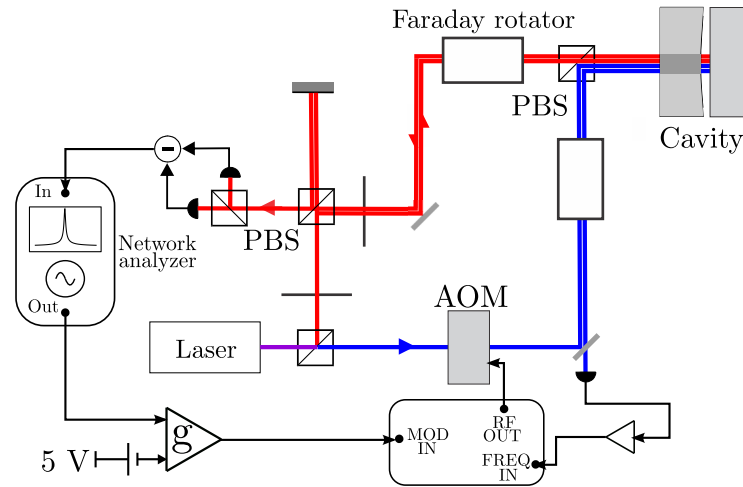


Figure 5.1: A network analyzer is used to measure the mechanical response of the movable mirror. It induces an intensity modulation via an acousto-optic modulator and monitors the output of the homodyne detection at the modulation frequency.

figure 3.21(b)). Indeed, the VCO driving the acousto-optic modulator can modulate the intensity of the beam by modulating the amplitude of the acoustic wave inside the AOM crystal. The corresponding setup is depicted on Figure 5.1. The network analyzer output provides a monochromatic signal which is sent to a pre-amplifier presenting a gain and an offset (TEGAM pre-amplifier). A 5 V offset is then added to the signal in order to set the working point of the AOM [70]. The signal is then sent to the chain of VCO and RF amplifier driving the crystal of the modulator. This results into a monochromatic intensity modulation of the pump beam which in turn applies a radiation-pressure force to the movable mirror. In parallel, the same AOM is also used to lock the laser frequency on the cavity. The probe beam, also coupled to the cavity, then probes the mirror displacement created by the pump beam. The read out of the homodyne detection is then plugged into the input of the network analyzer. This way, the mechanical response of the mirror can be measured at a specific frequency. The great advantage of the network analyzer is that it can perform frequency sweeps with the given resolution; large sweeps of the mechanical response can then be realized in order to demonstrate ratio spectral dependence of the signal-to-noise.

The procedure also requires to measure the thermal noise of the mirror. This is done by simply turning off the intensity modulation and sending the output of the homodyne detection to a spectrum-analyzer. It measures the noise on the same frequency range to be compared with the previous measurement. An additional programming work had to be done in order to completely automatize this measurement. In particular, we have written two LabVIEW routines controlling the two apparatuses by automatically changing the frequency range of the measurements, reading the data and saving them into a computer. The written routines are drawn on Figures 5.2(b) and 5.2(a). They are based on the official LabVIEW drivers, downloaded by the National Instruments website, for the spectrum analyzer N9020A MXA and the network analyzer E5061B ENA. Both routines consist in defining a start frequency and a span for each sweep, and, once the sweep is finished, a pace changing accordingly the sweep window. In particular, routine 5.2(a) contains two subroutines: one to set the sweep

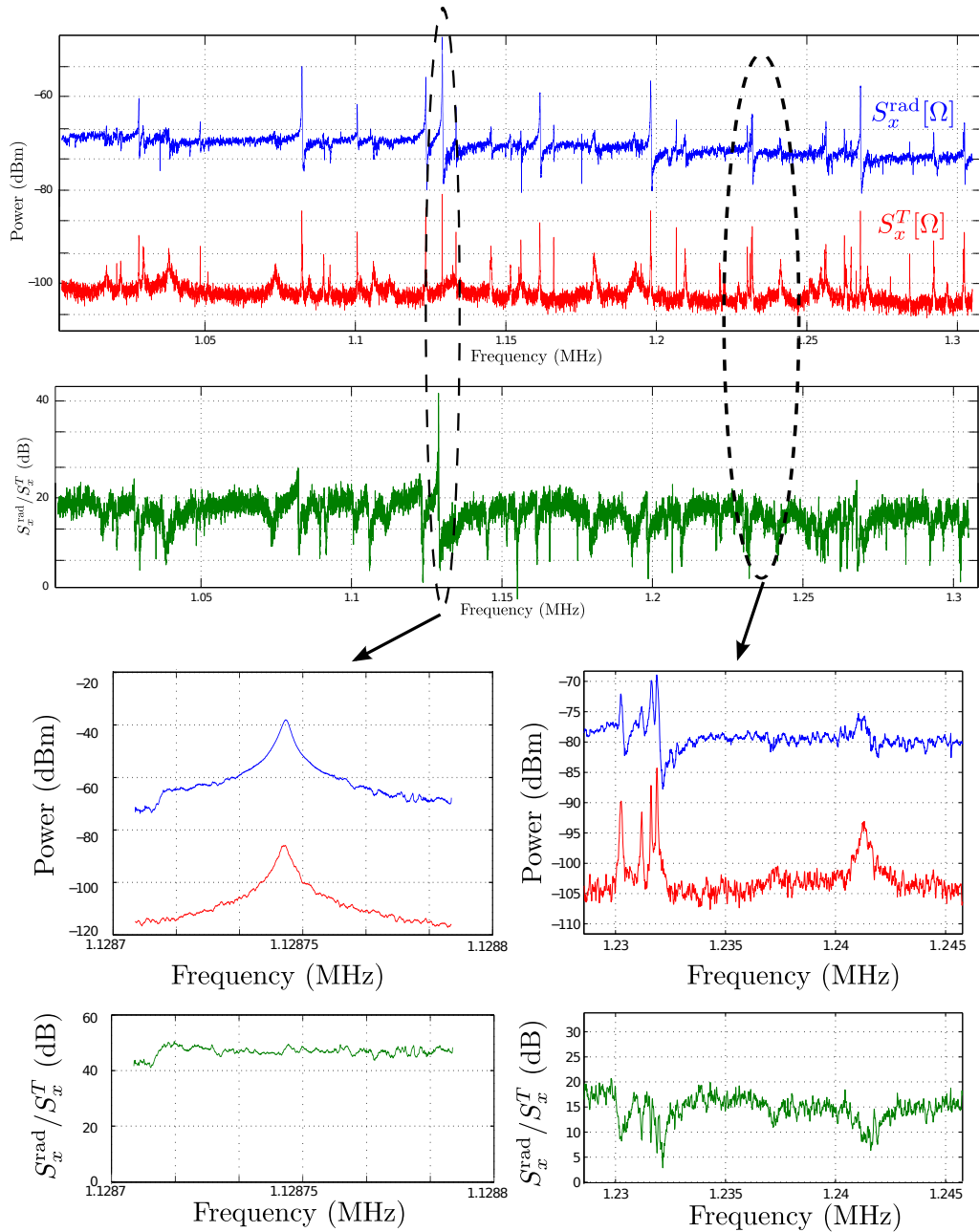


Figure 5.3: (a) The acquisitions as provided by the network and spectrum analyzer, $S_x^{\text{rad}}[\Omega]$ and $S_x^T[\Omega]$, respectively. (b) The obtained relative, signal-to-noise ratio between radiation-pressure effects and thermal noise.

note that the two measurements -thermal noise and mechanical response- were not performed simultaneously but rather with a time difference of a few hours. Therefore, a frequency offset due to thermal drifts between the blue and red curves naturally exists. These mechanical drifts are of the order of 1 Hz. This can be problematic only for the high-Q mechanical modes, such

as the fundamental gaussian mode at $\Omega/2\pi = 1.128$ MHz. Such a drift can lead to a wrong estimation of the signal-to-noise ratio around the fundamental mode. However, this is not the case for the other mechanical modes as they are large compared to the thermal drifts.

Furthermore, at the right of some vibrational modes, the anti-resonance can be observed caused by a destructive interference between the mechanical mode and the mechanical background as predicted in section 5.1.1. Figure 5.3 (green curves) shows the ratio between the two measurements: the mechanical response and the thermal noise. It provides an information on the relative signal-to-noise ratio between radiation-pressure and thermal noise. We observe that its spectral dependence is relatively flat out of mechanical resonance, with the exception of the high-frequency region where the anti-resonance appears. Indeed, a thermal drift leads to an overestimation of the signal-to-noise ratio at the fundamental mechanical resonance. We notice however that, for the high-Q mechanical modes the observed anti-resonance is in fact an artificial effect due to the sweep velocity of the monochromatic modulation. Indeed, Figure 5.3(c) depicts the fundamental mechanical resonance and its response for a close-in sweep. Both measurements were performed with a time gap of a few seconds only in order to avoid any drifts, due to the much smaller resolution bandwidth ($\nu_{\text{BP}} = 1$ Hz). When calculating the ratio of the two measurements we see that there is actually no difference in the mechanical response between the fundamental mode and the background. On the other hand, if we take a closer look on another frequency region, (Figure 5.3(d)) a different behaviour is observed: the mechanical background mechanical response to radiation pressure is up to 15 dB better than the resonance, as the dips in the green curve imply.

Indeed then, the response of the mechanical background is at least the same or better than the resonance and, moreover, its flat dependence over frequency provides a relative freedom on the frequency analysis window in which the correlation experiment can be performed. Finally, these graphs do not provide the absolute value of the signal-to-noise ratio S_x^{rad}/S_x^T . This can be done by comparing the intensity modulation used to apply the radiation pressure force with the intensity shot noise. This provided a calibration factor of the relative signal-to-noise ratio shown in 5.3. Let us note that when performing this measurement, the spectrum analyzer should be set to its maximal resolution bandwidth -in our case $\nu_{\text{RBW}} = 1$ Hz, in order not to overestimate the signal-to-noise ratio. In this case, the modulation peak is 70 dB over the intensity shot-noise, leading to an absolute signal-to-noise ratio of -40 dB at a pump power of 10 mW which, according to equation [70]

$$|C_{s-m}|^2 = \frac{S_x^{\text{rad}}}{S_x^{\text{rad}} + S_x^T}, \quad (5.13)$$

corresponds to a correlation coefficient $|C_{s-m}|^2 = 10^{-4}$.

Let us finally note that this estimation is done by considering a lossless cavity. Indeed, this calibration assumes no loss, thus underestimating the signal-to-noise ratio. We may adjust the above estimation by using equation (1.53). By assuming no cavity-filtering effects, the intracavity intensity fluctuations δp are:

$$\delta p[\Omega] = \frac{\sqrt{T}}{\gamma} \delta p_{\text{in}}[\Omega] + \frac{\sqrt{P}}{\gamma} \delta p_{\text{v}}[\Omega]. \quad (5.14)$$

In the calibration scheme described above. a classical intensity modulation $\delta p^{\text{mod}}[\Omega]$ is used

with a spectrum given by:

$$S_p^{\text{mod}}[\Omega] = \frac{T}{\gamma^2} S_{p,\text{in}}^{\text{mod}}[\Omega], \quad (5.15)$$

while the quantum fluctuation spectrum is:

$$S_p[\Omega] = \frac{2}{\gamma} S_{p,\text{in}}[\Omega], \quad (5.16)$$

where we used the equality $S_{p,\text{in}}[\Omega] = S_v[\Omega]$. The corresponding radiation-pressure effects are proportional to $S_p^{\text{mod}}[\Omega]$ and $S_p[\Omega]$ and their ratio is thus given by:

$$\frac{S_x^{\text{mod}}[\Omega]}{S_x^{\text{rad}}[\Omega]} = \frac{S_p^{\text{mod}}[\Omega]}{S_p[\Omega]} = \frac{T}{T+P} \times \frac{S_{p,\text{in}}^{\text{mod}}[\Omega]}{S_{p,\text{in}}[\Omega]}. \quad (5.17)$$

Let us assume the general case where an intensity modulation peak is n dB above shot noise; the second term of the above equation is $S_{p,\text{in}}^{\text{mod}}[\Omega]/S_{p,\text{in}}[\Omega] = 10^{n/10}$. If the intensity modulation peak induces a mirror displacement of m dB above thermal noise, such that $S_x^{\text{mod}}[\Omega]/S_T[\Omega] = 10^{m/10}$, we obtain:

$$\begin{aligned} \frac{S_x^{\text{mod}}[\Omega]}{S_T[\Omega]} &= \frac{S_x^{\text{mod}}[\Omega]}{S_x^{\text{rad}}[\Omega]} \times \frac{S_x^{\text{rad}}[\Omega]}{S_T[\Omega]} \\ &= \frac{T}{T+P} \times \frac{S_{p,\text{in}}^{\text{mod}}[\Omega]}{S_{p,\text{in}}[\Omega]} \times \frac{S_x^{\text{rad}}[\Omega]}{S_T[\Omega]}. \end{aligned} \quad (5.18)$$

Finally, the signal-to-noise ratio between radiation-pressure-induced displacement and thermal noise is given by:

$$\frac{S_x^{\text{rad}}[\Omega]}{S_T[\Omega]} = \frac{T+P}{T} 10^{(m-n)/10}. \quad (5.19)$$

Indeed, the lossless cavity estimation may lead to a slightly underestimated signal-to-noise ratio since taking into consideration the vacuum fluctuations leads to a correction factor of $(1+P/T)$. Our measurement cavity presents losses $P = 30$ ppm and $T = 10$ ppm leading to an increase of the signal-to-noise ratio by 40%.

5.3 Towards quantum radiation-pressure effects at room temperature

In this section we will describe the recent development of the existing experimental setup towards the observation of radiation pressure effects at room temperature by means of averaging the measured fluctuations in order to cancel thermal noise. We have also seen that the optical losses of the cavity in combination with an imperfect laser frequency stabilization lead to a huge phase-intensity quadrature coupling leading to fake optomechanical correlations. By modelling this effect we have derived a very strict stability criterion. In the following sections, we will briefly describe some theoretical ideas in order to make the stability criterion more flexible. Equation (4.16) implies that in order to do this, one must optimize the signal-to-noise ratio S_x^{rad}/S_x^T while at the same time minimizing thermal noise.

5.4 Stability criterion

Ideally, the optomechanical correlation measurement for our system should be carried out at low-frequency. At low frequency the mirror motion S_x is minimized while, at the same time, the signal-to-noise ratio S_x^{rad}/S_x^T can be the same or even better. Furthermore, out of resonance the measurement bandwidth can be increased, drastically decreasing the averaging time. Let us reduce the stability criterion, given by equation (4.16), for the low-frequency case by combining equations (4.16), (1.74), (5.8) and (5.9):

$$\frac{\bar{\Psi}_p}{\gamma} \simeq \frac{\sqrt{\mathcal{R}_0}}{2TP} \sqrt{\frac{T}{T+P}} \frac{\hbar\Omega}{k_B T_m} \frac{p}{\phi_0}, \quad (5.20)$$

where Ω is the frequency at which the correlations are measured, and ϕ_0 is the loss angle associated to the thermal background. Let us assume that the background losses are those of the plano-convex mirror modes ($\phi_0 = 10^{-6}$). In this case, the observation of optomechanical correlation would need a laser frequency stabilization reaching an efficiency of $\bar{\Psi}_p/\gamma \simeq 10^{-2}$. For a cavity with a bandwidth $\Omega_{\text{cav}}/2\pi = 1$ MHz this corresponds to a detuning tolerance of 10 kHz, which seems to be experimentally feasible.

5.5 Laser drift effects in optomechanical correlations

Let us re-examine the contamination signal measured by the reflected intensity quadrature. We will assume small detuning drifts $\bar{\Psi}$ compared to the cavity linewidth γ ($\bar{\Psi} \ll \gamma$) and estimate the corresponding result on the correlation function \mathcal{C}_{s-m} given by equation (2.20):

$$\mathcal{C}_{s-m}(T) \propto \frac{1}{T} \int_0^T \delta p_{\text{out}}^s(t) \delta q_{\text{out}}^m(t) dt. \quad (5.21)$$

In presence of such detunings the reflected signal fluctuations are given by equation (4.9) and take the form:

$$\delta p_{\text{out}}^s(t) = \alpha \delta p_{\text{in}}^s(t) + \beta \bar{\Psi}(t) \delta x(t). \quad (5.22)$$

Therefore, as done in chapter 2 (see equation (??)), the correlation function may be written as the sum of two terms:

$$\mathcal{C}_{s-m}(T) = \mathcal{C}_{\text{opto}}(T) + \mathcal{C}_x(T). \quad (5.23)$$

We will be interested in the contamination term:

$$\mathcal{C}_x(T) = \frac{\beta}{T} \int_0^T \bar{\Psi}(t) \delta x(t) \delta q_{\text{out}}^m dt. \quad (5.24)$$

By assuming now thermal noise much greater than radiation-pressure-induced displacement $\delta x_T \gg \delta x_{\text{rad}}$ and by neglecting the shot-noise contribution in the reflected probe beam fluctuations, one gets:

$$\mathcal{C}_x(T) \simeq \frac{8\mathcal{F}}{\lambda} \frac{\beta}{T} \int_0^T \bar{\Psi}(t) \delta x_T^2(t) dt. \quad (5.25)$$

Assuming that the detuning $\bar{\Psi}$ is a random noise statistically independent from thermal noise δx_T , this equation may be written¹:

$$C_x(T) \simeq \frac{8\mathcal{F}}{\lambda} \frac{\beta}{T^2} \int_0^T \bar{\Psi}(t) dt \int_0^T \delta x_T^2(t') dt'. \quad (5.26)$$

We have assumed that the measurement time T is much greater than the coherence times of the thermal τ_T and detuning noises $\tau_{\bar{\Psi}}$ ($T \gg \tau_{\bar{\Psi}}, \tau_T$). We have seen that at the thermal regime where $\delta x_T \gg \delta x_{\text{rad}}$ the optomechanical correlations are obtained over measurement times T greatly exceeding the mechanical coherence time τ_M . By then assuming the detuning fluctuations $\bar{\Psi}$ with a timescale larger than the mechanical coherence time $\tau_{\bar{\Psi}} \gg \tau_M$, the above equation becomes:

$$C_x(T) \simeq \frac{8\mathcal{F}\beta\langle\delta x_T^2\rangle}{\lambda} \frac{1}{T} \int_0^T \bar{\Psi}(t) dt. \quad (5.27)$$

Equation (5.27) shows that the contamination effect is simply filtered during the measurement time T . Averaging for a time long enough should therefore, in principle, enable cancelling the contamination issue. For example, detecting thermally-limited quantum optomechanical correlations at the level of 10^{-1} would require $\simeq 10$ s using a span of 500 Hz (deduced from equation (2.22)). The condition on the detuning (with losses on the order of $\phi_0 \simeq 10^{-3}$) is $\bar{\Psi}/\gamma \simeq 10^{-2}$, according to equation (5.20). Instead, it is enough to average the measurement for $\tau_d = 100 \times 10$ s, since the contamination effect would be filtered by a factor of 100, as equation (5.27) indicates.

In section 5.2.2 we have described the procedure in order to experimentally determine the signal-to-noise ratio of our system. We have found that the radiation-pressure effects over thermal noise are quite unfavourable ($S_x^{\text{rad}}/S_x^T \simeq 10^{-4}$), adding an extra difficulty to the measurement. For this signal-to-noise ratio, according to equation (2.44) an averaging time of 100 s is necessary to extract the radiation-pressure effects. As we have seen that our experimental setup can remain stable on a one-hour timescale this averaging time is completely realistic. At the same time, as equation (5.20) suggests, for a cavity finesse $\mathcal{F} = 100\,000$, optical losses $P = 0.25T$, a mass $M = 20$ mg, a mechanical quality factor $Q = 10^6$ and a mechanical resonance frequency $\Omega/2\pi \simeq \Omega_M/2\pi = 1$ MHz, the quantum radiation-pressure force related to an incident coherent beam with a power of 1 mW ($\bar{I}_{\text{in}} = 6 \times 10^{15}$ photons/sec, for a wavelength $\lambda = 800$ nm), at room temperature for signal-to-noise ratio $S_x^{\text{rad}}/S_x^T \simeq 10^{-4}$ can be demonstrated if $\bar{\Psi} \leq \bar{\Psi}_c \simeq 15 \times 10^{-8}\gamma$. For a cavity in the MHz range this corresponds to a drift tolerance in the 100 mHz range; which is a very stringent condition. We propose several solutions in order to relax this requirement [72]: a spectral deviation can be realized in order to distinguish the contamination from the radiation pressure, an active feedback loop can also be realized in order to enhance the measurement time while at the same time the contamination is reduced, or we can perform an independent high-accuracy contamination measurement and recover the radiation pressure a posteriori.

¹where we have used the ergodic theorem for two random independent and stationary variables a and b :

$$\lim_{T \rightarrow \infty} \frac{1}{T} \int_0^T a(t)b(t) dt = \langle ab \rangle = \langle a \rangle \langle b \rangle = \lim_{T, T' \rightarrow \infty} \frac{1}{TT'} \int_0^T a(t) dt \int_0^{T'} b(t') dt'.$$

Correlations in the presence of cooling

As equation (4.16) implies, a simple way in order to obtain a low contamination level consists in minimising the displacement spectral density S_x^T . This can be achieved by means of active cooling [42], [55] which permits to lower the motion variance while leaving the signal-to-noise ratio unaltered by preserving the relative contributions of the driving forces. In presence of a feedback, the mirror motion is:

$$\delta x[\Omega] = \chi[\Omega](F_T[\Omega] + F_{\text{rad}}[\Omega] + F_{\text{fb}}[\Omega]) + \delta x_{\text{bg}}, \quad (5.28)$$

where F_T , F_{rad} and F_{fb} are the Langevin, radiation-pressure and feedback forces, respectively, while δx_{bg} denotes the thermal background. The feedback force can be written:

$$F_{\text{fb}}[\Omega] = -igM\Omega\Gamma_M\delta x_{\text{err}}[\Omega], \quad (5.29)$$

where g denotes the gain of the feedback loop and $\delta x_{\text{err}}[\Omega] = \delta x[\Omega] + \delta x_{\text{shot}}[\Omega]$ is the measured signal containing the mirror motion with an imprecision set by the detection shot-noise δx_{shot} . It is straightforward to show that the mirror motion can be written:

$$\delta x = \chi_{\text{eff}}[\Omega](F_T[\Omega] + F_{\text{rad}}[\Omega]) + \frac{\chi_{\text{eff}}[\Omega]}{\chi[\Omega]}\delta x_{\text{bg}}[\Omega] + \left[\frac{\chi_{\text{eff}}[\Omega]}{\chi[\Omega]} - 1\right]\delta x_{\text{shot}}, \quad (5.30)$$

where χ_{eff} is the effective mechanical susceptibility given by:

$$\chi_{\text{eff}}^{-1}[\Omega] = \chi^{-1}[\Omega] - igM\Gamma_M\Omega. \quad (5.31)$$

Assuming that the feedback signal is independently obtained from the reflected probe phase, δx_{shot} does not contribute to the optomechanical correlations C_{s-m} , which is the sum of a term denoting the optomechanical correlations C_{opto} and another denoting the contamination signal C_x :

$$C_{s-m}[g, \Omega] = C_{\text{opto}}[g, \Omega] + C_x[g, \bar{\Psi}, \Omega]. \quad (5.32)$$

In the presence of a non-zero feedback gain the optomechanical correlations are given by:

$$C_{\text{opto}}[g, \Omega] = \frac{\chi_{\text{eff}}^*[\Omega]}{\chi^*[\Omega]} \times C_{\text{opto}}[g = 0, \Omega], \quad (5.33)$$

while the contamination is given by:

$$C_x[g, \bar{\Psi}, \Omega] = \left| \frac{\chi_{\text{eff}}[\Omega]}{\chi[\Omega]} \right|^2 C_x[g = 0, \bar{\Psi}, \Omega]. \quad (5.34)$$

Equations (5.33) and (5.34) show that dissipative feedback enables decreasing the relative contribution of the contamination by a factor $|\chi_{\text{eff}}[\Omega]/\chi[\Omega]|^2 \simeq 1/g^2$ around the mechanical resonance frequency $\Omega \simeq \Omega_M$. In practice, the gain is limited to values such that the motion contamination by the feedback noise $F_{\text{shot}} = -igM\Gamma_M\Omega\delta x_{\text{shot}}[\Omega]$ stands well below the radiation pressure force, which implies $g^2 \leq S_x^{\text{rad}}[\Omega_M]/S_I[\Omega_M]$.

Contamination-signal post-selection

The mechanical background of the plano-convex mirror presents a number of advantages: first, a large frequency span (~ 10 kHz as opposed to some Hz around the mechanical resonance) can be chosen to measure the optomechanical correlations, second, the out-of-resonance spectral density of the mirror motion S_x^T is 30 dB smaller than on resonance, thus lowering the contamination contribution and, third, its mechanical response is potentially up to 20 dB better than the mechanical resonance, due to destructive interference effects, as we experimentally demonstrated (see Figure 5.3).

Therefore, for this system, it is reasonable to work far from the mechanical resonance. While the previous proposal imply the demonstration of optomechanical correlations at the mechanical resonance, we have decided to experimentally pursue a solution to relax the stability restrictions out-of-resonance. In the following we will describe a post-selection technique in order to demonstrate optomechanical correlations using measurement points presenting a low contamination level. This can be done by performing an independent measurement of the cavity working point.

Most notably we will describe the implementation of the newly-developed contamination lock-on detection (CLI) scheme dynamically measuring the cavity detuning. In combination to the setup evolution as described in 3, these efforts were focused on three main aspects. First, the combination of the lock-in error signal along with the Pound-Drever signal to stabilize the laser frequency onto the measurement cavity. Second, the use of the same error signal in order to dynamically control the working point of the cavity in order to study a potential feed-forward technique applied to the data processing. Third, the development of a LabVIEW routine controlling all the associated devices and performing a real-time data upload on the computer.

5.5.1 Experimental setup

Figure 5.4 shows the global experimental setup. While the double-injection scheme and the homodyne detection remain unchanged, there exist several major differences with respect to the setup depicted on Figure 2.2. First the second mode-cleaner cavity providing a quantum-noise limited pump light field up to 10 mW is installed on the optical table. Second, in place of the photodiode Ph_1 , a balanced detection is installed and is used for three purposes at the same time: monitoring the intensity fluctuations δp_s^{out} , generating the Pound-Drever-Hall and the contamination lock-in error signals. Third, the contamination signal is derived by the auxiliary beam which is also implemented on the setup. Fourth, the laser frequency stabilization scheme has changed; a combination of both error signals (PDH and LI) is used to lock the measurement cavity. Finally, we have added a third spectrum analyzer to our read out configuration monitoring the contamination effect.

Feedback loops The frequency stabilization scheme is based on the splitting the error signal in two frequency components one driving the piezoelectric actuator of the laser cavity and one driving a double-pass configured acousto-optic modulator depicted in Figure 3.21(b). The major difference is the use of both the Pound-Drever and the contamination error signals for the lock-in feedback loop. The low-frequency component of the contamination error signal drives the piezoelectric actuator of the laser ring-cavity. A low-pass passive filter with a cut-

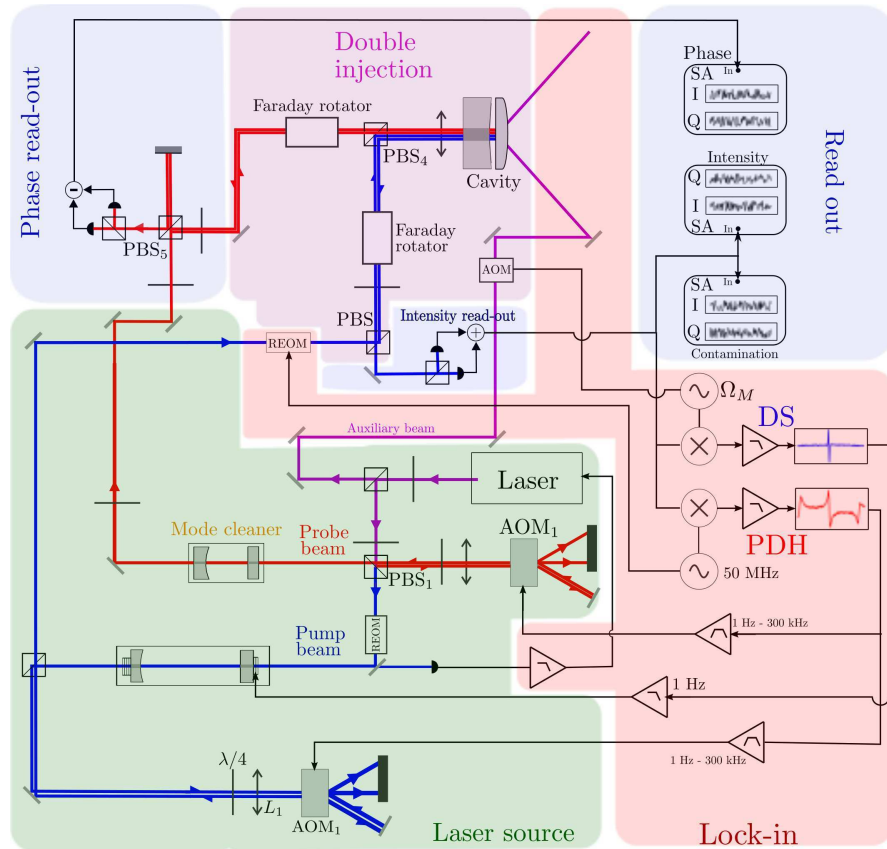


Figure 5.4: The complete experimental setup designed to observe radiation-pressure effects at room temperature. The measurement cavity is stabilized via a double feedback loop (LI+PDH) while the read-out is done by three synchronized and triggered spectrum analyzers monitoring the phase, the intensity and the contamination.

off frequency $f_c = 1$ Hz cuts the rapid components of the error signal. The high-frequency component of the Pound-Drever error signal drives the acousto-optic modulator; a high-pass filter ($f_c = 1$ Hz) is coupled to the input of the corresponding lock-box while at its output a low-pass filter at 300 Hz is coupled. The double feedback-loop is done with two identical lock-boxes (NewFocus LB1005) one for each frequency component. The locking protocol is the following: the cavity is manually maintained at resonance using the offset potentiometer of the high-voltage (0-1000 V) driving the piezoelectric actuator. The cavity resonance is monitored either by the webcam placed at the output of the measurement cavity, or by the DC-output of the balanced detection or by the error signal. The low-frequency gain is gradually increased until the cavity is locked at resonance and the manual track is no longer required. As soon as this is achieved, the fast gain is increased. At this point, the rapid oscillations start to be compensated by the feedback loop and the error signal begins to be stabilized around zero. Then, the low frequency gain is further increased until the feedback loop begins to oscillate. These oscillations can then be compensated by the rapid gain. This iteration is then repeated until the rapid loop also oscillates. The configuration of the gains just before the oscillations

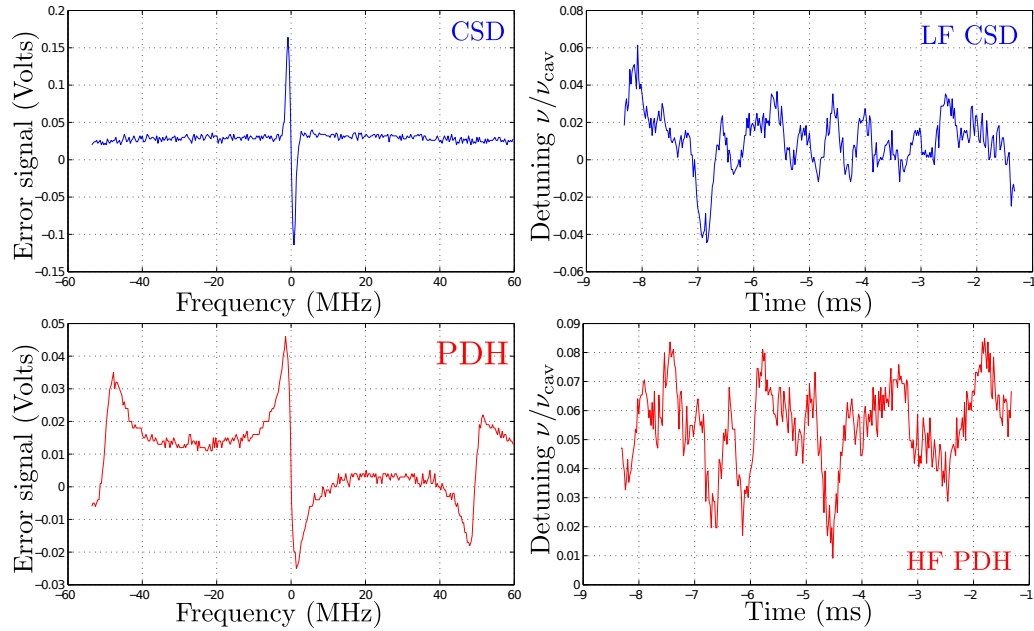


Figure 5.5: The two error signals used to stabilize the laser frequency on the measurement cavity. In blue the contamination error signal used to drive the LF channel of the servo loop. In red the Pound-Drever-Hall error signal driving the RF channel.

is considered to be optimal. Let us note that the input of the LF channel of the feedback loop can be coupled to either the contamination or the Pound-Drever error signal. All possible error combinations are open; one can lock the cavity using only the Pound-Drever signal, only the lock-in signal or a combination of both.

Read out configuration The contamination error signal is created with a home-made analog demodulator. However, a digital demodulation can be performed by a spectrum analyzer operating in I/Q mode. Therefore, we have at our disposal another way to monitor in real time the cavity detuning. The contamination signal can then be acquired at the same time as optomechanical correlations. It can be used to perform a post-selection and discard data taken with the lock imperfections. Once the optomechanical correlations are uploaded, the corresponding contamination signal can help to perform a data post-selection compensating any lock imperfections. Along with the two spectrum analyzers, monitoring the phase and the intensity, we have installed in our chain of detection a third analyzer monitoring the contamination. It is critical that all three analyzers are synchronized and triggered. The corresponding cable connection is depicted on Figure 5.5.1. The intensity spectrum analyzer is chosen to be the master apparatus. Analyzer 1 provides a 10-MHz frequency reference on which all other apparatuses are synchronized via their external reference input. All demodulation processes are then realized with the same reference. Furthermore, all acquisition should start simultaneously. For this purpose the master analyzer triggers the other two by their external trigger. The function generator driving the acousto-optic modulator used to modulate the intensity of the auxiliary beam is also synchronised on the 10 MHz modulation reference. The modulation signal delivered by the generator is synchronous with the demodulation frequency of the

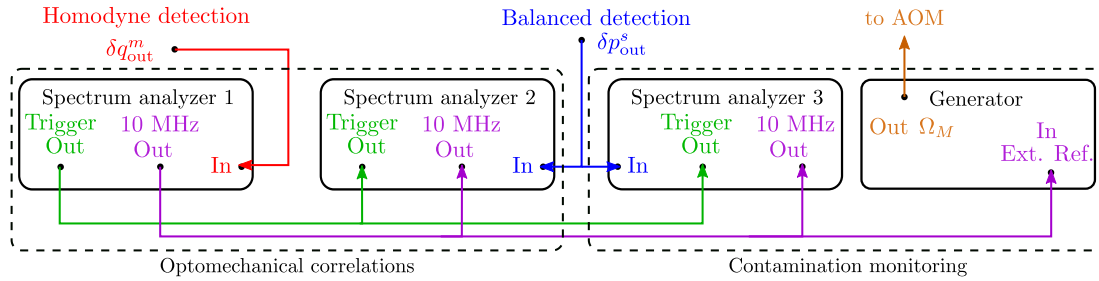


Figure 5.6: The connection configuration of the four apparatuses involved in the experiment. SA₁ has been chosen to be the master apparatus synchronizing the other 3 slave apparatuses, and triggering the simultaneous acquisitions of all 3 spectrum analyzers.

spectrum analyzer measuring the contamination signal.

Acquisition protocol In order to automatize the acquisition procedure, we have written a LabVIEW routine launching the acquisitions and uploading them to the computer. The program works as follows. All analyzers are set in single-run mode; then a single sweep is performed. The two slave analyzers are initialized first, then they wait for the triggering signal of the master analyzer. Then, the master analyzer is also initialized at which point it triggers the simultaneous triple measurement. Afterwards, the data are uploaded to the computer. The loop is then repeated as many times as necessary. The LabVIEW realization of the aforementioned program is drawn on Figure 5.5.1. It simply consists of a sequential structure repeated in a while-loop. Sequences A, B and C initialize the analyzer; the master analyzer being the last one. The rest of the sequence downloads the binary-encoded data. We use a queue processing technique (First In, First Out) in a parallel loop to write the data into manageable files. The FIFO queue allows to gain time; we achieved a duty cycle up to 80%.

In practice, a single loop lasts 1 second. The spectrum analyzers are configured in order to maximize the number of data acquired within this 1-second time-frame. The I/Q mode provides the two demodulated quadratures of the input signal under the form of two time series. The length of the time series is called sweep time and is set by the resolution bandwidth ν_{RBW} . In particular the resolution bandwidth is inversely proportional to the sweep time. In order to increase the data acquisition efficiency, the sweep time is set at approximately 1 second as well while at the same time the points are set to the maximum provided by the apparatus.

Experimental protocol Before launching the data acquisition a careful control protocol must be performed. After optimizing the laser output power and the alignment of both filtering cavities, a great attention must be paid to the double-pass acousto-optic modulators. Both are aligned so that their working point is set at the flat region of curve 3.20(b), cancelling this way any pointing noise. The frequency difference of the signal driving the modulators is set via the bias voltage to compensate the cavity birefringence. Then a control of the cat eye optical alignment is done (see Figure 3.20(a)). A thorough control of the acousto-optic modulator which is coupled to the intense beam must be done, mainly due to the fact that any misalignment or bad field-modulator coupling can lead to an excess of intensity noise possibly above shot-noise.

In chapter 3 we have explained that, when the laser frequency is locked to the measurement

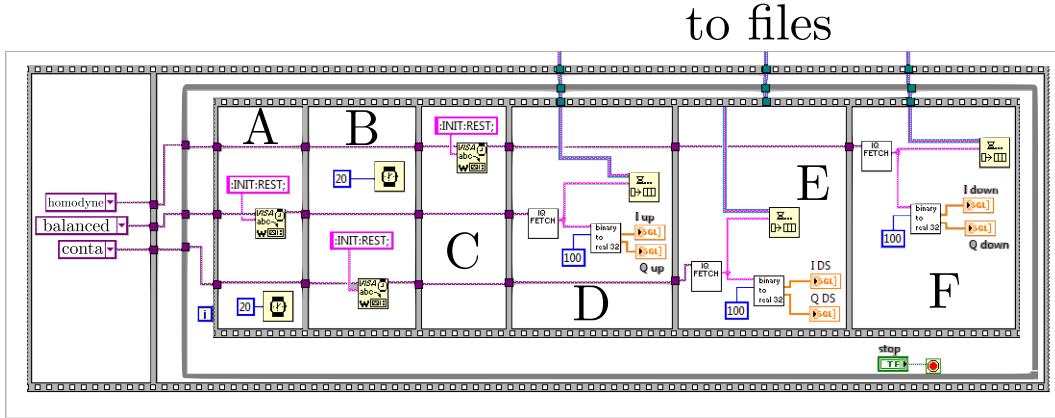


Figure 5.7: The LabVIEW routine controlling the intensity, phase and contamination acquisition by three spectrum analyzers. They are configured in a single-run mode. A and B sequences start the slave analyzer while sequence C starts the master analyzer triggering at the same time the slaves. Sequences D, E and F fetch and uploaded the measured data on the computer.

cavity, the frequency difference between the two beams is not constant over time. This results into a beating between the two beams contaminating both phase and intensity quadratures (see Figure 3.22). In order to ensure that this beating does not contaminate the measured optomechanical correlations, it is tuned away from the frequency span in which the optomechanical correlations are to be measured. As a precaution, we tune the beating by detuning the probe beam some hundreds of kHz away from the optical resonance; the bias voltage of the pump beam is left strictly unaltered in order not to perturb the double-pass optical alignment.

In the following, by using only the Pound-Drever-Hall signal the laser frequency is stabilized at the resonance of the cavity. The fundamental resonance of the movable mirror at $\Omega_M/2\pi = 1.128$ MHz is observed via the homodyne detection and the auxiliary beam is turned on. The coherent drive of the mirror is also monitored and optimized by either changing the auxiliary beam alignment and therefore the excitation point or the modulation depth provided by the acousto-optic modulation (see Figure 5.4). The frequency analysis window is chosen among the flat regions of Figure 5.3 and by observing the reflected intensity of the pump beam we ensure that no extra intensity noise is induced by the presence of the coherent drive. The laser frequency is then unlocked and the contamination lock-in signal is visualized, simultaneously with the Pound-Drever signal, and is coupled to the low-frequency channel of the feedback loop. The laser frequency is then relocked and the acquisition program is launched.

5.5.2 Experimental results

For these experiments we have used a Fabry-Perot cavity formed by a plano-convex movable mirror (reference: PC 3021/13) and a cylindrical coupler (reference: 07125/3). It is the same cavity used for the self-amplification experiment and its fundamental gaussian mode presents a quality factor $Q = 700\,000$, an effective mass $M_{\text{eff}} = 72$ mg, a resonance frequency $\Omega_M/2\pi = 1.128$ MHz and an optical finesse of $\mathcal{F} = 100\,000$. The read out is done with three identical MXA spectrum analyzers, one monitoring the reflected phase of the probe beam while the reflected intensity of the pump beam is simultaneously monitored by the other two analyzers.

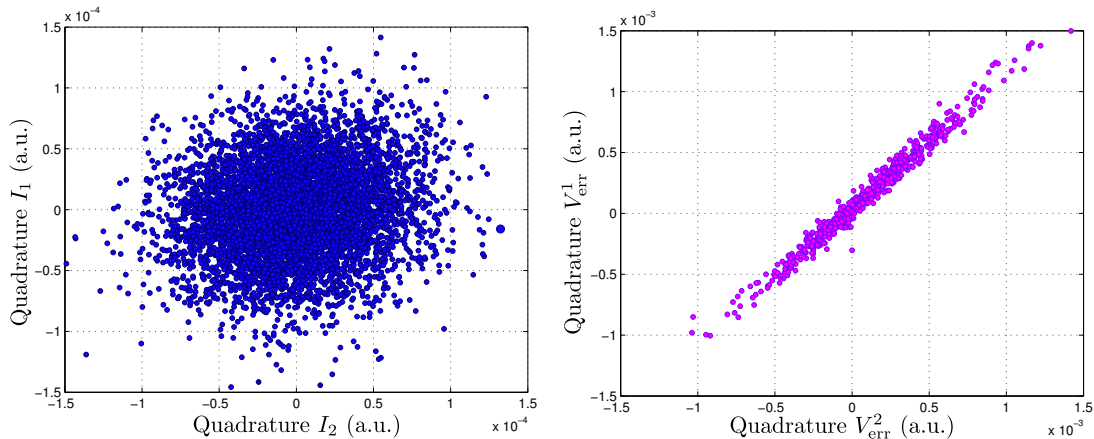


Figure 5.8: Left: an intensity shot-noise measurement of the reflected pump beam, represented in the phase-space. Right: the contamination synchronous detection error signal provided by the spectrum analyzer set in I/Q mode. Each point corresponds to a different cavity detuning.

Each one is set at a different frequency window: one is used to measure the optomechanical correlations, while the other one is used to independently measure the cavity detuning in real time. All three of them are set in I/Q mode. The center analysis frequency chosen to probe the optomechanical correlations is $\Omega/2\pi = 1.401$ MHz with a span of $\nu_{\text{span}} = 7.5$ kHz. Over this range, only the mechanical thermal background is present. The third analyzer center frequency is set around the fundamental resonance of the plano-convex mirror $\Omega_M/2\pi = 1.128$ MHz, coinciding with the frequency of the coherent drive. For all analyzers, the resolution bandwidth ν_{RBW} is set to 5 Hz which corresponds to 754-ms sweep time, each sweep giving 43845 points.

The input power of the probe beam is set to 100 μW and the pump beam to 1.5 mW. For this cavity, the input power can be increased up to 2.5 mW before bistability effects make the frequency lock-in impossible.

Figure 5.8 depicts a measurement provided by the two I/Q-mode configured spectrum analyzers monitoring the output of the balanced detection. Both measurements are represented in phase-space. In the left figure, the typical random walk of the intensity noise is depicted, measured around $\Omega/2\pi = 1.4$ MHz over a 7-kHz bandwidth. The coherent contamination induced by the auxiliary beam, is demodulated by the analyzer and drawn on the right part of the figure. Since the demodulation process is synchronously performed at the excitation frequency, all points are aligned on a straight line whose origin (0,0) corresponds to a zero cavity detuning. In fact, the width of this straight line indicates the signal-to-noise ratio of the contamination error signal over thermal noise, as the straight line tends to a circle if thermal noise dominates.

We have experimentally studied the dependence of the optomechanical correlations on the cavity working point. For this, we have acquired the correlations for various detunings by manually adding a voltage offset to the LF channel of the feedback loop. For a given offset the optomechanical correlations and the contamination signal are synchronously measured. Figure 5.9(a) depicts these results. On the top subfigure, we depict the time-accumulated detuning over a total acquisition time of 100 seconds. Each colour corresponds to a curve with the same colour of the bottom subfigure, depicting the optomechanical correlations. The level of contamination increases as the cavity is further detuned thus increasing the level of the

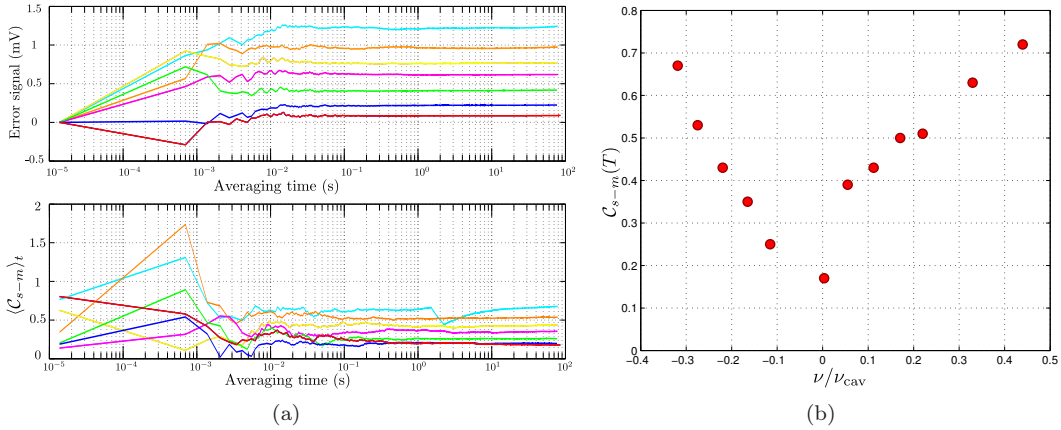


Figure 5.9: Left: Time-accumulated optomechanical correlations acquired (up) for various mean cavity detunings (down). Right: Resulting correlations $C_{s-m}(T)$ as a function of the induced detuning.

corresponding optomechanical correlations. We note the difficulty to set the contamination level mean value to a strictly null value. Indeed, before the experiment is performed the optimization of the working point of the cavity is done by monitoring the reflected intensity on a spectrum analyzer and minimizing it. However, this protocol is not very accurate since the fast components of the cavity vibrations prevent the direct observation of the mean value. Indeed, a certain time averaging is needed in order to measure the mean detuning of the cavity. Also, we have extracted the obtained optomechanical correlations $C_{s-m}(T)$ and plotted versus the corresponding detuning. The detuning is calibrated by comparing the offset to the peak-to-peak amplitude of the error signal. Again, very high correlations are observed for various detunings. For a “zero” detuning the curve reaches its minimum. However, correlations of 15% are measured, indicating a contamination effect.

In our final experiment the contamination error signal is used to post-select the data. The idea is to acquire a long series of data and reject or select them according to their level of contamination. All analyzers are triggered according to Figure 5.5.1 so that all three acquisitions start at the same time and the correspondence between each point of the three measurements can be made. Therefore, each point of the contamination measurement time-series at instant t_1 strictly corresponds to the phase and intensity point at the same time. During the data processing, a threshold can be defined. The points situated above this threshold are not taken into consideration when establishing the correlations. This threshold is defined by a user-defined window which is characterized by a width, the post-selection gain g_{ps} and an offset which corresponds to a mean cavity detuning $\bar{\Psi}$.

We have varied this window using two different techniques. First, by keeping a constant width and varying the offset in order to probe the optomechanical correlations by sweeping the Airy peak. Second, by choosing the offset in order for it to coincide with the zero-detuning situation and then by varying the post-selection gain, by decreasing the window width.

Figures 5.10(a) and 5.10(c) depict the experimental demonstration of the first technique. On Figure 5.10(a) a small sample of the contamination error signal, as provided by the third spectrum analyzer, is depicted. For each sample the threshold window is superimposed, implying

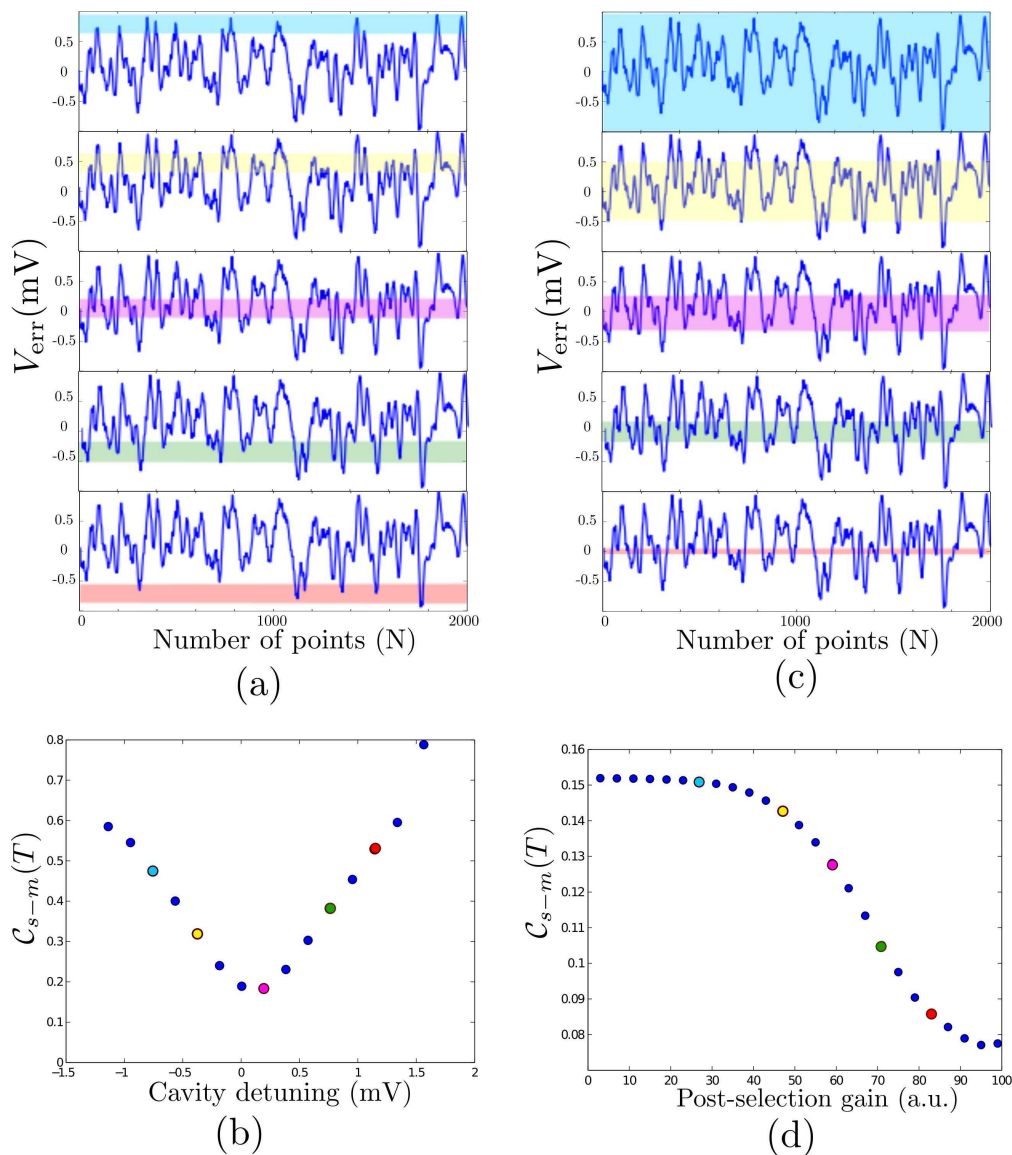


Figure 5.10: (a) The blue time-series depicts a small sample of the contamination signal provided by the analyzer. The offset of the threshold window is varied from the blue side of the fringe to the red one, both corresponding to high-level contaminations. (b) For each window, the optomechanical correlation function is estimated. A characteristic “V” dependence is observed whose minimum corresponds to the least contaminated case for the given window width. (c) By choosing the offset of the window, its width is varied in order to include less points as the width decreases. (d) For each case, the correlation function is estimated. As the post-selection gain is increased, more points are rejected leading to a decrease of the measured optomechanical correlations. This iteration is limited by the number of points.

that only point within this window is taken into account when estimating the optomechanical correlations. A constant window width is chosen and only its offset is varied. Each offset corre-

sponds to a different mean cavity detuning $\bar{\Psi}$. Therefore, the optomechanical correlations are probed from the blue to the red side of the Airy peak. Figure 5.10(c) depicts the resulted correlations for each case. In the extreme blue and red sides, the correlations are of the order of 60% and greater. As the mean detuning approaches the optical resonance the level of correlations decreases and reaches a minima. However, this minimum corresponds to a correlation level of almost 20%; some orders of magnitude greater than the expected optomechanical correlations ($\sim 10^{-3}$). The contamination is still present.

The second step, in order to optimize even more, is to wisely choose the offset corresponding to the lowest correlations and, around this offset, vary the width of the window. The experimental demonstration is drawn in Figures 5.10(b) and 5.10(d). On Figure 5.10(b), from top to bottom, the width of the window is decreased. In fact, it can be interpreted as an extra gain of the feedback loop, thus correcting some locking imperfections. Finally, Figure 5.10(d) depicts the acquired optomechanical correlations. A clear decrease of the correlations function is seen as the post-selection gain is increased. In this case, the post-selection gain has an upper-limit determined by the statistical cut-off due to the limited number of points.

Conclusion

The works presented in this manuscript is part of a general study of interferometric measurements and their fundamental quantum limits. The cornerstone of our experiment is a Fabry-Perot cavity with a moving end-mirror and the measurements are performed thanks to the optomechanical coupling. When the mirror is moving, it induces a phase shift to the reflected light. This phase-shift can be measured with an interferometric technique accessing this way the information on the mirror displacements. As the light is reflected by the mirror, a momentum exchange between the photons and the mirror occurs, resulting in the displacement of the mirror.

We have studied the sensitivity limits of such an interferometric measurement and seen that there are a number of noises that limit the sensitivity of the displacement measurement. These noises can be distinguished in two categories: classical noises and quantum noises. The classical noises are mainly environmental noises (seismic vibrations, etc...). The most important of these noises is the so-called thermal noise: the movable mirror is coupled to a thermal bath at temperature T . The quantum noises associated with this measurement are of two kinds: the quantum phase noise of the reflected laser light (the measurement noise) and the radiation-pressure (the back-action noise). The main objective of this work was to open the way towards the experimental demonstration of the back-action effect and therefore perform an ultra-sensitive measurement of the mirror position, only limited by the Standard Quantum Limit, which is the compromise between the measurement and the back-action noises.

We have developed an experimental setup based on a high-finesse Fabry-Perot cavity with a moving end-mirror is movable. Thanks to the know-how of the LMA in mirror coating, we have been able to construct cavities with very high finesse, of the order of 10^5 . We use a very elaborated tunable light source based on a Ti:Sa laser at 810 nm. The phase detection is done by a quantum-limited homodyne detection, allowing to measure the position of the mirror with an extreme sensitivity of the order of 10^{-20} m/ $\sqrt{\text{Hz}}$.

As the quantum effects are completely overwhelmed by thermal noise of the mirror, we have then used this setup in order to perform a proof-of-principle experiment, using two cross-polarized laser beams injected into the high-finesse cavity. A high-intensity pump beam is used to drive the mirror into motion while a second, much weaker, probe beam is used to probe the position of the mirror without disturbing it. We have simulated a quantum intensity noise of the pump beam and have established phase-intensity correlations between the lasers beams. We have also demonstrated an averaging technique in order to extract radiation-pressure effects even when thermal effects are predominant. This technique may be used to extract quantum optomechanical correlations at room temperature. However, cavity losses give rise to a contamination effect of the intensity quadrature of the pump beam, leading to fake correlations. This effect directly depends on cavity locking imperfections. When the laser frequency is locked to the cavity resonance, a residual frequency "jitter" still exists, imprinting the mirror motion onto the intensity fluctuations of the reflected beam. We have quantified this effect and established a laser stability criterion for the direct demonstration of the effect.

Nevertheless, we have started an effort to update our experimental setup in order to solve this technical problem. These efforts can be distinguished in two categories: (i) an increase of the measured signal by updating the experimental setup and (ii) a study of the feedback loop

imperfections present to our stabilization scheme.

In order to increase the signal-to-noise ratio (radiation-pressure effects over thermal noise S_x^{rad}/S_x^T) by one order of magnitude, we have implemented a new high-finesse filtering cavity providing a quantum-noise limited laser light up to 10 mW, at a frequency of 1 MHz. Moreover, the detection systems of the experiment were also updated. The intensity fluctuations are now monitored by a balanced detection and the photodiodes of the homodyne detection have been replaced by new ones with a high quantum efficiency (93%).

The implementation of the new filtering cavity led to important changes in the feedback loops. The laser frequency was locked on the cavity resonance of the movable mirror cavity but as the new filtering has a very narrow bandwidth, the feedback could no longer compensate the residual vibrations of the movable mirror cavity. For this, we have added a double-pass acousto-optic modulator installed after the filtering cavity. The feedback loops are driven using the well known Pound-Drever-Hall technique. During this work we have seen that the Pound-Drever error signal has some imperfections. Most notably, low-frequency drifts are present in the feedback loops, increasing the contamination of the reflected intensity and finally leading to a high-level of fake optomechanical correlations. We have seen, that these offsets are mostly due to parasitic intensity modulations present in the pump beam. In an effort to solve these imperfections we have designed a novel lock-in detection scheme based on a monochromatic contamination signal measured by the pump beam. This contamination signal is created via radiation pressure: an auxiliary laser beam is sent on the back of the movable mirror, modulating the length of the cavity. This way, an amplitude-rejection-free phase modulation of the laser beam is performed. We have modelled this lock-in scheme and installed into our experimental setup. Indeed, at low-frequency, it is very robust while at high-frequency it works equally well compared to the Pound-Drever scheme. We have also shown, that this novel scheme provides a high-precision measurement of the detuning of the cavity whose precision may be better than the Pound-Drever scheme.

Our mechanical resonator not only presents resonant modes but also a mechanical background where the tails of all resonances interfere either constructively or destructively. During this work, it has been decided to work out-of-mechanical resonance for three reasons: (i) we have seen that our resonators potentially present a response to radiation pressure out-of-resonance up to 100 times better than at resonance, (ii) thermal noise out-of-resonance is much smaller (~ 30 dB) than at resonance, which helps to relax the stability criterion and (iii) the frequency span can be substantially increased out-of-resonance (10 kHz, compared to a few Hz at resonance). For these reasons, we have designed an experimental protocol in order to demonstrate quantum optomechanical-correlations at room temperature and out of resonance. We have combined the lock-in scheme (low-frequency) and Pound-Drever-Hall error signal (high frequency) in order to stabilize the laser frequency onto the measurement cavity. We have also used a third spectrum analyzer in order to measure in real-time the detuning of the cavity and link it to the measured correlations. This way, we have demonstrated that a post-selection treatment of the acquired correlations in order to reject high-level contamination points may lead to a relaxation of the stability criterion.

The major experimental difficulty being the poor signal-to-noise ratio provided by our movable mirror cavity ($\sim 10^{-5}$ at an incident power of 1 mW) the next steps in order to demonstrate quantum radiation-pressure effects are the update of our resonators. Actually, two different approaches are investigated at the same time. First, similar plano-convex movable mirrors, but this time made of quartz which may provide the possibility of low-temperature operation.

Second, low-mass, high-Q micro-pillars are also developed by the group in order to perform experiments at mechanical resonance with a more favourable signal-to-noise ratio.

Bibliography

- [1] J. Taylor and J. Weisberg, “A new test of general relativity-Gravitational radiation and the binary pulsar PSR 1913+ 16,” *The Astrophysical Journal*, vol. 253, pp. 908–920, 1982. (Cited on page 2.)
- [2] R. Hulse and J. Taylor, “DISCOVERY OF A PULSAR IN A BINARY SYSTEM,” *The Astrophysical Journal*, vol. 195, pp. L51–L53, 1975. (Cited on page 2.)
- [3] N. Mio and K. Tsubono, “Vibration transducer using an ultrashort Fabry-Perot cavity,” *Applied Optics*, vol. 34, no. 1, pp. 186–189, 1995. (Cited on page 2.)
- [4] M. Bernardini, S. Braccini, C. Bradaschia, G. Cella, E. Cuoco, E. D’Ambrosio, V. Dattilo, R. De Salvo, A. di Virgilio, F. Fidicaro, *et al.*, “Plane parallel mirrors Fabry-Perot cavity to improve Virgo superattenuators,” *Physics Letters A*, vol. 243, no. 4, pp. 187–194, 1998. (Cited on page 2.)
- [5] I. Tittonen, G. Breitenbach, T. Kalkbrenner, T. Müller, R. Conradt, S. Schiller, E. Steinsland, N. Blanc, and N. De Rooij, “Interferometric measurements of the position of a macroscopic body: Towards observation of quantum limits,” *Physical Review A*, vol. 59, no. 2, pp. 1038–1044, 1999. (Cited on page 2.)
- [6] Y. Hadjar, P. Cohadon, C. Aminoff, M. Pinard, and A. Heidmann, “High-sensitivity optical measurement of mechanical Brownian motion,” *EPL (Europhysics Letters)*, vol. 47, p. 545, 1999. (Cited on page 2.)
- [7] A. Heidmann and S. Reynaud, “Photon noise reduction by reflection from a movable mirror,” *Physical Review A*, vol. 50, no. 5, pp. 4237–4243, 1994. (Cited on page 2.)
- [8] C. Fabre, M. Pinard, S. Bourzeix, A. Heidmann, E. Giacobino, and S. Reynaud, “Quantum-noise reduction using a cavity with a movable mirror,” *Physical Review A*, vol. 49, no. 2, pp. 1337–1343, 1994. (Cited on page 2.)
- [9] R. Weiss, “Electromagnetically coupled broadband gravitational antenna,” *Quart. Progress LIGO*, pp. 1–23, Oct 1972. (Cited on page 5.)
- [10] C. Bradaschia, R. Del Fabbro, A. Di Virgilio, A. Giazotto, H. Kautzky, V. Montelatici, A. Passuello, *et al.*, “The VIRGO Project: A wide band antenna for gravitational wave detection,” *Nuclear Instruments and Methods in Physics Research Section A: Accelerators, Spectrometers, Detectors and Associated Equipment*, vol. 289, no. 3, pp. 518–525, 1990. (Cited on page 5.)
- [11] B. Abbott, R. Abbott, R. Adhikari, A. Ageev, B. Allen, R. Amin, S. Anderson, W. Anderson, M. Araya, H. Armandula, *et al.*, “Detector description and performance for the first coincidence observations between LIGO and GEO,” *Nuclear Instruments and Methods in Physics Research Section A: Accelerators, Spectrometers, Detectors and Associated Equipment*, vol. 517, no. 1-3, pp. 154–179, 2004. (Cited on page 5.)

- [12] B. Willke *et al.*, “GEO600: status and plans,” *Classical and Quantum Gravity*, vol. 24, p. S389, 2007. (Cited on page 5.)
- [13] R. Takahashi, K. Arai, D. Tatsumi, M. Fukushima, T. Yamazaki, M. Fujimoto, K. Agatsuma, Y. Arase, N. Nakagawa, A. Takamori, *et al.*, “Operational status of TAMA300 with the seismic attenuation system (SAS),” *Classical and quantum gravity*, vol. 25, p. 114036, 2008. (Cited on page 5.)
- [14] D. Blair, P. BARRIGA, A. Brooks, P. Charlton, D. Coward, J. Dumas, Y. Fan, D. Galloway, S. Gras, D. Hosken, *et al.*, “The Science benefits and preliminary design of the southern hemisphere gravitational wave detector AIGO,” in *Journal of Physics: Conference Series*, vol. 122, p. 012001, IOP Publishing, 2008. (Cited on page 5.)
- [15] C. M. Caves, “Quantum-mechanical radiation-pressure fluctuations in an interferometer,” *Phys. Rev. Lett.*, vol. 45, p. 75, Jul 1980. (Cited on pages 5 and 11.)
- [16] C. M. Caves, “Quantum-mechanical noise in an interferometer,” *Physical Review D (Particles and Fields)*, vol. 23, p. 1693, Apr 1981. (Cited on page 5.)
- [17] G. Grynberg, A. Aspect, C. Fabre, and C. Cohen-Tannoudji, *Introduction to Quantum Optics: From the Semi-classical Approach to Quantized Light*. Cambridge University Press, Oct. 2010. (Cited on page 7.)
- [18] S. Reynaud and A. Heidmann, “A semiclassical linear input output transformation for quantum fluctuations,” *Optics Communications*, vol. 71, p. 209, May 1989. (Cited on page 8.)
- [19] E. G. C. F. S. Reynaud, A. Heidmann, “Quantum fluctuations in optical systems.,” *E. Wolf, (Ed.), Progress in optics*, pp. 1–226, Sept 1992. (Cited on pages 8 and 66.)
- [20] C. Fabre and S. Reynaud, “Fundamental Systems in Quantum Optics,” *1990 Les Houches Lectures*, 1992. (Cited on page 8.)
- [21] S. Reynaud, C. Fabre, E. Giacobino, and A. Heidmann, “Photon noise reduction by passive optical bistable systems,” *Physical Review A*, vol. 40, no. 3, pp. 1440–1446, 1989. (Cited on page 11.)
- [22] H. Kogelnik and T. Li, “Laser beams and resonators,” *Appl. Opt.*, vol. 5, pp. 1550–1567, Oct 1966. (Cited on page 15.)
- [23] L. D. Landau, L. P. Pitaevskii, E. M. Lifshitz, and A. M. Kosevich, *Theory of Elasticity, Third Edition: Volume 7 (Theoretical Physics)*. Butterworth-Heinemann, 3 ed., Jan. 1986. (Cited on pages 18, 21 and 45.)
- [24] T. Briant, “Caractérisation du couplage optomécanique entre la lumière et un miroir : bruit thermique et effets quantiques,” *PhD Université Pierre et Marie Curie*, pp. 1–226, Oct 2004. (Cited on pages 18, 62, 63, 130, 131, 133, 135 and 138.)
- [25] P. Grangier, R. E. Slusher, B. Yurke, and A. Laporta, “Squeezed-light-enhanced polarization interferometer,” *Physical Review Letters*, vol. 59, p. 2153, Nov 1987. (Cited on page 21.)

- [26] M. Xiao, L.-A. Wu, and H. J. Kimble, “Precision measurement beyond the shot-noise limit,” *Phys. Rev. Lett.*, vol. 59, p. 278, Jul 1987. (Cited on page 21.)
- [27] K. Mckenzie, D. Shaddock, D. McClelland, B. Buchler, and P. Lam, “Experimental demonstration of a squeezing-enhanced power-recycled michelson interferometer for gravitational wave detection,” *Phys. Rev. Lett.*, vol. 88, p. 231102, May 2002. (Cited on page 21.)
- [28] T. Caniard, P. Verlot, T. Briant, P.-F. Cohadon, and A. Heidmann, “Observation of back-action noise cancellation in interferometric and weak force measurements,” *Phys. Rev. Lett.*, vol. 99, p. 110801, Sep 2007. (Cited on page 21.)
- [29] P. Verlot, A. Tavernarakis, T. Briant, P.-F. Cohadon, and A. Heidmann, “Backaction amplification and quantum limits in optomechanical measurements,” *Phys. Rev. Lett.*, vol. 104, p. 133602, Mar 2010. (Cited on pages 21 and 72.)
- [30] M. T. Jaekel and S. Reynaud, “Quantum limits in interferometric measurements,” *Europhysics Letters*, vol. 13, pp. 1–7, Aug 1990. (Cited on page 21.)
- [31] T. Caniard, “Couplage optomécanique, action en retour et limites quantiques dans les mesures optique ultrasensibles,” *PhD Université Pierre et Marie Curie*, pp. 1–226, Sept 2007. (Cited on pages 22, 41 and 94.)
- [32] V. Braginsky and Y. Vorontsov, “Quantum-mechanical limitations in macroscopic experiments and modern experimental technique,” *Usp. Fiz. Nauk*, vol. 114, pp. 41–53, 1974. (Cited on page 24.)
- [33] V. Braginsky, Y. Vorontsov, and F. Khalili, “Quantum singularities of a ponderomotive meter of electromagnetic energy,” *Zh. Eksp. Teor. Fiz.*, vol. 73, pp. 1340–1343, 1977. (Cited on page 24.)
- [34] K. Thorne, R. Drever, C. Caves, M. Zimmermann, and V. Sandberg, “Quantum nondemolition measurements of harmonic oscillators,” *Phys. Rev. Lett.*, vol. 40, pp. 667–671, 1978. (Cited on page 24.)
- [35] W. Unruh, “Quantum nondemolition measurements of harmonic oscillators,” *Phys. Rev. B*, vol. 19, pp. 2888–2896, 1979. (Cited on page 24.)
- [36] V. B. Braginsky, F. Y. Khalili, and K. S. Thorne, *Quantum Measurement*. Cambridge University Press, first paperback edition ed., May 1995. (Cited on page 24.)
- [37] F. Biraben and P. Labastie, “Balayage d’un laser a colorant continu monomode sur 150 GHz,” *Optics Communications*, vol. 41, no. 1, pp. 49 – 51, 1982. (Cited on page 28.)
- [38] E. D. Black, “An introduction to Pound–Drever–Hall laser frequency stabilization,” *American Journal of Physics*, vol. 69, pp. 79–87, Jan. 2001. (Cited on page 33.)
- [39] U. Leonhardt and H. Paul, “Measuring the quantum state of light,” *Prog. Quant. Elect.*, vol. 19, p. 89, 1995. (Cited on page 37.)
- [40] O. Arcizet, “Mesure optique ultrasensible et refroidissement par pression de radiation d’un micro-résonateur mécanique.” *PhD Université Pierre et Marie Curie*, pp. 1–226, Sept 2006. (Cited on pages 40, 119, 132 and 133.)

- [41] T. Briant, P. F. Cohadon, M. Pinard, and A. Heidmann, “Optical phase-space reconstruction of mirror motion at the attometer level,” *The European Physical Journal D*, vol. 22, p. 131, Jan 2003. (Cited on pages 44 and 49.)
- [42] P. F. Cohadon, A. Heidmann, and M. Pinard, “Cooling of a mirror by radiation pressure,” *Phys. Rev. Lett.*, vol. 83, p. 3174, Oct 1999. (Cited on pages 45 and 146.)
- [43] T. Briant, M. Cerdonio, L. Conti, A. Heidmann, A. Lobo, and M. Pinard, “Thermal and back-action noises in dual-sphere gravitational-wave detectors,” *Physical Review D*, vol. 67, p. 102005, May 2003. (Cited on pages 47 and 66.)
- [44] T. Corbitt, Y. Chen, E. Innerhofer, H. Müller-Ebhardt, D. Ottaway, H. Rehbein, D. Sigg, S. Whitcomb, C. Wipf, and N. Mavalvala, “An all-optical trap for a gram-scale mirror,” *Phys. Rev. Lett.*, vol. 98, p. 150802, Apr 2007. (Cited on page 49.)
- [45] T. Corbitt, D. Ottaway, E. Innerhofer, J. Pelc, and N. Mavalvala, “Measurement of radiation-pressure-induced optomechanical dynamics in a suspended Fabry-Perot cavity,” *Phys. Rev. A*, vol. 74, p. 021802, Aug 2006. (Cited on page 49.)
- [46] T. Antoni, A. G. Kuhn, T. Briant, P.-F. Cohadon, A. Heidmann, R. Braive, A. Beveratos, I. Abram, L. Le Gratiet, I. Sagnes, and I. Robert-Philip, “Deformable two-dimensional photonic crystal slab for cavity optomechanics,” *Optics Letters*, vol. 36, pp. 3434–3436, SEP 1 2011. (Cited on page 49.)
- [47] T. Antoni, K. Makles, R. Braive, T. Briant, P.-F. Cohadon, I. Sagnes, I. Robert-Philip, and A. Heidmann, “Nonlinear mechanics with suspended nanomembranes,” *EPL (Europhysics Letters)*, vol. 100, no. 6, p. 68005, 2012. (Cited on page 49.)
- [48] A. G. Kuhn, M. Bahriz, O. Ducloux, C. Chartier, O. Le Traon, T. Briant, P. F. Cohadon, A. Heidmann, C. Michel, L. Pinard, and R. Flaminio, “A micropillar for cavity optomechanics,” *Applied Physics Letters*, vol. 99, Sep 19 2011. (Cited on page 49.)
- [49] D. Kleckner and D. Bouwmeester, “Sub-kelvin optical cooling of a micromechanical resonator,” *Nature*, vol. 444, pp. 75–78, Nov2 2006. (Cited on page 49.)
- [50] S. Gröblacher, J. B. Hertzberg, M. R. Vanner, G. D. Cole, S. Gigan, K. C. Schwab, and M. Aspelmeyer, “Demonstration of an ultracold micro-optomechanical oscillator in a cryogenic cavity,” *Nature Physics*, vol. 5, pp. 485–488, June 2009. (Cited on page 49.)
- [51] J. Hofer, A. Schliesser, and T. J. Kippenberg, “Cavity optomechanics with ultrahigh- q crystalline microresonators,” *Phys. Rev. A*, vol. 82, p. 031804, Sep 2010. (Cited on page 49.)
- [52] A. Schliesser, P. Del’Haye, N. Nooshi, K. J. Vahala, and T. J. Kippenberg, “Radiation pressure cooling of a micromechanical oscillator using dynamical backaction,” *Phys. Rev. Lett.*, vol. 97, p. 243905, Dec 2006. (Cited on page 49.)
- [53] L. Ding, C. Baker, P. Senellart, A. Lemaitre, S. Ducci, G. Leo, and I. Favero, “High Frequency GaAs Nano-Optomechanical Disk Resonator,” *Phys. Rev. Lett.*, vol. 105, p. 263903, Dec 2010. (Cited on page 49.)

- [54] K. H. Lee, T. G. McRae, G. I. Harris, J. Knittel, and W. P. Bowen, “Cooling and control of a cavity optoelectromechanical system,” *Phys. Rev. Lett.*, vol. 104, p. 123604, Mar 2010. (Cited on page 49.)
- [55] E. Gavartin, P. Verlot, and T. J. Kippenberg, “A hybrid on-chip optomechanical transducer for ultrasensitive force measurements,” *Nat Nano*, vol. 7, no. 8, pp. 509–514, 2012. 10.1038/nnano.2012.97. (Cited on pages 49 and 146.)
- [56] J. D. Thompson, B. M. Zwickl, A. M. Jayich, F. Marquardt, S. M. Girvin, and J. G. E. Harris, “Strong dispersive coupling of a high-finesse cavity to a micromechanical membrane,” *Nature*, vol. 452, pp. 72–75, Mar. 2008. (Cited on pages 49 and 73.)
- [57] E. Gavartin, R. Braive, I. Sagnes, O. Arcizet, A. Beveratos, T. J. Kippenberg, and I. Robert-Philip, “Optomechanical coupling in a two-dimensional photonic crystal defect cavity,” *Phys. Rev. Lett.*, vol. 106, p. 203902, May 2011. (Cited on page 49.)
- [58] M. Eichenfield, R. Camacho, J. Chan, K. J. Vahala, and O. Painter, “A picogram- and nanometre-scale photonic-crystal optomechanical cavity,” *Nature*, vol. 459, pp. 550–555, May 2009. (Cited on page 49.)
- [59] J. Chan, T. P. M. Alegre, A. H. Safavi-Naeini, J. T. Hill, A. Krause, S. Gröblacher, M. Aspelmeyer, and O. Painter, “Laser cooling of a nanomechanical oscillator into its quantum ground state,” *Nature*, vol. 478, pp. 89–92, Oct. 2011. (Cited on page 49.)
- [60] K. Børkje, A. Nunnenkamp, B. M. Zwickl, C. Yang, J. G. E. Harris, and S. M. Girvin, “Observability of radiation-pressure shot noise in optomechanical systems,” *Phys. Rev. A*, vol. 82, p. 013818, Jul 2010. (Cited on page 50.)
- [61] J. Laurent, A. Mosset, O. Arcizet, J. Chevrier, S. Huant, and H. Sellier, ““Negative” Backaction Noise in Interferometric Detection of a Microlever,” *Phys. Rev. Lett.*, vol. 107, p. 050801, Jul 2011. (Cited on page 50.)
- [62] F. Marino, F. S. Cataliotti, A. Farsi, M. S. de Cumis, and F. Marin, “Classical signature of ponderomotive squeezing in a suspended mirror resonator,” *Phys. Rev. Lett.*, vol. 104, p. 073601, Feb 2010. (Cited on page 50.)
- [63] J. B. Hertzberg, T. Rocheleau, T. Ndukum, M. Savva, A. A. Clerk, and K. C. Schwab, “Back-action-evading measurements of nanomechanical motion,” *Nature Physics*, vol. 6, pp. 213–217, Dec. 2009. (Cited on page 50.)
- [64] Y. M. Sua and K. F. Lee, “Macroscopic mechanical correlations using single-photon spatial compass state and operational Wigner distribution,” *Phys. Rev. A*, vol. 85, p. 062113, Jun 2012. (Cited on page 50.)
- [65] M. Tsang and C. M. Caves, “Coherent quantum-noise cancellation for optomechanical sensors,” *Phys. Rev. Lett.*, vol. 105, p. 123601, Sep 2010. (Cited on page 50.)
- [66] T. P. Purdy, R. W. Peterson, and C. A. Regal, “Observation of Radiation Pressure Shot Noise on a Macroscopic Object,” *Science*, vol. 339, pp. 801–804, Feb. 2013. (Cited on page 50.)

- [67] O. Arcizet, R. Rivière, A. Schliesser, G. Anetsberger, and T. J. Kippenberg, “Cryogenic properties of optomechanical silica microcavities,” *Phys. Rev. A*, vol. 80, p. 021803, Aug 2009. (Cited on page 51.)
- [68] George and M. E. Muller, “A note on the generation of random normal deviates,” *Ann. Math. Stat.*, vol. 29, no. 2, pp. 610–611, 1958. (Cited on page 57.)
- [69] P. Verlot, A. Tavernarakis, T. Briant, P.-F. Cohadon, and A. Heidmann, “Scheme to probe optomechanical correlations between two optical beams down to the quantum level,” *Phys. Rev. Lett.*, vol. 102, p. 103601, Mar 2009. (Cited on page 59.)
- [70] P. Verlot, “Etudes des effets de pression de radiation et des limites quantiques du couplage optomécanique,” *PhD Université Pierre et Marie Curie*, pp. 1–226, Sept 2010. (Cited on pages 66, 71, 137, 139 and 142.)
- [71] G. C. Wick, “The evaluation of the collision matrix,” *Phys. Rev.*, vol. 80, pp. 268–272, Oct 1950. (Cited on page 68.)
- [72] P. Verlot, A. Tavernarakis, T. Briant, P.-F. Cohadon, and A. Heidmann, “Experimentally measuring quantum optomechanical correlations,” *NJP*, 2012. (Cited on pages 70 and 145.)
- [73] O. Arcizet, T. Briant, A. Heidmann, and M. Pinard, “Beating quantum limits in an optomechanical sensor by cavity detuning,” *Phys. Rev. A*, vol. 73, p. 033819, Mar 2006. (Cited on page 72.)
- [74] O. Arcizet, P. F. Cohadon, T. Briant, M. Pinard, and A. Heidmann, “Radiation-pressure cooling and optomechanical instability of a micro-mirror,” *Nature*, vol. 444, p. 71, 2006. (Cited on pages 72, 73 and 119.)
- [75] C. Molinelli, “Interaction optomécanique à trois modes et refroidissement d’un micro-résonateur mécanique,” *PhD Université Pierre et Marie Curie*, pp. 1–226, Jul 2011. (Cited on page 72.)
- [76] S. Gigan, H. R. Böhm, M. Paternostro, F. Blaser, G. Langer, J. B. Hertzberg, K. C. Schwab, D. Bäuerle, M. Aspelmeyer, and A. Zeilinger, “Self-cooling of a micromirror by radiation pressure,” *Nature*, vol. 444, pp. 67–70, Nov. 2006. (Cited on page 73.)
- [77] A. Schliesser, R. Riviere, G. Anetsberger, O. Arcizet, and T. J. Kippenberg, “Resolved-sideband cooling of a micromechanical oscillator,” *Nature Physics*, vol. 4, pp. 415–419, Apr. 2008. (Cited on page 73.)
- [78] I. Wilson-Rae, N. Nooshi, W. Zwerger, and T. J. Kippenberg, “Theory of ground state cooling of a mechanical oscillator using dynamical backaction,” *Phys. Rev. Lett.*, vol. 99, p. 093901, Aug 2007. (Cited on page 73.)
- [79] F. Marquardt, J. P. Chen, A. A. Clerk, and S. M. Girvin, “Quantum theory of cavity-assisted sideband cooling of mechanical motion,” *Phys. Rev. Lett.*, vol. 99, p. 093902, Aug 2007. (Cited on page 73.)
- [80] Y. Hadjar, “Etude du couplage optomecanique dans une cavite de grande finesse. observation du mouvement brownien d’un miroir,” *PhD Université Pierre et Marie Curie*, pp. 1–226, Sept 1999. (Cited on pages 82 and 84.)

-
- [81] J. Poirson, F. Bretenaker, M. Vallet, and A. L. Floch, “Analytical and experimental study of ringing effects in a fabry–perot cavity. application to the measurement of high finesses,” *J. Opt. Soc. Am. B*, vol. 14, pp. 2811–2817, Nov 1997. (Cited on pages 88, 92 and 93.)
- [82] E. A. Donley, T. P. Heavner, F. Levi, M. O. Tataw, and S. R. Jefferts, “Double-pass acousto-optic modulator system,” *Review of Scientific Instruments*, vol. 76, no. 6, p. 063112, 2005. (Cited on page 106.)
- [83] J. Sathian and E. Jaatinen, “Intensity dependent residual amplitude modulation in electro-optic phase modulators,” *Appl. Opt.*, vol. 51, pp. 3684–3691, Jun 2012. (Cited on pages 123 and 133.)
- [84] Y. Levin, “Internal thermal noise in the ligo test masses: A direct approach,” *Phys. Rev. D*, vol. 57, pp. 659–663, Jan 1998. (Cited on page 137.)
- [85] F. Bondu, P. Hello, and J. Y. Vinet, “Thermal noise in mirrors of interferometric gravitational wave antennas,” *Physics Letters A*, vol. 246, no. 3-4, pp. 227–236, 1998. (Cited on page 137.)
- [86] Y. T. Liu and K. S. Thorne, “Thermoelastic Noise and Homogeneous Thermal Noise in Finite Sized Gravitational-Wave Test Masses,” *Physical Review D*, vol. 62, no. 12, p. 10, 2000. (Cited on page 137.)
- [87] V. B. Braginsky, M. L. Gorodetsky, and S. P. Vyatchanin, “Thermodynamical fluctuations and photo-thermal shot noise in gravitational wave antennae,” *Physics Letters A*, vol. 264, no. December, p. 20, 1999. (Cited on page 137.)